

**Developing novel nano-structured  
dielectric materials for energy  
applications using gel coating  
nanotechnology**

James Thomas Rawlings

A thesis submitted in partial fulfilment of the requirements of  
Nottingham Trent University for the degree of  
Doctor of Philosophy

September 2020

This work is the intellectual property of the author, and may also be owned by Nottingham Trent University. You may copy up to 5% of this work for private study, or personal, non-commercial research. Any re-use of the information contained within this document should be fully referenced, quoting the author, title, university, degree level and pagination. Queries or requests for any other use, or if a more substantial copy is required, should be directed in the owner(s) of the Intellectual Property Rights.

*“Sir Isaac Newton, renowned inventor of the milled-edge coin and the catflap!”*

*“The what?” said Richard.*

*“The catflap! A device of the utmost cunning, perspicuity and invention. It is a door within a door, you see, a ...”*

*“Yes,” said Richard, “there was also the small matter of gravity.”*

*“Gravity,” said Dirk with a slightly dismissive shrug, “yes, there was that as well, I suppose. Though that, of course, was merely a discovery. It was there to be discovered.” ... “You see?” he said dropping his cigarette butt, “They even keep it on at weekends. Someone was bound to notice sooner or later. But the catflap ... ah, there is a very different matter. Invention, pure creative invention. It is a door within a door, you see.”*

Douglas Adams,

*Dirk Gently’s Holistic Detective Agency*

## Acknowledgements

Doing this PhD has been a journey to summarise it simply. But it was a journey worth taking. There are several people who deserve thanks for being a part of this with me, first and foremost my director of studies Dr Fengge Gao, who has tirelessly worked to help me become a more competent researcher, and always found time for me when I've needed it. I'll remember fondly our early morning and late evening chats in the Cat lab. My second bout of thanks goes to my second supervisor Professor Carl Brown, for his constant support and encouragement and always making time for science despite how busy he may have been, not to mention keeping my head in the physics. My thanks go to our research group too; Elena and Isaiah you know what the journey of a PhD is like, and I'll always laugh at the complaining we used to do about it.

I am also very grateful to the technical support at NTU across both Chemistry and Physics for helping to teach me how to work equipment, the best way to run and experiment, and fixing all manner of issues, Mary (I hope you're enjoying your much deserved retirement!), Mike, Ellen and Graham thanks for all the help. The work in this thesis would also not be possible without the combined efforts of our wider collaborators; Dr Matthew Krzystyniak and Dr Giovanni Romanelli from Rutherford Labs for helping us to perform neutron based experiments and Prof. George Chen, Haowei and Luming of the University of Southampton for subjecting our materials to significantly high voltage and helping us understand the results. I am also very grateful to the DTA in Energy scheme for providing funding for this PhD project, and bringing in a diverse cohort of science to explore.

Finally, to my friends, family I am grateful for the never ending support you have provided, even if the majority of you don't really know what it is I do. Within said group I would like to give a special thanks to Jack, for being there when needed and providing unconditional support.

## **Abstract**

Sustainable systems are required in order to tackle the major issue of energy saving. The motivation in this project is focused on energy conversion rates within electrical generators, with particular focus on the electrical insulation material. While the current state-of-the-art technology uses nanocomposite technology, nanoparticle fillers embedded within a polymer matrix, current generators employ microcomposite technology, typically formed of polymer and micro sized mica flakes. While this technology shows great promise as insulation material, it is not to say there are no drawbacks. One of the biggest challenges for the production of filler loaded composite materials, are producing well dispersed matrices, as the particles tend to agglomerate and fail to provide the predicted performance. Along with this issue there are also problems with compatibility between filler particles and polymer matrices. For example, hydrophilic particles show poor affinity within a hydrophobic polymer network.

The aim of this study is to develop a novel nano-structured dielectric material, through the use of gel coatings, to produce a continuous layer-structured material. Following this approach allows filler dispersion problems to be overcome, and compatibility can be increased through surface modification, without removing the dielectric properties that are desired.

In this investigation the focus is on nanoclay particles from within the smectite family, due to both their self-cross linking behaviour and use within the field of clay-polymer nanocomposites. The gel forming ability of two types of commercial nanoclay, Cloisite Na<sup>+</sup> and Lucentite SWN, and an understanding of their differing gel forming ability is discussed. Of particular importance in nanoclay materials, and other 2-D structured materials, the separation of the layers is a particular challenge. Through the use of liquid shear exfoliation techniques, the exfoliation of clay layers was successfully

achieved within water, providing a method that produces high yield of single layers, while avoiding the common use of organic solvents in order to achieve the result. Dynamic light scattering, zeta potential and rheological studies of the colloidal nature of these clay show a dependence on the colloid concentration for particle interaction and aggregation to form a gel network. The differing ability to form a gel between the two types of clay, has been determined by the use of neutron compton scattering and is related to the nature of particle-particle and particle-water bonding interactions. The smaller aspect ratio SWN shows a greater tendency to form particle-particle bonds, likely attributed to the smaller path length for collisions and also the larger number density of particles at a given concentration in comparison to Cloisite Na<sup>+</sup>. Using the lower gelling concentration ability of SWN, hybrid clay gels have also been formed, allowing for lower mass loadings of clay within the gel used for coating, confirmed by thermogravimetric methods. The formation of hybrid gel systems shows the promise that SWN can be used as an initiator with non-gelling nanoparticle species such as hexagonal boron nitride, to form hybrid gel coatings. This allows further additions to the coating properties to be provided such as greater thermal conductivity or non-linear conduction behaviour.

The produced gel materials were used to produce coatings on low density polyethylene (LDPE) films, due to both the use of LDPE within insulation materials and also the challenges associated with dispersal of hydrophilic nano fillers within the hydrophobic LPDE polymer matrix. Through a combination of UV irradiation ( $\lambda = 184.9$  and  $253.7$  nm) and layer-by-layer surface modification methods, the surface properties were transformed to become more hydrophilic, as shown by measurement of the contact angle of water on the surface, allowing the simple production of a continuous gel coating upon the polymer. The loading of clay within the coating was determined through the use of thermogravimetric analysis, and a relation is seen between the relative mass percentage of the coating and the applied coating thickness. Observation of coated polymers observed by scanning electron microscopy show that there is a dependence upon the ap-

plied thickness to preventing the surface forming cracks, which subsequently effect the electrical performance. Preliminary results on the dielectric behaviour show a poorer than predicted performance in the electrical breakdown strength, with only SWN coating showing an increase to the DC breakdown strength. Dielectric spectroscopy shows the samples possess loss peaks centred around 50 Hz, which would lead to issues for domestic power application, however it is expected this peak could be present due to water molecules hydrogen bonded to the hydroxyl surface groups within the clay. Analysis of the surface properties shed insight into the reasoning for this. Mapping of the surface uniformity through contact angle measurements showed regions of surface inhomogeneity for samples with applied coating of 75  $\mu\text{m}$ , which when increased to a 200  $\mu\text{m}$  coating significant improvement to sample uniformity is seen. Thus, it is proposed the surface uniformity plays a significant role in the dielectric properties, and thicker applied films should lead to the improved performance predicted. Further factors specific to the use of nanoclay materials is careful consideration of any excess charge carrying species such as adsorbed water molecules and cations, present within the clay structure. Vacuum drying techniques shows that the water content within the film can be reduced and this is expected to reduce undesirable conduction behaviour. The results presented within this study show a deep understanding of the gelling properties of two commercial nanoclay materials, that can be exploited to produce surface coatings for new dielectric materials. However, these are preliminary results of this technology, and subsequent study of the coating thickness, water content and adsorbed species will allow greater understanding of the electrical behaviour, and help to deliver the desired dielectric performance.

## **Declaration**

The work described in this thesis was carried out by myself and, where indicated, in collaboration with colleagues. The data analysis and interpretation is my own work. This thesis has been written entirely by myself.

James T. Rawlings B.Sc. M.Res. MInstP

# Contents

<b>1</b>	<b>Introduction</b>	<b>1</b>
1.1	Introduction . . . . .	2
1.2	The aim of this thesis . . . . .	3
1.3	Thesis outline . . . . .	4
<b>2</b>	<b>The need for development of new insulating materials</b>	<b>6</b>
2.1	Principles of electrical conduction . . . . .	7
2.2	Fundamentals of dielectric materials . . . . .	9
2.2.1	Electrical dipole moment . . . . .	9
2.2.2	Polarisation and permittivity . . . . .	12
2.2.3	Types of polarisation . . . . .	15
2.2.4	Dielectric relaxation . . . . .	23
2.3	The key parameters leading to the failure of insulation materials . . . . .	24
2.3.1	Electrical ageing . . . . .	25
2.3.2	Electrical discharge . . . . .	25
2.3.3	Electrical breakdown . . . . .	26
2.4	Introduction to nanocomposites . . . . .	35
2.5	The road from micro to nano . . . . .	36
2.6	High-voltage uses of nanocomposites . . . . .	37
2.7	Choices of polymer and filler material . . . . .	39
2.7.1	Polymers . . . . .	39
2.7.2	Filler particles . . . . .	40

2.7.3	Filler treatment processes . . . . .	42
2.8	The interfacial region between polymer and particle . . . . .	43
2.9	Electrical performance of nanocomposites . . . . .	45
2.9.1	Permittivity . . . . .	45
2.9.2	Partial discharges . . . . .	46
2.9.3	Space charges . . . . .	48
2.9.4	Electrical breakdown strength . . . . .	49
2.10	Thermal properties of nanocomposites . . . . .	50
2.11	The outlook for nanocomposite technology . . . . .	52
<b>3</b>	<b>Experimental methodologies</b>	<b>53</b>
3.1	Materials . . . . .	54
3.2	Microscopical analysis . . . . .	54
3.2.1	Optical microscopy . . . . .	54
3.2.2	Scanning electron microscopy . . . . .	55
3.3	X-Ray diffractometry . . . . .	56
3.4	Chemical composition . . . . .	57
3.5	Surface charge . . . . .	57
3.6	Contact angle measurements . . . . .	61
3.7	Surface free energy . . . . .	62
3.7.1	Owens-Wendt-Rabel-Kälble model . . . . .	62
3.7.2	Inverse gas chromatography . . . . .	64
3.8	Adsorption isotherms . . . . .	67
3.8.1	Surface area determination . . . . .	69
3.8.2	Pore size analysis . . . . .	71
3.9	Thermogravimetric analysis . . . . .	75
3.10	Dynamic light scattering . . . . .	75
3.10.1	Particle aggregation . . . . .	78
3.11	Zeta potential . . . . .	80
3.12	Rheology . . . . .	82

3.12.1	Viscosity and elasticity . . . . .	82
3.12.2	Viscoelasticity . . . . .	84
3.13	Neutron Compton scattering . . . . .	86
3.14	Electrical testing . . . . .	90
3.14.1	Dielectric spectroscopy . . . . .	90
3.14.2	Electrical conductivity . . . . .	92
3.14.3	Electrical breakdown strength . . . . .	93
<b>4</b>	<b>Structure, morphology and properties of the applied clays</b>	<b>95</b>
4.1	The micro structure of the clay . . . . .	96
4.1.1	SEM analysis . . . . .	96
4.1.2	Particle size distribution . . . . .	98
4.2	Nano structures of the clays . . . . .	103
4.2.1	Particle inter-planar spacing . . . . .	103
4.3	Physical and chemical properties . . . . .	105
4.3.1	Chemical structure of the clay . . . . .	105
4.3.2	Surface charge . . . . .	108
4.3.3	Surface free energy . . . . .	111
4.3.4	Surface area and porosity . . . . .	116
4.3.5	The thermal stability of clay . . . . .	122
4.4	Summary . . . . .	124
<b>5</b>	<b>The stability and gelling behaviour of clay colloids</b>	<b>126</b>
5.1	Liquid phase exfoliation of clay particles . . . . .	127
5.2	Colloidal stability . . . . .	131
5.2.1	The effect of layer exfoliation on colloidal stability . . . . .	133
5.3	The early stages of particle interactions . . . . .	135
5.3.1	The effect of salt concentration on colloidal stability and particle interactions . . . . .	136

5.3.2	The effect of clay concentration on colloidal stability and particle interactions . . . . .	144
5.4	Determination of the type of gel formed . . . . .	150
5.5	Detecting the onset of gelation . . . . .	156
5.5.1	Gelation in clay particle colloids . . . . .	159
5.5.2	Gelation in exfoliated clay particle colloids . . . . .	162
5.6	The role of particle interactions in the gelation process . . . . .	165
5.7	Summary . . . . .	168
<b>6</b>	<b>Development of novel nanodielectric materials</b>	<b>170</b>
6.1	Gel formation in mixed clay systems . . . . .	171
6.2	Preparing the polymeric film for coating . . . . .	174
6.2.1	Transforming the surface from hydrophobic to hydrophilic . . .	176
6.2.2	Improving surface compatibility . . . . .	182
6.3	The structure and morphology of the produced coating. . . . .	185
6.4	Reducing the effect of moisture adsorption . . . . .	193
6.5	Final sample fabrication process . . . . .	196
6.6	Summary . . . . .	197
<b>7</b>	<b>Electrical performance of the developed nanodielectric materials</b>	<b>199</b>
7.1	Samples produced for testing . . . . .	200
7.2	The dielectric response under alternating current . . . . .	200
7.3	High field conductivity . . . . .	206
7.4	Electrical breakdown performance . . . . .	210
7.4.1	Under DC field . . . . .	211
7.4.2	Under AC field . . . . .	213
7.5	Considerations from electrical testing . . . . .	215
7.6	Summary . . . . .	220
<b>8</b>	<b>Summary</b>	<b>222</b>
8.1	Thesis summary . . . . .	223

8.2 Future work . . . . .	225
<b>References</b>	<b>227</b>

# List of Figures

2.1	Schematic diagram of the electronic band structure in different materials at equilibrium. Black shading represents filled states and white shading unfilled states. For metals the Fermi level $E_F$ lies within at least one band, for semiconducting materials and insulators $E_F$ lies within a band gap but for the case of semiconductors electrons can be thermally excited into the next band due to the close placement to the $E_F$ . . . . .	8
2.2	Schematic showing the formation of an electric dipole moment between two oppositely charged point sources. . . . .	9
2.3	Charge distribution of $\text{CO}_2$ . Blue and red coloured regions represent negative and positively charged regions, respectively. The bond dipoles are shown by the black arrows. Since the dipole moments of the Carbon-Oxygen bonds, point in opposite parallel directions, this leads to a net zero dipole moment. . . . .	11
2.4	Charge distribution of $\text{H}_2\text{O}$ . Blue and red coloured regions represent negative and positively charged regions, respectively. The bond dipoles are shown by the black arrows. The dipole moment of the Hydrogen-Oxygen bonds point in the same direction at an angle of $104.5^\circ$ , which leads to a net dipole moment of 1.84 D for the molecule, as shown by the blue arrow. . . . .	11
2.5	Schematic diagram for determination of the local electric field at a dipole.	14
2.6	Electronic polarisation of an atom. Note that the presence of an electric field causes a shift in the charge centres of the nucleus and electron cloud.	16

2.7	Ionic polarisation of a material. The presence of an electric field causes a shift of the positive and negative charge centres towards each other, away from their equilibrium positions. . . . .	17
2.8	The effect of orientational polarisation on a material. The electric field causes the dipoles to align with the electric field lines. . . . .	19
2.9	Schematic plot of the Langevin function (blue curve). The black dashed line represents a line of gradient $\frac{1}{3}$ for the scenario where $\vec{\mu}E/k_B T \ll 1$ . . . . .	20
2.10	Variation of the relative permittivity with temperature for (a) Nitrobenzene adapted with permission from [11], Copyright ©1930, Springer Nature and (b) Hydrogen Sulfide adapted with permission from [12], Copyright ©1934, American Chemical Society. . . . .	21
	(a) Nitrobenzene, $C_6H_5NO_2$ . . . . .	21
	(b) Hydrogen sulfide, $H_2S$ . . . . .	21
2.11	Schematic diagrams showing mechanisms of partial discharge. Sub-figures (a)-(d) represent the effects discussed in the main body of text. . . . .	27
	(a) Corona . . . . .	27
	(b) Surface . . . . .	27
	(c) Internal . . . . .	27
	(d) Treeing . . . . .	27
2.12	Schematic diagram showing the band structure of a dielectric solid, and the associated electron trap energy states. . . . .	31
2.13	Schematic diagram showing Zener tunnelling of an electron from the valence band to the conduction band, under a high external electric field. . . . .	32
2.14	Schematic diagram showing Tanaka's multi-core model. Adapted with permission from [59], ©2005, IEEE. The white shaded circle represents the nanoparticle, with the yellow ring showing the 1 <sup>st</sup> bonded layer, the purple ring showing the 2 <sup>nd</sup> bound layer and the blue ring showing the 3 <sup>rd</sup> loose layer. . . . .	44

---

3.1	Left to right: The increasing concentration of surfactant in water leading to the formation of an interfacial layer and subsequent formation of micelles at (or above) the point of CMC. . . . .	59
3.2	Schematic diagram showing the cationic exchange process between inter-layer cations and the introduced surfactant molecules. . . . .	59
3.3	Structural model of the hexadecylpyridium chloride molecule . . . . .	60
3.4	Schematic diagram showing the contact point of a liquid droplet on an ideal solid surface . . . . .	61
3.5	Schematic diagram showing the relationship between contact angle and surface wettability. Sub-figures (A)-(D) represent decreasing contact angle to the surface, and increasing wettability. . . . .	62
3.6	Schematic diagram showing the basic operating principles of iGC. . . . .	64
3.7	Schematic diagram showing the experimental stages in the process of an adsorption isotherm measurement. . . . .	69
3.8	Schematic diagram showing the principles of a DLS experiment, and the resultant scattering signal observed for differing particle sizes. . . . .	76
3.9	Schematic diagram of the electrical double layer and the position of the zeta potential. . . . .	81
3.10	Diagram showing the definition of shear deformation on a material . . . . .	83
3.11	Circuit diagram showing the measurement of impedance for a test sample. . . . .	92
4.1	SEM micrographs of the two types of clay taken at 100× magnification, at 5 kV acceleration voltage. Scale bar represents 100 μm . . . . .	96
	(a) Cloisite Na <sup>+</sup> . . . . .	96
	(b) SWN . . . . .	96
4.2	A schematic representation of the differing structures seen within smectite clay minerals. Sub-figures (a) - (d) show the varying states of a clay crystal leading to the formation of a clay aggregated system. . . . .	97
	(a) Single clay mineral layer . . . . .	97
	(b) System of stacked layers forming a particle . . . . .	97

---

(c)	System of particles forming an aggregate . . . . .	97
(d)	An assembly of aggregates . . . . .	97
4.3	Particle size distributions determined from measurements of the particles in the SEM micrographs. . . . .	98
(a)	Cloisite Na <sup>+</sup> . . . . .	98
(b)	SWN . . . . .	98
4.4	DLS particle size distributions determined for Cloisite Na <sup>+</sup> dispersed in water at 25°C. Sub-figures (a) - (f) show the distributions with the change in clay concentration. . . . .	100
(a)	0.5 wt.% . . . . .	100
(b)	1.0 wt.% . . . . .	100
(c)	1.5 wt.% . . . . .	100
(d)	2.0 wt.% . . . . .	100
(e)	2.5 wt.% . . . . .	100
(f)	3.0 wt.% . . . . .	100
4.5	DLS particle size distributions determined for SWN dispersed in water at 25°C. Sub-figures (a) - (f) show the distributions with the change in clay concentration. . . . .	101
(a)	0.5 wt.% . . . . .	101
(b)	1.0 wt.% . . . . .	101
(c)	1.5 wt.% . . . . .	101
(d)	2.0 wt.% . . . . .	101
(e)	2.5 wt.% . . . . .	101
(f)	3.0 wt.% . . . . .	101
4.6	Possible scenarios developed when clay particles are added into solvent.	102
4.7	Cu source powder XRD spectra of Cloisite Na <sup>+</sup> obtained using orien- tated samples placed on a glass plate. The blue data shows the collected spectra while the red lines represent key <i>hkl</i> peaks obtained from the literature [152]. . . . .	104

4.8	Cu source powder XRD spectra of SWN obtained using orientated samples placed on a glass plate. The blue data shows the collected spectra while the red lines represent key <i>hkl</i> peaks obtained from the literature [153]. . . . .	104
4.9	FTIR spectra of solid Cloisite Na <sup>+</sup> after drying at 150°C for 24 hours. . . . .	106
4.10	FTIR spectra of solid SWN after drying at 150°C for 24 hours. . . . .	106
4.11	FTIR spectra of ultrapure water (18.2 MΩ). . . . .	107
4.12	Determination of the CMC for the cationic surfactant CPC in water. Straight lines show the linear regions used for determination of the CMC point. . . . .	109
4.13	Determination of the CEC for Cloisite Na <sup>+</sup> by measurement of the surface tension at increasing surfactant concentration. . . . .	110
4.14	Determination of the CEC for SWN by measurement of the surface tension at increasing surfactant concentration. . . . .	110
4.15	Surface free energy profile of Cloisite Na <sup>+</sup> , showing the contributions of both the dispersive and specific components as a function of the amount of probe molecule per the monolayer capacity. . . . .	111
4.16	Surface free energy profile of SWN, showing the contributions of both the dispersive and specific components as a function of the amount of probe molecule per the monolayer capacity. . . . .	112
4.17	Dispersive surface energy profile of the two types of clays, plotted as a function of the area increment. . . . .	113
4.18	Specific surface energy profile of the two types of clays, plotted as a function of the area increment. . . . .	113
4.19	The surface energy profile of the two types of clays, plotted as a function of the area increment. . . . .	114
4.20	The surface polarity of the two types of clay evaluated as a function of the surface coverage. . . . .	115

4.21	The thermodynamic work of cohesion of the different clay as a function of the surface coverage. . . . .	116
4.22	N <sub>2</sub> adsorption isotherm of Cloisite Na <sup>+</sup> conducted at 77 K. . . . .	117
4.23	Evaluation of the specific surface area of Cloisite Na <sup>+</sup> , by use of the BET method. . . . .	118
4.24	BJH pore size distribution of Cloisite Na <sup>+</sup> . . . . .	119
4.25	N <sub>2</sub> adsorption isotherm of SWN conducted at 77 K. . . . .	120
4.26	BJH pore size distribution of SWN. . . . .	120
4.27	Evaluation of the specific surface area of SWN, by use of the BET method. . . . .	121
4.28	TGA curve of Cloisite Na <sup>+</sup> . . . . .	123
4.29	TGA curve of SWN. . . . .	123
5.1	DLS particle size distributions obtained for Cloisite Na <sup>+</sup> at 3.0 wt.%, showing the effect of LSE treatment time on average particle size. Sub figures (a)-(g) show the increasing treatment time. . . . .	128
(a)	0 min treatment . . . . .	128
(b)	5 min exfoliation . . . . .	128
(c)	10 min treatment . . . . .	128
(d)	15 min treatment . . . . .	128
(e)	20 min treatment . . . . .	128
(f)	25 min treatment . . . . .	128
(g)	30 min treatment . . . . .	128
5.2	DLS particle size distributions obtained for SWN at 2.0 wt.%, showing the effect of LSE treatment time on average particle size. Sub figures (a)-(g) show the increasing treatment time. . . . .	130
(a)	0 min treatment . . . . .	130
(b)	5 min treatment . . . . .	130
(c)	10 min treatment . . . . .	130
(d)	15 min treatment . . . . .	130
(e)	20 min treatment . . . . .	130

---

(f)	25 min treatment . . . . .	130
(g)	30 min treatment . . . . .	130
5.3	Stability of the two types of clay as colloidal solutions as a function of their concentration, evaluated through the zeta potential. . . . .	132
5.4	The stability of colloidal Cloisite Na <sup>+</sup> at varying concentration as a function of the exfoliation treatment time. . . . .	133
5.5	The stability of colloidal SWN at varying concentration as a function of the exfoliation treatment time. . . . .	134
5.6	Schematic diagram of the total interaction potential curve for a charge stabilised colloid system [172]. . . . .	136
5.7	Schematic diagram showing how the addition of an electrolyte influences the total interaction potential curve for a charge stabilised colloid system. . . . .	137
5.8	Time dependent DLS measurements of Cloisite Na <sup>+</sup> 0.5 wt.% showing the change in hydrodynamic diameter over time under the addition of small amounts of NaCl at different molarities. . . . .	138
5.9	The determined aggregation rate ( $k$ ) and stability ratio ( $W$ ) of Cloisite Na <sup>+</sup> 0.5 wt.% colloid as a function of the added NaCl molarity. . . . .	138
5.10	Time dependent DLS measurements of SWN 0.5 wt.% showing the change in hydrodynamic diameter over time under the addition of small amounts of NaCl at different molarities. . . . .	140
5.11	The determined aggregation rate ( $k$ ) and stability ratio ( $W$ ) of SWN 0.5 wt.% colloid as a function of the added NaCl molarity. . . . .	140
5.12	Time dependent DLS measurements of exfoliation treated Cloisite Na <sup>+</sup> 0.5 wt.% showing the change in hydrodynamic diameter over time under the addition of small amounts of NaCl at different molarities. . . . .	141
5.13	The determined aggregation rate ( $k$ ) and stability ratio ( $W$ ) of exfoliation treated Cloisite Na <sup>+</sup> 0.5 wt.% colloid as a function of the added NaCl molarity. . . . .	142

---

5.14	Time dependent DLS measurements of exfoliation treated SWN 0.5 wt.% showing the change in hydrodynamic diameter with the addition of small amounts of NaCl at different molarities. . . . .	143
5.15	The determined aggregation rate ( $k$ ) and stability ratio ( $W$ ) of exfoliation treated SWN 0.5 wt.% colloid as a function of the added NaCl molarity. . . . .	143
5.16	Time dependent DLS measurements of Cloisite Na <sup>+</sup> showing the change in hydrodynamic diameter as a function of the clay colloid concentration.	145
5.17	The determined aggregation rate ( $k$ ) and stability ratio ( $W$ ) of Cloisite Na <sup>+</sup> colloid as a function of the clay concentration. . . . .	145
5.18	Time dependent DLS measurements of SWN showing the change in hydrodynamic diameter as a function of the clay colloid concentration.	146
5.19	The determined aggregation rate ( $k$ ) and stability ratio ( $W$ ) of SWN colloid as a function of the clay concentration. . . . .	147
5.20	Time dependent DLS measurements of exfoliation treated Cloisite Na <sup>+</sup> showing the change in hydrodynamic diameter as a function of the clay colloid concentration. . . . .	148
5.21	The determined aggregation rate ( $k$ ) and stability ratio ( $W$ ) of exfoliation treated Cloisite Na <sup>+</sup> colloid as a function of the clay concentration.	148
5.22	Time dependent DLS measurements of exfoliation treated SWN showing the change in hydrodynamic diameter as a function of the clay colloid concentration. . . . .	149
5.23	The determined aggregation rate ( $k$ ) and stability ratio ( $W$ ) of exfoliation treated SWN colloid as a function of the clay concentration. . . . .	150
5.24	Rheological flow curve of gelled Cloisite Na <sup>+</sup> at 5.0 wt.%. Closed symbols represent increasing shear and open symbols represent decreasing shear. . . . .	151
5.25	Rheological flow curve of gelled SWN at 3.0 wt.%. Closed symbols represent increasing shear and open symbols represent decreasing shear.	152

---

5.26	Rheological flow curve of exfoliation treated gelled Cloisite Na <sup>+</sup> at 5.0 wt.%. Closed symbols represent increasing shear and open symbols represent decreasing shear. . . . .	152
5.27	Rheological flow curve of exfoliation treated gelled SWN at 3.0 wt.%. Closed symbols represent increasing shear and open symbols represent decreasing shear. . . . .	153
5.28	3iTT of Cloisite Na <sup>+</sup> 5 wt.%. The test is performed in three steps: firstly a constant shear of 0.05 for 60 seconds, second a constant shear of 10 for 60 seconds and finally no shear and the recovery observed. . . . .	154
5.29	3iTT of SWN 3.0 wt.%. The test is performed in three steps: firstly a constant shear of 0.05 for 60 seconds, second a constant shear of 10 for 60 seconds and finally no shear and the recovery observed. . . . .	154
5.30	3iTT of exfoliation treated Cloisite Na <sup>+</sup> 5.0 wt.%. The test is performed in three steps: firstly a constant shear of 0.05 for 60 seconds, second a constant shear of 10 for 60 seconds and finally no shear and the recovery observed. . . . .	155
5.31	3iTT of SWN 3.0 wt.%. The test is performed in three steps: firstly a constant shear of 0.05 for 60 seconds, second a constant shear of 10 for 60 seconds and finally no shear and the recovery observed. . . . .	155
5.32	Physical observation of the physical cross linking gel network in Cloisite Na <sup>+</sup> at 5.0 wt.%. Sub-figures (a) - (c) show the change in the sample state with shear and subsequent recovery of structure. . . . .	156
	(a) Initial state . . . . .	156
	(b) After applying shear . . . . .	156
	(c) Sample after waiting 2 hours . . . . .	156
5.33	Physical observation of the physical cross linking gel network in SWN at 3.0 wt.%. Sub-figures (a) - (c) show the change in the sample state with shear and subsequent recovery of structure. . . . .	157
	(a) Initial state . . . . .	157

---

(b) After applying shear . . . . .	157
(c) Sample after waiting 15 minutes . . . . .	157
5.34 Rheological curve for determination of the linear viscoelastic region of Cloisite Na <sup>+</sup> colloid at 5.0 wt.%. . . . .	158
5.35 Rheological curve for determination of the linear viscoelastic region of SWN colloid at 3.0 wt.%. . . . .	158
5.36 Monitoring of the gelation process in Cloisite Na <sup>+</sup> , through measurement of the rheological properties of storage and loss moduli. Sub-figures (a) - (e) show the results obtained at the given clay concentration. The vertical scale is chosen to best show the trend of the data. . . . .	160
(a) 2.0 wt.% . . . . .	160
(b) 3.0 wt.% . . . . .	160
(c) 4.0 wt.% . . . . .	160
(d) 5.0 wt.% . . . . .	160
(e) 6.0 wt.% . . . . .	160
5.37 Monitoring of the gelation process in SWN, through measurement of the rheological properties of storage and loss moduli. Sub-figures (a) - (d) show the results obtained at the given clay concentration. The vertical scale is chosen to best show the trend of the data. . . . .	161
(a) 1.0 wt.% . . . . .	161
(b) 1.5 wt.% . . . . .	161
(c) 2.0 wt.% . . . . .	161
(d) 3.0 wt.% . . . . .	161
5.38 Monitoring of the gelation process in exfoliated treated Cloisite Na <sup>+</sup> , through measurement of the rheological properties of storage and loss moduli. Sub-figures (a) - (e) show the results obtained at the given clay concentration. The vertical scale is chosen to best show the trend of the data. . . . .	163
(a) 2.0 wt.% . . . . .	163

---

(b)	3.0 wt.% . . . . .	163
(c)	4.0 wt.% . . . . .	163
(d)	5.0 wt.% . . . . .	163
(e)	6.0 wt.% . . . . .	163
5.39	Monitoring of the gelation process in exfoliated treated SWN, through measurement of the rheological properties of storage and loss moduli. Sub-figures (a) - (d) show the results obtained at the given clay concentration. The vertical scale is chosen to best show the trend of the data. . . . .	164
(a)	1.0 wt.% . . . . .	164
(b)	1.5 wt.% . . . . .	164
(c)	2.0 wt.% . . . . .	164
(d)	3.0 wt.% . . . . .	164
5.40	VESUVIO measured time-of-flight data for scattered neutrons from solid state clay samples. Sub-figure (a) and (b) show the results for Cloisite Na <sup>+</sup> and SWN, respectively. . . . .	166
(a)	Cloisite Na <sup>+</sup> . . . . .	166
(b)	SWN . . . . .	166
5.41	VESUVIO measured time-of-flight data for scattered neutrons from 3.0 wt.% colloidal clay samples. Sub-figure (a) and (b) show the results for Cloisite Na <sup>+</sup> and SWN, respectively. . . . .	166
(a)	Cloisite Na <sup>+</sup> . . . . .	166
(b)	SWN . . . . .	166
5.42	Analysed momenta distributions from the solid clay ToF data, the computed data is shown in blue with the best fit of the distribution given in red. Sub-figure (a) and (b) show the results for Cloisite Na <sup>+</sup> and SWN, respectively. . . . .	167
(a)	Cloisite Na <sup>+</sup> . . . . .	167
(b)	SWN . . . . .	167

---

5.43	Analysed momenta distributions from the colloidal clay ToF data, the computed data is shown in blue with the best fit of the distribution given in red. Sub-figure (a) and (b) show the results for Cloisite Na <sup>+</sup> and SWN, respectively. . . . .	167
(a)	Cloisite Na <sup>+</sup> . . . . .	167
(b)	SWN . . . . .	167
6.1	Monitoring of the gel formation process in mixed Cloisite Na <sup>+</sup> and SWN colloids, through the use of oscillatory rheology. Sub-figures (a) - (c) show the differing amount of SWN added to the mix. The vertical scale is chosen to best show the trend of the data. . . . .	172
(a)	Cloisite Na <sup>+</sup> with SWN 0.5 wt.% . . . . .	172
(b)	Cloisite Na <sup>+</sup> with SWN 1.0 wt.% . . . . .	172
(c)	Cloisite Na <sup>+</sup> with SWN 1.5 wt.% . . . . .	172
6.2	Monitoring of the gel formation process in exfoliated treated mixed Cloisite Na <sup>+</sup> and SWN colloids, through the use of oscillatory rheology. Sub-figures (a) - (c) show the differing amount of SWN added to the mix. The vertical scale is chosen to best show the trend of the data. . . . .	173
(a)	Cloisite Na <sup>+</sup> with SWN 0.5 wt.% . . . . .	173
(b)	Cloisite Na <sup>+</sup> with SWN 1.0 wt.% . . . . .	173
(c)	Cloisite Na <sup>+</sup> with SWN 1.5 wt.% . . . . .	173
6.3	Physical observation of the effect of spreading the Cloisite Na <sup>+</sup> 2.0 wt.% with SWN 1.0 wt.% gel onto the LDPE surface for use as a coating. Note that the gel beads into discrete regions of drops rather than producing a uniform film of gel, due to the hydrophobic nature of the polymer. . . . .	175
6.4	Determination of the surface free energy of LDPE through application of the OWRK method, with contact angle measurements of ultrapure water and diiodomethane on the sample surface. . . . .	176

6.5	Predicted wetting envelopes for LDPE, showing the surface tension properties a liquid requires to form a contact of $0^\circ$ , $45^\circ$ and $90^\circ$ , as shown by the blue, orange and yellow curves, respectively. The blue marker shows the expected contact angle to be adopted by water on the surface. . . . .	177
6.6	The variation of the water contact angle on the LDPE surface with increasing exposure to the UV/ozone irradiation. . . . .	178
6.7	Optical images showing if there are any macroscopic changes to the LDPE surface after being exposed to UV/ozone irradiation. Sub-figure (a) shows the surface before and sub-figure (b) shows the surface after treatment, respectively. Scale bar represents $10\ \mu\text{m}$ . . . . .	179
	(a) LDPE pre-UV treatment . . . . .	179
	(b) LDPE post-UV treatment . . . . .	179
6.8	Determination of the surface free energy of the LDPE after treatment with 40 mins of UV/ozone irradiation, through application of the OWRK method, with contact angle measurements of ultrapure water and diiodomethane on the sample surface. . . . .	180
6.9	Predicted wetting envelopes for LDPE after treatment with 40 mins of UV/ozone irradiation, showing the surface tension properties a liquid requires to form a contact of $0^\circ$ , $45^\circ$ and $90^\circ$ , as shown by the blue, orange and yellow curves, respectively. The blue marker shows the expected contact angle to be adopted by water on the surface. . . . .	181
6.10	Physical observation of the effect of spreading the Cloisite $\text{Na}^+$ 2.0 wt.% with SWN 1.0 wt.% gel onto the LDPE surface after treatment with 40 mins of UV/ozone irradiation, for use as a coating. Note that the gel can now form a continuous film upon the surface due to the increased hydrophilicity of the surface . . . . .	181
6.11	Schematic diagram showing the process by which immersive LbL assembly is performed. . . . .	182

6.12	Determination of the surface free energy of the LDPE after treatment with 40 mins of UV/ozone irradiation and LbL treatment, through application of the OWRK method, with contact angle measurements of ultrapure water and diiodomethane on the sample surface. . . . .	183
6.13	Predicted wetting envelopes for LDPE after treatment with 40 mins of UV/ozone irradiation and LbL treatment, showing the surface tension properties a liquid requires to form a contact of 0°, 45° and 90°, as shown by the blue, orange and yellow curves, respectively. The blue marker shows the expected contact angle to be adopted by water on the surface. . . . .	184
6.14	Dynamic contact angle measurements of ultrapure water on the treated LDPE surfaces, showing the variation in contact angle over 10 minutes.	185
6.15	Low magnification SEM images showing the cross section of the clay coating on LDPE at 75 $\mu\text{m}$ clay coating applied thickness. Scale bar represents 10 $\mu\text{m}$ . The red arrow indicates the polymer layer, while the blue arrow indicates the coated surface. This designation applies across all the images. . . . .	187
(a)	Region 1 . . . . .	187
(b)	Region 2 . . . . .	187
(c)	Region 3 . . . . .	187
(d)	Region 4 . . . . .	187
(e)	Region 5 . . . . .	187
6.16	Low magnification SEM images showing the cross section of the clay coating on LDPE at 100 $\mu\text{m}$ clay coating applied thickness. Scale bar represents 10 $\mu\text{m}$ . The red arrow indicates the polymer layer, while the blue arrow indicates the coated surface. This designation applies across all the images. . . . .	188
(a)	Region 1 . . . . .	188
(b)	Region 2 . . . . .	188

---

(c) Region 3 . . . . .	188
(d) Region 4 . . . . .	188
(e) Region 5 . . . . .	188
6.17 Low magnification SEM images showing the cross section of the clay coating on LDPE at 200 $\mu\text{m}$ clay coating applied thickness. Scale bar represents 10 $\mu\text{m}$ . The red arrow indicates the polymer layer, while the blue arrow indicates the coated surface. This designation applies across all the images. . . . .	189
(a) Region 1 . . . . .	189
(b) Region 2 . . . . .	189
(c) Region 3 . . . . .	189
(d) Region 4 . . . . .	189
(e) Region 5 . . . . .	189
6.18 Low magnification SEM images showing the cross section of the clay coating on LDPE at 400 $\mu\text{m}$ clay coating applied thickness. Scale bar represents 10 $\mu\text{m}$ . The red arrow indicates the polymer layer, while the blue arrow indicates the coated surface. This designation applies across all the images. . . . .	190
(a) Region 1 . . . . .	190
(b) Region 2 . . . . .	190
(c) Region 3 . . . . .	190
(d) Region 4 . . . . .	190
(e) Region 5 . . . . .	190
6.19 Typical obtained thermograms of coated samples heated to 600°C under an air atmosphere. . . . .	191
6.20 Variation of the clay mass percentage remaining at 600°C with the applied coating thickness. . . . .	192
6.21 Schematic diagram showing the reaction mechanism for producing a hydrophobic coating upon the clay coated surface. . . . .	193

6.22	The contact angle of a water droplet on a glass slide coated using a trichlorosilane of varying alkyl chain length. . . . .	194
6.23	The change in water contact angle for the un-treated and hydrophobic treated Cloisite Na <sup>+</sup> /SWN gel coating. . . . .	195
6.24	The change in water contact angle for the un-treated and hydrophobic treated SWN gel coating. . . . .	196
7.1	Measurement of the real permittivity for the samples produced. Sub-figures (a) - (e) show the results of different sample types. Refer to Table 7.1 for their designation. . . . .	202
(a)	Sample Type 1 . . . . .	202
(b)	Sample Type 2 . . . . .	202
(c)	Sample Type 3 . . . . .	202
(d)	Sample Type 4 . . . . .	202
(e)	Sample Type 5 . . . . .	202
7.2	Measurement of the imaginary permittivity for the samples produced. Sub-figures (a) - (e) show the results of different sample types. Refer to Table 7.1 for their designation. . . . .	203
(a)	Sample Type 1 . . . . .	203
(b)	Sample Type 2 . . . . .	203
(c)	Sample Type 3 . . . . .	203
(d)	Sample Type 4 . . . . .	203
(e)	Sample Type 5 . . . . .	203
7.3	Determined measurements of tan ( $\delta$ ) for the samples produced, discounting sample type 3. Sub-figures (a) - (d) show the results of different sample types. Refer to Table 7.1 for their designation. . . . .	204
(a)	Sample Type 1 . . . . .	204
(b)	Sample Type 2 . . . . .	204
(c)	Sample Type 4 . . . . .	204
(d)	Sample Type 5 . . . . .	204

7.4	Evaluation of potential conduction behaviour in sample type 3 within the low frequency regime. Note the logarithmic axes scale. . . . .	205
7.5	Measured $E - \sigma$ curves for the samples produced. Note the scale on each plot which is chosen to show the trend most clearly. Sub-figures (a) - (e) show the results of different sample types. Refer to Table 7.1 for their designation. . . . .	207
	(a) Sample Type 1 . . . . .	207
	(b) Sample Type 2 . . . . .	207
	(c) Sample Type 3 . . . . .	207
	(d) Sample Type 4 . . . . .	207
	(e) Sample Type 5 . . . . .	207
7.6	Time dependent conductivity measurements for the samples produced. Results shown in this Figure represent the start of the measurement process, where the electric field strength is 5 kV/mm. Sub-figures (a) - (e) show the results of different sample types. Refer to Table 7.1 for their designation. . . . .	209
	(a) Sample Type 1 . . . . .	209
	(b) Sample Type 2 . . . . .	209
	(c) Sample Type 3 . . . . .	209
	(d) Sample Type 4 . . . . .	209
	(e) Sample Type 5 . . . . .	209
7.7	Weibull probability plots for the DC electrical breakdown measurements of the produced samples. Sub-figures (a) - (e) show the results of different sample types. Refer to Table 7.1 for their designation. . . . .	212
	(a) Sample Type 1 . . . . .	212
	(b) Sample Type 2 . . . . .	212
	(c) Sample Type 3 . . . . .	212
	(d) Sample Type 4 . . . . .	212
	(e) Sample Type 5 . . . . .	212

7.8	Weibull probability plots for the AC electrical breakdown measurements of the produced samples. Sub-figures (a) - (e) show the results of different sample types. Refer to Table 7.1 for their designation. . . . .	214
(a)	Sample Type 1 . . . . .	214
(b)	Sample Type 2 . . . . .	214
(c)	Sample Type 3 . . . . .	214
(d)	Sample Type 4 . . . . .	214
(e)	Sample Type 5 . . . . .	214
7.9	Positions for the placement of the droplets onto the sample surface. . .	216
7.10	Surface uniformity evaluation through measurement of contact angles across the surface for the LDPE substrate. Colour bar is used as a guide to the vertical scale. . . . .	216
7.11	Surface uniformity evaluation through measurement of contact angles across the surface for the 75 $\mu\text{m}$ coated LDPE substrate. Colour bar is used as a guide to the vertical scale. . . . .	217
7.12	Surface uniformity evaluation through measurement of contact angles across the surface for the 200 $\mu\text{m}$ coated LDPE substrate. Colour bar is used as a guide to the vertical scale. . . . .	217
7.13	Determined water content for samples at varying vacuum oven drying times. . . . .	219

# List of Tables

2.1	Examples of natural, organic and inorganic materials for use as possible filler materials, adapted with permission from [69]. . . . .	41
2.2	Example thermal conductivities of some inorganic filler particles. Adapted with permission from [70], ©2005, IEEE. . . . .	50
3.1	Surface tension properties for the solvent used during the OWRK method.	63
3.2	Quantification of a materials conductive and dielectric properties based on the magnitude of the loss tangent. . . . .	91
4.1	Average value of the dispersive component of the clay surface free energy, along with the values showing the range of the distribution. . . . .	112
4.2	Average value of the specific component of the clay surface free energy, along with the values showing the range of the distribution. . . . .	114
4.3	Average value for the surface free energy of the clay surface, along with the values showing the range of the distribution. . . . .	114
4.4	Results of fitting from the BET surface area analysis of Cloisite Na <sup>+</sup> . . . . .	118
4.5	Results of fitting from the BET surface area analysis of SWN . . . . .	121
5.1	Evaluated hydrogen atom binding energy for the solid and colloidal clay samples. The binding of water is presented as a reference measurement.	168
7.1	Types of samples prepared for electrical testing . . . . .	200

7.2	Scale and shape parameter analysis for the Weibull plots of samples tested for DC electrical breakdown. Given uncertainties are the standard errors of the fits. . . . .	211
7.3	Scale and shape parameter analysis for the Weibull plots of samples tested for AC electrical breakdown. Given uncertainties are the standard errors of the fits. . . . .	213

# Chapter 1

## Introduction

## 1.1 Introduction

The saving of energy is one of the major social issues of our time and it encompasses many areas. Sustainable systems need to be developed in order for these needs to be met. Sustainability is not just focused on renewable energy resources, but also new technologies to support current energy systems [1].

The primary motivation of this project is the restriction on the energy conversion rates of electrical generator systems, as this efficiency is hindered by electrical strength restrictions and thermal limitations. A central element of all power systems is insulation, and consequently the development of advanced material solutions that can enhance the electrical and thermal limitations on system performance is vital in energy conservation. Many of these issues arise from the insulation materials used in these systems, which are arguably far behind the enhanced properties that are offered by the state-of-art nanocomposite technology [2]. It has already been shown, that on the European scale, even a small increase in generator conversion efficiency ( $\sim 0.2\%$ ) could lead to the saving of the equivalent of one nuclear power plant (around 1000 MW) or conversely ten fossil fuel plants, while also saving an equivalent measure in  $\text{CO}_2$  production [2]. The development of new insulation materials is of course not limited to power generator systems; the applications can stretch into transformers, conventional insulation, high voltage cables and high voltage electrical devices.

Polymeric materials are ubiquitous in everyday life, thanks to their: ease of production, low cost and usual ductile nature. However, polymers suffer from relatively low physical strengths (such as tensile strength, stiffness and toughness) in comparison to materials such as metals and wood [3]. An approach to alleviate this issue was through the introduction of filler particles, leading to the formation of micro and nano composite materials. Significant improvements to the physical properties, such as strength and toughness, can be seen at even low levels of particle filler concentrations (i.e.  $< 5$  wt.%) [4]. But, the incorporation of these filler particles is often at the expense of

another physical property [5]. The challenge to overcome in the field is finding the correct balance of filler material and polymer, that allows the material to function for the purpose it is required. For example, in insulation materials it is key to have high electrical resistance but also desirable to have good thermal conduction to help alleviate effects such as Joule heating. However, despite the clear ability to make these composite materials there are still many challenges to be overcome before the materials, can find commercial use. Some particular examples of this are discussed here. Many nanocomposite materials rely on the addition of nano particles, which if produced from 2-D layered materials, face challenges in both achieving high yield of the separated layers and maintaining their separation. This is further complicated when these single layers are produced in solution. This then follows into the next point, where there are challenges associated with the compatibility of the filler material and the host matrix. For example, hydrophilic clay particles do not disperse well into hydrophobic polymers, so it is desirable that both filler and matrix possess similar chemical properties, hindering choices of filler particle [6]. Perhaps the most obvious issue is maintaining the dispersion of the filler particles within the matrix, as aggregation of particles will feed into the failure of the material sooner than what might be predicted. The work in this thesis seeks to overcome some of the issues presented here by the use of a continuous layer of filler particles rather than the dispersion of fillers, with the aim to alleviate some of the difficulties presented.

## **1.2 The aim of this thesis**

The currently employed state-of-art in tackling these demands is through the application of nanocomposite dielectric tapes, in which the dispersed nanoparticle fillers act to disrupt the flow of current through the dielectric material, thus increasing the resistance to electrical breakdown. However, it can be imagined that if continuous insulation barrier layers could be formed, the efficiency of the tapes could be much further improved. The aim of this work is therefore to develop a new novel continuous insulation layered structure within the dielectric tape to further enhance efficiency.

To achieve the aim of this thesis the following objectives have been met:

- An understanding of the physical properties and structure of the two types of clay employed has been investigated.
- The ability and mechanism behind these types of clays being able to form a gel has been explored, and the process by which the interaction occurs evaluated.
- An understanding of the relation between substrate and developed gels and how these can be made to be compatible and produce continuous layers.
- The electrical performance of the developed materials has been determined. Understanding their electrical breakdown strength and their conduction under high field strengths.

## 1.3 Thesis outline

This thesis is divided into three main sections: background and current developments in Chapter 2, experimental methodologies and techniques in Chapter 3 and experimental results and discussion in Chapters 5, 6 and 7.

Chapter 2 introduces the reader to the concept of dielectric materials and then mechanisms that cause them to have this nature. This is then followed by a review of the parameters that are key for energy saving in systems that incorporate dielectric materials and finally a review of the development of nanocomposite dielectrics is discussed.

Chapter 3 is designed as an experimental manual for the interested reader, providing details on the experimental set up and fundamental knowledge of the experimental approach. For those who are well versed in the techniques discussed, this chapter could be initially skipped and referred back to when the need arises.

Chapter 4 begins the results section of this thesis. The first results chapter provides information on the nature and structure of the employed nanoclay materials, and key knowledge to help the reader understand the later chapters of this work.

Chapter 5 provides a detailed study of the stability and gelation effects within clay colloids, while also providing knowledge on the mechanisms behind the process of particle interactions and aggregation.

Chapter 6 begins the work on development of the novel nanodielectric materials, exploring the properties of the polymer films and the processes by which gel coatings can be applied.

Chapter 7 is the final results chapter and explores the electrical properties of the developed nanodielectric material.

Chapter 8 finally draws some conclusions on the various branches of work within this thesis and presents ideas for future work and developments.

## **Chapter 2**

# **The need for development of new insulating materials**

In this chapter the concepts of dielectric materials and how they are different to electrical conductors is first discussed, with explicit mention of the physical mechanisms of dielectric polarisation. Following this, a discussion of key electrical parameters required in the insulation industry are presented. Finally, this Chapter ends with its third section introducing the reader to the field of nanocomposite dielectrics and their strengths and weaknesses, along with an outlook of the future of the technology.

## 2.1 Principles of electrical conduction

Electrical conductivity,  $\sigma$  (and its inverse electrical resistivity,  $\rho$ ) is a fundamental property of a material that describes its ability to pass electrical charge through itself. Generally the magnitude of this conductivity for a given point in the material is given by the ratio of the current density and electric field strength at that point in the material,

$$\sigma = \frac{\vec{J}}{\vec{E}} \quad (2.1)$$

The definition of a material as a conductor or insulator is determined by its band structure. Electrons within an atom can only have specified discrete energy levels, when a large number of these energy levels with close energy levels are together they combine to form an energy band. There can be many of these energy bands in a material depending upon its constituent atoms and their distribution in the structure. The electrons within the structure seek to minimise the energy of the material, and thus begin to fill up the energy bands from the bottom. The electrons fill the bands to a characteristic level known as the Fermi level, and the position of the Fermi level with respect to the band structure determines the material's electrical conduction properties. A schematic description of band structure is shown by Fig. 2.1. Drude [7] introduced a model for electron conduction in materials (more appropriate to metals) where the outermost electrons of the atoms are free to delocalise amongst the ionic lattice, and

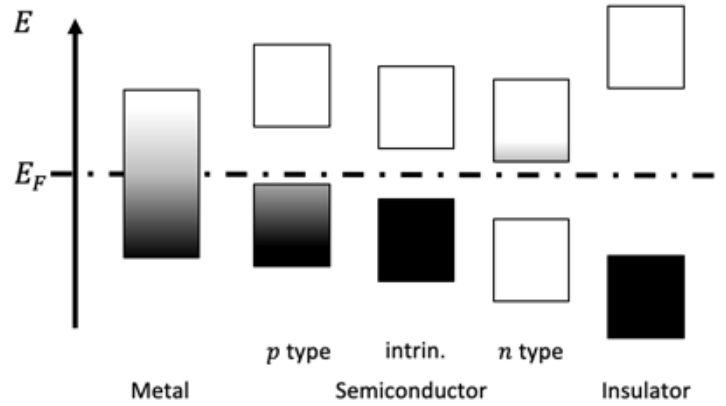


Figure 2.1: Schematic diagram of the electronic band structure in different materials at equilibrium. Black shading represents filled states and white shading unfilled states. For metals the Fermi level  $E_F$  lies within at least one band, for semiconducting materials and insulators  $E_F$  lies within a band gap but for the case of semiconductors electrons can be thermally excited into the next band due to the close placement to the  $E_F$ .

thus are “free charges”. This allowed him to reformulate eqn. 2.1 to describe the conductivity in terms of the electrons properties as,

$$\vec{J} = \left( \frac{nq^2\tau}{m_e} \right) \vec{E} \quad (2.2)$$

where  $n$ ,  $q$ ,  $\tau$  and  $m_e$  are the number density, charge, mean free path time and mass of the electron, respectively. However, in insulating materials, the large forbidden region within the band structure leads to the atoms being firmly bound to their host atoms, hence they do not possess the free charge attributed to conducting materials.

A particular class of materials used for electrical insulation materials are polymers. These are usually long chained molecules formed of a base repeating unit. In comparison to conducting materials like metals, which are formed from electrostatic metallic bonds, the atoms in a polymer are strongly covalently bonded. This difference in bonding leads to the difference in electrical conductivity. For metallic bonds the electrons are loosely bound to the metal atoms and thus it takes little energy to move them

from atom to atom. In covalent bonds the electrons are held much tighter and thus it requires much more energy to share the electrons with other atoms, hence the minimal electrical conductivity. This makes polymer materials ideal for use in high-voltage insulation applications. There is a particular class of insulators known as dielectrics, which are insulators that become polarised under the influence of an electric field.

## 2.2 Fundamentals of dielectric materials

### 2.2.1 Electrical dipole moment

Atoms combine to form molecules by sharing electrons between them. This causes a redistribution of the charge of the atoms, due to this there may be the generation of a permanent electrical dipole moment. This means that molecules can either be polar, possessing this electrical dipole moment or non-polar, having no dipole moment. Dielectrics can be made from either polar or non-polar materials.

Two equal but opposite charges, which are separated by a small distance, will generate an electrical dipole as shown by Fig. 2.2. The strength of the electric dipole is measured in terms of its electrical dipole moment,  $\vec{\mu}$ . In order to characterise this

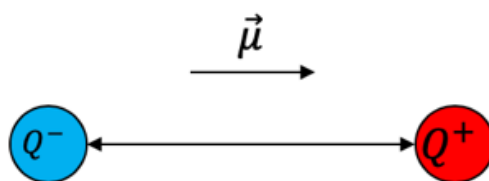


Figure 2.2: Schematic showing the formation of an electric dipole moment between two oppositely charged point sources.

dipole, the magnitude of the charge and the position vector between the charges must be known. The larger the magnitude of  $\vec{\mu}$  the stronger the resultant dipole field. Note that this field is cylindrically symmetric about the direction of  $\vec{\mu}$ . To determine the strength of the field we first need to know the electrical potential - which in this case is the sum of the two charge components.

$$\phi(\vec{r}) = \frac{1}{4\pi\epsilon_0} \left[ \frac{Q}{\sqrt{x^2 + y^2 + \left(z - \frac{d}{2}\right)^2}} + \frac{-Q}{\sqrt{x^2 + y^2 + \left(z + \frac{d}{2}\right)^2}} \right] \quad (2.3)$$

Solving this the electrical dipole potential  $\phi(\vec{r})$ , can be expressed as

$$\phi(\vec{r}) = \frac{\vec{\mu} \cdot \hat{r}}{4\pi\epsilon_0 r^2} \quad (2.4)$$

The electric field strength for this dipole is then the gradient of this function

$$\vec{E} = -\nabla\phi(\vec{r}) = \frac{3(\vec{\mu} \cdot \hat{r})\hat{r} - \vec{\mu}}{4\pi\epsilon_0 r^3} \quad (2.5)$$

The net charge within an electric dipole is zero, however, when the charges are separated by a distance the electric field strength decays inversely, with the distance cubed.

### Non-polar dielectrics

Non-polar dielectrics are ones in which the molecules that make up their structure are non-polar. In non-polar molecules the centre of gravity of the nucleus and electron cloud are concentric in the absence of an external electric field. As there is no separation between the positive and negative charge centres, they are said to have no intrinsic dipole moment. Examples of non-polar molecules include: O<sub>2</sub>, C<sub>6</sub>H<sub>6</sub>, CO<sub>2</sub> etc. An example non-polar molecule is shown by the schematic in Fig. 2.3. In the presence of an external electric field the positive and negative charge centres experience drag forces along and against the direction of the applied field respectively. This causes the charge centres to move away from one another, and causes the centre of mass to no longer coincide. Due to this separation the molecule acquires an induced dipole moment, this effect is known as polarisation.

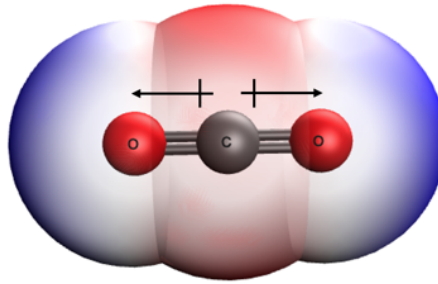


Figure 2.3: Charge distribution of CO<sub>2</sub>. Blue and red coloured regions represent negative and positively charged regions, respectively. The bond dipoles are shown by the black arrows. Since the dipole moments of the Carbon-Oxygen bonds, point in opposite parallel directions, this leads to a net zero dipole moment.

### Polar dielectrics

Polar dielectrics on the other hand are formed of polar molecules. In polar molecules the centres of gravity of the nucleus and electron cloud do not coincide, even in the absence of an electric field. Due to the separation between the two charge centres, the molecule possess an intrinsic dipole moment. Examples of polar molecules are: H<sub>2</sub>O, NH<sub>3</sub>, SO<sub>2</sub> etc. An example polar molecule is shown by the schematic in Fig. 2.4. On

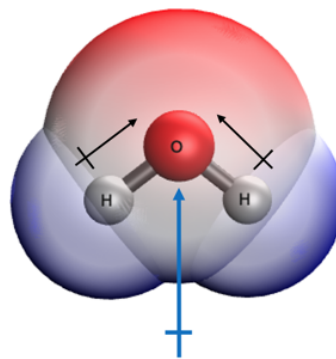


Figure 2.4: Charge distribution of H<sub>2</sub>O. Blue and red coloured regions represent negative and positively charged regions, respectively. The bond dipoles are shown by the black arrows. The dipole moment of the Hydrogen-Oxygen bonds point in the same direction at an angle of 104.5°, which leads to a net dipole moment of 1.84 D for the molecule, as shown by the blue arrow.

the macroscopic scale the dipole moments of these molecules are randomly orientated over the sample due to thermal motions. Hence, the overall electric dipole moment of the sample is zero in the absence of an external electric field. In the presence of an

external electric field polar molecules are stretched like their non-polar counterparts but this induced dipole is much smaller than their permanent dipole. The external field in this case also causes the molecules to experience an equal but opposite force, which generates a torque,  $qd\vec{E} \sin(\theta)$ , where the angle is between the dipole moment direction and the applied electric field. The molecular dipoles rotate in the direction of the applied field and thus the dielectric is said to be polarised and acquires a net dipole moment. The complete alignment of the molecular dipoles is not possible due to thermal agitation, but the permittivity of a polar dielectric is greater than that of a non-polar dielectric due to the additional oriental polarisation from the molecules.

### 2.2.2 Polarisation and permittivity

The concept of polarisation can be represented best through the description of a parallel plate capacitor. If the capacitor is taken to be two plates separated by a distance,  $d$ , with a constant applied voltage of  $V_0$  across the plates, the capacitance can be described by,

$$Q = C_0 V_0 \tag{2.6}$$

where  $Q$  is the net charge between the plates,  $C_0$  is the capacitance and  $V_0$  is the applied voltage. If a polarisable medium is introduced between the capacitor plates with the voltage kept constant, the net charge must also be constant. Externally this increase in charge due to the polarisable material looks like an increased capacitance i.e.,

$$Q = CV_0 \tag{2.7}$$

Therefore the capacitance has increased by a certain factor in the presence of the polarisable material. This factor is known as the dielectric permittivity,  $\epsilon_r$ . A medium

with a polarised charge in free space with permittivity,  $\varepsilon_0$ , is described by replacing the charge by a region of permittivity  $\varepsilon_r\varepsilon_0$ . It can then be shown that the polarisation induced by a macroscopic electric field within the polarisable medium is given by

$$\vec{P} = \varepsilon_0\chi_e\vec{E} \quad (2.8)$$

Where  $\vec{P}$  is the polarisation density,  $\vec{E}$  is the macroscopic electric field within the medium and the term  $\chi_e = \varepsilon_r - 1$  known as the electrical susceptibility is introduced. A theoretical value of the susceptibility can be calculated by considering the dipole moment of a single atom,

$$\vec{\mu} = \alpha\vec{E}_{Loc} \quad (2.9)$$

where  $\vec{\mu}$  is the induced dipole moment,  $\alpha$  is the atomic polarisability and  $\vec{E}_{Loc}$  is the electric field at the dipole. Thus, we can also say that the polarisation is proportional to the applied field since

$$\vec{P} = N\vec{\mu} = N\alpha\vec{E}_{Loc} = \varepsilon_0\chi_e\vec{E} \quad (2.10)$$

In the case of  $\vec{E} = \vec{E}_{Loc}$  then we have

$$\chi_e = \varepsilon_r - 1 = \frac{N\alpha}{\varepsilon_0} \quad (2.11)$$

Therefore the permittivity is directly related to the polarisability. However, in deriving the relation for the macroscopic polarisation, it is assumed the dipoles within the medium produce net surface charges. Inside the dielectric the situation is not so simple.

Each dipole has an associated electric field, and every dipole experiences the field of all the other dipoles within the medium. To estimate the field at any given dipole, it must be assumed the dipole occupies only a small spherical cavity within the dielectric, as shown by Fig. 2.5. The effect of all other dipoles are assumed to only give a surface charge around the cavity. In order to calculate the magnitude of the field over the

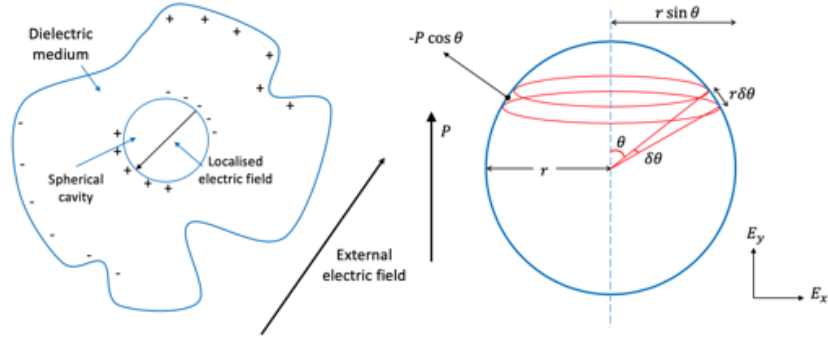


Figure 2.5: Schematic diagram for determination of the local electric field at a dipole.

cavity, we first consider the total field for a point charge

$$\vec{E} = \frac{Q}{4\pi\epsilon_0 r^2} \hat{r} \quad (2.12)$$

The electric field strength at any point of radius  $r$  and angle  $\theta$  is given by

$$\vec{E}_y = \vec{E} \cos(\theta) = \frac{Q \cos(\theta)}{4\pi\epsilon_0 r^2} \quad (2.13)$$

The total charge contained within the ring of radius  $r \sin(\theta)$  and width  $r \delta\theta$  is

$$Q_{ring} = 2\pi r \sin(\theta) r \delta\theta - \vec{P} \cos(\theta) \quad (2.14)$$

Therefore the total charge in the  $y$  plane due to the charge within the ring is

$$\vec{E}_y = -\frac{\vec{P} \cos^2(\theta) \sin(\theta)}{2\epsilon_0} \delta\theta \quad (2.15)$$

The field caused by the charge at the surface of the entire sphere is then simply

$$\vec{E}_y = -\frac{\vec{P}}{2\epsilon_0} \int_0^\pi \cos^2(\theta) \sin(\theta) d\theta = \frac{\vec{P}}{3\epsilon_0} \quad (2.16)$$

Therefore, the field experienced by a dipole within this cavity is the combination of the externally applied field and the field due to the presence of other dipoles,

$$\vec{E}_{Loc} = \vec{E} + \frac{\vec{P}}{3\epsilon_0} \quad (2.17)$$

Previously the polarisation was found to be described using eqn. 2.8, we can substitute in equations 2.10 and 2.17 to obtain

$$\frac{N\alpha}{3\epsilon_0} = \frac{\epsilon_r - 1}{\epsilon_r + 2} \quad (2.18)$$

which is known as the *Clausius-Mosotti* relationship [8, 9]. The Clausius-Mosotti relationship relates the relative permittivity of a material to its atomic polarisability of the constituent atoms and/or molecules. The relation can be applied to gases, liquids and amorphous solids, but should be treated with caution when used in more dense systems.

### 2.2.3 Types of polarisation

The polarisation of a material is made of a combination of different atomic effects. The total polarisability  $\alpha$  can therefore be expressed as a sum of these components. The differing types of polarisability are discussed below.

### Electronic

There are two ways in which the electronic polarisability can be determined - classically and quantum mechanically. In the classical approach the polarisability  $\alpha_e$  depends on the atomic number and the number of electrons in the outer shell. Therefore the polarisability decreases from group I to group VIII elements as the increasing electron number screens the nucleus from the influence of the electric field [10]. The applied electric field causes a small shift in the equilibrium positions of the nucleus and electrons, as shown by Fig. 2.6. By considering the Coulombic force on the nucleus and

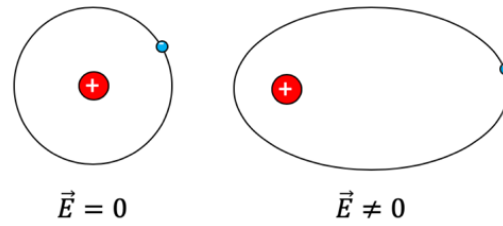


Figure 2.6: Electronic polarisation of an atom. Note that the presence of an electric field causes a shift in the charge centres of the nucleus and electron cloud.

electron cloud separated by a distance,  $r$ , the dipole moment and hence polarisability can be determined as,

$$\alpha_e = 4\pi\epsilon_0 r^3 = 3\epsilon_0 V_a \quad (2.19)$$

So  $\alpha_e$  is proportional to the volume of the atom. The average electronic polarisability can then be obtained by the summation of the contributions of all the atoms divided by the total number of atoms. Only the outermost electrons are considered in this approach due to the negligibly small contribution of the inner electrons. Therefore the electronic susceptibility is given by,

$$\chi_e = \frac{N\alpha_e}{\epsilon_0} = \frac{N}{\epsilon_0} \left[ \frac{(ZQ)^2}{m\omega_0^2} \right] \quad (2.20)$$

where  $Z$  is the atomic number,  $m$  is the atom mass and  $\omega_0$  is the natural vibrational frequency. Thus the relative permittivity is given by,

$$\varepsilon_r = 1 + \chi_e = 1 + \frac{N}{\varepsilon_0} \left[ \frac{(ZQ)^2}{m\omega_0^2} \right] \quad (2.21)$$

### Ionic

Generally speaking there are two types of ionic solids. Those with permanent dipole moments, and those without. The possession of permanent dipoles is simply a case of the magnitude of the dipole within the positive and negative species and their resultant magnitude. We can model a material under the assumption it is a linear chain of atoms, with the positive species at position A and the negative species at position B. Under thermal equilibrium the atoms undergo lattice vibrations, but on average are separated by a distance,  $a$ . With the application of an electric field, the positive and negative charge centres will cause a shift of the atomic positions by  $a \pm \Delta x$ , as shown schematically by Fig. 2.7. This displacement from the equilibrium positions generates

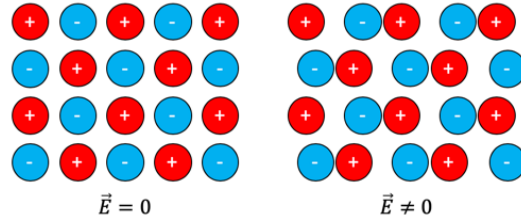


Figure 2.7: Ionic polarisation of a material. The presence of an electric field causes a shift of the positive and negative charge centres towards each other, away from their equilibrium positions.

a restoring force that tends to align the atoms back to their equilibrium positions. Thus, two equations of motion can be written for the behaviour of the atoms within the material. Combining these equations and accounting for the presence of the electric field, the equation of motion is written as,

$$m_r \frac{d^2 \Delta x}{dt^2} = -2\gamma_i \Delta x - \beta \frac{d\Delta x}{dt} - ZQ \vec{E}_{Loc} \quad (2.22)$$

where  $m_r$  is the reduced mass of the cation-anion pair,  $\gamma_i$  is the restoring force,  $\Delta x$  is the relative displacement of the cation-anion pair and  $\beta$  is a damping factor. The solution of this equation, assuming an oscillating electric field, and  $\gamma_i$  is expressed in terms of the lattice vibration frequency  $\gamma_i = m_r\omega_0^2$ , is given by,

$$\Delta x = \frac{ZQ\vec{E}_{Loc}}{m_r(\omega_0^2 - \omega^2) + i\beta\omega} \quad (2.23)$$

Thus the atomic polarisability is given by,

$$\alpha_i = \frac{(ZQ)^2}{m_r(\omega_0^2 - \omega^2) + i\beta\omega} \quad (2.24)$$

In static fields this simply reduces to

$$\alpha_i = \frac{(ZQ)^2}{m_r\omega_0^2} \quad (2.25)$$

There is a similarity between the ionic and electronic polarisations as the displacement of ions is always accompanied by a displacement of the electrons. It should also be noted it is much easier experimentally to determine the electronic polarisability over the ionic polarisability.

### **Oriental**

Oriental polarisation arises within molecules that possess permanent dipole moments. Typically molecules that possess permanent dipoles have one of the following properties; asymmetric structure or higher electron densities closer to the more electronegative atom. Examples of dipolar molecules include: H<sub>2</sub>O, NH<sub>3</sub>, HCl etc. If a fluid of molecules possessing permanent dipole moments is imagined, then the molecules will be in constant thermal motion. The classical degree of freedom gives  $\frac{1}{2}k_B T$  of energy

per molecule per degree of freedom. Since the orientation of the molecules is random, there is no net dipole moment for the fluid. If this fluid is then subjected to an external electric field, it will try to align the dipole moments but this aligning force is frustrated by the thermal motion of the molecules. This effect is shown schematically by Fig. 2.8. Under these influences the probability that the dipole will lie at an angle  $\theta$  is given by

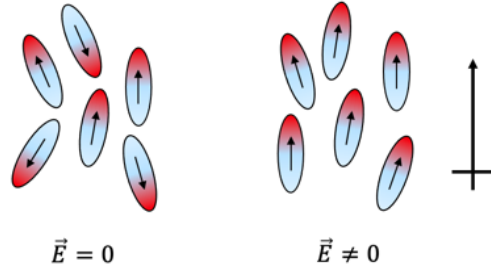


Figure 2.8: The effect of orientational polarisation on a material. The electric field causes the dipoles to align with the electric field lines.

the Boltzmann factor

$$p(\theta) \approx e^{-\frac{E}{k_B T}} \approx e^{\frac{\vec{\mu} \vec{E} \cos \theta}{k_B T}} \quad (2.26)$$

Without the electric field the dipoles are randomly orientated therefore  $p(\theta)$  is the same for all  $\theta$ . To determine the polarisation it is necessary to know the average number of dipoles aligned along the field,

$$\frac{\bar{\mu}}{\mu} = \langle \cos \theta \rangle \quad \text{where,} \quad \langle \cos \theta \rangle = \frac{\int p(\theta) \cos \theta d\Omega}{\int p(\theta) d\Omega} \quad (2.27)$$

The integral is over all solid angles, thus,

$$\frac{\bar{\mu}}{\mu} = \frac{\int_0^\pi e^{\frac{\vec{\mu} \vec{E} \cos \theta}{k_B T}} \cos \theta \sin \theta d\theta}{\int_0^\pi e^{\frac{\vec{\mu} \vec{E} \cos \theta}{k_B T}} \sin \theta d\theta} \quad (2.28)$$

This has an analytical solution given by

$$\frac{\bar{\mu}}{\mu} = \coth\left(\frac{\bar{\mu}\vec{E}}{k_B T}\right) - \frac{1}{\left(\frac{\bar{\mu}\vec{E}}{k_B T}\right)} \quad (2.29)$$

This can be described mathematically by a function known as the Langevin function. This is shown schematically in Fig. 2.9. Provided that we are considering a region in

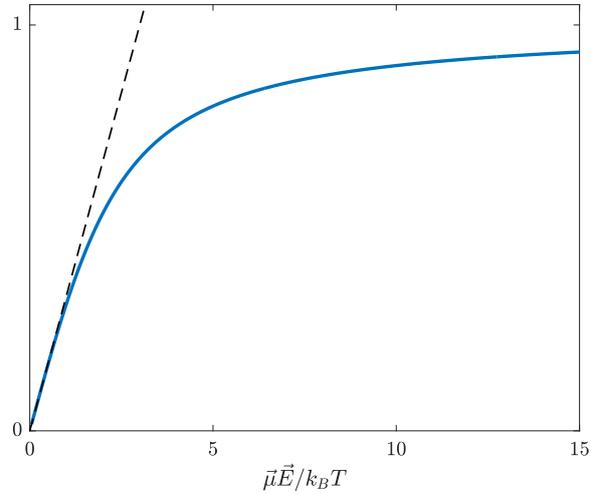


Figure 2.9: Schematic plot of the Langevin function (blue curve). The black dashed line represents a line of gradient  $\frac{1}{3}$  for the scenario where  $\bar{\mu}\vec{E}/k_B T \ll 1$ .

which  $\bar{\mu}\vec{E}/k_B T$  is much smaller than one, then there is a constant gradient of  $\frac{1}{3}$  and therefore

$$\frac{\bar{\mu}}{\mu} \approx \frac{\bar{\mu}\vec{E}}{3k_B T} \quad (2.30)$$

And hence the orientational polarisability can be expressed as

$$\alpha_o = \frac{\bar{\mu}^2}{3k_B T} \quad (2.31)$$

Typically  $\alpha_o$  is much larger than both  $\alpha_e$  and  $\alpha_i$  due to the strong dependence on temperature. Here  $\alpha_o$  has been derived assuming the material is in a fluid state in the solid state the situation is slightly different. In a solid dipoles are unable to rotate freely as they do in a fluid, due to the crystalline field causing them to be constricted to a few discrete orientations. In some solids at temperatures below the melting point the dipoles are “frozen” in fixed positions and therefore do not contribute to the total polarisability (i.e.  $\alpha_o = 0$ ), even under the influence of an electric field. An example of this type of behaviour is seen within nitrobenzene, as shown by Fig. 2.10a. As

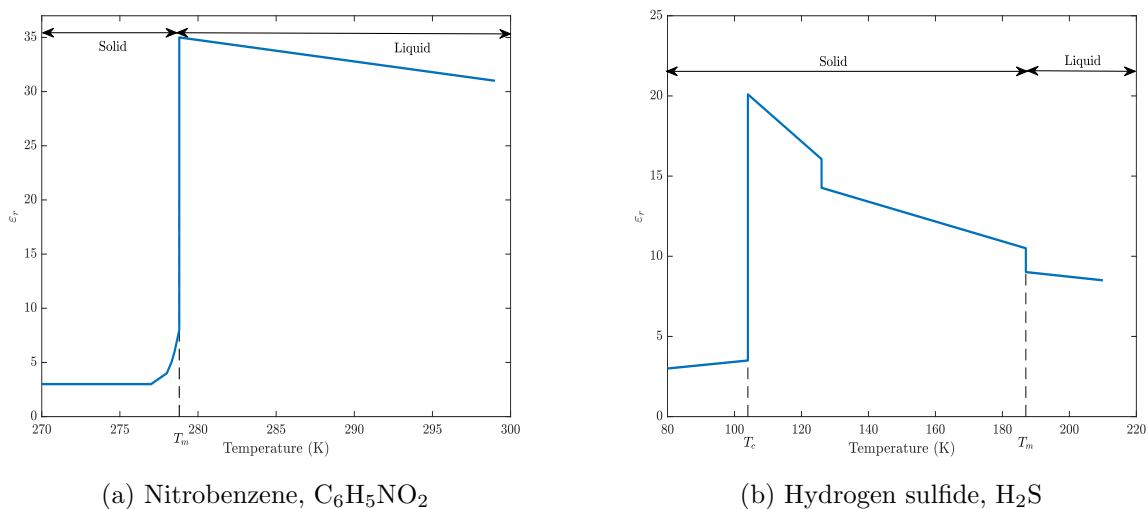


Figure 2.10: Variation of the relative permittivity with temperature for (a) Nitrobenzene adapted with permission from [11], Copyright ©1930, Springer Nature and (b) Hydrogen Sulfide adapted with permission from [12], Copyright ©1934, American Chemical Society.

can be seen from Fig. 2.10 there is a sharp decrease in the relative permittivity at 278 K, the melting point of the material. Therefore, for  $T < 278$  K, only  $\alpha_e$  and  $\alpha_i$  contribute to  $\epsilon_r$ , and for  $T > 278$  K,  $\alpha_e$ ,  $\alpha_i$  and  $\alpha_o$  contribute to  $\epsilon_r$ . However, this behaviour is not consistent for all materials. In hydrogen sulfide, for example there is an increase in  $\epsilon_r$  even below the melting temperature. This increase in  $\epsilon_r$  continues until a critical temperature, at which point there is a sudden decrease and the dipoles are frozen in place. The reason for this behaviour arises from the potential equilibrium states of the dipoles. At the minimum energy level the dipole has the same probability as orientating to the left or right, giving no net polarisation. If  $p(\theta)$  represents the

probability of dipoles aligning to the left and  $1 - p(\theta)$  represents dipoles aligning to the right, using Boltzmann statistics we can say

$$p(\theta) = \frac{e^{\left(-\frac{2\vec{\mu}\vec{E}}{k_B T}\right)}}{1 + e^{\left(-\frac{2\vec{\mu}\vec{E}}{k_B T}\right)}} \quad (2.32)$$

Since in general  $\vec{\mu}\vec{E}$  is much smaller than  $k_B T$ , the equation can be simplified to

$$p(\theta) = \frac{1}{2} e^{\left(-\frac{2\vec{\mu}\vec{E}}{k_B T}\right)} \quad (2.33)$$

Using this model the percentage of dipole moments in the direction opposite the applied field is  $p(\theta)$  and the percentage of dipole moments in the direction parallel to the field is  $1 - p(\theta)$ . Thus,

$$\vec{\mu}(\vec{E}_{\parallel}) = \vec{\mu}(1 - p(\theta)) - \vec{\mu}(p(\theta)) = \vec{\mu} \left[ 1 - e^{\left(-\frac{2\vec{\mu}\vec{E}}{k_B T}\right)} \right] \quad (2.34)$$

The  $e^{\left(-\frac{2\vec{\mu}\vec{E}}{k_B T}\right)}$  term can be expanded as a series since  $\vec{\mu}\vec{E} \ll k_B T$ . Keeping only the first two terms,

$$\vec{\mu}(\vec{E}_{\parallel}) = \frac{2\vec{\mu}^2 \vec{E}}{k_B T} \quad (2.35)$$

Hence the polarisability is,

$$\alpha_o = \frac{2\vec{\mu}^2}{k_B T} \quad (2.36)$$

which has a similar form to that of eqn. 2.31. The difference in the equations show that at the melting temperature,  $\alpha_o$  is larger in the solid state than the fluid state.

### 2.2.4 Dielectric relaxation

Under the influence of a changing electric field, there may be a delay in the molecular polarisation with respect to this oscillating field, and this effect is known as dielectric relaxation. Relaxation is usually measured as a function of the relative permittivity with respect to the frequency of the oscillations of the field. The effect can be thought of as analogous to hysteresis within a changing magnetic field. For ideal systems this behaviour can be described by the Debye equation (eqn. 2.37).

$$\frac{\varepsilon_r - 1}{\varepsilon_r + 2} = \frac{N}{3\varepsilon_0} \left( \alpha + \frac{\bar{\mu}^2}{3k_B T} \right) \quad (2.37)$$

If the relaxation is assumed to have an exponential dependence then, the polarisation can be described as

$$\vec{P} = \vec{P}_s \left( 1 - e^{-\frac{t}{\tau}} \right) \quad (2.38)$$

where  $\vec{P}_s$  is the equilibrium polarisation distribution in the field,  $t$  is the time from the field switch-on and  $\tau$  is the characteristic re-orientation time. For an exponential dependence the governing equation is

$$\vec{P} + \tau \frac{d\vec{P}}{dt} = \vec{P}_0 = \varepsilon_0 \chi_s \vec{E} \quad (2.39)$$

Where  $\chi_s$  is the equilibrium (or static) dielectric susceptibility. Assuming the oscillating field has the form  $\vec{E} = \vec{E}_0 \cos(\omega t)$ , substituting this into the equation and solving gives,

$$\vec{P} = \frac{\varepsilon_0 \chi_s}{1 + \tau^2 \omega^2} \left[ \vec{E}_0 \cos(\omega t) + \tau \omega \vec{E}_0 \sin(\omega t) \right] \quad (2.40)$$

This gives two components to the polarisation. An in phase component,  $\vec{E}_0 \cos(\omega t)$  and a component  $90^\circ$  out of phase,  $\vec{E}_0 \sin(\omega t)$ . The in-phase and out-of-phase components are typically given in terms of a complex permittivity as

$$\vec{P} = \varepsilon_0(\varepsilon_r^* - 1)\vec{E} = \varepsilon_0((\varepsilon_r' + i\varepsilon_r'') - 1)\vec{E} \quad (2.41)$$

Using this relation and the solution for  $\vec{P}$ , the two components known as the permittivity,  $\varepsilon_r'$ , and loss,  $\varepsilon_r''$ , can be determined as,

$$\varepsilon_r' = 1 + \frac{\varepsilon_s - 1}{1 + \omega^2\tau^2} \quad (2.42)$$

and

$$\varepsilon_r'' = 1 + \frac{(\varepsilon_s - 1)\omega\tau}{1 + \omega^2\tau^2} \quad (2.43)$$

These two equations are typically referred to as the Debye dispersion equations [13]. Knowledge of the loss factor allows an understanding on the loss due to effects such as the friction accompanying polarisation and the orientation of the electric dipoles.

## **2.3 The key parameters leading to the failure of insulation materials**

In this section some of the key properties related to the failure of electrical insulating systems will be discussed.

### 2.3.1 Electrical ageing

Perhaps the most important property to consider from an industrial setting is the lifetime of an insulating material. The subjection of an insulator to electrical stresses will cause it to enter a non-equilibrium state and thus its properties will change over time. This gradual change is referred to as *electrical aging*. This process is a gradual degradation of the insulating material, and is highly dependent on the electrical stresses it undergoes and the duration these effects continue. It is clear that this is a major concern to industrial power generation plants, as the need to continuously replace and maintain the insulation within generators would be a costly and time consuming process [14]. The effects of electrical ageing occur due to the injection of electrons (or holes under high field strengths) into the insulator material from the electrical contact through Fowler-Nordheim tunnelling [15]. The injected electrons will typically become trapped after a few scattering events due to their short mean free paths. These trapped electrons form negative charged homo-space charges near the point of injection, and subsequently create an opposing internal electrical field, reducing the electron injection rate. This space charge accumulation causes a shift in the field towards the anode and will increase the hole injection concentration. Despite many theories on both the macro and microscopic properties of the space charge accumulation [16–20], there is still no clear theory on the precise mechanism that space charge accumulation has on the electrical ageing of insulating materials [21].

### 2.3.2 Electrical discharge

Atoms and molecules become electrically charged due to ionisation effects from the cascade of injected carriers (electrons or holes). Electrical bridging between charged molecules causes an effect known as electrical discharge. Discharges that do not bridge two electrically conducting points are known as partial discharges. Partial discharges always occur in gaseous states [22]. Generally partial discharges can be classed into one of four groups:

- Corona discharge: This type of discharge generally occurs at a sharp point, such

as the tip of an electrical probe or a charged particle with a high field surrounding it.

- Surface discharge: Discharges that occur at the surface of a dielectric material.
- Internal discharge: Discharges occurring within cavities or defects within a dielectric material. These can also occur in channels generated through electrical stressing of a material [23].
- Electrical treeing: This can be thought of as a combination of corona and internal discharge effects. It typically occurs in materials under high electrical stress, with the discharge paths resembling the branches of a tree.

These effects are shown schematically in Figures 2.11a to 2.11d. All forms of electrical discharge are destructive to dielectric materials and can reduce the breakdown voltage the material can endure due to changes in chemical structures.

### 2.3.3 Electrical breakdown

In this section the process leading to electrical breakdown within insulators is discussed. Although this can occur in solids, liquids and gases, this section will focus on solid materials due to the work of this thesis considering solid materials.

#### Thermal breakdown

All electrical breakdown effects, regardless of the state of the material, are fundamentally caused by thermal instabilities leading to the destruction of the material. The thermal breakdown effects are typically caused through Joule heating within the dielectric, due to the electrical conduction and polarisation. The relationship between the generation and rate of heat transfer through the material is given by

$$c_V \frac{dT}{dt} - k \nabla^2 T = \sigma \vec{E}^2 \quad (2.44)$$

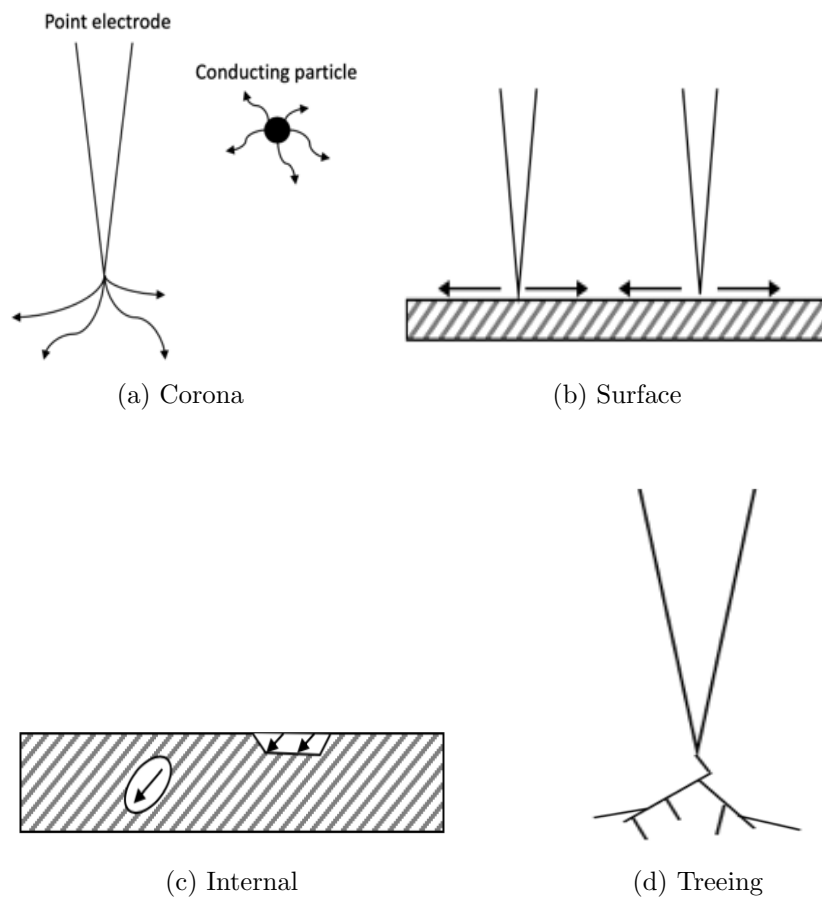


Figure 2.11: Schematic diagrams showing mechanisms of partial discharge. Sub-figures (a)-(d) represent the effects discussed in the main body of text.

where  $c_V$  is the specific heat capacity per unit volume,  $T$  is the absolute temperature,  $k$  is the thermal conductivity,  $\sigma$  is the electrical conductivity and  $\vec{E}$  is the electric field strength. For DC fields  $\sigma$  is simply the DC conductivity, but for AC fields  $\sigma$  includes the conductivity due to the dielectric polarisation loss i.e.  $\omega\epsilon_0\epsilon_r''$ . Equation 2.44 is difficult to solve analytically as  $c_V, k$  and  $\sigma$  are functions of temperature and in the case of  $\sigma$  also a function of the applied field. However, there are two simple cases that can be considered as the solutions to the equation.

In the first case it is assumed the electric field build-up is so rapid there is no heat loss to the surroundings and so this term becomes negligible. This reduces the equation to the simpler form of

$$c_V \frac{dT}{dt} = \sigma \vec{E}^2 \quad (2.45)$$

Assuming also that the electric field strength is ramped up linearly, then the ramp rate can be expressed as  $r_g = d\vec{E}/dt$  thus  $\vec{E}$  is

$$\vec{E}(t) = r_g t \quad (2.46)$$

Making the assumption that  $\sigma$  is a function of temperature with the following relation

$$\sigma = \sigma_0 e^{-\frac{E_\sigma}{k_B T}} \quad (2.47)$$

where  $E_\sigma$  is the activation energy. Substituting equations 2.46 and 2.47 into equation 2.45 gives

$$c_V \frac{dT}{dt} = \sigma_0 (r_g t)^2 e^{-\frac{E_\sigma}{k_B T}} \quad (2.48)$$

This equation can then be solved by separation of the variables and integrating  $T$  from  $T_0$  to  $T$  and  $\vec{E}$  from 0 to  $\vec{E}$  [24] giving

$$\frac{k_B}{E_\sigma} \left[ T_0^2 e^{\frac{E_\sigma}{k_B T_0}} - T^2 e^{\frac{E_\sigma}{k_B T}} \right] \simeq \frac{\sigma_0 \vec{E}^2}{3c_V r_g} \quad (2.49)$$

This equation is known as the impulse thermal breakdown approximation. It is valid for most cases under the assumption that  $c_V$  is independent of temperature,  $\sigma$  is independent of electric field strength and  $E_\sigma \gg k_B T$ . The thermal breakdown of the sample occurs when the specimen temperature reaches  $T$  and under the applied field that is reached at a time  $t = \vec{E}/r_g$ . The electrical breakdown of NaCl and KCl have been investigated using the theoretical predictions of this equation [24–26]. Where it was shown that the equations were well obeyed for a NaCl crystal, with a clear dependence of the electrical conductivity on the thermal conduction. It is also of note that the presence of impurities within the crystal was also shown to effect the breakdown strength, with the higher purity crystal showing greater breakdown strengths, 0.096 MV/cm for a pure crystal and 0.032 MV/cm for a doped crystal.

The second case considers the scenario where there is a finite maximum thermal voltage for a very thick specimen. In this case the voltage is only dependent on the physical properties of the dielectric material and the initial temperature. Here all the heat generated is assumed to be carried to the surroundings, such that the term  $c_V \frac{dT}{dt}$  becomes negligible. This then reduces equation 2.44 to the following, for the 1-D case

$$-k \frac{d^2 T}{dz^2} = \sigma \frac{dV^2}{dz} \quad (2.50)$$

We can now substitute equation 2.47 into this. Then integrating temperature from the specimen surface to the electrode surface with sample thickness  $d$  we arrive at

$$V^2 = 8 \int_{T_1}^{T_m} \left[ \frac{k}{\sigma_0 e^{-\frac{E_\sigma}{k_B T}}} \right] dT \quad (2.51)$$

$V$  represents the critical thermal breakdown voltage, for which there is a critical temperature  $T_{mc}$  at the center of the specimen. Thus

$$V_c^2 \simeq \sqrt{\frac{8kk_B T_0^2}{\sigma_0 E_\sigma}} e^{\frac{E_\sigma}{2k_B T}} \quad (2.52)$$

The thermal breakdown voltage becomes significant when the sample is thin, being proportional to the square root of the thickness. The heat generated within the sample is also more significant within AC fields when compared to DC fields. Due to this the breakdown strength is typically lower in AC than DC fields and decreases with the increasing frequency [27]. For AC fields it is beneficial to know the  $\tan \delta$  parameter as this is directly related to the breakdown voltage.

### Electrical breakdown

Electrical breakdown, while seemingly simple to explain as the sudden change of a material from insulating to conducting under a critical electric field strength, is far from this simple in practice. The breakdown of a dielectric material depends firstly upon its state of matter, i.e. solid, liquid or gaseous, but even within these states the type of material can also play a different role in the breakdown mechanism. Again since this work concerns the breakdown of solid dielectrics, this section will focus on theories of electrical breakdown within solids. Firstly, the difference between thermal and electrical breakdown must be understood. While thermal breakdown is mainly caused by the temperature rise, leading to Joule heating, and thermal excitations, electrical breakdown is contributed to more by electrical process than just thermal excitations.

The first proposed mechanism of electrical breakdown is known as *intrinsic breakdown*.

Here the breakdown strength is an intrinsic property of the dielectric material, that depends only on the temperature. Intrinsic breakdown typically occurs within very short timescales (10-100 ns), and is also independent of the waveform and duration of the electrical pulse applied. This means intrinsic breakdown is purely an electronic process. This effect arises due to the presence of impurities, defects and dislocations within the material. The presence of these defects cause electron traps within the material, which have ground state energies and excited energy states just below the materials conduction band, as shown schematically in Fig. 2.12. Under an applied

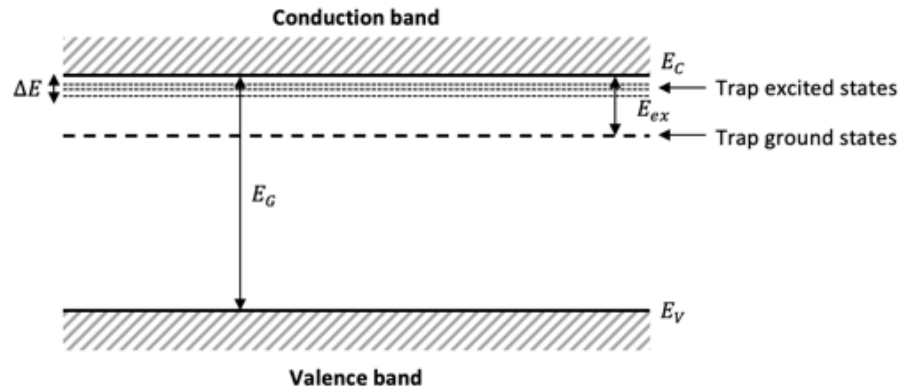


Figure 2.12: Schematic diagram showing the band structure of a dielectric solid, and the associated electron trap energy states.

electric field,  $\vec{E}$ , free electrons within the conduction band gain energy at a rate  $P_e$ , which can be expressed as,

$$P_e = \sigma \vec{E}^2 = \frac{dE}{dt} \quad (2.53)$$

where  $\sigma$  is the electrical conductivity and  $E$  is the energy gained by the electron. This acquired energy is used up in electron-electron scattering within the conduction band, electron-trapped electron scattering and electron-phonon scattering. In the case of metallic crystals where the free electron concentration is low, the main loss of the electron energy is through the electron-phonon collisions. Considering this the energy gain,  $P_e$ , will be a function of the field strength, electron energy and lattice vibration

temperature. While, the loss of energy,  $P_r$ , is a function of the field strength and the lattice vibrational temperature. By equating the energy gain and loss, it can be shown an instability occurs when  $P_e > P_r$  and hence the material will undergo breakdown.

The first theory of intrinsic breakdown was proposed by Zener [28]. This is a relatively simple mechanism in which free electrons are generated by tunnelling between the valence and conduction bands of the material, while under the presence of a high electric field. This process is shown schematically in Fig. 2.13. If an electron under-

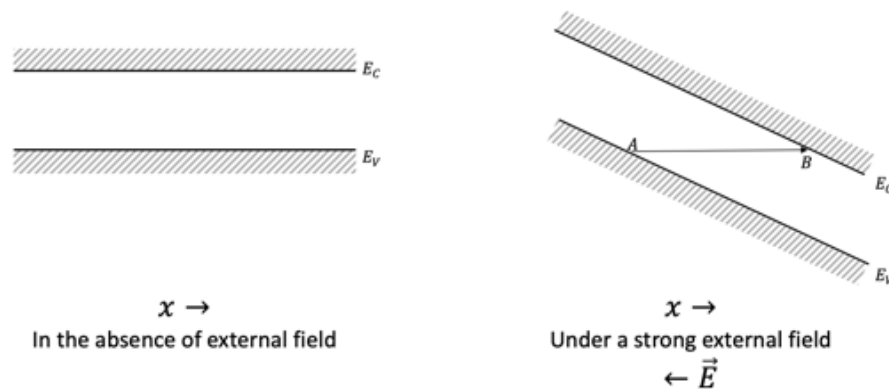


Figure 2.13: Schematic diagram showing Zener tunnelling of an electron from the valence band to the conduction band, under a high external electric field.

goes a Bragg reflection at a Brillouin zone boundary, it will usually reflect into the next zone. However, there is a finite possibility that the electron will instead transition by tunnelling to a higher energy band, i.e. the conduction band. Under the electric field the electron is accelerated until its wave vector increases to a value of  $k = \pi/a$ , with  $a$  being the lattice constant [29]. Although Zener intended to use this theory to explain breakdown in solid dielectrics, the large band gap usually makes this effect negligible. However, it may provide insight within narrow band gap semiconductors.

This was followed by a theory suggested by Seitz [30] that breakdown in solids and gases is similar, and arises due to electron avalanches. This is a questionable theory however, since the mean free path in solids is much shorter than gases and so how the electrons gain enough energy for impact ionisation is open to questioning. O'Dwyer

[31] pointed out that actually a model incorporating impact ionisations is important, provided that an assumption is made about the applied electric field not being uniform. It is also necessary to assume the mobility of the electrons is much greater than that of the holes, and injection of electrons from the cathode is also significant. The positive space charge from the holes enhances the field in the direction of the cathode and subsequently promotes electron injection. The combination of electron injection and impact ionisations act in a way to promote each other, and hence cause significant deformation of the electric field around the cathode, which in turn causes an increase in electron injection and hence further distortion of the field. These processes eventually lead to the electrical breakdown of the material. One of the strengths of this theory are its ability to show the thickness dependence of breakdown strength, but it fails to describe other breakdown phenomena.

The presence of a dielectric material between two conductive metallic electrodes acts to reduce the electric field strength. The high field strengths, however, cause the dielectric material to become compressed in the plane of the electric field. For fields of order  $10^6$  V/cm, the compression forces can reach several kN/m<sup>2</sup>. The elastic force works to compensate this compression force, but the stress-strain relationship can be complicated. For polymeric materials Stark and Garton [32] proposed a logarithmic relationship. The change in sample thickness can be evaluated through the relationship,

$$\frac{1}{2}\epsilon_r\epsilon_0 E^2 = Y \ln\left(\frac{x_0}{x}\right) \quad (2.54)$$

where  $Y$  is the materials Young modulus and  $x_0$  and  $x$  are the sample thickness before and after application of the field. The maximum applied voltage can be determined by differentiating eqn. 2.54 with respect to  $x$  to give,

$$\frac{x}{x_0} = e^{-\frac{1}{2}} = 0.6$$

The sample will therefore become unstable if  $x/x_0 < 0.6$ . Therefore we can express the breakdown voltage as

$$E_B = \frac{V}{x_0} = 0.6 \sqrt{\left( \frac{Y}{\varepsilon_r \varepsilon_0} \right)} \quad (2.55)$$

Electromechanical breakdown has been reported to occur in polyethylene and some other polymers within the high-temperature regime [33]. But this form of breakdown can be prevented through the use of encapsulation [34–36].

A theory put forward by Budenstein [37, 38] proposes that electrical breakdown follows four stages. Initially a formative stage, followed by tree initiation, tree growth and a return streamer. In the formative stages the electric field is stored within the dielectric material, causing the local rearrangement of the charge distribution through polarisation, impact ionisation, electron trapping and atomic displacements. This imbalance of charge distribution causes the breaking of atomic bonds. It is theorised, that at this stage, there is a phase change from solid to gaseous, if localised charge densities are present to such an extent that non-bonding orbitals are formed. The formation of a gaseous state allows an electrical tree to form, and the growth of the tree is dependent on the energy transfer from the electric field into the gaseous phase, usually via electrical discharges. These discharges tend to cause erosion of the material. The tree growth continues until it stretches between the two electrodes, resulting in a highly conductive channel, and hence the subsequent electrical breakdown of the material. While the electric treeing through the gaseous phase is convincing, it is difficult to imagine the phase transition within the material forming the gaseous state allowing the tree formation.

As can be seen here, theories of dielectric breakdown despite their merits often have many short comings due to the complexity of the process. In order to develop an effective model it is necessary to know all the prebreakdown and breakdown phenomena,

and ensure the developed model is consistent with all known experimental evidence.

## 2.4 Introduction to nanocomposites

The use of nanocomposite technology within the field of electrical engineering has evolved over the last few decades, after an advancing paper by Lewis in 1994 [39]. It was confirmed in experimental work by Henk *et al.* [40] and Nelson *et al.* [41] that there may be promise in the use of nano scale filler particles, for the enhancement of electrical properties. This led to increased attention in the use of nanocomposites for high-voltage and power system applications [42–46]. The use of both micro and nanocomposite technology show the promise to provide improved electrical insulation systems, capable of providing higher electrical resistances and operation at higher temperatures. Composite materials are typically formed by combining two or more components that provide a material with characteristics different to the components that make it up. A nanocomposite is simply an extension of this definition, such that for a nanocomposite one of the constituent phases of the material must have at least one dimension in the nanometer range. Nanocomposites also differ from conventional composites through the following: (i) they typically contain only a very small fraction of their respective filler material ( $\sim 10\%$ ); (ii) the length scale of the filler material is on the order of  $10^{-9}$  m as opposed to  $10^{-6}$  m; (iii) due to the small length scale of the filler particles, there is a very large specific surface area, when compared to conventional composites [43]. Due to the ability to form nanocomposites using a variety of matrix materials, they are classed into three main areas: ceramic matrix, metal matrix and polymer matrix nanocomposites [44], and within these categories there are further distinctions related to the choice of filler. This review will primarily focus on polymer nanocomposites. In the power industry inorganic fillers are typically used within polymer composites as they can be used to tailor specific desired electrical, mechanical and thermal properties of the composites [42, 46].

## 2.5 The road from micro to nano

Insulation materials themselves are sometimes argued to be a “mature science” and there is often a reluctance from industries to invest within insulation research. This is a surprising stance since all electrical systems rely on insulation in one form or another [47]. As the continuing developments on energy generation grow, the harsher environments insulation materials are subjected to cannot be overlooked, whether these be higher electrical stresses, higher operating temperatures, environmental exposures or even radiation exposures.

The first developed insulation materials were also composite materials, but formed using natural materials. Some of the filler materials available included: cellulose fibres, silk, wool, asbestos, sand, quartz etc. and these were dispersed into a naturally derived resin matrix from sources such as: trees, plants, insects, pitch, linseed oil etc. [48]. These materials however, possessed low electrical and mechanical properties so electrical machines could only operate within these limiting restrictions.

During the 1940s further material developments began to occur. One of the most significant of these was the invention of plasticised PVC, which subsequently led to the first patent for vinyl electrical tape by Snell, Oace and Eastwood in 1946. Further materials were developed by the incorporation of the natural mineral mica. These mica flakes were sandwiched between thin sheets of cellulose paper, occasionally with the addition of asphalt or bitumen [48], giving rise to kraft paper. The use of mica flakes became increasingly popular due to their high dielectric strength, surface resistance and low dielectric loss [49]. Initially mica was employed as small flakes embedded within a natural or synthetic resin for use in medium and high power applications. Currently however, mica is typically employed as mica paper, which is composed of very small flakes of mica processed in the same way as conventional paper is produced. Experimental work on the most effective mica composites was investigated by Park [50]. In this work, epoxy/mica composites were tested for their electrical breakdown, and also

the effect of mica concentration. The composites' viscosity was reduced using either a plasticiser or low molecular weight aliphatic epoxy. It was found that an optimum concentration of mica was around 20 wt.% and the electrical breakdown strength was higher through the use of the aliphatic epoxy.

This time period also gave rise to a large proportion of synthetic polymers and resins such as: polyesters and polyethylenes, fluorocarbons, silanes, epoxies, polyurethane, polypropylene and polycarbonate [48]. Epoxy based composites are typically employed due to their electrical, mechanical and thermal properties, while also being exploitable across different scales of electronic devices. While the composite industry began to mature in the 1970s, there is still a continued development. The term *nanocomposite* was originally given to a new class of materials developed by Toyota research group in the 1990s, which were termed clay-polymer nanocomposites [51]. The addition of clay into a nylon-6 matrix provided the needed thermal and mechanical improvement for use in timing belt covers. Although the term nanometric dielectrics was introduced by Lewis in 1994 [39], and although experimental work was performed to assess the properties of these new materials [39, 40, 52, 53], interest in the application of these nanodielectrics was only finally sparked after work by Nelson and Fothergill [41]. In this work they sought to obtain a fundamental theory of how the filler particles could enhance the dielectric properties of the polymeric materials. Following this, research focused on the development and characterisation of these materials [54–57]. It became apparent that the unique properties provided by nanodielectric is heavily influenced by the interfacial region between the filler and matrix.

## 2.6 High-voltage uses of nanocomposites

While nanocomposites can exhibit vastly increased physical and barrier properties, of greater importance in this work is the enhancement they provide to electrical performance. Here the specific case of high-voltage applications will be discussed. It has been shown for epoxy based composites that the introduction of filler particles leads

to increased mechanical and dielectric properties when compared to the epoxy alone [58, 59]. The use of filler particles within epoxy resins has also shown that the permittivity is reduced [58–60] along with the accumulation of space charges [61, 62]. The accumulation of space charge is a particular issue, as the presence of it can alter the local electric field within the dielectric and subsequently lead to effects such as electrical treeing and partial discharging [63]. A specific case of the use of nanodielectrics in high-voltage applications was performed by Gröpper *et al.* [64]. In this approach silica nanoparticles were incorporated into epoxy-mica stator windings used within large electrical generators, where they subsequently saw an increase in the resistance to electrical treeing and partial discharge, which lead to a longer lifetime of the material before breakdown. It was also seen that the mechanical and thermal properties were increased [64] showing the potential ability for these materials to be used in harsher environments.

Although improvement can be shown in the electrical properties of the nanocomposites, industrially there is also a key focus on the thermal conductivity of the insulation. The improvement to the thermal conduction of the insulation will lead into an improvement of the efficiency of the generator. Thermal conduction is expected to be improved though the addition of high conductivity filler particles [42] but this could come at the cost of reducing the electrical performance of the material. Studies by Zweifel *et al.* [65] investigated the influence of micron and sub-micron filler particles on the thermal conduction of the composites. It was shown for epoxy laminate composites that there was an increase of the thermal conduction without significant change to the dielectric properties. This was further investigated by Zhang *et al* [66] where the choice of filler was investigated. It was shown that BN provided the most improvement to the thermal conduction, and for low loading concentration the size of the particle, micro, meso or nano, had a minimal effect on the thermal conductivity of the composite.

Another key area of research focuses on the transmission of power through high voltage

cables. In the 1970s the insulation of both medium and high voltage cables was performed using polyethylene. These materials however, suffered heavily from moisture diffusion, which led to many failures. The insulation was thus replaced by a cross linked polyethylene (XLPE) instead. In the initial state this insulation was only suited to AC applications, but nowadays is mature enough for use in both AC and DC scenarios. The use in DC application arose from the incorporation of inorganic fillers into the XLPE matrix [67]. The incorporation of inorganic fillers led to an increase in the performance of the material, though the space charge accumulation, electrical breakdown and lifetime before breakdown.

With the growing needs to transmit and store electrical energy with ease, further developments in the insulation of high voltage cables is clearly key. Since transmission lines can often be buried underground or underwater, it is also of great importance the insulation has a significant lifetime, as replacing it regularly would become a costly and difficult process.

## 2.7 Choices of polymer and filler material

### 2.7.1 Polymers

With the large choice of polymeric materials available, it can become a difficult starting point to determine which polymer will provide the necessary properties to enhance the electrical performance of the nanodielectric. Typically the choices of polymers are divided into three categories based on their physical and chemical properties: thermoplastics, thermosets and elastomers.

Thermoplastic polymers are polymers that can become mouldable over a certain temperature, and solidify once cooled. Examples of these types of polymers include: polyethylene, polypropylene, polyvinyl-chloride, linear polyesters and poly-amides. This group of polymer is also classified dependent on their degree of crystallinity. Amor-

phous polymers are usable above their glass transition temperature where they become more liquid like, while crystalline polymers typically require processing temperatures above their melting points [68].

The second class of polymer materials are thermosetting polymers. These materials form their three dimensional network upon curing. This curing step typically takes the form of heating. Examples of this type of polymer include: epoxy resins, polyester resins, polyurethane and polyimide. A complication of this class of polymers is that they are often very brittle so, without reinforcement with fillers, they can become useless.

The final class of polymer materials are elastomers. These are flexible polymers with a low degree of cross-linking in their structure. Elastomers are classed into two categories depending on if they possess alkane or alkene bonds.

The most commonly applied polymers include polyethylene within electrical power cables, epoxy resins in electric machines and silicone rubbers as electrical insulators. Polyethylenes (low, medium and high densities) are popular choices due to their high electrical and mechanical properties and resistance to environmental conditions but fall short with low operating temperatures and in some cases difficulty in homogenous dispersion of filler particles. Thermosetting resins are useful due to their higher operating temperature but lack significant thermal conductivity when compared to the machine parts they are attached to.

### **2.7.2 Filler particles**

The second component of the composite material is the filler. The filler can be present as either one or multiple different materials. The geometry of the filler can vary dramatically as the requirement of the nanocomposite is simply for the filler to possess one dimension within the nanometer range. Some possible filler geometries include: fi-

bres, flakes, spheres, platelet, cubic etc. and they typically only represent a low overall volume percentage of the composite, unlike microcomposite materials. There is a large variety of filler particles available, dependent upon the end use of the composite, and some examples of these are shown in Table 2.1. As can be seen from the table various

Table 2.1: Examples of natural, organic and inorganic materials for use as possible filler materials, adapted with permission from [69].

Origin	Chemical nature	Examples
Natural	Animal	Silk, wool, hair
	Mineral	Asbestos
	Cellulose	Wood, Leaf, Stalk, Grass
Synthetic	Inorganic	Oxides: $\text{TiO}_2$ , $\text{SiO}_2$ , $\text{Al}_2\text{O}_3$ , $\text{ZnO}$ , $\text{MgO}$
		Hydroxides: $\text{Al}(\text{OH})_3$ , $\text{Mg}(\text{OH})_2$
		Metals: Al, Au, Ag, B, Sn, Cu
		Silicates: Talc, Mica, Nanoclay, Kaolin
		Salts: $\text{CaCO}_3$ , $\text{BaSO}_4$ , $\text{CaSO}_3$
		Carbides and nitrides: $\text{AlN}$ , $\text{BN}$ , $\text{SiC}$
Synthetic	Organic	Graphite flakes and fibres, Carbon nanotubes, Carbon black, Graphene, Graphene oxide
		Natural polymers: Cellulose, Wood fibres, Cotton Synthetic polymers: Aramid, Polyester, Polyamide, Polyvinyl alcohol

types of nanoparticle can be dispersed within the polymer matrix, improving electrical, thermal and mechanical properties as desired. The properties of these materials are however, derived from a variety of factors. The most influential being the choice of filler particle and polymer matrix. The dispersibility of the filler within the chosen polymer matrix can cause significant changes to the expected properties as it is ideal to have a well dispersed filler material with a good interaction between the matrix and filler. Knowledge of the filler particles properties and the desired properties is also important, as the fillers can have effects ranging from electrical resistance to conductance, thermal resistance, mechanical strength, optical, fire-retardancy etc. [70, 71]. So while one property is enhanced, another may be hindered.

### 2.7.3 Filler treatment processes

One of the biggest challenges related to polymer composite technology is achievement of well dispersed fillers within the polymer matrix [72]. This issue is further complicated by the tendency of particles to agglomerate due to their surface energy. A solution to this problem is to treat the surface of the filler to electrically stabilise the particles and prevent agglomeration. Due to the small size of the filler particles, it is important to consider the effect of these surface treatments as they could adversely effect the electrical performance of the material, through changes to the particle interface [73–75]. While there are many treatments for the functionalisation of the particle surface, they typically fall into one of three categories: (i) chemical treatment, (ii) grafting and (iii) plasma treatment.

In chemical surface modification non-polar species are reacted with the filler particles to chemically bond to the surface. These reactions are typically performed on fillers that possess surface groups such as OH, which allows a condensation reaction to occur between the OH groups of the chemical agent and the surface of the filler particle. A typical choice of coupling agent is a silane species, as these can interact with both organic and inorganic surfaces [76]. The addition of the species onto the particle surface causes a change in the polarity and enhances steric repulsion between particles leading to a more uniform dispersion and helping to reduce particle aggregation.

Grafting is similar to chemical modification however, it is usually performed using functional polymer molecules. This is again performed by allowing the polymer material to form covalent bonds to the surface of the filler particle and effectively become “grafted” onto the surface. The alternative to directly grafting a polymer chain onto the surface is to polymerise monomers that have already grafted onto the surface, allowing control over the length of the polymer chain attached [77]. The addition of the polymer chain transforms the surface to either a hydrophilic or hydrophobic nature, and allows good miscibility with the polymer matrix.

The final possible treatment method is through the use of plasma radiation. The use of plasma causes physical and chemical changes to the surface of the particle, but doesn't cause changes to the bulk properties of the material. The use of plasma radiation can cause surface functionalisation leading to increases of hydrophilicity or hydrophobicity, and subsequently make the dispersion of the particles much easier. Modification via plasma treatment often provides good levels of integration between filler and matrix [72].

## 2.8 The interfacial region between polymer and particle

The interfacial region between filler and matrix is theorised to have a significant impact on the properties of a nanocomposite [54]. As the size of the filler particles decreases, the overall surface area increase significantly. This is particularly important for nanomaterials, where a majority of the atoms will possess surface properties rather than bulk like properties. In this case each atom of the nanoscale filler has the potential to interact with the polymer matrix. In order to understand how this filler interface impacts the dielectric properties of the composite, several theories have been put forward to help predict the effect of particle shape and size on the effective dielectric properties.

A model was put forward by Lewis in order to attempt to explain the interfacial region between two adjacent particles [39]. In this model Lewis proposed that for two uniform material phases, A and B, the relative intensity  $I_\alpha$  for any material property  $\alpha$ , remains constant within the uniform regions of A and B, but becomes significantly altered as the interface to a different phase is entered [78, 79].  $\alpha$  typically characterises a parameter such as electric field or dielectric permittivity but could be used to characterise any chemical or physical property. Lewis also proposed that an electric double layer would form around the particle within their interfacial region.

The ideas of this model were developed by Tanaka [59] to modify and explain the way polymer nanocomposites interact to change the dielectric properties. Tanaka's model explains the way in which the electrical structure of the interface region interacts. A schematic diagram explaining the model is given in Fig. 2.14. In this model

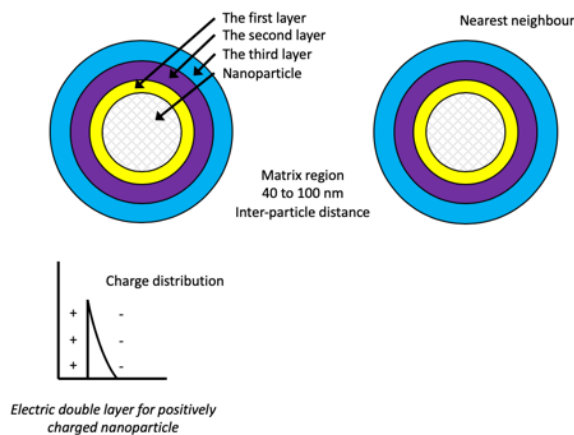


Figure 2.14: Schematic diagram showing Tanaka's multi-core model. Adapted with permission from [59], ©2005, IEEE. The white shaded circle represents the nanoparticle, with the yellow ring showing the 1<sup>st</sup> bonded layer, the purple ring showing the 2<sup>nd</sup> bound layer and the blue ring showing the 3<sup>rd</sup> loose layer.

the nanoparticle is surrounded by three phases. The first phase is a bonded layer in which the polymer matrix is directly bonded to the nanoparticles surface. The second phase is a bounded layer in which polymer molecules within the matrix are adsorbed at the interface to the first layer. The final phase is a loose phase where there is a small amount of coupling of the polymer matrix to the second layer. Over these three layers a Gouy-Chapman electric double layer is formed. The presence of this double layer can cause the nanoparticles to interact through the far-field effect. The model has been shown to successfully describe partial discharges in PA/LS nanocomposites [59].

While these models give an idea of the effect of the interfacial region on the dielectric properties of nanocomposites, further study is required to accurately explain the effect of this interface on the associated electrical properties.

## 2.9 Electrical performance of nanocomposites

Perhaps the most important application of polymer nanocomposites for dielectric applications is the improvement they provide to associated dielectric parameters. In this section a discussion of the use of nanodielectric within the applications of permittivity, discharges, space charge accumulation and breakdown strength will be discussed.

### 2.9.1 Permittivity

Generally it is typical to see an increase to the relative permittivity of a composite upon the addition of an inorganic filler material, due to the often higher permittivity of the filler (there are some exceptions to this such as mica and  $\text{SiO}_2$ ) when compared to the base polymer [59]. The introduction of the fillers causes Maxwell-Wagner interfacial polarisation, which provides information on charge trapping and relaxation of dipole reorientation [80], which typically causes an increase of the permittivity at low frequencies. However, when nano fillers are introduced, the converse is observed and the relative permittivity decreases [41]. For example, from this data, at 1 kHz and 393 K, the relative permittivity of the base resin was 9.99, and with the introduction of micro  $\text{TiO}_2$  the permittivity rises to 13.8 and with nano  $\text{TiO}_2$  it falls to 8.49. It is theorised that this decrease in relative permittivity is an effect of the particle interfacial region, providing a collaborative effect of dipole relaxation [41, 80]. In the low frequency domain there is also a difference observed in the loss tangent. The nanocomposite saturates to a consistent value, showing that the loss tangent is independent of the frequency for this low frequency region. This independence to frequency was described as low-frequency dispersion by Jonscher [81]. Similar results to Nelson *et al.* were produced by Singha *et al.* [82] where they investigated the effect of micro and nano fillers of  $\text{Al}_2\text{O}_3$  and  $\text{TiO}_2$  on the permittivity of epoxy resin. As before they saw significant difference between the micro and nanocomposite formed, with the permittivity increasing with filler loading for microcomposite, but a lower permittivity in the nanocomposite when compared to the base resin. They suggested that the permittivity is highly dependent on the filler particle and its loading concentration. It was also ob-

served that there was a minimal change to the loss tangent regardless of filler loading. Studies on epoxy resins with other filler materials was performed by Kochetov *et al.* [83] where the additional fillers AlN, MgO, SiO<sub>2</sub> and BN were investigated. These fillers were first treated using a silane agent to improve the dispersibility into the epoxy resin. For filler loadings below 5 wt.%, it was observed there was a minimal change to the loss tangent with the frequency, however, the nanocomposites all show permittivity below that of the original resin. Similar studies have been performed using epoxy resins and different filler particles, and the interested reader is directed to the following sources [59, 84–88]. Although most research suggests that the use of nanofillers is of great benefit to improving the dielectric losses, a theory of the mechanisms behind the process needs to be understood such that the ideal conditions for producing a nanocomposite can be determined and evaluated against the experimental data produced.

### 2.9.2 Partial discharges

Of particular importance in high voltage applications of insulation is the resistance to partial discharges, especially when considering uses such as stator end windings, wires of wound motors and HVDC cables. Partial discharges will gradually wear down the insulator, and cause electrical breakdown [56]. There are different methods to evaluate partial discharges, and one of particular importance is the characterisation of the erosion depth, which can be used to compare micro and nanocomposites resistances [89].

The erosion resistance for epoxy micro and nanocomposites was investigated by Krivda *et al.* [56], using a rod-to-plane electrode setup. In this work it was shown that the time to failure for both micro and nano composites were improved compared to that of the base resin. However, it was also shown that the combined effect of micro and nano fillers provided even longer times to failure than the base resin, microcomposite or nanocomposite alone. The partial discharge is highly dependent on applied voltage however so it is unsure if this trend would continue when the voltage is operated higher than 4 kV/600 Hz. The addition of microparticles within the epoxy resin can

be thought of as providing a barrier to the penetration of the current, and the extra inclusion of nanoparticles within this matrix fill the space between the microparticles providing extra barriers to be penetrated. In the nanocomposite alone it is theorised that as the surface of the resin is degraded the nanoparticles are exposed at the surface and due to their high resistance provide a stronger barrier to the penetration of the current and hence increase the lifetime. The effect of composite preparation was studied by Iizuka *et al.* [90], where two types of commercial SiO<sub>2</sub> nanoparticles were prepared in epoxy. It was found improvement was only seen in the samples produced by adding the fillers and coupling agents into the base resin. Tanaka *et al.* [91] studied the effect of filler loading, and effect of changing the filler from SiO<sub>2</sub> to SiC. While the addition of both fillers showed the erosion performance could be improved, the SiC showed much broader erosion profiles showing that as the resin degrades the SiO<sub>2</sub> appear more exposed on the surface and provide a stronger barrier than the SiC fillers. The effects of concentration were again studied by Preetha *et al.*, [92] using Al<sub>2</sub>O<sub>3</sub> nano fillers. It was shown here that even a very small loading of filler (0.1 wt.%) showed significant improvement in comparison to the base resin. It was theorised that the inter-particle distance plays a significant role on the erosion characteristics, and interactions between filler and polymer may also be contributors. The combined effect of nano and micro fillers was again studied by Li *et al.* [93, 94]. In this work it was found that the nanocomposite had the longest breakdown time (307 min) when compared to the micro/nanocomposite (275 min), microcomposite (94 min) and base resin (186 min). As can be seen from these results, the addition of the micro fillers hinders the life time of the material, unlike the nano fillers which make a significant improvement to the lifetime. It should be noted, however, that the addition of the microfillers does help to improve the thermal conduction [93], so there may be some compromise with the use of microcomposites. Similar work to this has been presented by Henk *et al.* [40], Li *et al.* [95], Zhang *et al.* [96] and Imai *et al.* [97].

### 2.9.3 Space charges

Space charge accumulation occurs within a dielectric when the rate of charge accumulation is different to the rate of charge removal. The presence of space charge will cause deformation of the localised electric field within the dielectric, leading it to a premature breakdown. The space charge accumulation ability is seen as a key factor in the dielectric properties of polymeric insulation, and is complex in nature when compared to other forms of dielectric behaviour and also varies depending on the nature of the material. For example, when considering a semi-crystalline material such as polyethylene, there is an interfacial region between the crystalline and amorphous regions of the material providing sites in which space charge can accumulate, due to an increased presence of trap sites forming at the interface of the two regions [98]. The addition of fillers further complicates this as it introduces more interfacial sites where space charge can accumulate [99]. The first reports on the difference in space charge accumulation between micro and nanocomposites were presented by Nelson *et al.* [41]. From their results it was observed that in microcomposites the maximum field observed builds up to around twice the magnitude of the applied field, while in the nanocomposite the field stabilised slightly above the applied field. It has been shown that the space charge accumulation is reduced within nanocomposite systems for a variety of fillers, epoxy/TiO<sub>2</sub>, Al<sub>2</sub>O<sub>3</sub>, ZnO, PP/layered silicate and LDPE/TiO<sub>2</sub> [59]. LDPE/TiO<sub>2</sub> nanocomposites produced by Yin *et al.* [100] showed that the hetero-space charge generation near the electrode was significantly reduced with the nanocomposite when compared to the base polymer. In work presented by Tanaka *et al.* [55] an investigation of commercially used XLPE and its nanocomposites using fumed SiO<sub>2</sub> were investigated. It was seen that the functionalised silica particles performed the best in regards to the space charge reduction. It was evaluated that the nanofillers reduce the charge accumulation, as they are characteristic for impurity absorbance. The use of nanocomposites for space charge accumulation have the following effects: there is an increase in space charge in low fields but this decreases with field strength, space charge is formed internally and the charge decays over time but this decreases with filler loading [80].

### 2.9.4 Electrical breakdown strength

Electrical breakdown strength is of key importance within high-voltage applications. The incorporation of fillers into the polymer matrix can have significant effects on the breakdown strength, but this is highly dependent on the shape, size, surface modification and electric properties of the employed fillers. It is important to not provide significant differences in dielectric strength of matrix and filler materials as this can distort the electric field locally, and subsequently reduce the breakdown strength [70]. The choice of filler can also influence the application use of the formed nanocomposite. For example, high permittivity or high conductivity fillers can reduce the electrical breakdown, however, they can be essential in situations requiring high thermal conductance. Electrical breakdown strengths are typically expressed in terms of a Weibull plot, representing the cumulative probability of breakdown for a large number of samples [80].

The effect of filler concentration on breakdown strength is debated, with some authors showing the breakdown varies with low concentrations, while others propose that a critical concentration is needed for the electric breakdown to change. The effect of filler concentration on epoxy nanocomposites with fillers of  $\text{Al}_2\text{O}_3$ ,  $\text{SiO}_2$  and  $\text{AlN}$  showed that the breakdown strength was highest for loadings of 0.5 wt.% in  $\text{Al}_2\text{O}_3$  and  $\text{SiO}_2$  but was highest in  $\text{AlN}$  at 2 wt.% loading, the results however, varied with the filler loading up to 10 wt.% [101]. While other authors show there is no significant variation in breakdown strength for filler loadings below 10 wt.%, for microcomposites of similar loadings there is a significant decrease in the breakdown strength with the filler loading [43]. A similar difference was observed in the reduction of breakdown strength with the addition of microparticles and an increase with nanoparticles by Roy *et al.*, when loading  $\text{SiO}_2$  in cross-linked polyethylene (XLPE) [102]. In a review by Li *et al.* [103] they further confirmed that the DC breakdown strength decreased with the increase of filler concentration when nanoparticles are employed. While the converse was true for microparticle fillers, which have a relative negative effect on the breakdown

strength of the polymer.

While the electrical breakdown strength is of key importance for insulation purposes, the choice to add nano sized filler particles could be seen as either a help or a hindrance depending upon factors such as: the choice of filler, their loading concentration and dispersion within the polymer matrix. However, as previous results show there are significant increases to the breakdown strength through the incorporation of nano fillers, but for nanodielectrics to become standard within electrical systems, highly systematic studies are required to find the optimum conditions for producing the material.

## 2.10 Thermal properties of nanocomposites

While perhaps an overlooked property when considering nanodielectric materials, the thermal conduction is of key importance to increase the overall efficiency of the electrical system. Although polymers are a popular material for insulation due to their high insulative properties and low production costs, they typically provide limited thermal conduction, acting more as insulators with conductivities in the range of 0.1 to 0.5 W/m K [70]. An obvious solution to this is to develop nanocomposite that employ filler particles with high thermal conductivity. Some examples are shown in table 2.2. Although

Table 2.2: Example thermal conductivities of some inorganic filler particles. Adapted with permission from [70], ©2005, IEEE.

High-conductivity filler	Thermal conductivity (W/m K)
Fused SiO <sub>2</sub>	1.5-1.6
Crystalline SiO <sub>2</sub>	3
Al <sub>2</sub> O <sub>3</sub>	38-42
BeO	300
ZnO	60
Si <sub>3</sub> N <sub>4</sub>	86-120
BN	29-300
AlN	150-220
SiC	85
BaTiO <sub>3</sub>	6.2
Diamond	2000

there are several types of fillers presented in the table, only some of these find real applications within nanodielectrics. This is mostly attributed to the fact some of these fillers possess undesirable electrical properties, thus hindering the electrical properties while improving the thermal ones. Other hinderances include issues such as: toxicity, corrosion resilience and oxidation resilience. AlN is a popular material of choice as it possesses good thermal conductivity but is hindered by its high permittivity and low resistance to oxidation. The most popular candidate for high thermal conduction nanodielectrics is BN, as it possesses the thermal conductivity, high temperature resilience and low permittivity. It is however, challenging to exploit the nano structures of BN.

The conductivity of a composite material is a complex matter, requiring knowledge of the conductivity of the matrix and filler particles, the thermal resistance between these components when combined, the size and orientation of the filler and how dispersed within the matrix it becomes. This makes predictive modelling of thermal conduction of composites very challenging. In modelling work by Nielsen [104] it is proposed that with a spherical filler particle, of packing volume 0.637, there may be a limit to the thermal conductivity, that is irrespective of the relative conductivity of the filler and matrix. In contrast to the electrical properties that typically improve with the loading of nano scale fillers, it is expected the thermal conduction would improve through the use of larger scale particles. Since the heat transfer mechanism is through the scattering of phonons, a larger interfacial area will provide more scatterings, and subsequently a lower thermal conduction. In work performed by Han *et al.* [105] the thermal conductivity of micro and nano BN was investigated as a function of volume fraction. Based on the experimental work presented the conductivity of both micro and nano BN is the same at loadings of 10 %. Once, the loading begins to increase the nano BN increase rapidly giving around 0.6 W/m K at a loading of 30 %, while the micro BN provides a value of around 0.5 W/m K. Only when the micro BN is loaded to 50 % does the conductivity increase to a similar level as the nano BN. With no experimental data for nano BN beyond 30 % loading, it is difficult to say if the micro sized particles

surpassed the nano sized particles. If it is indeed the case that the nano BN exceeds the micro, then the theory of larger particles improving the thermal conductivity becomes questionable. It is of note that higher surface areas can lead to a reduction in thermal sensitivity, and thus the use of a nano-filler with a much greater surface area than a micro-filler could subsequently lead to a poorer than expected thermal conductivity when compared to a microcomposite of the same filler material.

While progress has been made on increasing the thermal conduction of nanocomposites, there are still many questions that remain to be answered. The most important of these from an application perspective are: the ability to run the equipment at lower operating temperatures, the service life of the material and increased operating stresses without causing temperature related damage. All of these desirable traits come with the desire to continue the physical and electrical properties already possessed by nanocomposite materials.

## **2.11 The outlook for nanocomposite technology**

The future for nanodielectrics is one that is expected to continue as new fillers are found and materials developed. It could however, be expected that development in the field will follow the current research trends focusing on high electric strength, low dielectric losses and good thermal conduction. The overall goal for new nanocomposite technology is the materials are effective for electrical insulation purposes, reliable and long lived and not overly costly to produce. Of course further developments in the field of composites as a whole could open up new routes, such as, novel nano-scale filler particles, self-healing polymers and new production techniques. It is clear, despite the challenges that accompany them, nanodielectric materials will become the key players in the design of future electrical power and generation systems.

## Chapter 3

# Experimental methodologies

### 3.1 Materials

This work has studied two types of commercially available nanoclay minerals. A natural clay sodium montmorillonite, commercially referred to as Cloisite Na<sup>+</sup> (BYK Additives, USA) and a synthetic hectorite clay Lucentite SWN (CO OP, Japan). In this work clay sols are prepared using ultrapure water, 18.2 M $\Omega$  (Triplered, UK), as a solvent and in concentrations of wt.%, unless otherwise stated. All samples were weighed using a Mettler AE 200 balance (Mettler-Toledo (HK), MTCN Limited, Hong Kong) where required, to an accuracy of 0.05 mg.

### 3.2 Microscopical analysis

#### 3.2.1 Optical microscopy

Optical microscopy is a technique that uses visible light and a system of lenses to provide magnification of small objects, typically to the micrometer range. Since optical microscopy was used to view the surface structure of polymer films, a stereo optical microscope was used for the imaging. The stereo microscope uses light reflected from the sample surface as apposed to transmitted through the sample. All optical images presented were obtained using a AmScope SE306R-P stereo microscope (AmScope, UK). Images were captured using a MU303 3.1M pixel USB3.0 CMOS camera (AmScope, UK) connected through the microscope eye piece and connected to a PC running AmScope 3.7. An advantageous use of a stereo microscope, over other types of optical microscope, is that the light is not transmitted through the sample, rather reflected from the sample, allowing opaque samples to be viewed with greater ease. Typically, however, stereo microscopes are hindered by low magnification levels, making them suitable for a limited number of tasks.

### 3.2.2 Scanning electron microscopy

Scanning electron microscopy (SEM) is a technique that at its core is similar to that of an optical microscope, however, to beat the diffraction limit of an optical microscope, a “beam” of electrons rather than a light source is employed. Due to the de Broglie relation, the electrons behave as waves with a wavelength dictated by their accelerating voltage. The electron beam is focused onto the sample through a combination of lenses and apertures. The electron beam is rastered across the surface of the sample, and in doing so, causes an interaction with the sample. This interaction can lead to Auger electrons, secondary electrons, backscattered electrons and X-rays. Through the use of specific detectors an image can be produced from the signals obtained from these interactions. The SEM images presented in this work were obtained using a JSM-7100F Field Emission Scanning Electron Microscope (JEOL, USA), with the experimental conditions presented in the corresponding images. While SEM is a powerful tool, it requires samples to be small enough to fit on the sample stage and be able to withstand the vacuum environment. This makes a conventional SEM unsuitable for “wet” samples, such as gels or biological samples. But environmental SEMs (ESEM) are available that can be used for direct imaging of such samples, avoiding damage during any sample preparation process for standard SEM analysis.

SEM also provides a method through which qualitative analysis of the elemental composition of a sample can be determined. The impacting electrons can excite the electrons within the sample and cause them to be ejected from their shell, leaving an effective hole. An electron in a higher energy orbital will subsequently drop in energy to fill this hole, and emit a photon in the process. The wavelength of such photons are typically within the X-ray region of the spectrum, with each element emitting at a characteristic wavelength. Hence, the technique being named energy-dispersive X-ray spectroscopy (EDXS). While a useful technique, it was not explored in this thesis due to the expected similar chemical composition of the types of clay under study.

### 3.3 X-Ray diffractometry

X-ray diffraction (XRD) techniques allow detailed studies of crystalline materials, allowing studies of the position of atoms and the bonds between them. X-rays are ideal for the study of crystalline structures due to the typical wavelength of an X-ray being the same order of magnitude as the atomic spacing of a crystal. Due to the ordered arrangement of the atoms within the crystal the incident X-rays are scattered elastically by the atoms electrons. In most conditions these scattered rays cause destructive interference, but in specific directions they produce constructive interference instead. The specific directions within which constructive interference occurs is determined by Braggs law,

$$2d \sin(\theta) = n\lambda \quad (3.1)$$

Where  $d$  is the spacing between the diffracting planes,  $\theta$  is the incident angle,  $n$  is an integer and  $\lambda$  is the wavelength of the incident X-rays. In this work the technique of powder XRD (pXRD) has been employed, which is used for the structural characterisation of powdered materials. In pXRD the sample is referred to as isotropic as each crystal orientation is equally represented, and it is assumed the sample is arranged randomly. Therefore, statistically it is possible to detect each plane within the pXRD spectrum. Due to the presence of characteristic peaks of crystals, it provides a powerful analytical tool for the identification of materials, which can then be further used to evaluate the material structure. In this work pXRD spectra were obtained using a PANalytical X'Pert pro (DY2010) powder X-ray diffractometer (Malvern Panalytical, Netherlands) operating with a Cu anode providing incident X-rays with wavelengths of  $K_{\alpha_1} = 1.540598 \text{ \AA}$  and  $K_{\alpha_2} = 1.544426 \text{ \AA}$ . Concentrated solutions of samples were prepared and deposited onto glass microscope slides and left to dry. Once dried the prepared sample was held in a fixed position within the instrument, with the detector rotating about it. During the scan, the generator was operated at a voltage of 45 kV

and current of 40 mA with an X-ray monochromator employed. The scan was collected in a continuous manner, with a step size of  $0.002^\circ$  with each step lasting for 10.16 s. Characterisation of the *hkl* peaks was performed using literature references.

## 3.4 Chemical composition

Molecular absorption of electromagnetic radiation within the infrared region of the spectrum causes energy transitions between ground states and vibrational energy levels within molecules. These modes of vibration can include: symmetric or asymmetric stretching, rocking, scissoring, wagging and twisting. Due to this, the same bonds may emit at different frequencies, for example, a C-H bond exhibits both stretching and bending modes, which occur within the bands of  $2850\text{-}3400\text{ cm}^{-1}$  and  $1260\text{-}1470\text{ cm}^{-1}$ , respectively. Fourier transform infrared spectroscopy (FTIR) is a popular method for the determination of molecular functional groups due to the characteristic wavelengths at which atomic bonds vibrate. In this work FTIR has been used to determine the bonds present within the clay structure and hence evaluate the chemical structure. FTIR spectra were obtained using a Cary 630 FTIR Spectrometer (Agilent, USA). Powdered samples were placed onto a diamond ATR crystal and then spectra were collected using the full spectral range available, which was averaged over a total of ten scans, with a resolution of  $4\text{ cm}^{-1}$ .

## 3.5 Surface charge

The surface charge of nanoclay materials is a fundamental property, which arises due to the isomorphic substitutions of ions within the clay layer i.e.  $\text{Mg}^{2+}$  for  $\text{Al}^{3+}$  within the octahedral layer and the exchange of  $\text{Si}^{4+}$  for  $\text{Al}^{3+}$  in the tetrahedral layer. This charge is often referred to as the cation exchange capacity (CEC) and is most often expressed in terms of mEq/100g of clay [106]. In order to determine the value of this CEC, some analytical method must be employed to exchange the original cations within the clay. Common approaches to this include: the ammonium exchange method [107], colori-

metric titration by hexaminocobaltchloride [108], the methylene blue test [109] and the barium exchange methods [110]. However, here a simple technique involving the surface tension developed by Burrafato and Miano will be employed [111]. The method is based upon the affinity of the cationic surfactant, hexadecylpyridium chloride (CPC) with the clay surface [112], however, this limits the method slightly due to the tendency of the surfactant to form a multi-layer upon the surface.

To understand the principles of this method, first, the mechanistic interactions of surfactant molecules in solution must be understood. Typically surfactant molecules are organic in origin and are amphiphilic, meaning they possess both hydrophobic (the heads) and hydrophilic (the tails) groups. They diffuse into solutions and then will adsorb at the interface region for the two phases: the liquid-gaseous interface. The water insoluble hydrophobic tail will often extend out of the liquid phase at the interface into the gaseous phase, while the water soluble hydrophilic portion remains within the liquid phase. The adsorption of surfactant into the interface lowers the interfacial free energy (the surface tension) of the liquid phase, and a gradual decrease in the surface tension is seen as the concentration of the surfactant increase. Eventually the interfacial region is covered by a layer of surfactant molecules after which further increase in surfactant concentration will not lead to further decreases in surface tension. However, if the concentration is increased, the free surfactant within the liquid phase will begin to form micelles. A micelle is simply an aggregated system of surfactant molecules. The point at which this occurs is known as the critical micelle concentration (CMC). A schematic explanation of this process is shown by Fig. 3.1 when instead the surfactant is added into a solution containing clay particles. If the surfactant has a counter-charge to the charge on the clay surface, it will instead favour this rather than the interfacial layer between liquid and air. In this process the omium ion of the surfactant exchanges with the inter-layer cations within the clay structure and intercalates the structure as shown in Fig. 3.2. This in turn causes the surface tension to remain unchanged up until the point that all the adsorbed cations have been exchanged for the omium ions, this

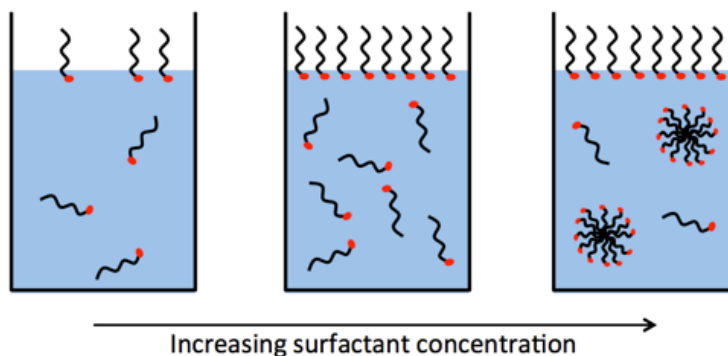


Figure 3.1: Left to right: The increasing concentration of surfactant in water leading to the formation of an interfacial layer and subsequent formation of micelles at (or above) the point of CMC.

is the point at which the cation exchange capacity (CEC) is reached. When this point is reached, it can be determined that the surfactant molecules have fully exchanged the cations and adsorbed onto the clay surface. After the CEC point is reached the surfactant molecules will again form a layer at the interface and reduce the surface tension until the CMC concentration is reached.

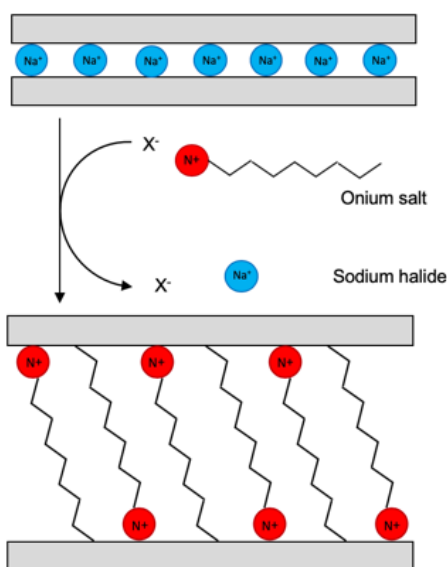


Figure 3.2: Schematic diagram showing the cationic exchange process between inter-layer cations and the introduced surfactant molecules.

In this work the surface charge of the two clays Cloisite  $\text{Na}^+$  and Lucentite SWN have been determined. The surfactant of choice for this was the cationic hexadecylpyridium chloride (CPC) as outlined in the method published by Burrafato and Miano. The

CPC surfactant molecule is formed of a hydrophilic positively charged head group and a hydrophobic carbon chain tail, as shown by Fig. 3.3. CPC (Sigma Alrich, UK) was



Figure 3.3: Structural model of the hexadecylpyridium chloride molecule

prepared at a concentration of 0.025 N, and clay suspensions of 0.5 wt.% were prepared at 50 ml total volume, both using ultrapure water as a solvent. A set volume of CPC was titrated into the clay solution using a volumetric burette. The clay-surfactant suspension was then mixed using an auto-shaker for twenty minutes in order to encourage the interaction between surfactant and clay particles. Once shaken, the suspension was filtered using gravitational filtration, with filter paper of pore size 5-13  $\mu\text{m}$  (Fisher Brand, UK). The surface tension of the filtrated suspension was then measured using a KRÜSS tensiometer (model K6) with a platinum-iridium ring, to within an accuracy of 0.5 mN/m. This process was repeated for a range of CPC volumes, with each point corresponding to a fresh clay solution. In order to determine the CEC of the clay, the following equation is employed

$$\text{CEC (mEq/100g)} = \text{CPC}_{\text{added}} (\text{cm}^3) \times 10 \quad (3.2)$$

where the volume of CPC added is determined from the equivalence point of the titration, represented by the intersection of two linear regions of the plot. The intersection point of these linear regions was determined by solving the set of simultaneous equations for the  $x$ -axis intercept value, and then applying eqn. 3.2. This allows for direct determination of the clays CEC and hence its relative surface charge.

### 3.6 Contact angle measurements

The presence of a liquid on a solid surface is something that is often seen in every day life, and typically one of two scenarios occur; the liquid spreads over the solid producing a continuous film or the liquid beads up and forms a discrete droplet. In the case of a droplet the shape is defined by many parameters such as: the liquid, temperature, pressure etc. and so the liquid will form a droplet with a defined shape depending on the environmental conditions. A schematic diagram of a droplet on a surface is shown by Fig. 3.4. The point of contact is characterised as the thermodynamic equilibrium

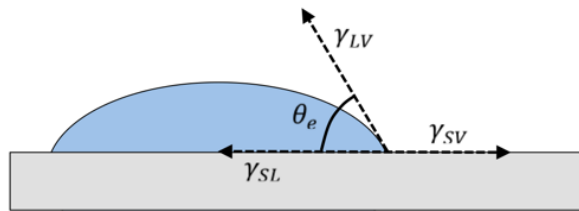


Figure 3.4: Schematic diagram showing the contact point of a liquid droplet on an ideal solid surface

of three phases: namely solid ( $s$ ), liquid ( $l$ ) and vapour ( $v$ ) (Note that the vapour phase can be replaced by another immiscible liquid phase). The interfacial energies of the three phases are denoted as  $\gamma_{sv}$ ,  $\gamma_{sl}$  and  $\gamma_{lv}$  for the solid-vapour, solid-liquid and liquid-vapour phases, respectively. The angle made by the contact line to the solid surface is known as the equilibrium contact angle, and was described mathematically by Young [113] as

$$\gamma_{sv} - \gamma_{sl} - \gamma_{lv} \cos \theta_e = 0 \quad (3.3)$$

An easy method to determine the wettability of a surface is to measure the contact angle formed by the liquid on the solid surface. Fig. 3.5 shows how the contact angle can be used to determine wettability. For contact angles of  $\theta = 180^\circ$  the surface is said to be perfectly non-wetting (A), contact angles of  $90^\circ \leq \theta < 180^\circ$  have low wetting

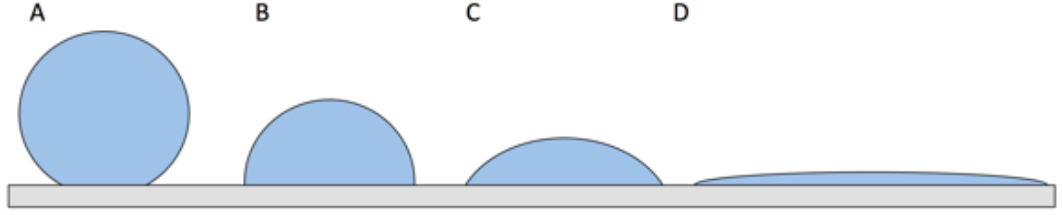


Figure 3.5: Schematic diagram showing the relationship between contact angle and surface wettability. Sub-figures (A)-(D) represent decreasing contact angle to the surface, and increasing wettability.

(B), contact angles of  $0^\circ \leq \theta < 90^\circ$  have high wetting (C) and contact angles of  $\theta = 0^\circ$  are perfectly wetting (D). In the case of water, surfaces that are wetting are described as *hydrophilic* and surfaces that are not wetting *hydrophobic*. In the special case of contact angles of  $\sim 150^\circ$  or greater the surfaces are described as superhydrophobic, and this effect can be seen in natural systems such as, lotus leaves [114]. Contact angle measurements in this work were performed to assess the wettability of surfaces and the degree of hydrophobicity they possess. Contact angle measurements were performed using a KRÜSS Drop Shape Analyser DSA100 (KRÜSS GmbH, Germany). The contact angle is determined as the average of the left and right angles, for a typical drop size of  $5 \mu\text{L}$ , by applying the Young-Laplace fitting algorithm.

## 3.7 Surface free energy

### 3.7.1 Owens-Wendt-Rabel-Kälble model

The Owens-Wendt-Rabel-Kälble (OWRK) model is an approach for the determination of a solids surface energy, based on the Fowkes assumption of two types of interfacial interactions between a solid and liquid [115]. The SFE of the solid (or liquid) is split into its dispersive and polar components, which are themselves related by geometrical mean values. This allows the solid-liquid interfacial tension to be described as

$$\gamma_{sl} = \gamma_l + \gamma_s - 2 \left( \sqrt{\gamma_l^d \gamma_s^d} + \sqrt{\gamma_l^p \gamma_s^p} \right) \quad (3.4)$$

where  $\gamma_l$  is the total surface tension of the liquid,  $\gamma_s$  is the total SFE of the solid and the  $d$  and  $p$  superscripts refer to the dispersive and polar components, respectively. By inserting eqn. 3.4 into eqn. 3.3 the following is obtained,

$$\frac{\gamma_l(1 + \cos(\theta))}{2\sqrt{\gamma_l^d}} = \sqrt{\gamma_s^p} \frac{\sqrt{\gamma_l^p}}{\sqrt{\gamma_l^d}} + \sqrt{\gamma_s^d} \quad (3.5)$$

which provides a linear equation from which the dispersive and polar components of a solids SFE can be determined through contact angle measurements with test liquids of known surface tensions. This equation can be converted into a polar co-ordinate system as

$$r(\varphi) = \left( \frac{\sqrt{\cos(\varphi)\gamma_s^d} + \sqrt{\sin(\varphi)\gamma_s^p}}{\cos(\varphi) + \sin(\varphi)} \right)^2 \left( \frac{2}{1 + \cos(\theta)} \right)^2 \quad (3.6)$$

in which  $r(\varphi)$  represents the wetting parameter, from which the solid wetting envelope can be determined for a desired contact angle. The wetting envelope allows prediction of the liquids, that will completely wet the solid surface, based on the determination of its SFE. The solid SFE was evaluated using the OWRK method by measuring the contact angles of two test liquids, with properties as shown by Table 3.1, using the KRÜSS Drop Shape Analyser DSA100. A 5  $\mu$ L droplet of the test liquid was placed onto the surface and allowed to equilibrate for two minutes before measurement of the contact angle, at room temperature ( $22 \pm 1^\circ\text{C}$ ). The surface energy was determined using the linear model, with the wetting curve evaluated by the in-built software, applying an inverse distance weighting interpolation.

Table 3.1: Surface tension properties for the solvent used during the OWRK method.

Test liquid	$\gamma_l$ (mN/m)	$\gamma_l^d$ (mN/m)	$\gamma_l^p$ (mN/m)	Supplier
Diiodomethane	50.8	50.8	0	Sigma Aldrich, 158429 [116]
Water (18.2 M $\Omega$ )	72.8	21.8	51.0	Triplered, UK [117]

While OWRK method provides a simple process for determining the surface energy of a solid, it only divides the surface energy components into polar and dispersive contributions, with the dispersive component accounting for hydrogen bonding, inductive and acid-base interactions. Further methods developed by Wu [118, 119] and Van Oss, Chaudhury and Good (vOCG) [120] account for some of these additional effects. However, all these methods show advantages to the method proposed by Zisman [121], which typically only applies to low-energy surfaces with no distinction between interactions.

### 3.7.2 Inverse gas chromatography

Inverse gas chromatography (iGC) developed from techniques of standard gas chromatography (GC) in which Kiselev and co-workers [122] discussed the potential for GC to be used for determination of several solid surface properties. Due to this, iGC attracted the attention of many researchers across many disciplines [123–126]. One of the most common applications of iGC is determination of surface free energy of materials such as, powders and fibres that are challenging to do via other methods. This is achieved by measuring the retention response of the interaction between an injected probe molecule and the stationary solid phase, as shown in Fig. 3.6. Solid surfaces are

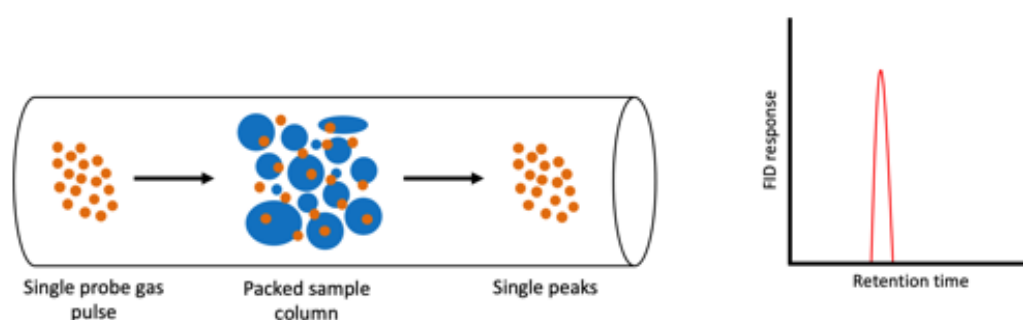


Figure 3.6: Schematic diagram showing the basic operating principles of iGC.

described by both dispersive and specific properties. The dispersive components are calculated through the dispersive properties of the surface and the specific components are determined by the tendency of the surface to be either be an electron acceptor or

electron donor. The sum of these components gives the total surface energy of the solid [127]. The most commonly applied method for determination of the dispersive component is the Schultz method [128, 129]. These calculations are based on the retention times of n-alkane probes at infinite dilution where Henry's law is obeyed [130], these are used as there are no acid-base interactions. All the interactions between the adsorbent and adsorbate are either dispersive or specific, and these components can be calculated through thermodynamic interactions. The Gibbs free energy change for the net retention volume,  $V_N$  is [131]

$$\Delta G_{de}^0 - \Delta G_{ad}^0 = RT \ln(V_N) + C \quad (3.7)$$

where  $\Delta G_{ad}^0$  and  $\Delta G_{de}^0$  are the standard Gibbs free energy changes of adsorption and desorption,  $R$  is the molar gas constant,  $T$  is the absolute temperature and the constant  $C$  is related to the reference states. The standard Gibbs free energy of adsorption is the sum of the dispersive and specific components

$$\Delta G_{ad}^0 = \Delta G_d^0 + \Delta G_{sp}^0 \quad (3.8)$$

If  $n$ -alkanes are used as probes, then the value of  $\Delta G_{sp}^0$  is zero since there are no specific interactions with the stationary phase, and so the quantities depend upon the number of carbons within the alkane chain [132]. This then allows the free energy of adsorption to be expressed as,

$$-\Delta G_{ad}^0 = N_A a W_{adh} \quad (3.9)$$

where  $N_A$  is the Avogadro number,  $a$  is the probe molecule cross-sectional area and  $W_{adh}$  is the work of adhesion. The work of adhesion can be related to the dispersive

free energy of the solid and liquid interaction through the Fowkes' equation [133],

$$W_{adh} = 2\sqrt{\gamma_s^d \gamma_l^d} \quad (3.10)$$

where  $\gamma_s^D$  and  $\gamma_l^D$  are the dispersive components of the solid and probe molecule respectively. Combining equations 3.7, 3.9 and 3.10 we arrive at

$$RT \ln(V_N) = 2N_A a \sqrt{\gamma_s^d \gamma_l^d} + C \quad (3.11)$$

Therefore a plot of  $RT \ln(V_N)$  as a function of  $a\sqrt{\gamma_s^d}$  for a series of  $n$ -alkanes will yield a straight line, for which the gradient will give the dispersive solid free energy.

The specific component of the surface energy (also referred to as the acid-base component) is typically obtained by calculating the retention time for well-described polar solvents. However, the specific component of surface energy covers all categories of interaction i.e. acid-base, magnetic, metallic and hydrogen-bonding [130]. With the Van Oss description, the specific surface energy components can be broken down into the Lewis acid  $\gamma_s^+$  and Lewis base  $\gamma_s^-$  components as [134]

$$-\Delta G = 2N_A a \left( \sqrt{\gamma_s^+ \gamma_l^-} \sqrt{\gamma_s^- \gamma_l^+} \right) \quad (3.12)$$

The more compact form of eqn. 3.12 proposed by Owens and Wendt makes the measurement possible by considering only two monopolar acidic and basic probes as

$$\gamma_s^{sp} = \sqrt{\gamma_s^+ \gamma_s^-} \quad (3.13)$$

The iGC results presented in this thesis were performed in collaboration with Surface

Measurement Systems (UK). All analyses were performed using an iGC surface energy analyser, with the data processed using the SEA analysis software. Approximately 20 mg of sample was packed into an individual iGC silanised glass column and run with a series of surface coverage alkanes and polar probe molecules to determine the dispersive and specific surface energy components. The sample column was first pre-conditioned for one hour at 120°C and 0% RH with 10 mL/min nitrogen gas carrier. The experiment was then conducted at 120°C with 10 mL/min flow rate of nitrogen gas and used methane for the dead volume corrections. The elutants used in this experiment were heptane, octane and nonane for non-polar species and dichloromethane and toluene for polar species.

## 3.8 Adsorption isotherms

Adsorption is a physical phenomena that can occur at any interface, be it solid, liquid or vapour. This occurs at interfaces due to the presence of the surface tension of the material. The unbalanced force at the surface of an adsorbent cause a film of adsorbate to build up on the surface, which is described as adsorption. The reverse process of this in which adsorbate is removed from the surface of the adsorbent, is known as desorption. This process usually takes the form of either a physical adsorption (physisorption), due to the Van der Waal's force, or chemical adsorption (chemisorption), in which chemical bonds are formed between the adsorbent and adsorbate. This work will only look at the effects of physisorption at the solid-vapour interface. Much of the information sought from adsorption experiments can be derived by appropriately treating the adsorption isotherm. Isotherms are grouped into six types according to IUPAC definitions [135]. A type I isotherm is typically exhibited by microporous solids, and tends to show saturation as  $p/p_0 \sim 1$ . These isotherms are typical of monolayer adsorption and are so treated using Langmuir methods. Both type II and III isotherms represent unrestricted mono-multilayer adsorption, with type II typically showing a linear like region in the middle of the adsorption, attributed to monolayer formation being complete and multilayer formation beginning. In contrast type III isotherms show a

convex shape in relation to the  $x$ -axis, due to lateral interactions between adsorbed molecules being stronger than that of adsorbent-adsorbate. Type IV and V isotherms represent microporous materials, with adsorption processes leading with multilayer adsorption and then capillary condensation. They typically also show hysteresis loops in the desorption branch attributed to the capillary filling. The differences between type IV and V can be thought of as akin to type II and III. Type VI isotherms show step like behaviour characteristic of non-porous materials, where each step represents the formation of a monolayer upon the surface. By studying the adsorption isotherm, properties, such as, surface area and surface porosity can be determined. Before an adsorption experiment can be performed the sample first must undergo an outgassing stage to remove all the physisorbed species from the surface, without physically changing the structure of the surface. This process is usually performed under high vacuum and often elevated temperature. The adsorption isotherms presented in this work were performed using a Autosorb AS-1 Gas Sorption System (Quantachrome Instruments, USA). This method uses a volumetric technique to measure the volume of adsorbed (or desorbed) gas on the surface at a given relative pressure. In each sample adsorption and desorption isotherms were collected. Isotherms were collected using nitrogen as an adsorbate molecule with a bath temperature of 77.3 K. Approximately 80 mg of sample was loaded into a glass analysis tube, and placed under vacuum to allow degassing, at a temperature of 200°C for 48 hours. Following this, the sample was moved to the analysis station, where the sample tube and a reference tube were filled with He in order to measure the dead volume. The He was then subsequently evacuated from the tubes, for the injection of N<sub>2</sub> to begin, and measure the adsorption branch of the isotherm. After reaching the maximum pressure, the sample was evacuated under the same process to measure the desorption branch of the isotherm. A schematic diagram of the measurement process is shown in Fig. 3.7.

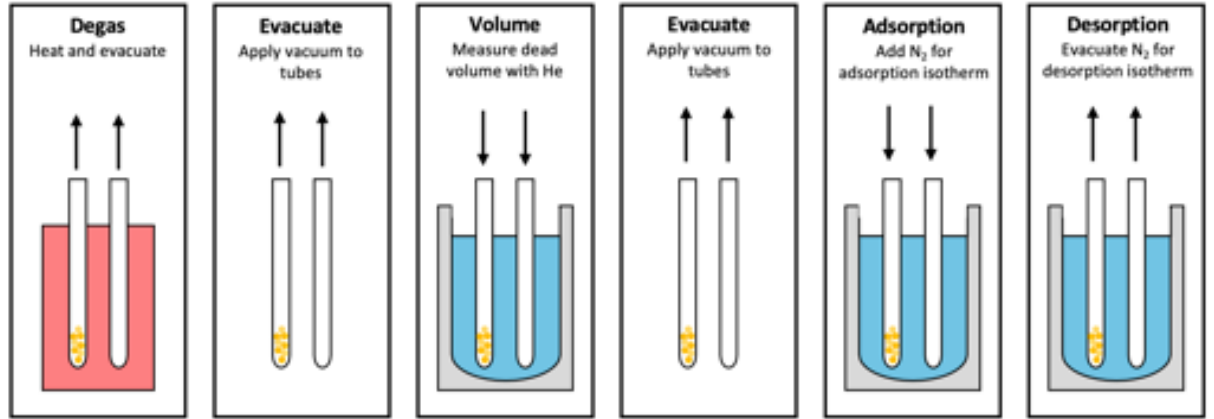


Figure 3.7: Schematic diagram showing the experimental stages in the process of an adsorption isotherm measurement.

### 3.8.1 Surface area determination

Determination of surface area by gas adsorption techniques is a simple process in design. The total surface area can be determined from the number of adsorbate molecules to form a complete monolayer upon the surface through the relation shown by eqn. 3.14,

$$S = a_x N \quad (3.14)$$

where,  $S$  is the total surface area,  $a_x$  is the cross section of the adsorbate molecule and  $N$  is the number of adsorbate molecules required to form a complete monolayer. The determination of this monolayer volume requires an appropriate theory, typical choices are the Langmuir [136] and Brunauer, Emmett, Teller (BET) [137] methods.

The Langmuir theory typically only applies to type I isotherms. The assumptions of this method are that there is only monolayer adsorption of the carrier gas, the surface is energetically uniform and there are no interactions between the surface and adsorbate. The appropriate description of this model is given by eqn. 3.15

$$\theta = \frac{V}{V_m} = \frac{Kp}{1 + Kp} \quad (3.15)$$

Where  $\theta$  is the fractional occupancy of the adsorption sites,  $V$  is the volume of adsorbed adsorbate,  $V_m$  is the volume of the monolayer,  $p$  is the adsorbate partial pressure and  $K$  is an equilibrium constant. This equation can be linearised for determination of the surface area as

$$\frac{p}{V} = \frac{1}{KV_m} + \frac{p}{V_m} \quad (3.16)$$

The second common approach applied is the BET theory. This theory considers some of the same effects as the Langmuir model, such as, the adsorbate molecules do not interact with the surface under test, but instead with a monolayer of adsorbate, this theory thus considers multi-layer adsorption. The further assumptions to this model from the Langmuir model are that gas molecules physically adsorb on the solid in layers infinitely, gas molecules only interact with adjacent layers and the Langmuir theory applies to each layer. Doing this allows derivation of the BET equation as shown by eqn. 3.17,

$$\frac{1}{V \left[ \left( \frac{p_0}{p} - 1 \right) \right]} = \frac{C - 1}{V_m C} \left( \frac{p}{p_0} \right) + \frac{1}{V_m C} \quad (3.17)$$

where symbols have the same meanings as before with the introduction of  $C$  the BET constant. The BET theory typically only applies to type II and IV isotherms. This equation can again be plotted linearly as  $\frac{1}{V \left[ \left( \frac{p_0}{p} - 1 \right) \right]}$  against  $\frac{p}{p_0}$ , however this linear relationship is only maintained within the region of  $0.05 < \frac{p}{p_0} < 0.35$ . The gradient  $m$  and  $y$ -intercept  $c$  can be used to determine the monolayer capacity and BET constant as

$$V_m = \frac{1}{m + c} \quad (3.18)$$

and

$$C = 1 + \frac{m}{c} \quad (3.19)$$

The surface area is then given by

$$S_{total} = \frac{V_m N_A a_x}{V} \quad (3.20)$$

and the BET surface area by

$$S_{BET} = \frac{S_{total}}{m_{ads}} \quad (3.21)$$

where  $m_{ads}$  is the mass of the adsorbent.

### 3.8.2 Pore size analysis

Pore sizes described using gas adsorption techniques are grouped into three categories:

- macropore,  $> 500 \text{ \AA}$
- mesopore,  $20 - 500 \text{ \AA}$
- micropore,  $< 20 \text{ \AA}$

The two most common techniques for describing porosity are total pore volume and pore size distribution. The total pore volume is derived from the amount of vapour adsorbed at a relative pressure close to 1, and under the assumption that the pores are filled with the liquid adsorbate. The shape of the isotherm can give ideas of the porosity of the sample, as if there are no macropores present the isotherm remains nearly horizontal over the  $p/p_0$  range, but where as if macropores are present there is a

rapid increase as the relative pressure approaches 1. The total volume of liquid nitrogen contained in the pores can be determined from the volume of adsorbed nitrogen gas through the relationship

$$V_{liq} = \frac{p_a V_{ads} V_m}{RT} \quad (3.22)$$

for which  $p_a$  and  $T$  are the ambient pressure and temperature respectively and  $V_m$  is the molar volume of the liquid adsorbate, for nitrogen this is  $34.7 \text{ cm}^3/\text{mol}$ . Since pores, which would not be filled below a relative pressure of 1 have negligible contributions, the average pore size can be estimated from the pore volume. For example, for cylindrical pore geometries the average pore radius can be determined as,

$$r_p = \frac{2V_{liq}}{S_{BET}} \quad (3.23)$$

Pore sizes are typically represented as distributions of the relative pore sizes. Mesopore calculations are made by assuming cylindrical pore geometries and the Kelvin equation in the form shown in eqn. 3.24,

$$r_K = \frac{-2\gamma V_m}{RT \ln\left(\frac{p}{p_0}\right)} \quad (3.24)$$

for which  $\gamma$  is the surface tension of the adsorbent,  $V_m$  is the molar volume,  $R$  is the gas constant,  $T$  is the boiling point of the adsorbent,  $p/p_0$  is the relative pressure of the adsorbent and  $r_K$  is the Kelvin radius of the pore. The Kelvin equation represents the pore radius at a specific relative pressure, but at this pressure it is possible some adsorption has already taken place. Therefore, the actual pore radius is given by,

$$r_p = r_K + t \quad (3.25)$$

where  $t$  is the adsorbed layer thickness. A method for determining the magnitude of  $t$  was proposed by de Boer [138] as shown by eqn. 3.26.

$$t(\text{\AA}) = \sqrt{\frac{13.99}{\log\left(\frac{p_0}{p}\right) + 0.034}} \quad (3.26)$$

The pore size distribution in this work were determined using the method proposed by Barrett, Joyner and Halenda (BJH) [139]. In this method it is assumed the relative pressure is initially close to unity and all pores are filled with liquid. The largest pore,  $r_{p1}$  will have a physically adsorbed layer of molecules of thickness  $t_1$ . Within the thickness there is an inner capillary of radius  $r_K$  from which the evaporation occurs as the relative pressure is lowered. The relative volume of the pore and the inner capillary is given by

$$V_{p1} = V_{K1} \frac{r_{p1}^2}{r_{K1}^2} \quad (3.27)$$

As the relative pressure decreases, a volume of  $V_1$  will have desorbed from the surface. This causes a decrease in the relative thickness of the physically adsorbed layer by an amount  $\Delta t_1$ . The pore volume for the largest pore can now be described as

$$V_{p1} = V_1 \left( \frac{r_{p1}}{r_{K1} + \frac{1}{2}\Delta t_1} \right)^2 \quad (3.28)$$

With the next step in relative pressure reduction, the pore volume contains both the condensate from the pore but also the second decrease in the physically adsorbed layer. Therefore, the volume  $V_{p2}$  desorbed is now given by

$$V_{p2} = \left( \frac{r_{p2}}{r_{K2} + \frac{1}{2}\Delta t_2} \right)^2 (V_2 - V_{\Delta t_2}) \quad (3.29)$$

The expression for the pore thickness is,

$$V_{\Delta t_2} = \Delta t_2 A_{c1} \quad (3.30)$$

which can be generalised into a stepwise function representing any step within the desorption process as

$$V_{\Delta t_n} = \Delta t_n \sum_{j=1}^{n-1} A_{cj} \quad (3.31)$$

Substitution of eqn. 3.30 into eqn. 3.29, gives an exact equation for calculating pore volumes at varying relative pressure. The area of each pore  $A_p$  is constant and can be calculated from the pore volume,

$$V_{pm} = \left( \frac{r_{pm}}{r_{Kn} + \frac{1}{2}\Delta t_n} \right)^2 \left( \Delta V_n - \Delta t_n \sum_{j=1}^{n-1} A_{cj} \right) \quad (3.32)$$

assuming cylindrical pores, such that  $A_p$  is

$$A_p = \frac{2V_p}{r_p} \quad (3.33)$$

The pore sizes can be cumulatively summed so that for any step in the desorption process  $A_p$  is known. The BJH method provides a way of determining  $\sum A_{cj}$  from  $A_p$  for each relative pressure as

$$c = \frac{\bar{r}_c}{r_p} = \frac{\bar{r}_p - t_{\bar{r}}}{\bar{r}_p} \quad (3.34)$$

where  $\bar{r}_c$  is the average capillary radius,  $\bar{r}_p$  is the average pore radius and  $t_{\bar{r}}$  is the thickness of the adsorbed layer at the radius in the interval of the relative pressure increment. Data reduction was performed using the AS1Win ver. 2.55 software (Quantachrome Instruments, USA), under the principles of the BJH pore distribution, discussed above.

## 3.9 Thermogravimetric analysis

Thermogravimetric analysis (TGA) is a thermal analysis technique that monitors the mass change of a sample as the temperature is varied. This mass loss curve can provide information on parameters, such as, changes in sample composition, thermal stabilities, kinetic parameters of chemical reactions, etc. In this work TGA is used as a method to monitor the thermal stability and degradation of samples. In each case approximately 5 mg of sample was placed inside a ceramic crucible and placed within the instrument. Powdered samples were heated within a nitrogen environment, with a gas flow rate of 30 mL/min, while polymer samples were heated under open air atmosphere in order to allow the complete combustion of the polymer sample. The heating rate was controlled at 10°C/min in all samples evaluated. All TGA measurements were performed using a TGA4000 thermogravimetric analyser (Perkin Elmer, USA).

## 3.10 Dynamic light scattering

Dynamic light scattering (DLS) is a common technique used to study colloid solutions for parameters such as the particle size distribution and polydispersive index (PDI). Incident light shone into a colloidal system will be diffracted by the particles (via Rayleigh scattering), provided that the particle size is small in comparison to the wavelength of the incident light. By monitoring the intensity of these fluctuations as a function of time, the diffusion of the particles through Brownian motion can be observed. A schematic of this approach is shown by Fig. 3.8. The fluctuations are directly related to the particle size; with small particles having short fluctuations in intensity and large particles having much greater fluctuations in intensity due to the

velocity at which they diffuse through the solvent. Since the intensity fluctuations are

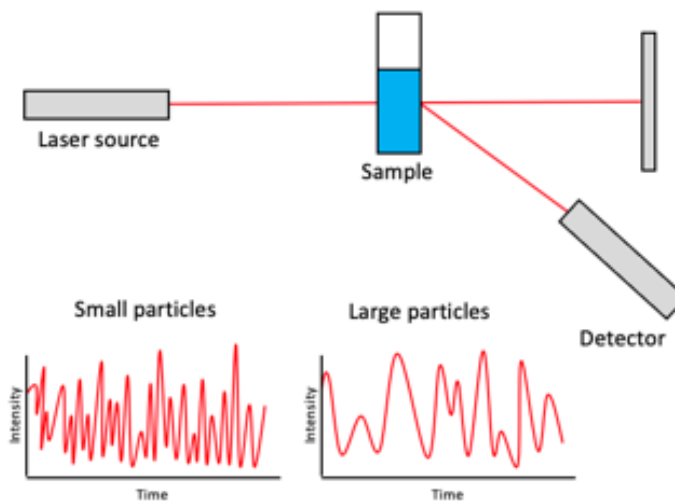


Figure 3.8: Schematic diagram showing the principles of a DLS experiment, and the resultant scattering signal observed for differing particle sizes.

random, it is necessary to use an auto-correlation function of the intensity trace in order to determine the time dependent parameters, this is achieved using the relationship shown in eqn. 3.35,

$$g_2(q; \tau) = \frac{\langle I(t) \cdot I(t + \tau) \rangle}{\langle I(t) \rangle^2} \quad (3.35)$$

for which  $g_2(q; \tau)$  is the normalised intensity autocorrelation function at particular wave vector  $q$ ,  $I(t)$  is the intensity detected at time  $t$ ,  $\tau$  is the delay time and  $\langle I(t) \rangle^2$  is a normalisation factor. The autocorrelation function is simply an exponential function (or sum of exponentials). It is therefore useful to use the Siegert relationship to convert this function of intensity to a function of the electric field of the scattered light as

$$g_2(\tau) = g_1(\tau)^2 + 1 \quad (3.36)$$

In the case of a monodisperse sample  $g_1(\tau)$  is a single exponential of the form

$$g_1(\tau) = Be^{-\Gamma\tau} \quad (3.37)$$

Where  $B$  is an instrument dependent constant and  $\Gamma$  is the decay constant, which can be related to the diffusion coefficient by

$$\Gamma = Dq^2 \quad (3.38)$$

With  $q$  being the magnitude of the scattering vector given by,

$$q = \frac{4\pi n \sin\left(\frac{\theta}{2}\right)}{\lambda} \quad (3.39)$$

where  $n$  is the refractive index of the medium,  $\theta$  is the scattering angle and  $\lambda$  is the wavelength of the incident light. In the case of a monodisperse sample taking the logarithm of eqn. 3.37 will yield a straight line, however, in a polydisperse sample the logarithm will have curvature, therefore a method is needed to resolve the particle size distribution from the autocorrelation function. In this work the well documented inverse Laplace transform method, known as the CONTIN algorithm [140, 141] is employed to determine the particle diffusion coefficient and subsequently through the Stokes-Einstein relation (eqn. 3.40), the size of the particle,

$$D = \frac{k_B T}{3\pi\eta r_h} \quad (3.40)$$

where  $D$  is the diffusion coefficient,  $k_B$  is the Boltzmann constant,  $T$  is the absolute temperature,  $\eta$  is the solvent viscosity and  $r_h$  is the particle hydrodynamic radius. It is of note that DLS measurements are best suited to spherical particles due to the assumptions made in the derivation, so care should be taken when dealing with particles

that differ widely from this assumption, and the effect this has on their hydrodynamic size.

In this work all DLS experiments were performed using a NanoPlus Zeta and Particle Size Analyser (Particulate Systems, USA) using a He-Ne laser operating at 665 nm and detector angle of 165°, using water as a bulk media at a temperature of 25°C where the refractive index and viscosity are 1.333 and 0.890 mPas, respectively.

Samples for DLS size distribution measurements were produced by dispersing a set mass of clay within ultrapure water, made up to 100 g total mass, in order to produce a colloid of a desired clay wt.% concentration. Samples were shaken vigorously by hand in order to disperse the particles within the solution. In order to get a true representation of the particle state, samples were not subjected to sonication in order to break down aggregates. Approximately 1 ml of prepared sample was placed inside a polystyrene cuvette (Fisher Scientific, UK) for measurement. In each case a pre-measurement intensity check was performed to ensure the sample was appropriate for analysis. Samples were allowed to rest for 1 minute before the measurement began to promote the settling of any large particles (circa.  $>5 \mu\text{m}$ ) that are too large for accurate DLS measurement.

#### 3.10.1 Particle aggregation

In a well dispersed stable sol the particles remain separated and stabilised by the inter-particle repulsive forces. If these forces weaken or become attractive, then the particles will begin to aggregate following a simple additive law as



In this early regime of the aggregation process the sol is primarily made of monomers

and dimers, and so the rate of this reaction can be characterised by a kinetic law as

$$\frac{dN_2}{dt} = \frac{1}{2}kN_1^2 \quad (3.42)$$

where the monomers and dimers are represented by  $N_1$  and  $N_2$  and  $k$  describes the aggregation rate constant. It is possible to influence the strength of the attractive inter-particle forces by adding counter ions to the sol. The charged colloidal particles will show a dependence on the molarity of the ions added to the system, and the aggregation regime can be divided into two distinct regions of slow and fast. The point of intersection of these regions is referred to as the critical coagulation concentration (ccc).

### **Time dependent dynamic light scattering**

A simple method to probe the aggregation rate coefficient is to monitor the colloid using time dependent DLS measurements. DLS experiments were performed using the same process as described in the previous section. However, in these experiments, the hydrodynamic diameter was evaluated as a function of time, with measurements taken every minute over the course of twenty minutes. In each experiment two to three drops of a sodium chloride (Sigma Aldrich, UK) solution were added to the prepared suspension just before measurement, to monitor the effect of salt molarity on the aggregation rate. Both Cloisite Na<sup>+</sup> and SWN colloids were evaluated at concentrations of 0.5 wt.%, considering both the cases of un-exfoliated and exfoliated systems. Although typically early interactions are investigated as a function of added electrolyte concentration, a further method investigating the early stage interactions as a function of clay concentration was also performed. For these experiments the same procedure was followed for sample preparation as for the DLS, with fresh samples prepared each time.

### Particle stability ratio

It is common to express the aggregation rate constant as a function of the stability ratio,  $W$ , which is described as

$$W = \frac{k_{fast}}{k} \quad (3.43)$$

with  $k_{fast}$  being the rate constant in the fast regime and  $k$  being the actual interaction rate. The ccc point can be interpreted from this data as within the fast aggregation regime the stability ratio is of a uniform value. The stability ratios presented in this work have been determined from the aggregation rate coefficients obtained from the time dependent DLS measurements.

## 3.11 Zeta potential

When dispersed into a solvent most, particles will possess a positive or negative surface charge. The ions within the liquid that have the counter charge to the particles will gather at the particle surface in order to maintain electrical neutrality. Subsequently this layer will also gain a layer of counter charge ions, as shown in the schematic in Fig. 3.9. The diffusion of the particles through the solvent, causes the concentration of the counter ions to be higher, nearer to the particle surface and decrease exponentially with the distance from the particle surface. Equal numbers of positive and negative ions exist even in this area far from the particle surface to maintain the electrical neutrality. The distribution of the ions is known as the diffuse electrical double layer. This layer is further divided based on the strength of the ions attraction. The layer of ions surrounding the particle is referred to as the Stern layer, and the layer surrounding this is known as the diffuse layer. It is assumed that when the particle moves, this doesn't consider the movement of the Stern and diffuse layers with the particle. The field through which this movement takes place is called the slipping plane, and this is used as a measure of the zeta potential. The zeta potential can be used to deduce

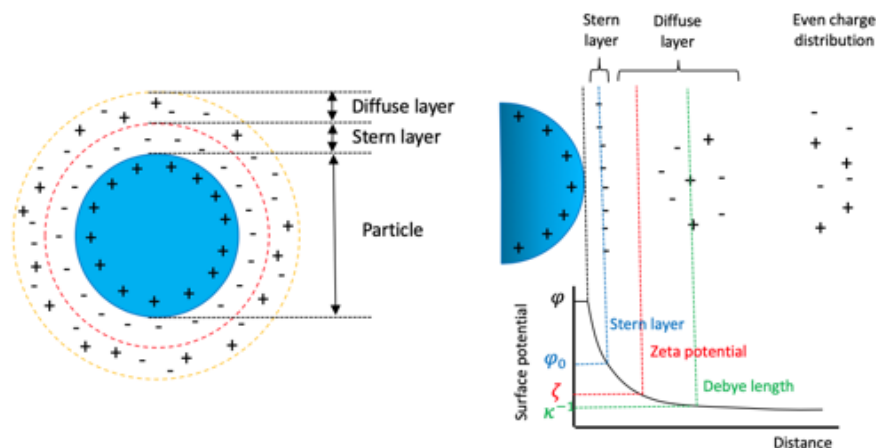


Figure 3.9: Schematic diagram of the electrical double layer and the position of the zeta potential.

the stability of colloid particles through the magnitude of the electrostatic repulsion, where a value of 30 mV (either positive or negative) is used as a boundary for a high level of stability.

The zeta potential cannot be measured directly but can be calculated using theoretical models and experimentally determined values, such as, ones from electrophoretic light scattering. When an electric field is applied to charged particles in solution, they will move towards the electrode with the opposite charge. The velocity with which the particles move is proportional to their charge. Electrophoretic light scattering is a technique that can be used to evaluate the velocity of the particles. The particles are irradiated with a laser light and the light scattered from the particles is detected. The frequency of the light is shifted due to the movement of the particles, and the mobility of the particles can be determined from this Doppler shift of the light.

The zeta potential results in this work were obtained using the NanoPlus Zeta and Particle Size Analyser (Particulate Systems, USA) using a He-Ne laser operating at 665 nm and scattering angle of  $165^\circ$ , using water as a bulk media at a temperature of  $25^\circ\text{C}$  where the refractive index, viscosity and dielectric constant are 1.333, 0.890 mPas and 78.3, respectively. The frequency shift  $\nu_D$  of the scattered light is related to

the particle mobility  $v$  by,

$$\nu_D = \frac{vq}{2\pi} \cos\left(\frac{\theta}{2}\right) = \frac{vn}{\lambda} \sin(\theta) \quad (3.44)$$

where  $q$  is the scattering vector,  $\lambda$  is the incident wavelength,  $n$  is the refractive index,  $\theta$  is the scattering angle. In many aqueous solutions the zeta potential can be determined with the Smoluchowski equation,

$$\zeta = \frac{\eta}{\varepsilon_0 \varepsilon_r} v \quad (3.45)$$

where  $\zeta$  is the zeta potential,  $\eta$  is the viscosity and  $\varepsilon_0$  and  $\varepsilon_r$  are the dielectric constants of the vacuum and solvent, respectively.

Samples were prepared using the same process as outlined for the DLS measurements, but placed within a quartz cell connected to two electrodes for zeta potential measurements. Care was taken to ensure no bubbles were present within the cell. Measurements were performed in triplicate with error bars representing the standard error of the mean.

## 3.12 Rheology

### 3.12.1 Viscosity and elasticity

Condensed matter has a differing response to applied shear stress depending on if it is a solid or a liquid. Here a brief discussion of the concepts of elasticity and viscosity will be presented in order to understand the response of soft condensed matter systems to shear. Firstly, the idealised cases of perfect systems will be examined Hookean solids and Newtonian fluids.

To do this we must define what is meant by shear stress,  $\sigma$ . Fig. 3.10 shows a diagram of the plane of a material with a fixed position at the base being dragged by an applied force per unit area ( $\sigma = F/A$ ). The shear strain,  $\gamma$  on the material is the

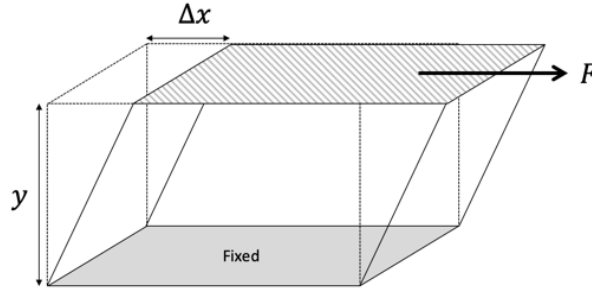


Figure 3.10: Diagram showing the definition of shear deformation on a material

deformation it experiences in the direction of the applied force with respect to the fixed position of the bottom ( $\gamma = \Delta x/y$ ). If the material is a perfect Hookean solid, then the applied shear stress leads to a constant shear strain, with a proportionality constant known as the shear modulus,  $G$ ,

$$\sigma = G\gamma \quad (3.46)$$

If, however, the material under test is a fluid, the molecules will rearrange themselves as the top plate moves along the fluid surface with velocity  $v_p$ . The fluid therefore has a velocity profile, with  $v = 0$  at the bottom. The strain required now to move the top plate at a constant velocity against the resistance of the fluid is proportional to the area and the perpendicular velocity gradient,

$$\sigma = \eta \frac{\partial v(y)}{\partial y} \quad (3.47)$$

where the constant of proportionality this time,  $\eta$ , is known as the viscosity. As the fluid velocity is given by  $dx/dt$ , this can be instead written in terms of the shear strain time derivative,

$$\sigma = \eta\dot{\gamma} \tag{3.48}$$

This equation is only true for Newtonian fluids. Many fluids instead exhibit non-Newtonian behaviour in which the viscosity is a function of the shear rate. This leads into the definition of shear thickening, where  $\eta$  increases with  $\dot{\gamma}$ , and shear thinning,  $\eta$  decreases with  $\dot{\gamma}$ , fluids.

### 3.12.2 Viscoelasticity

Many materials, however, do not show this ideal solid or liquid like behaviour, and instead exhibit a combination of both elastic and viscous properties. Materials like this are known as viscoelastic - and this is further subdivided into viscoelastic solids and viscoelastic liquids depending on how far along the ideal scale they lie. The methodology to determine the properties of a viscoelastic material is through an oscillatory rheology test. The model used to describe rheological parameters can be extended to describe an oscillatory test. If a sample is sheared while sandwiched between two plates, in which the upper plate moves and the bottom is stationary, the upper plate is sheared back and forth parallel to the the sample. If this shearing is done in a constant time period then the plate is operating at a constant oscillation frequency. The deflection of the plate as it moves is monitored and rheologically evaluated as the strain (or deformation)  $\gamma$ . As the movement is oscillating at a constant frequency the strain applied varies with a sinusoidal form, with a maximum strain amplitude  $\gamma_0$ . In addition to this, the force exerted on the lower fixed plate is measured. This force acts as a counter force to keep the lower plate stationary. The signal determined from this is rheologically evaluated as the shear stress,  $\sigma$ . If the sample is strained by a small enough deformation, then the resulting shear stress will also follow a sinusoidal pattern, where the amplitude is the maximum shear stress,  $\sigma_0$ . An oscillatory rheology measurement therefore monitors both the input sinusoidal signal and the output sinusoidal signal. The material under test will then dictate how these signals respond to

one another. For the ideal Hookean solid the two curves are in phase with one another, and in the ideal Newtonian fluid the curves are 90° out of phase with one another. Since most materials are viscoelastic and possess both elastic and viscous components, they will have a phase difference,  $\delta$  somewhere between 0° and 90°. The applied strain to the sample is often described by the function

$$\gamma(t) = \gamma_0 e^{i\omega t} \quad (3.49)$$

and the shear stress response by the function

$$\sigma(t) = \sigma_0 e^{i(\omega t + \delta)} \quad (3.50)$$

In an oscillatory experiment the law of elasticity is described as a complex function of the shear stress and the shear strain,

$$G^* = \frac{\sigma_0}{\gamma_0} \quad (3.51)$$

where  $G^*$  is the complex shear modulus, and describes the entire viscoelastic response of the sample. The complex modulus is formed of the elastic storage modulus,  $G'$  and the viscous loss modulus  $G''$ . The complex modulus can be interpreted as

$$G^* = G' + iG'' = \frac{\sigma_0}{\gamma_0} \cos(\delta) + i \frac{\sigma_0}{\gamma_0} \sin(\delta) \quad (3.52)$$

In this work both viscometry and deformation rheology methods have been employed. All rheological measurements were performed using a Bohlin C-VOR rheometer (Malvern, UK) equipped with a Peltier temperature control unit. Viscometry measurements were

performed using a parallel plate geometry of diameter 40 mm. As the viscometry measurements are more qualitative and used to explore the properties of gels, a parallel plate was chosen to reduce the applied shear at the start of the measurement. Approximately 0.5 ml of sample was loaded onto the bottom plate and the geometry was lowered to the experimental gap height of 400  $\mu\text{m}$ . Samples were sheared from a rate of 0.001 to 10, and then from 10 to 0.001 with the viscosity measured. In the 3 interval time test (3iTT) samples were sheared at a constant rate of 0.05 for 60 seconds and then sheared at a rate of 10 for 60 seconds before the shear was removed and the sample allowed to relax. For this experiment the viscosity was measured as a function of time.

Deformation rheology measurements were performed on the same rheometer. In this experiment a cone-plate geometry was employed of diameter 40 mm and cone truncation of 4°. The cone-plate geometry was employed in order to ensure a uniform shear was applied to the sample during the measurement. The bottom plate was loaded with 1.25 ml of the sample and the geometry brought to the experimental gap height of 150  $\mu\text{m}$ . These experiments were performed under a controlled strain of 0.05 and frequency of 0.5 Hz. All rheological tests were performed at 25°C, unless otherwise stated.

Samples were prepared by dispersing clay within ultrapure water (to a total mass of 100g) to give the desired wt.% concentration. The sample was then loaded into a syringe and ejected onto the centre of the bottom plate for the measurement to begin. Exfoliated samples were evaluated in the same way but with exfoliation treatment prior to being loaded onto the bottom plate. A delay of approximately 30 seconds occurred between the sample being loaded and the geometry reaching the desired gap height.

## 3.13 Neutron Compton scattering

Neutron Compton scattering (NCS) techniques were employed using the VESUVIO spectrometer at the ISIS Pulsed Neutron and Muon Source (Rutherford Appleton

Laboratory, UK)\*. This is a unique design of spectrometer that is used to probe the kinematic region of neutron scattering [142]. VESUVIO performs measurements using high-energy neutrons in the epithermal region (5-150 eV) to investigate scattering processes. This technique is termed deep inelastic neutron scattering. As with many spectrometers on a pulsed neutron source, VESUVIO uses a time-of-flight (ToF) approach in design. The ToF value,  $t$ , for a detected neutron is given by [142],

$$t = \frac{L_0}{v_0} + \frac{L_1}{v_1} \quad (3.53)$$

where  $L_0$  is the distance of the sample from the neutron source,  $L_1$  is the distance from the detector,  $v_0$  is the incident neutron velocity and  $v_1$  is the detected neutron velocity. The neutron velocity is related to its energy from the relationship  $v = \sqrt{\frac{2E}{m_n}}$ , where  $m_n$  is the neutron mass. From this knowledge the energy transfer,  $\hbar\omega$ , and momentum transfer,  $q$ , can be determined as [143]

$$\hbar\omega = E_0 - E_1 \quad (3.54)$$

$$q = \sqrt{2m_n} \left( E_0 + E_1 - 2\sqrt{E_0 E_1 \cos \theta} \right)^{\frac{1}{2}} \quad (3.55)$$

As VESUVIO operates with a reverse geometry,  $E_1$  is fixed at 4897 meV. This definition of energy is determined through the use of gold foil analysers, which absorbs neutrons at a calibrated energy value of 4897 meV. The aim of the measurement with VESUVIO is to probe the atomic dynamics of the system [144], which is achieved through the determination of the atomic momenta distributions. The raw data reduction and analysis is performed using the time of flight or mass-specific response function in  $y$ -space,

---

\*Experimental reference: Fengge Gao, Elena Budennaia, James Rawlings and Matthew Krzystyniak, 2017, RB1710036 Better understanding of self-linking behaviour of smectite clays, STFC ISIS Facility doi:10.5286/ISIS.E.86389063

rather than the scattering vector.

For high energy transfer scattering events, the impulse approximation is employed, where the conservation of the momentum and kinetic energy between incident neutron and target nucleus occurs. The scattering law for such an interaction is expressed as [144–146],

$$S(q, \omega) = \int n_M(\vec{p}) \delta \left( \omega + \frac{p^2}{2M} - \frac{(\vec{p} + \vec{q})^2}{2M} \right) d\vec{p} = \frac{M}{q} J_M(y_M, \hat{q}) \quad (3.56)$$

where

$$J_M(y_M, \hat{q}) = \int n_M(\vec{p}) \delta (y_M - \vec{p} \cdot \hat{q}) d\vec{p} \quad (3.57)$$

and

$$y_M = \frac{M}{q} \left( \omega - \frac{q^2}{2M} \right) \quad (3.58)$$

for which  $n_M(\vec{p})$  is the radial nuclear momenta distribution of an atomic species of mass  $M$ , and  $J(y, \vec{q})$  is the momenta distribution along the direction  $\hat{q}$ . Within the impulse approximation there is a mass dependence, with the transform centring each atomic species contribution about  $y = 0$ , dependent on the recoil energy of the specific mass. This gives the count rate for VESUVIO spectra as,

$$C(t) = \frac{E_0 I(E_0)}{q} \sum_M A_M M J_M(y_M) \otimes R_M \quad (3.59)$$

where  $I(E_0)$  is the incident flux of neutrons with energy  $E_0$ .  $A$  is a mass dependent amplitude factor, which is proportional to the number density and scattering cross-section

of the species and  $R$  is an instrument resolution function. Therefore, an experiment on VESUVIO will consist of a set of peaks within the ToF domain, with centring related to the recoil energy of the atomic species. The most common model employed for  $J(y)$  is a Gaussian in  $y$ , due to the isotropic nature of samples for a harmonic potential. Thus,

$$J_M(y_M) = \frac{1}{\sqrt{2\pi\sigma_M^2}} \exp\left(\frac{-y_M^2}{2\sigma_M^2}\right) \quad (3.60)$$

and the atomic kinetic energy is simply related to the standard deviation of the Gaussian given by

$$\langle E_k \rangle = \frac{3\hbar\sigma_M^2}{2M} \quad (3.61)$$

Four experiments were performed using the VESUVIO spectrometer, to investigate the binding of hydrogen within clay systems. In order to understand the difference between both types of clay and their gelling behaviour, both solid state and aqueous samples were investigated. The aqueous samples were prepared in ultrapure water to a concentration of 3.0 wt.% and exfoliated prior to measurement. Each sample was loaded into an aluminium holder and sandwiched with a second aluminium plate. The structure was then bolted together and tightened by hand. The sandwich structure was then secured to a specimen holder and lowered into the spectrometer. The ToF data was obtained using the back scattering detectors, and the evaluation of the molecular binding of hydrogen was performed with Dr. Krzystyniak, by using the data analysis software Mantid Plot.

## 3.14 Electrical testing

The following experiments were performed in collaboration with the University of Southampton.

### 3.14.1 Dielectric spectroscopy

As discussed in Chapter 2, when a dielectric material is subject to an electrical field it generates a change in the capacitance of the material. The magnitude of this change in capacitance is referred to as the absolute permittivity. More specifically the permittivity is a measure of the amount of charge required to generate one unit of electric flux within a medium. The electric displacement field,  $\vec{D}$ , represents how the electric field,  $\vec{E}$ , influences the organisation of the electric charges within the medium. For the simplest case of a linear, homogeneous, isotropic medium, that has “instantaneous” responses to the change in the electric field is

$$\vec{D} = \epsilon \vec{E} \quad (3.62)$$

However, materials generally cannot polarise instantaneously in response to applied fields, so the polarisation is more generally described as a function of time as

$$\vec{P}(t) = \epsilon_0 \int_{-\infty}^t \chi(t-t') \vec{E}(t') dt' \quad (3.63)$$

By performing the Fourier transform of the function into the frequency domain, the relationship can instead be written as a product though the convolution theorem giving

$$\vec{P}(\omega) = \epsilon_0 \chi(\omega) \vec{E}(\omega) \quad (3.64)$$

Thus, the frequency dependent susceptibility means there is also a frequency dependent

permittivity. The response of a material to an external electric field is highly dependent on its frequency, with the response being always *causai*, meaning that a phase difference must be present. Therefore, the permittivity is instead treated as a complex function of the angular frequency. The definition of the permittivity now becomes,

$$D_0 e^{-i\omega t} = \varepsilon^*(\omega) E_0 e^{-i\omega t} \quad (3.65)$$

where  $\varepsilon^*$  represents the complex permittivity defined as

$$\varepsilon^*(\omega) = \varepsilon'(\omega) - i\varepsilon''(\omega) = \left| \frac{D_0}{E_0} \right| (\cos(\delta) - i \sin(\delta)) \quad (3.66)$$

From this  $\varepsilon'$  describes the lossless permittivity, the energy storage (capacitance and inductance) and  $\varepsilon''$  describes the lossy permittivity, the energy lost (resistance and conductance). The phase angle is defined by  $\delta$  and can be used to evaluate if the material is a dielectric or a conductor depending on its value (0 to  $\infty$ ).

By performing a dielectric spectroscopy scan a permittivity spectra of the material can be derived as a function of the field frequency to determine its behaviour as either a conductor or dielectric, and also show frequencies at which loss most strongly occurs. Through use of the loss tangent we can classify materials using the generalisation presented in Table 3.2. Dielectric spectroscopy is a technique through which the complex

Table 3.2: Quantification of a materials conductive and dielectric properties based on the magnitude of the loss tangent.

$\tan(\delta)$	Properties	
0	Perfect dielectric	
$\ll 1$	Poor conductor	Good dielectric
1	Lossy conducting medium	Lossy propagating medium
$\gg 1$	Good conductor	Poor dielectric
$\infty$	Perfect conductor	

permittivity can be evaluated. Typically this measurement is performed by evaluating the impedance ( $Z$ ) of a circuit akin to that shown in Fig. 3.11. The total impedance

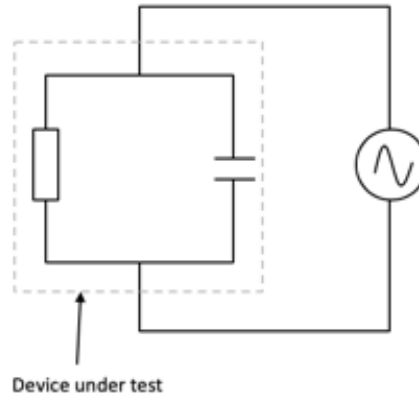


Figure 3.11: Circuit diagram showing the measurement of impedance for a test sample.

through the circuit can be shown to be equal to,

$$Z_{Total} = G + i\omega C \quad (3.67)$$

where  $G$  is the electrical conductance. By introducing the complex permittivity, the real and imaginary components can be determined as

$$\varepsilon' = \varepsilon_r \quad \text{and} \quad \varepsilon'' = \frac{G}{\omega C_0} \quad (3.68)$$

The complex permittivity of the samples were measured using a Solartron 1296 Dielectric Interface with a Schlumberger SI 1260 Impedance/Gain-Phase Analyzer (Ametek, USA), with a 3 V AC signal, across a frequency range of  $10^{-1}$  -  $10^5$  Hz. All tests were performed at 20°C.

### 3.14.2 Electrical conductivity

Electrical conductivity represents the ability of a material to conduct electrical charge. Electrical conductivity is the inverse property to a materials resistivity, which is simply

a measure of how strongly it resists the flow of electrical current. For a general case the electrical conductivity can be expressed using Ohm's law,

$$\vec{J} = \sigma \vec{E} \quad (3.69)$$

where  $\vec{J}$  is the electrical current density,  $\vec{E}$  is the electric field strength and  $\sigma$  is the electrical conductivity. Due to the large band-gap of insulators ( $\sim 15$  eV), they typically have very low electrical conductivities. However, under large electric field strengths, the magnitude of this conductivity can increase, leading to a subsequent reduction in the electrical breakdown strength. In this work the electrical conductivity of the sample was measured using a Keithley 6487 picoammeter (Keithley, USA). The sample was placed between two 20 mm diameter electrodes, and subjected to the applied electric field strength for one hour. A stepped voltage source was used to monitor the conductivity under 5, 10, 20, 30, 40 and 50 kV/mm field strengths, as an uninterrupted process. Measurements within each hour were taken every 10 seconds to allow capacitive current to dissipate. The last stable conductivity value at each field strength was then used to produce a  $\sigma$  - E curve.

### 3.14.3 Electrical breakdown strength

One of the key properties to over-come in developing insulation materials is their electrical breakdown strength. As previously discussed, this is the electric field strength under which the dielectric material becomes conductive, and thus no longer effective as an insulator. Since the electrical breakdown strength can vary with the sample morphology, due to defects etc., the electrical breakdown was performed twelve times on differing regions of a sample in order to determine the average breakdown strength. The electrical breakdown tests were performed using in-house apparatus, where the sample is placed between two opposing 6.25 mm steel ball bearings, immersed in a tank of silicone fluid. It is possible using this apparatus to consider both DC and AC

electrical breakdown phenomena. In each experiment the voltage was ramped at a rate of 100 V/s and continued until the sample underwent breakdown. The results of the measurements were fitted to a Weibull probability distribution [147] as

$$f(x; \alpha, \beta) = \begin{cases} \frac{\beta}{\alpha} \left(\frac{x}{\alpha}\right)^{\beta-1} e^{-\left(\frac{x}{\alpha}\right)^\beta} & x \geq 0 \\ 0 & x < 0 \end{cases} \quad (3.70)$$

where  $x$  represents the electrical breakdown data,  $\alpha$  is the scale parameter and  $\beta$  is the shape factor, in order to determine the average electrical breakdown strength of the produced materials.

## Chapter 4

# Structure, morphology and properties of the applied clays

In this Chapter, the physical properties of the two types of commercial clay mineral were investigated. This study focuses on the natural montmorillonite, Cloisite Na<sup>+</sup> and the synthetic hectorite, Lucentite SWN. These clays were chosen in this study due to their known differing gelling ability and aspect ratios, and this allows the subsequent dielectric performance of their insulation materials to be investigated and compared.

## 4.1 The micro structure of the clay

### 4.1.1 SEM analysis

In order to understand the structure of the clay particles, a micrograph was taken using SEM to observe the size and shape of the particles within the natural dry powder. A small amount of the clay was spread evenly onto an aluminium stub coated with carbon tape, and gold coated to a thickness of 10 nm for observation under the SEM. The obtained micrographs are shown in Figures 4.1a and 4.1b, respectively. In order to

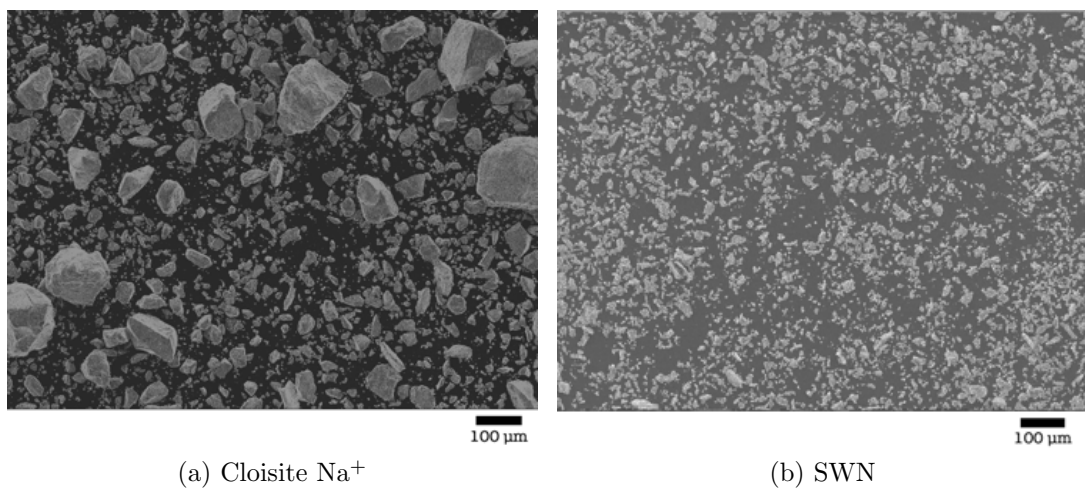


Figure 4.1: SEM micrographs of the two types of clay taken at 100× magnification, at 5 kV acceleration voltage. Scale bar represents 100 μm

understand what the SEM shows, it is important to understand the structure of the clay itself. These clays belong to the smectite family, meaning they are comprised of alumina octahedral and silica tetrahedral sheets [148], bonded together through a shared plane of common oxygen or hydroxyl groups [149], to form stacks referred to as 2:1 layers, in which there are two tetrahedral sheets sandwiching an octahedral sheet [150]. The

single layers of clay stack together in a ‘deck of cards’ style, to form single particles of clay. These clay particles can interact together to form aggregates of particles and these aggregates can also interact to form assemblies of aggregates. A schematic description of these scenarios is shown in Fig. 4.2. From simple observation of these

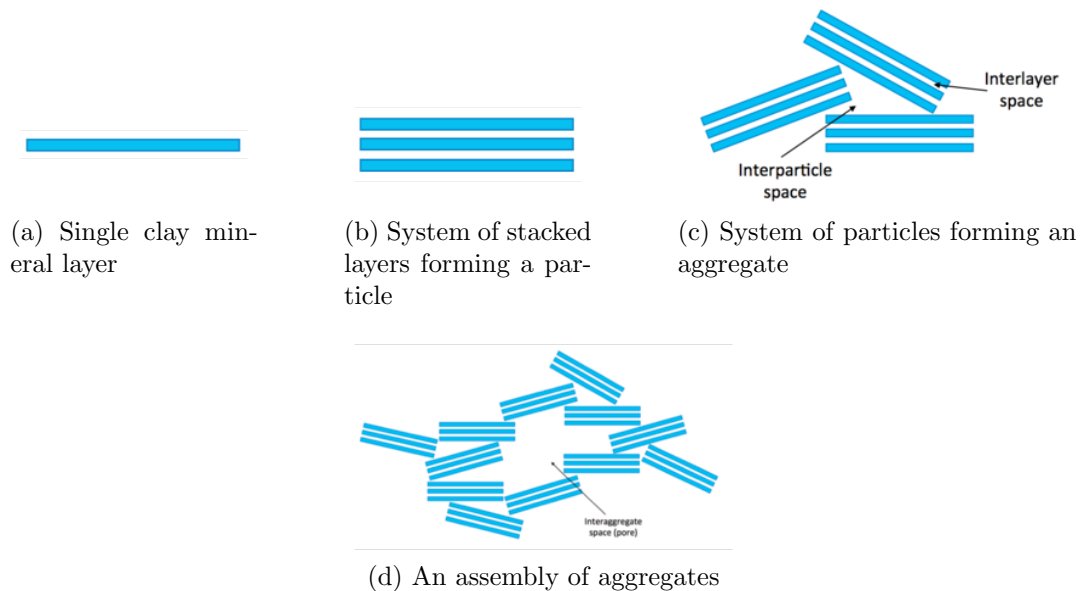


Figure 4.2: A schematic representation of the differing structures seen within smectite clay minerals. Sub-figures (a) - (d) show the varying states of a clay crystal leading to the formation of a clay aggregated system.

images it is clear that the Cloisite Na<sup>+</sup> is formed of larger particles in comparison to the SWN. However, the state of the clay here is most likely the situation of assemblies of aggregates, therefore the true micro state of the particles cannot be observed. This is not to say that there are no micro form particles within the images, but the assemblies of the aggregates are the dominant feature. Using image processing software ImageJ [151] the particle size distribution within the micrographs was determined for a sample size of 100 particles. These distributions are shown in Figures 4.3a and 4.3b for Cloisite Na<sup>+</sup> and SWN, respectively. From these distributions an average particle size can be determined for the two types of clay. In the case of Cloisite Na<sup>+</sup> an average particle size of  $26.01 \pm 1.46 \mu\text{m}$  is found, and for SWN an average size of  $12.57 \pm 1.37 \mu\text{m}$ . From the average particle size it is clear that the clay must mostly be formed of assemblies of micro particles with possibly some micro particles being present. This means that the

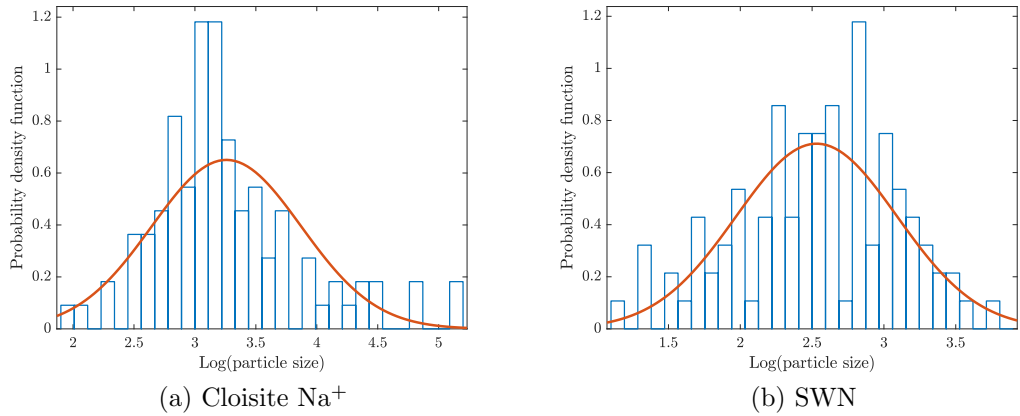


Figure 4.3: Particle size distributions determined from measurements of the particles in the SEM micrographs.

smaller structures, such as, single particles and single layers of clay are not observable under the SEM, at least without difficult sample processing. While it is possible to obtain single layers of clay within solution, the particles are likely to aggregate during any deposition and drying process ahead of imaging, removing the efforts of preparing single layers. There are also challenges with the imaging of the layers themselves, due to their thin nature (circa. 1 nm) they are typically optically transparent and thus difficult to image on even an electron microscope, due to the lack of contrast.

#### 4.1.2 Particle size distribution

As determined from the SEM analysis, representation of the clay particle size distribution is not a simple task, due to the varying scenarios that occur within the clay structure. Therefore, a method is required that gives a more accurate representation of the different particle states. A powerful way of doing this is through dynamic light scattering (DLS). Incident light shone into a colloidal solution will cause the light to scatter depending on the relative diffusion of the particles through Brownian motion, and the relative intensity of the scattered light can be used to gauge the particle diffusion rate and hence its relative size. Further particle size distributions were obtained using DLS for the clay particles after being suspended in water. Each sample was prepared at a certain concentration, as indicated within the Figure legend, by dispersing a

set mass of clay within ultrapure water to a total mass of 100 g and shaken vigorously by hand to ensure the particles distributed uniformly into the solution. As discussed in the previous Chapter samples were not sonicated to allow a true representation of the particle state to be evaluated. Samples were, however, rested for 1 minute prior to measurement to allow any overly large particles ( $>5 \mu\text{m}$ ) to settle out of solution and provide accurate DLS measurements. Samples under test were diluted  $100\times$  in water prior to measurement and placed into the cuvette. The size distributions obtained are shown in Fig. 4.4 and Fig. 4.5 for Cloisite  $\text{Na}^+$  and SWN, respectively. Before an interpretation of these distributions can be made, it is necessary to understand what happens when clay particles are dispersed into a solvent. This is a complicated matter, as several scenarios can evolve as shown schematically by Fig. 4.6. This means care is needed when interpreting the size distributions obtained from DLS. To begin with the Cloisite  $\text{Na}^+$  cases will be discussed. If we first look at the 0.5 wt.% concentration there, are 3 peaks occurring around 1 nm, 200 nm and 3000 nm. As there are multiple peaks, it is clear there is a mixture of scenarios occurring. It is likely at this concentration there are some single layers, corresponding to the 1 nm peak, some single particles of clay corresponding to the 200 nm peak and some unbroken aggregates corresponding to the 3000 nm peak. When the concentration is increased to 1.0 wt.%, a very similar scenario occurs, however, the broken clay aggregates appear as two distribution peaks around 100 nm and 500 nm, suggesting that the broken aggregates may possess a much wider distribution of sizes. At 1.5 wt.% the distribution is very similar to that observed at 1.0 wt.% with two peaks at around 100 nm and 400 nm corresponding to broken aggregates and a peak at 10000 nm corresponding to unbroken aggregates. But the exfoliated layers have been lost, as there are no peaks between 1 and 10 nm as in the previous distributions. Once the concentration is at 2.0 wt.%, there is now only one peak in the distribution, but with a wider range. The range over which is covers suggests that a combination of larger separated particles and aggregated particles are present. This trend continues throughout the 2.5 and 3.0 wt.% concentrations. It is clear from these results that the concentration of the clay has an effect upon the state

#### 4.1. The micro structure of the clay

---

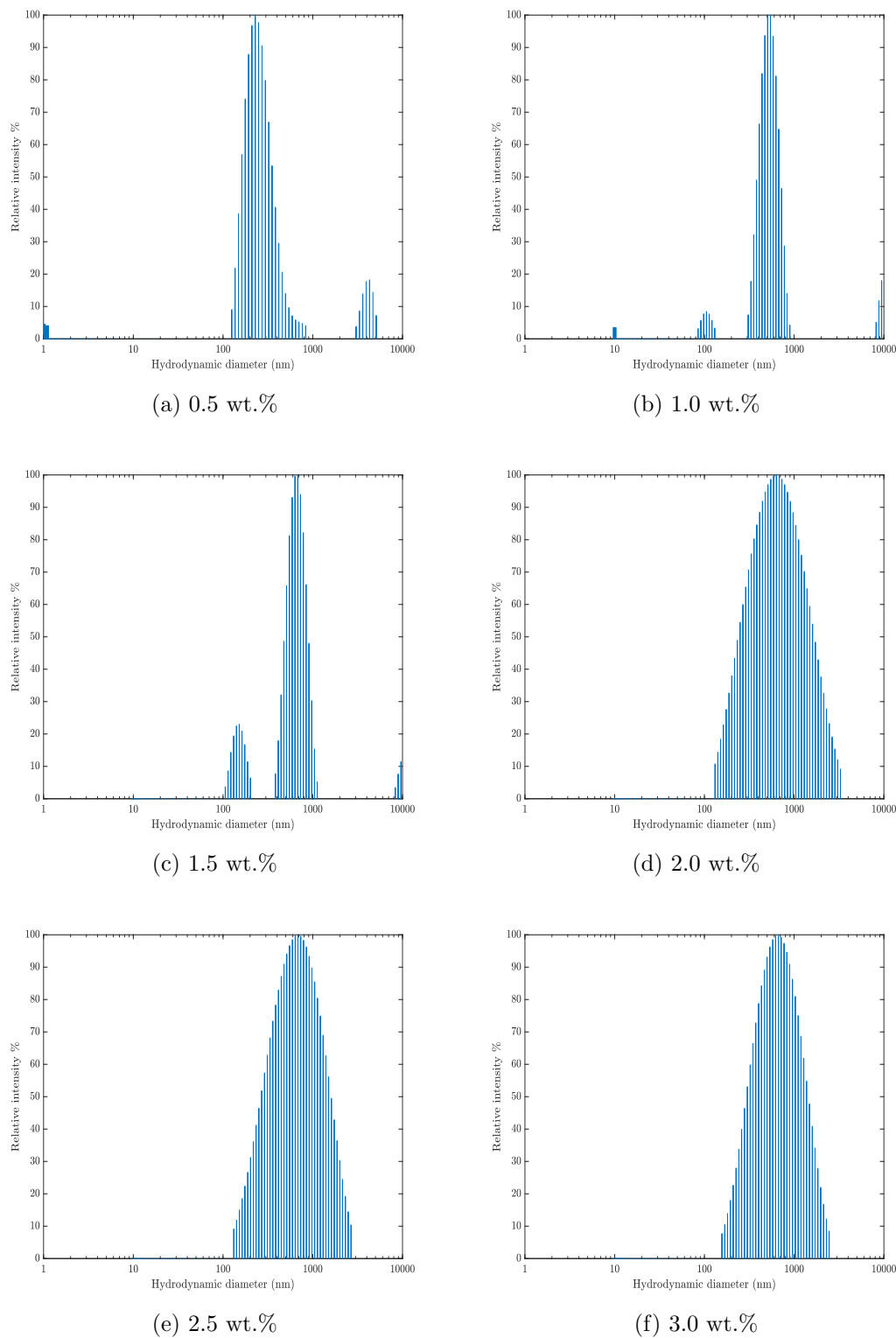


Figure 4.4: DLS particle size distributions determined for Cloisite Na<sup>+</sup> dispersed in water at 25°C. Sub-figures (a) - (f) show the distributions with the change in clay concentration.

#### 4.1. The micro structure of the clay

---

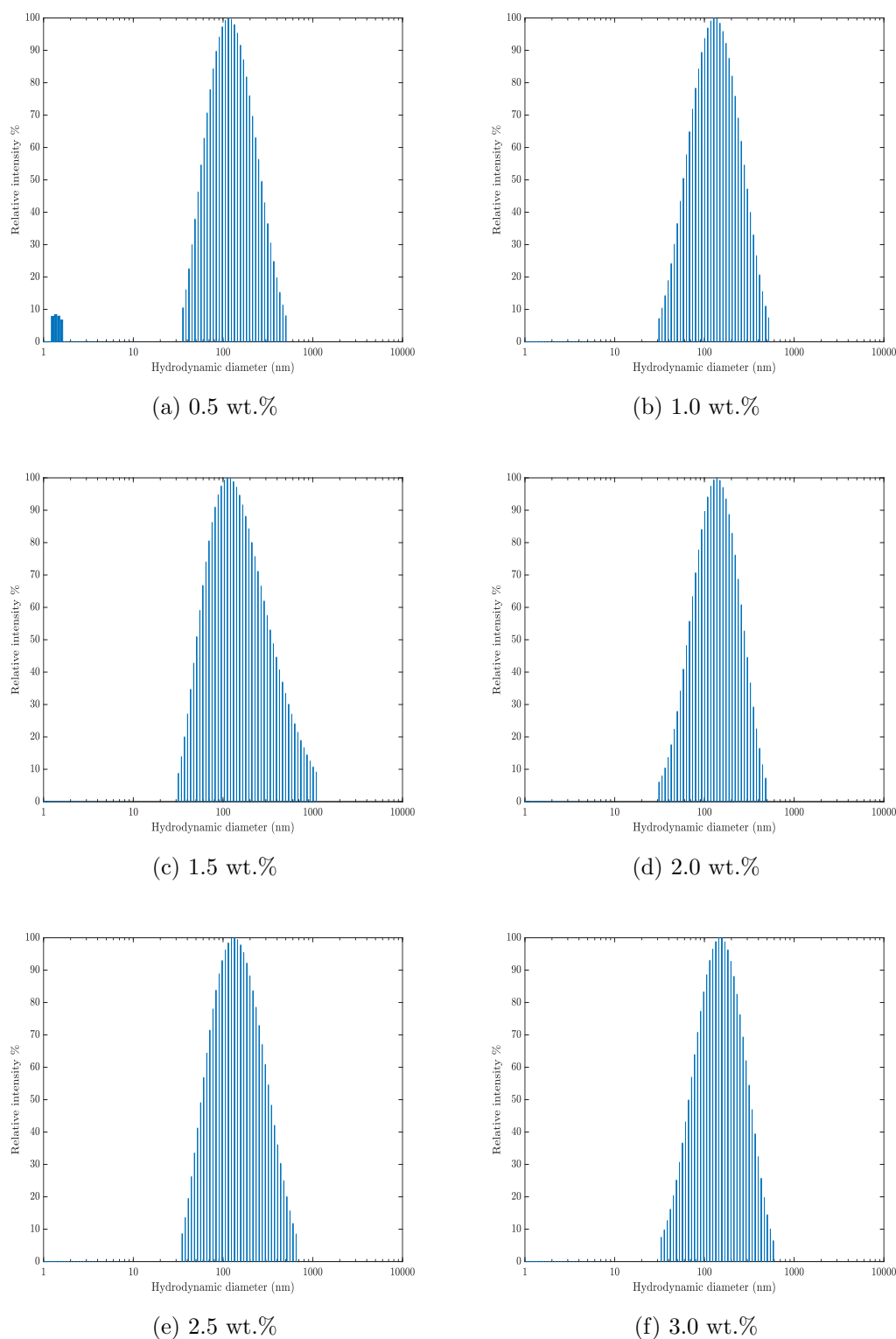


Figure 4.5: DLS particle size distributions determined for SWN dispersed in water at 25°C. Sub-figures (a) - (f) show the distributions with the change in clay concentration.

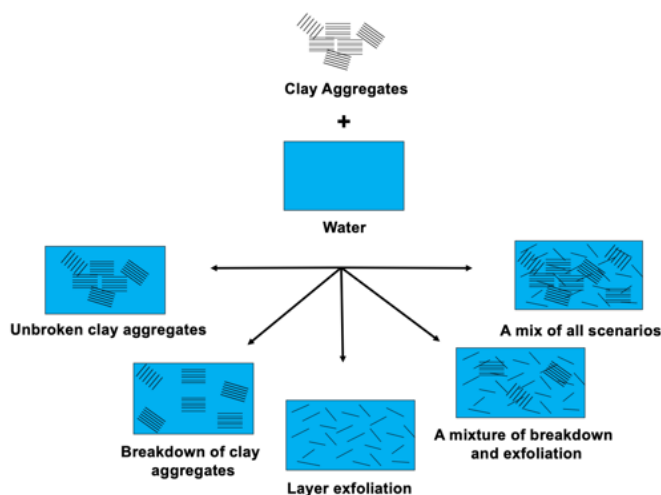


Figure 4.6: Possible scenarios developed when clay particles are added into solvent.

the particles are in, which should be taken into consideration, if further application of the clay is required, such as, in the preparation of single clay layers for nanocomposites.

Now the case of the SWN particles will be discussed. In comparison to the distributions obtained for Cloisite Na<sup>+</sup>, the distributions show much less variation with the change in sample concentration. The only distribution to show more than one peak is at a concentration of 0.5 wt.% where peaks are observed around 2 nm and 100 nm, suggesting single layers of clay and separated clay particles. At the concentration of 1.0 wt.% there is a single peak centred around 200 nm, suggesting separated particles. As the concentration of the sample increases, there remains a single peak, but there is a slight shift towards the right as the concentration increases. This suggests that, in each concentration the particles have separated from, the aggregated state. This is in contrast to the Cloisite Na<sup>+</sup> where aggregated particles can still be seen across the concentration range. This also suggests that the SWN is much easier to separate from aggregates than the Cloisite Na<sup>+</sup>. It is clear from the DLS measurements that the situation is much more complex than the SEM results suggest, therefore development of uniform colloidal systems is not a straight forward process.

## 4.2 Nano structures of the clays

### 4.2.1 Particle inter-planar spacing

Powder XRD was employed to determine the inter-layer spacing of the clay platelets. This spacing is often referred to as the clay basal spacing and represents the (001) crystal plane. Due to the nature of the clays to adsorb water molecules and swell, this spacing can vary in value depending upon the degree of hydration. Compared to other samples when investigated using powder XRD, clay samples are preferable to have as many of the platelet crystals aligned as possible as this maximises the reflections from planes aligned to the  $z$  direction. This is important as the  $z$  plane is often used as the distinguishing feature between different types of clay minerals due to the similar dimensions of the  $x$  and  $y$  planes.

The powder XRD spectra were obtained using the glass slide method as previously described. Concentrated colloids of the clay were prepared and then coated onto a glass microscopic slide and allowed to dry. Once dry the slides were placed within a fixed position inside the scanner and the X-ray diffraction spectra were collected. Samples were prepared this way in order to maximise the reflections from  $00l$  planes within the sample. The obtained spectra are shown in Fig. 4.7 and Fig. 4.8 for Cloisite  $\text{Na}^+$  and SWN, respectively. From these spectra the basal spacing can be seen at an angle of  $7.667^\circ$  for Cloisite  $\text{Na}^+$  and  $6.831^\circ$  for SWN, this then leads to basal spacings of  $d_{001} = 11.52 \text{ \AA}$  and  $d_{001} = 12.93 \text{ \AA}$ , respectively. It is noted here that a good agreement to the literature is seen for the 001 peaks. As can be seen here, the values of the basal spacing in smectite clays is much larger than many other crystalline materials, and this is due to the ability of the clays to swell and adsorb charge balancing cation species between the platelets.

While the clay deposited in such a way that the 001 plane was made prominent, other  $hkl$  planes may be observed in the spectrum due to the presence of randomly orientated

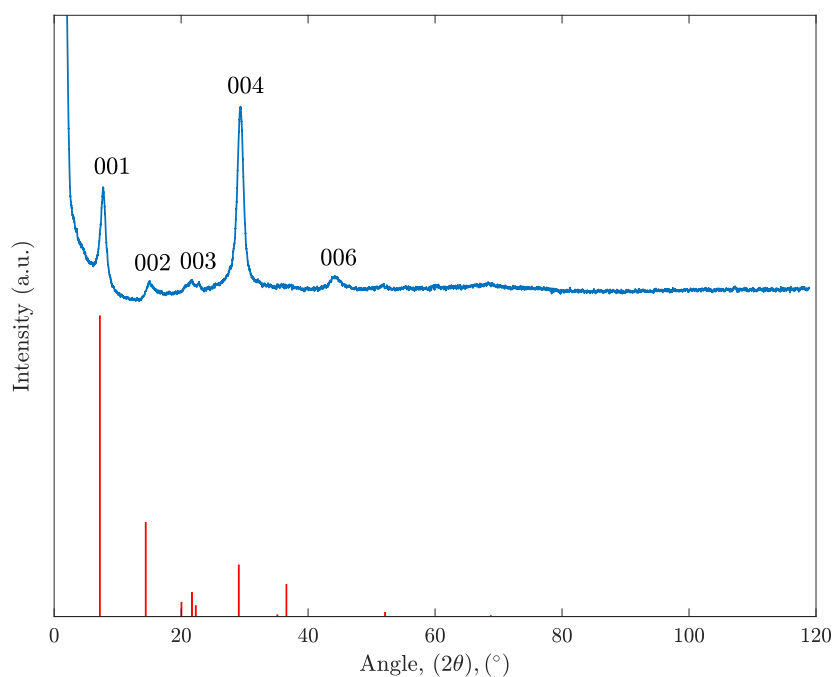


Figure 4.7: Cu source powder XRD spectra of Cloisite Na<sup>+</sup> obtained using orientated samples placed on a glass plate. The blue data shows the collected spectra while the red lines represent key  $hkl$  peaks obtained from the literature [152].

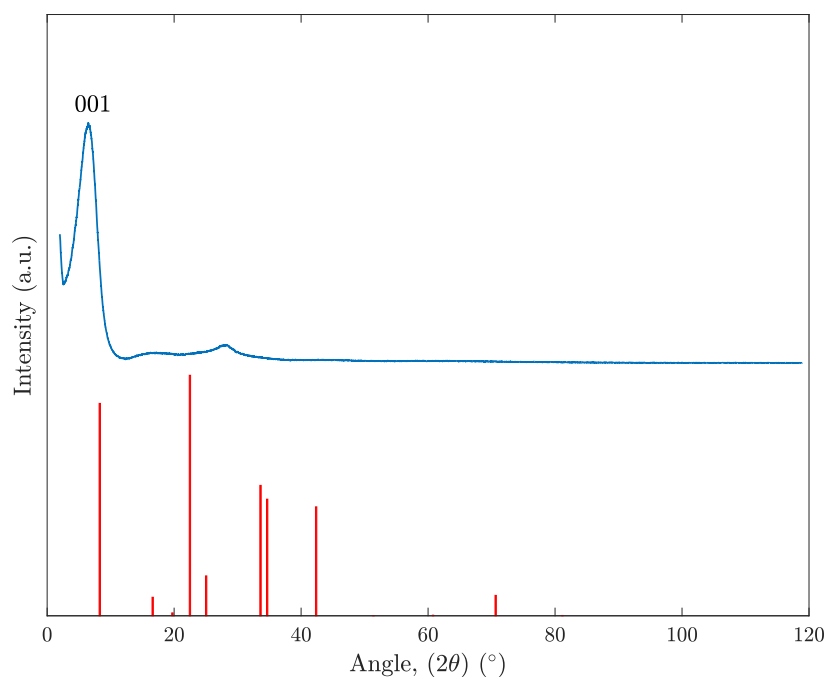


Figure 4.8: Cu source powder XRD spectra of SWN obtained using orientated samples placed on a glass plate. The blue data shows the collected spectra while the red lines represent key  $hkl$  peaks obtained from the literature [153].

crystals. It could be expected most of these observed peaks would correspond to  $00l$  peaks due to the orientation of the crystals. Comparing the obtained spectra to reference spectra for these clays [154], it is clear some of these expected planes are missing, which is most prominent in the SWN sample. This lack of peaks within the SWN can be inferred to be attributed to a smaller particle size leading to a lower degree of random orientation in the sample and hence lower intensity reflections from other  $hkl$  planes, thus leading to a loss of peaks in the spectra. This result is supported by the smaller particle size observed in the particle size distributions determined from both SEM and DLS.

## 4.3 Physical and chemical properties

In this section, chemical and physical properties of the clay are analysed to determine the similarities and differences between the two materials, to determine if any of these are prominent factors that can influence the gelation process.

### 4.3.1 Chemical structure of the clay

The chemical structure of the clay has been investigated using Fourier transform infrared spectroscopy (FTIR). The peaks within the FTIR spectra can be used to characterise the atomic bonds within the material, and hence provide information on the chemical nature of the material. The FTIR spectra presented in this work were performed on powdered samples that were first dried in an oven for 24 hours at  $150^{\circ}\text{C}$ . This was done to try and limit the amount of adsorbed water within the clay structure and give misinterpretations of the FTIR spectra. The spectra of Cloisite  $\text{Na}^+$  is shown in Fig. 4.9, and the spectra of SWN in Fig. 4.10. As both the materials may possess adsorbed water, a reference FTIR spectra of water was also obtained, as shown by Fig. 4.11. The assignment of peaks within the spectra was conducted using “The handbook of infrared and Raman characteristic frequencies of organic molecules” [155]. Firstly, the reference spectra of water will be evaluated. The first peak is identified at 3300

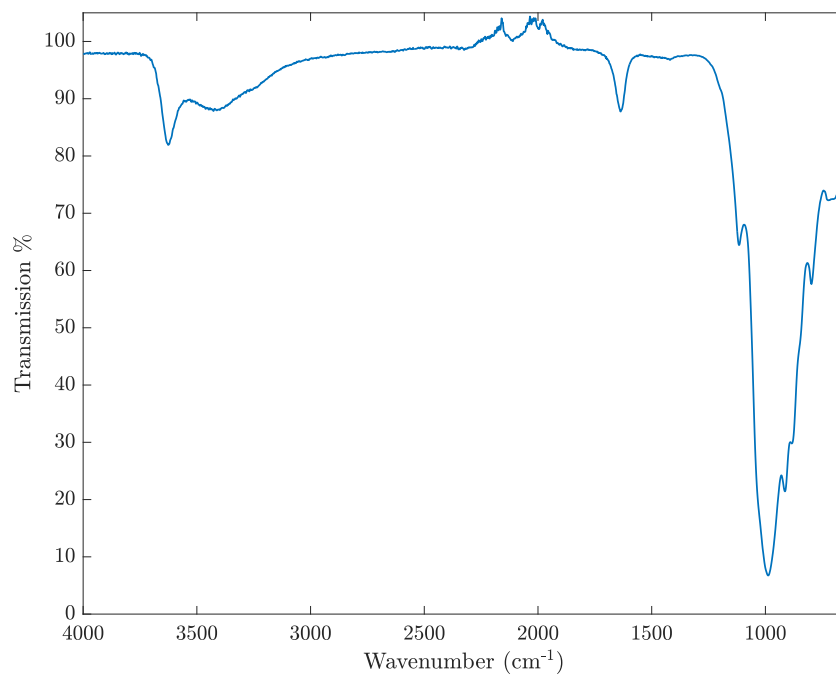


Figure 4.9: FTIR spectra of solid Cloisite Na<sup>+</sup> after drying at 150°C for 24 hours.

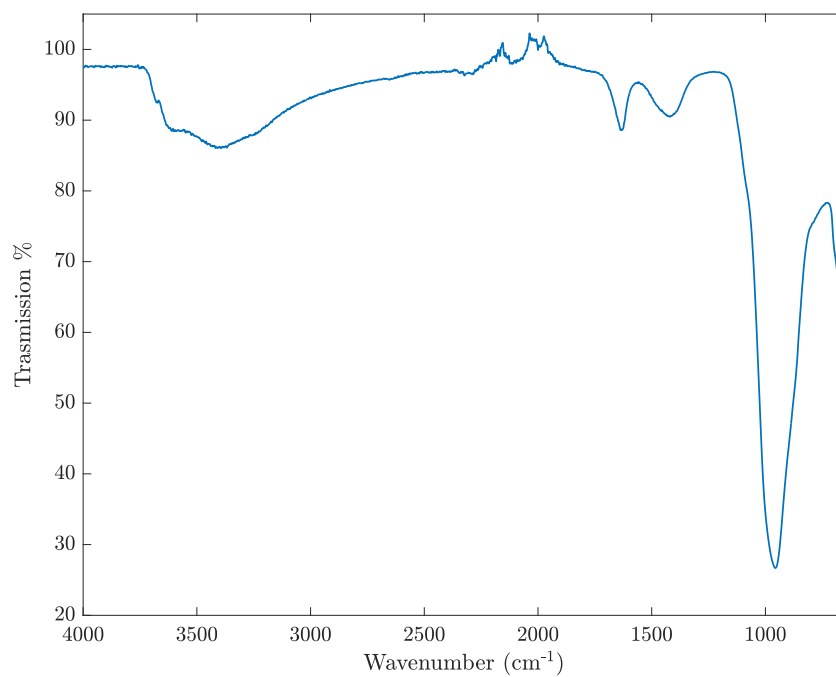


Figure 4.10: FTIR spectra of solid SWN after drying at 150°C for 24 hours.

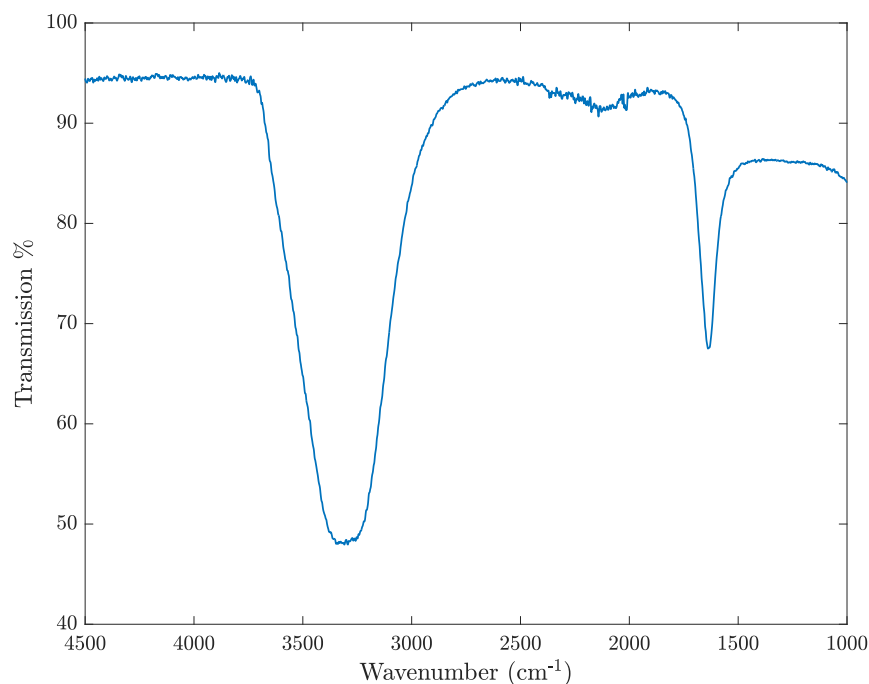


Figure 4.11: FTIR spectra of ultrapure water (18.2 MΩ).

$\text{cm}^{-1}$  corresponding to O-H stretching. A second peak is observed at  $1640 \text{ cm}^{-1}$  corresponding to O-H bending. Using this information, assignment of the peaks within the clay spectra can be made and any remaining adsorbed water can also be identified. Considering the Cloisite  $\text{Na}^+$  first, the first peak is seen at  $3621 \text{ cm}^{-1}$  corresponding to the structural OH groups on the clay, while peaks at  $3379 \text{ cm}^{-1}$  and  $1634 \text{ cm}^{-1}$  relate to  $\text{H}_2\text{O}$ , as seen from the reference spectra, hence there is still some adsorbed water within the structure. The most prominent peak, however, is at  $984 \text{ cm}^{-1}$  corresponding to a Si-O bond. With the clay being composed of mostly silicate structures it is not surprising this peak is highly prominent. It may also be expected to see Si-O-Al and Si-O-Si bonds, but these occur at wavenumbers below the measurement range of the employed FTIR. Now we can consider the SWN. A very similar pattern of peaks is seen within this spectra. The first peak is however broader, and two smaller peaks can be identified at  $3600 \text{ cm}^{-1}$  and  $3382 \text{ cm}^{-1}$ , corresponding to the structural OH and adsorbed  $\text{H}_2\text{O}$ . The SWN sample has two more peaks at  $1628 \text{ cm}^{-1}$  and  $1408 \text{ cm}^{-1}$ , both again representing  $\text{H}_2\text{O}$ . Therefore, it is clear, the SWN sample is more hydrated than

the Cloisite Na<sup>+</sup>. The final peak at 948 cm<sup>-1</sup> corresponds to the Si-O bond, and again with the structure being silicate dominant it is no surprise to see this peak as the most prominent. Again, peaks similar to the Cloisite Na<sup>+</sup> case may have been observed but due to the limitations of the instrument it is not possible to determine this. These results suggest that the SWN has a higher affinity for water, which could be a cause for it to more readily form a gel structure when exposed to water.

#### 4.3.2 Surface charge

The surface charge of clay is a fundamental property that arises from isomorphic substitutions within the clay layers. This often leads to the surface possessing a net negative charge, which is counterbalanced by the adsorption of cations within the gallery spacing. The presence of this surface charge can have significant effects in the colloidal stability of clay, and subsequently effect the formation of a gel network. In this work 50 mL of 0.5 wt.% clay solution was titrated with increasing volumes of CPC surfactant at a concentration of 0.025 N, with the surface tension measured at each interval of addition. In order to determine the effect of the clay on the adsorption of surfactant at the interfacial region, a preliminary experiment was performed on water with added surfactant in order to determine the point of critical micelle concentration (CMC). These results are shown in Fig. 4.12. To determine the CMC value of the surfactant, the intersection of two straight lines is evaluated, as shown by the additional straight lines on the plot. The points fitted are chosen such that they both maximise the R<sup>2</sup> regression parameter, and connect the transition regions between decreasing surface tension and saturated surface tension. It is of note that more points would be necessary to reduce the uncertainty. Evaluating the intersection point of these curves yields a value of  $0.63 \pm 0.27$  g/L, for the CMC of CPC in water. The addition of the clay into the solution causes the surfactant molecules to instead adsorb onto the clay surface rather than at the liquid-vapour interface, and so before the CMC point is reached, a plateau is first observed, which allows determination of the CEC of the clay. Following this the surfactant adsorbs at the liquid-vapour interface and causes the surface

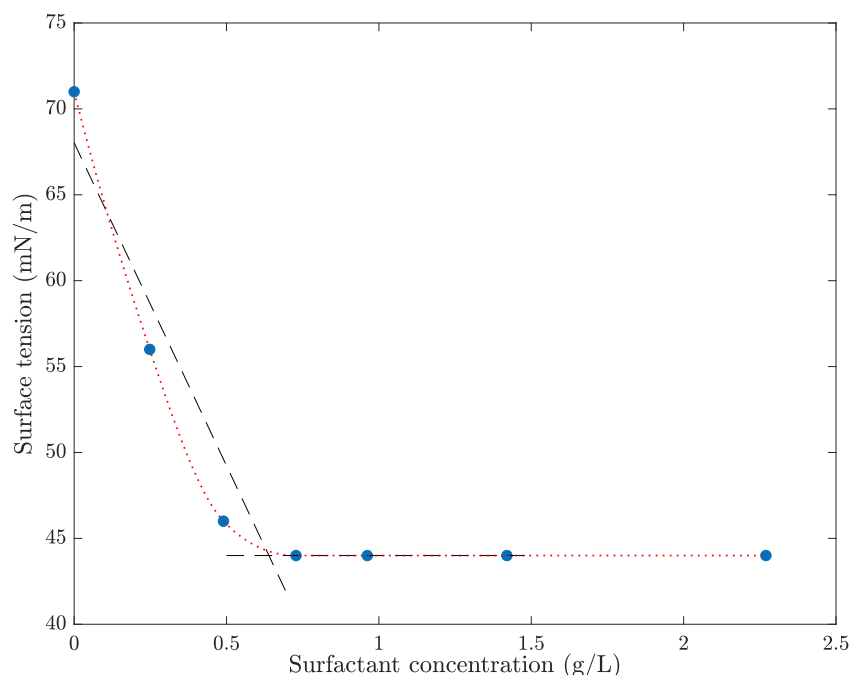


Figure 4.12: Determination of the CMC for the cationic surfactant CPC in water. Straight lines show the linear regions used for determination of the CMC point.

tension to decrease until the CMC point is reached. The results of these experiments are shown within Figures 4.13 for Cloisite  $\text{Na}^+$  and 4.14 for SWN. By extrapolating the linear regions of the titration curve, the equivalency point can be determined from the intersection of the two lines. This provides a value for the amount of surfactant required in order to balance the surface charge of the clay, which can be inserted into eqn. 3.2 to determine the CEC for the two types of clay. By doing this, values of  $84.00 \pm 4.83$  mEq/100g and  $49.94 \pm 10.22$  mEq/100g are determined for the CEC of Cloisite  $\text{Na}^+$  and SWN, respectively. This shows that the Cloisite  $\text{Na}^+$  has almost double the surface charge of the SWN and this could be attributed to the diameter of the platelets for each type of clay, as the larger platelet will have more regions for isomorphic substitutions to occur within a single layer. This is expected as smectite clays are known to undergo a large degree of isomorphic substitutions, with sodium montmorillonite being particularly known for a high exchange because of its large particle size [149]. A good comparison for the CEC of Cloisite  $\text{Na}^+$ , can be found when searching the literature [156], however, the comparison for SWN shows a significant discrepancy [157]. How-

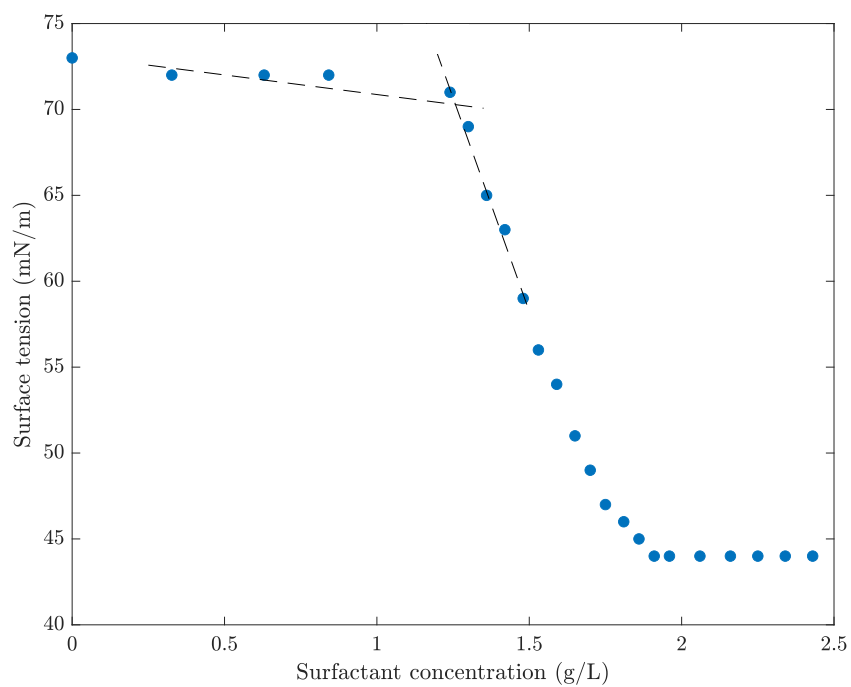


Figure 4.13: Determination of the CEC for Cloisite  $\text{Na}^+$  by measurement of the surface tension at increasing surfactant concentration.

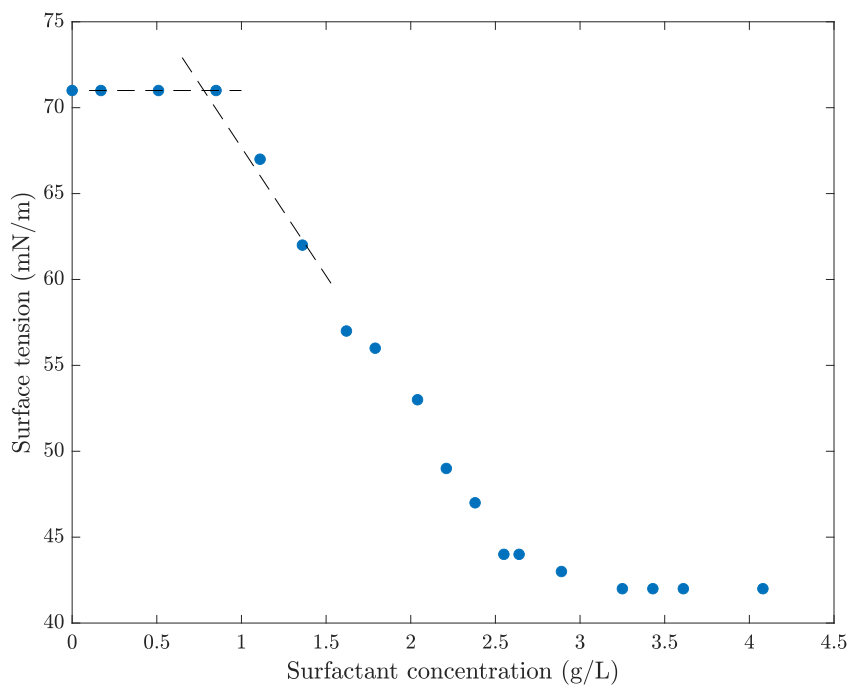


Figure 4.14: Determination of the CEC for SWN by measurement of the surface tension at increasing surfactant concentration.

ever, the SWN results could be taken with some scepticism in the comparison, since the results were obtained using the methylene blue titration method instead.

### 4.3.3 Surface free energy

iGC was used to determine surface energy profiles for the two types of clay considering the dispersive ( $\gamma^d$ ) and specific ( $\gamma^s$ ) contributions to the surface energy. These measurements were performed in collaboration with Surface Measurement Ltd. The surface energy profiles are shown in Fig. 4.15 for Cloisite Na<sup>+</sup> and Fig. 4.16 for SWN.

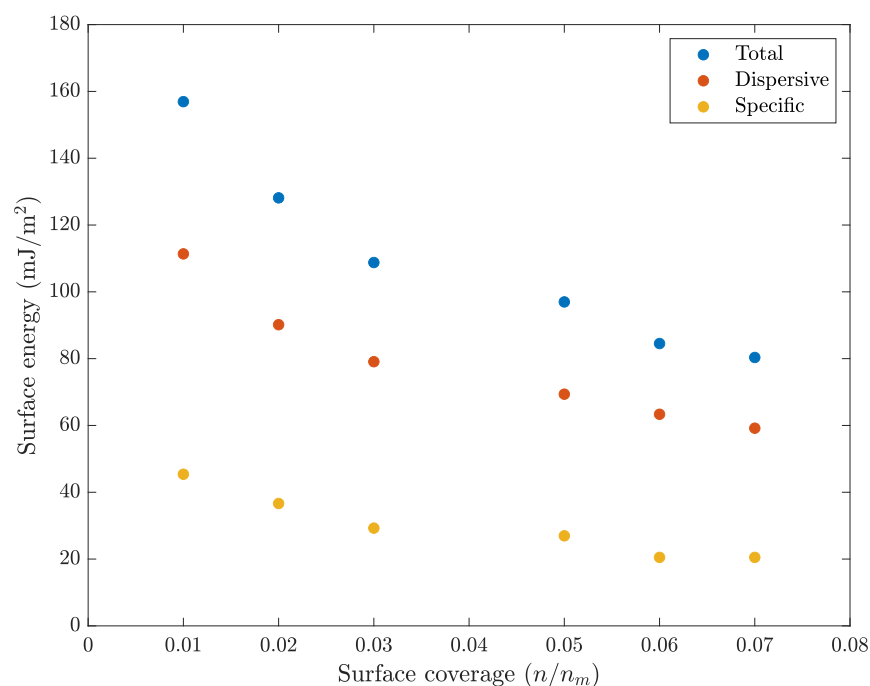


Figure 4.15: Surface free energy profile of Cloisite Na<sup>+</sup>, showing the contributions of both the dispersive and specific components as a function of the amount of probe molecule per the monolayer capacity.

It is clear from these plots, that the surface energy changes as a function of the surface coverage which suggests the surfaces to be energetically heterogeneous. The surface energy also appears to be contributed to more by the dispersive component rather than specific component. The specific components of the samples were calculated under the van Oss approach [158] using a pair of mono-functional acidic and basic probe molecules (dichloromethane  $\gamma^+ = 124.58$  mJ/m<sup>2</sup> and toluene  $\gamma^- = 16.23$  mJ/m<sup>2</sup>) with the Della

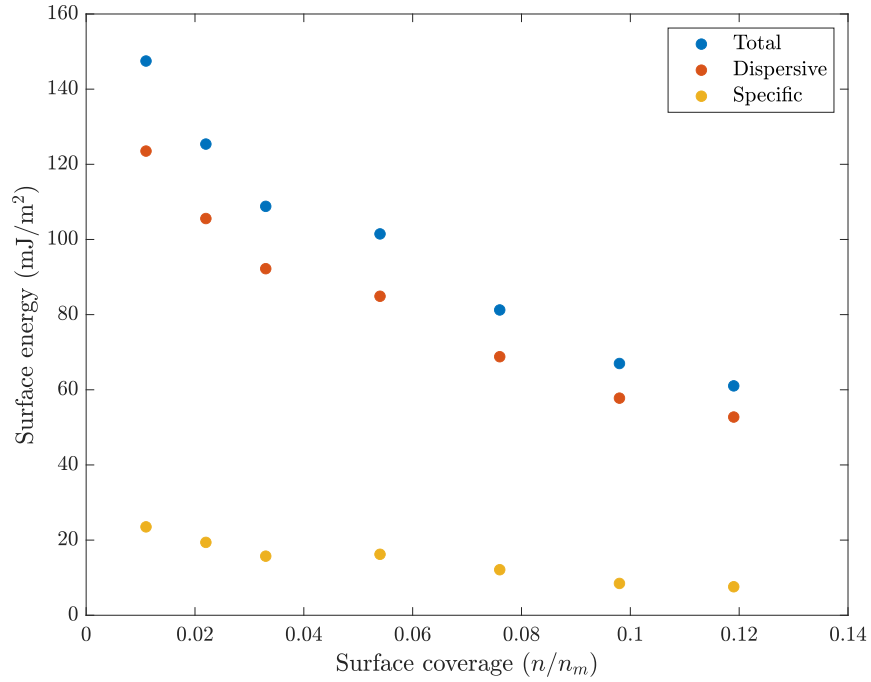


Figure 4.16: Surface free energy profile of SWN, showing the contributions of both the dispersive and specific components as a function of the amount of probe molecule per the monolayer capacity.

Voipe scale employed [159]. In order to better represent the surface heterogeneity, surface energy distributions were obtained from point-by-point integration of the surface energy profiles, resulting in plots of surface energy as a function of the percentage of the surface (area increment). The heterogeneity of the surface can be evaluated from the width of the distribution, with a wider distributions showing a more heterogeneous surface. These results are shown in Figures 4.17, 4.18 and 4.19, along with their values in Tables 4.1, 4.2 and 4.3.

Table 4.1: Average value of the dispersive component of the clay surface free energy, along with the values showing the range of the distribution.

Sample	Min (mJ/m <sup>2</sup> )	$\gamma^d$ (mJ/m <sup>2</sup> )	Max (mJ/m <sup>2</sup> )
Cloisite Na <sup>+</sup>	57.88	72.61	136.70
SWN	39.08	60.32	152.82

From this we can see the Cloisite Na<sup>+</sup> is more homogeneous than the SWN, and so possess more stable flow behaviour. The more heterogeneous surface of the SWN suggests

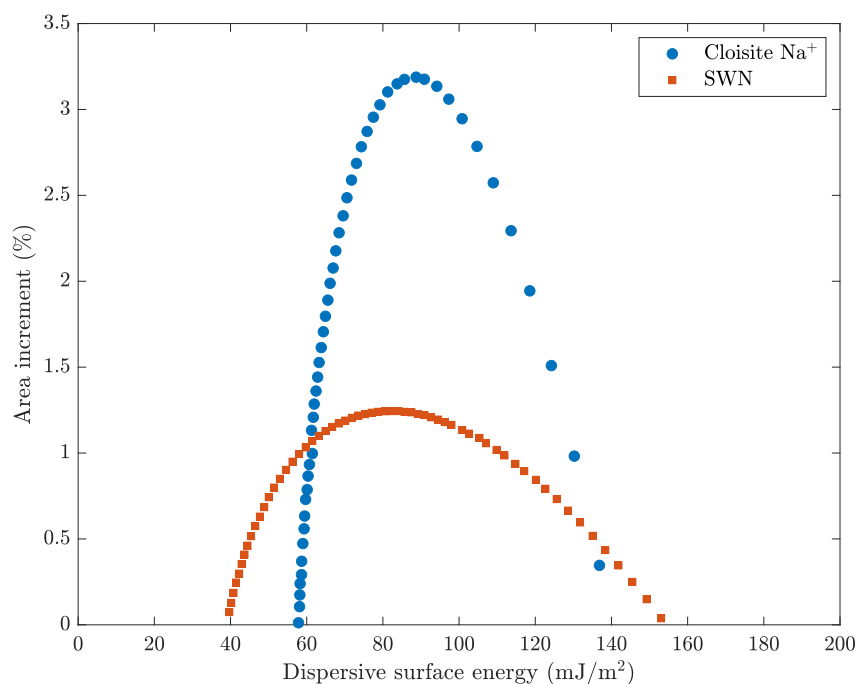


Figure 4.17: Dispersive surface energy profile of the two types of clays, plotted as a function of the area increment.

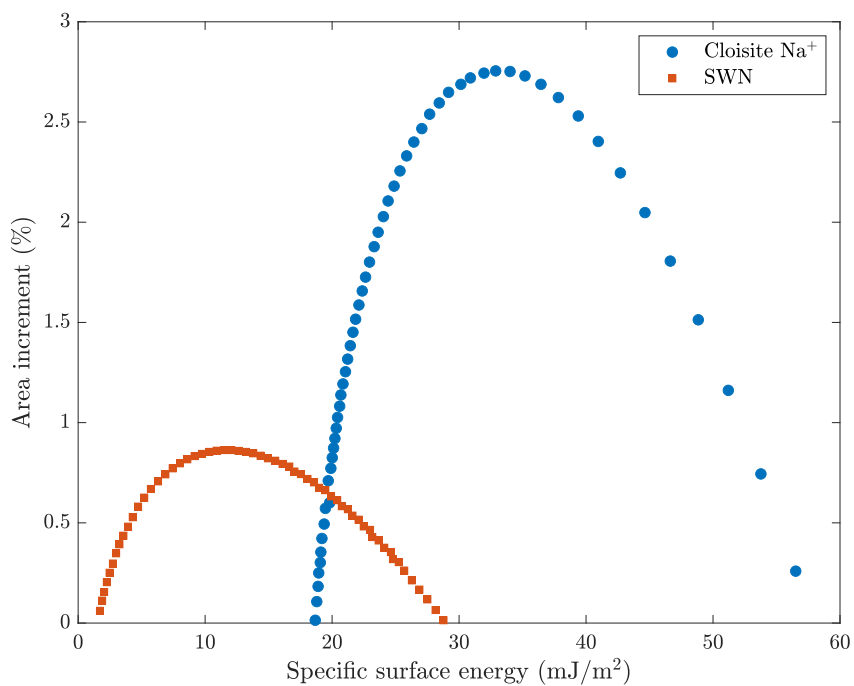


Figure 4.18: Specific surface energy profile of the two types of clays, plotted as a function of the area increment.

Table 4.2: Average value of the specific component of the clay surface free energy, along with the values showing the range of the distribution.

Sample	Min (mJ/m <sup>2</sup> )	$\gamma^s$ (mJ/m <sup>2</sup> )	Max (mJ/m <sup>2</sup> )
Cloisite Na <sup>+</sup>	18.65	25.72	56.45
SWN	1.50	6.58	28.71

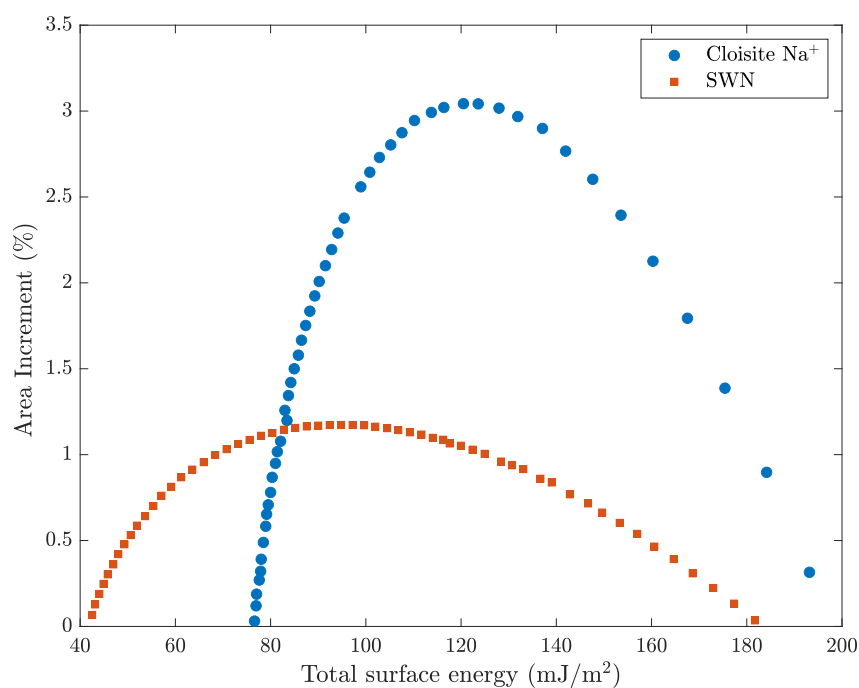


Figure 4.19: The surface energy profile of the two types of clays, plotted as a function of the area increment.

Table 4.3: Average value for the surface free energy of the clay surface, along with the values showing the range of the distribution.

Sample	Min (mJ/m <sup>2</sup> )	$\gamma$ (mJ/m <sup>2</sup> )	Max (mJ/m <sup>2</sup> )
Cloisite Na <sup>+</sup>	76.65	98.39	193.04
SWN	41.66	67.76	181.43

it has the most surface sites with differing energy levels. The total and specific surface energies were further used to evaluate the polarity of the clay surfaces. Fig. 4.20 shows the polarity of the clay surface as a function of the surface coverage. From this plot it

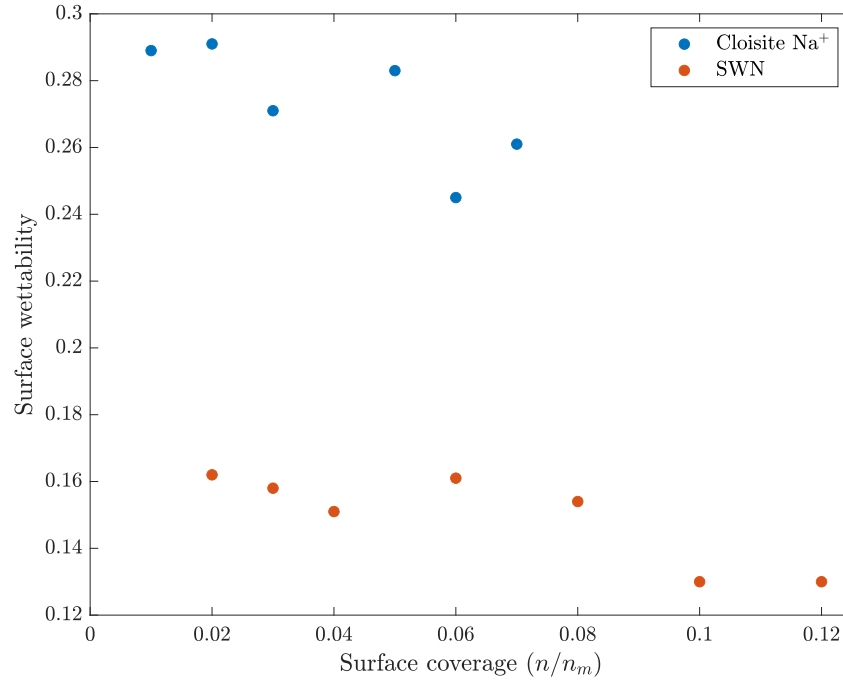


Figure 4.20: The surface polarity of the two types of clay evaluated as a function of the surface coverage.

is clear that the Cloisite Na<sup>+</sup> shows a higher degree of polarity in comparison to the SWN leading to a higher degree of hydrophilicity. Since surface energy is also directly related to the thermodynamic work of adhesion between two phases, this property can also be determined. The work of adhesion refers to the free energy difference between two states, defined for two states as [160]

$$W_a = \gamma_1 + \gamma_2 - \gamma_{12} \quad (4.1)$$

In the simplicity of a single phase this is refined as the thermodynamic work of cohesion expressed as

$$W_c = 2\gamma_1 \quad (4.2)$$

The thermodynamic work of adhesion for the clays was determined through the geometric mean method. Fig. 4.21 shows the thermodynamic work of cohesion as a function of the surface coverage. From this it is clear both clays have a relatively

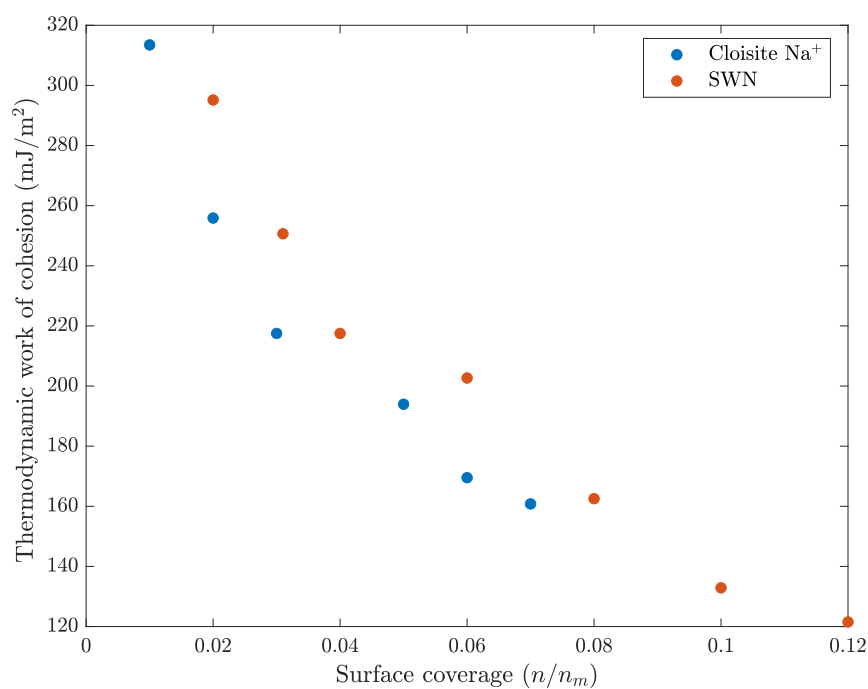


Figure 4.21: The thermodynamic work of cohesion of the different clay as a function of the surface coverage.

high work of cohesion which would suggest a high tendency for aggregation within the sample, which is supported by the images obtained from SEM.

#### 4.3.4 Surface area and porosity

The difference in lateral size of these types of clay has been shown previously. It is of interest within this work to evaluate the physical properties of these clays in terms of their specific surface area and pore sizes, to determine if this is a contributing factor to the gelation mechanism. In order to evaluate these properties, surface adsorption

isotherms were obtained. The first type of isotherm presented show the physisorption of the non-polar nitrogen molecule onto the clay surface. From this isotherm, properties such as the specific surface area and porosity can be evaluated. The isotherm for Cloisite Na<sup>+</sup> is shown in Fig. 4.22. The isotherm most closely resembles that of a

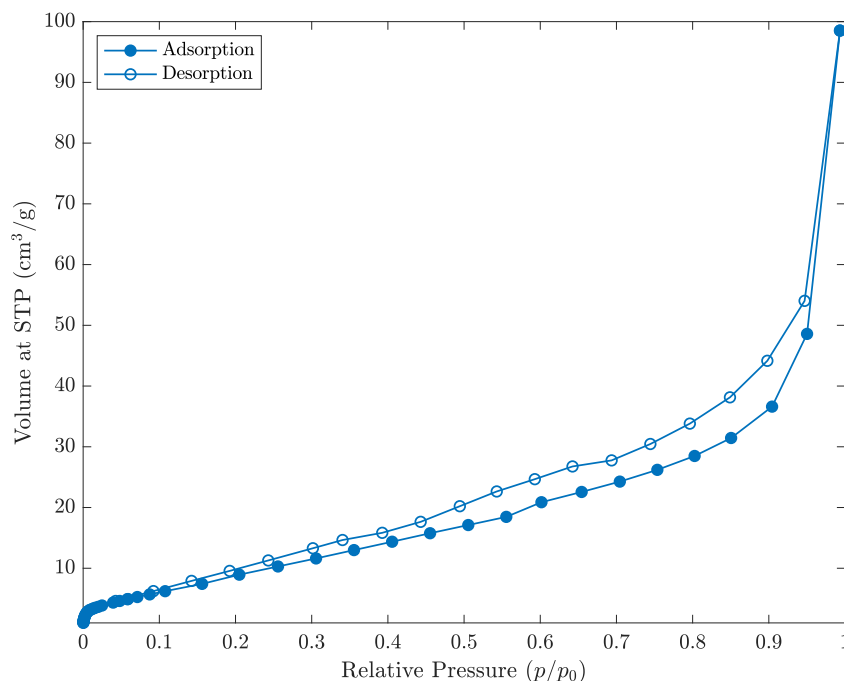


Figure 4.22: N<sub>2</sub> adsorption isotherm of Cloisite Na<sup>+</sup> conducted at 77 K.

Type IV under the IUPAC classification. The isotherm also shows a distinct hysteresis loop that resembles that of the type H3. This form of hysteresis is often characteristic of slit-shaped pores or assemblages of platy particles. As clay is known to be formed of assemblies of particle layers, this type of hysteresis should be expected. Note that the pore filling seen in this isotherm refers to the interparticle and interaggregate pores and not the interlayer space, as shown by the schematic in Fig. 4.2. The type of isotherm points towards the clay being a mesoporous material, suggesting pore sizes between 2 and 50 nm. It should also be noted that there is no plateau at high  $p/p_0$  which strongly suggests there is no indication of complete mesopore filling.

Since this isotherm is of a Type IV, the determination of the specific surface area

can be performed using the BET method. The adsorption points within the relative pressure range of 0.05 to 0.35 were used for this analysis, with a linear fitting applied to the results. This data is shown in Fig. 4.23. The BET analysis data for Cloisite Na<sup>+</sup> is

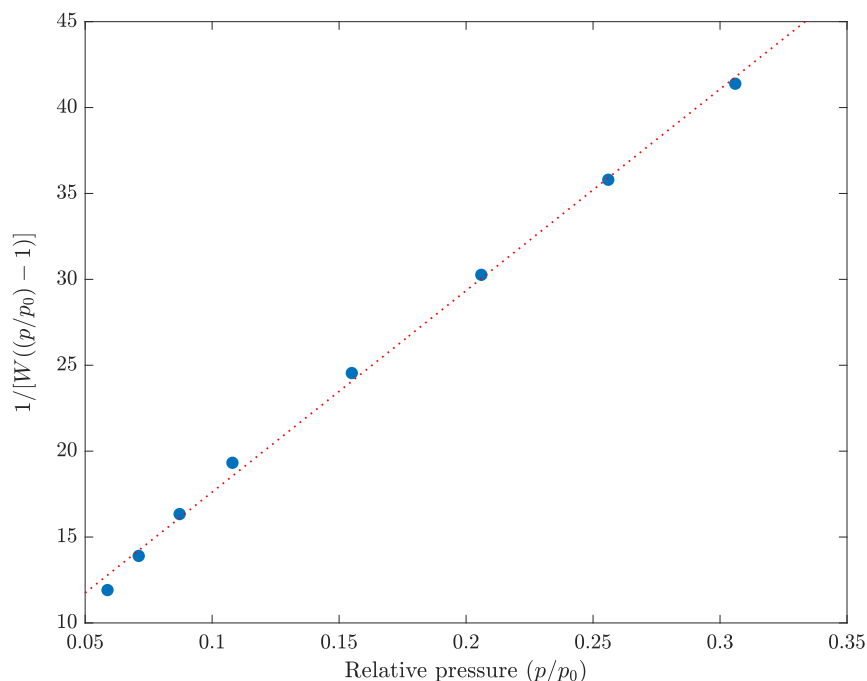


Figure 4.23: Evaluation of the specific surface area of Cloisite Na<sup>+</sup>, by use of the BET method.

given in Table 4.4. The relatively small specific surface area suggests the particles are

Table 4.4: Results of fitting from the BET surface area analysis of Cloisite Na<sup>+</sup>.

BET Summary	
Sample mass (mg)	$81.1 \pm 0.05$
Gradient	$117.423 \pm 2.384$
Intercept	$5.878 \pm 0.432$
Correlation coefficient	0.997533
BET Constant	$20.976 \pm 1.443$
Specific surface area (m <sup>2</sup> /g)	$28.244 \pm 0.019$

quite large in size, as was seen in both the SEM micrograph and particle size distributions. Of other interest is the information the isotherm provides on the porosity of the material. The shape of the isotherm and presence of hysteresis suggests the presence of mesopores, and this can be confirmed by obtaining the pore size distribution using the

BJH method. The distribution is shown in Fig. 4.24. From this data an average pore

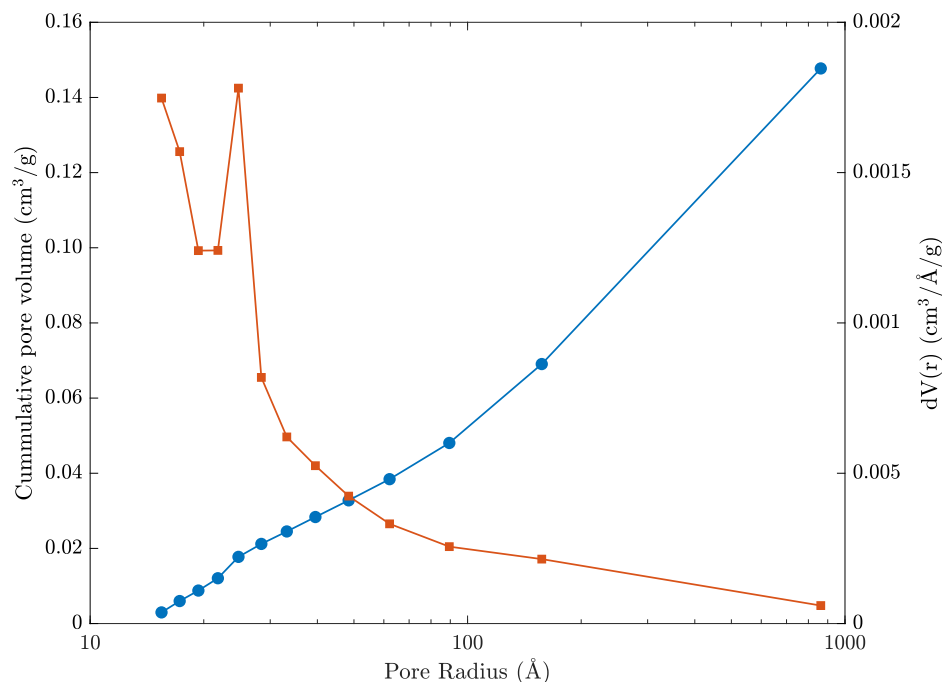


Figure 4.24: BJH pore size distribution of Cloisite Na<sup>+</sup>.

volume of  $0.131 \text{ cm}^3/\text{g}$ , and pore radius of  $24.716 \pm 14.18 \text{ \AA}$  is obtained. These values show that the material is indeed mesoporous in nature. The values determined here are in line with the literature for other montmorillonite clays [161]. The SWN clay will now be considered. The nitrogen adsorption isotherm is shown in Fig. 4.25. This isotherm also resembles that of Type IV, however, the sharp increase at low  $p/p_0$  suggests the filling of micropores (i.e. pores  $< 2 \text{ nm}$ ). The lack of plateau in the curve suggest the material still possess some mesopores. The isotherm also shows a small amount of type H4 hysteresis, which again is a characteristic property of microporous materials. To confirm the size of the pores within the clay, the pore size distribution was again evaluated, these results are shown in Fig. 4.26. From the pore size distribution, an average pore radius of  $17.017 \pm 6.867 \text{ \AA}$  and pore volume of  $0.091 \text{ cm}^3/\text{g}$  were obtained. This, therefore, shows that the SWN clay is microporous, and also shows another distinction between the two types of clay related to their respective pore sizes. The surface area of the particles will again be determined in the same way as the Cloisite Na<sup>+</sup> using

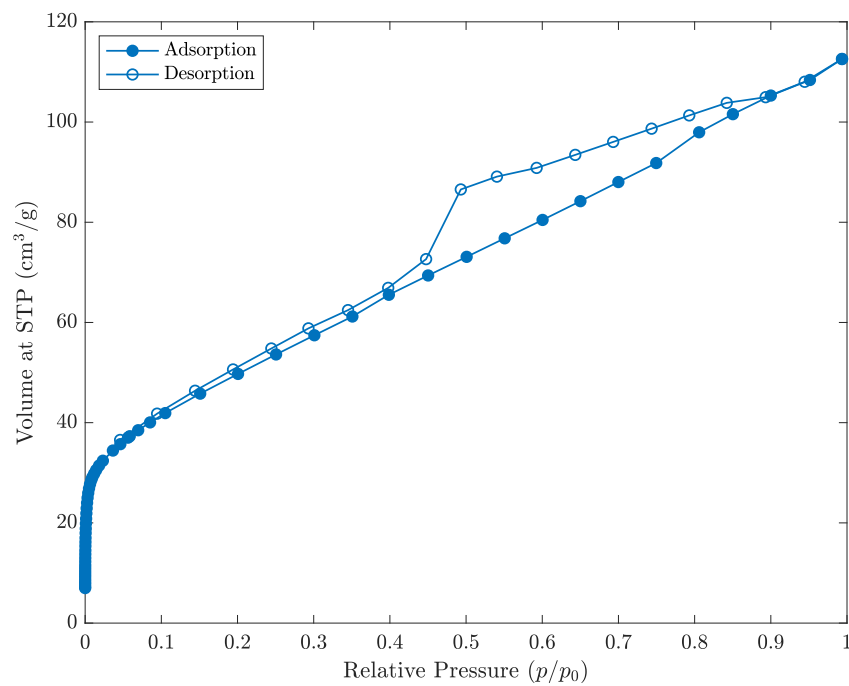
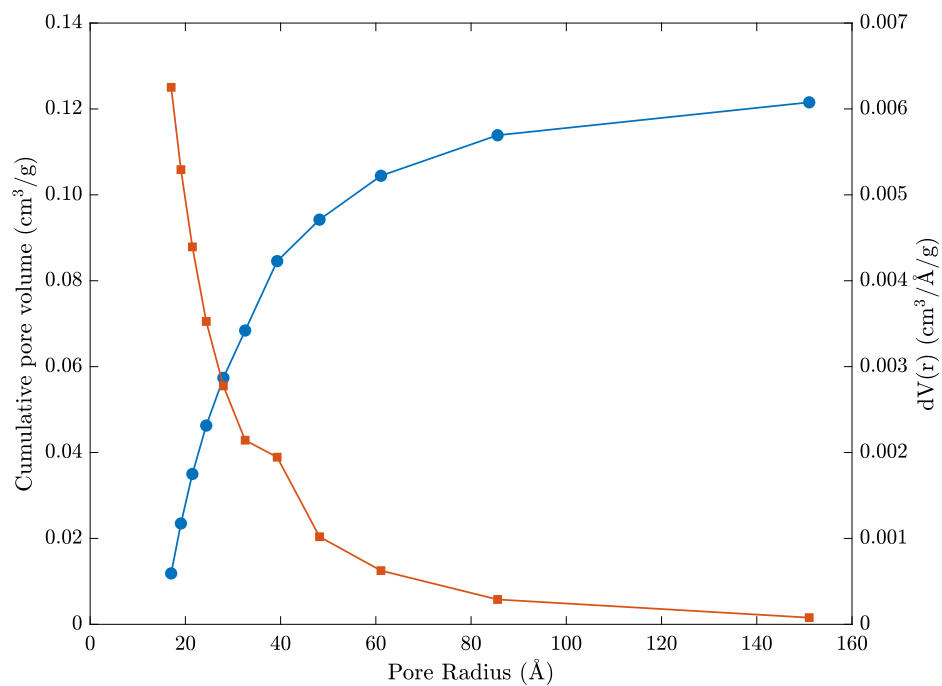
Figure 4.25:  $\text{N}_2$  adsorption isotherm of SWN conducted at 77 K.

Figure 4.26: BJH pore size distribution of SWN.

the BET method. The results of this analysis is shown in Fig. 4.27. The resulting

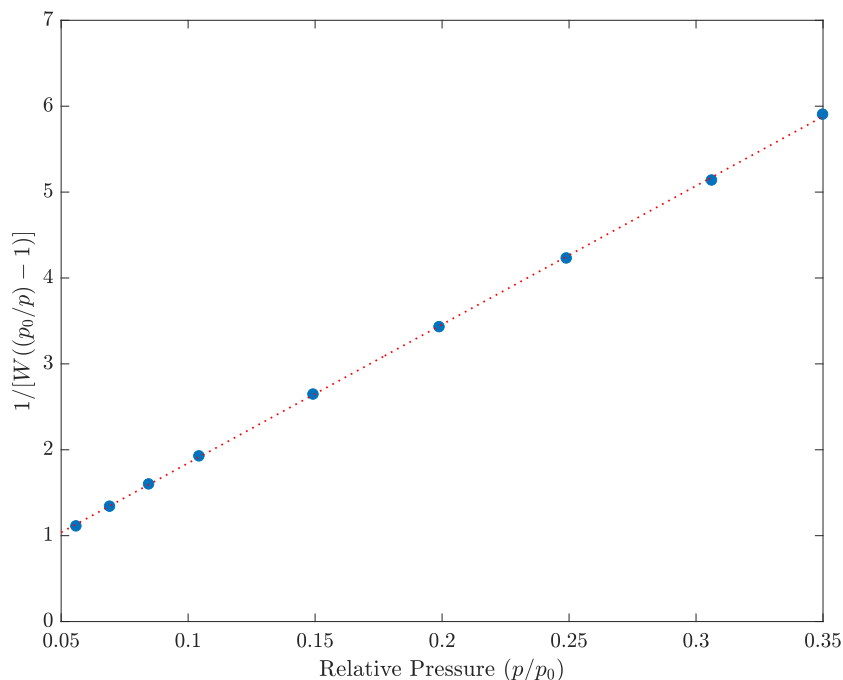


Figure 4.27: Evaluation of the specific surface area of SWN, by use of the BET method.

data evaluated from this fit process is presented in Table 4.5. From this the specific

Table 4.5: Results of fitting from the BET surface area analysis of SWN

BET Summary	
Sample mass (mg)	$80.05 \pm 0.05$
Gradient	$18.590 \pm 0.139$
Intercept	$0.0911 \pm 0.0280$
Correlation coefficient	0.999805
BET Constant	$205.038 \pm 62.627$
Specific surface area ( $\text{m}^2/\text{g}$ )	$186.415 \pm 0.116$

surface area of SWN was determined as  $186.415 \text{ m}^2/\text{g}$ . From this the significance of particle size on the specific surface area is highly obvious. The much smaller SWN particles possess nearly five times the surface area of the Cloisite  $\text{Na}^+$  particles. While an explicit reference to SWN cannot be found in the literature, comparing to other hectorites and the similar synthetic laponite, surface areas reported from  $5 \text{ m}^2/\text{g}$  [162] to  $300 \text{ m}^2/\text{g}$  [163] have been reported, with it more commonly lying at the higher end of

this range [164]. Therefore the determined surface area is concluded to be reasonable. This shows another physical difference between the two types of clay, along with the aspect ratio and porosity. These could be physical factors that influence the gelling abilities of these different types of clay.

#### 4.3.5 The thermal stability of clay

Thermal gravimetric methods are used to investigate changes of materials as they are heated. These effects can show changes such as: phase transitions, decomposition etc. Since the clay is to be used for energy applications, which can involve high temperatures, it is important to understand if the clay possess any transitions under the influence of temperature that may hinder its ability to be used in high-voltage applications. In this work thermal gravimetric analysis (TGA) was performed to investigate the change in mass of a sample with temperature. As clays are hydrated minerals, it can be expected an initial loss in sample mass can be attributed to the dehydration of the clay as the adsorbed water is released. Following this any further mass losses can be attributed to structural changes of the material. The TGA curve for Cloisite Na<sup>+</sup> is shown in Fig. 4.28 and the curve of SWN in Fig. 4.29. In each case the total weight loss of the sample is less than 15%. The minimal weight loss with temperature shows that the clays possess good thermal stability and do not appear to decompose, within the tested temperature range. In the case of Cloisite Na<sup>+</sup> there is an initial decrease in mass up to around 100°C, which could be attributed to the inter-layer adsorbed water. The continuing decrease in the mass up to around 500°C is most likely to also be the release of adsorbed water, but that which is bound to the exchangeable cations. From around 500°C the structural hydroxyl units begin to be breakdown, which continues up to around 700°C before, the curve begins to saturate [165]. The SWN shows a similar trend, however the initial release of water shows a more pronounced decrease up to around 200°C, after which the mass loss drops minimally up to around 650°C where there is another drop in the mass which could represent the breakdown of the structural hydroxyl groups. Both types of clay, however, do show a good level of thermal

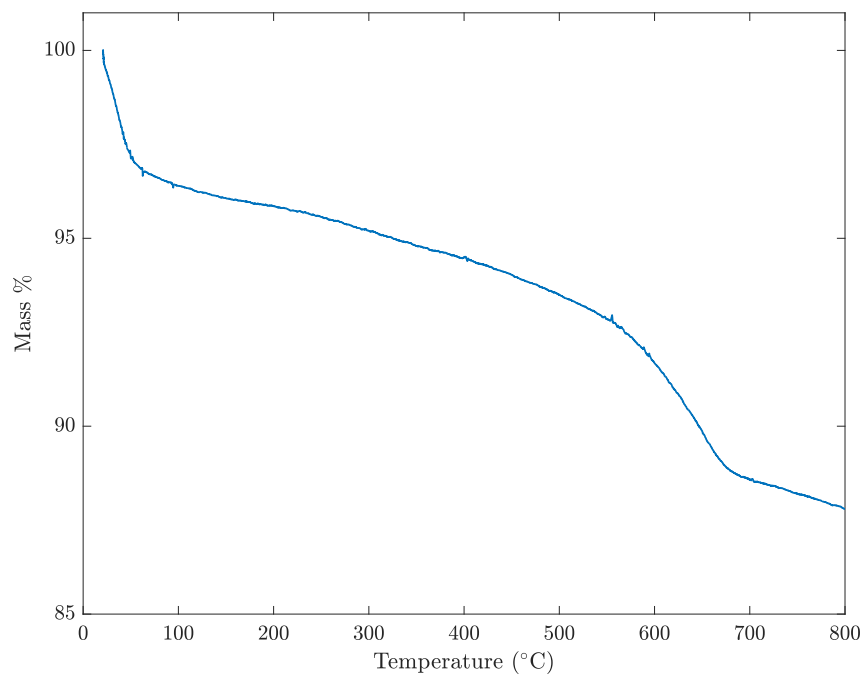


Figure 4.28: TGA curve of Cloisite Na<sup>+</sup>.

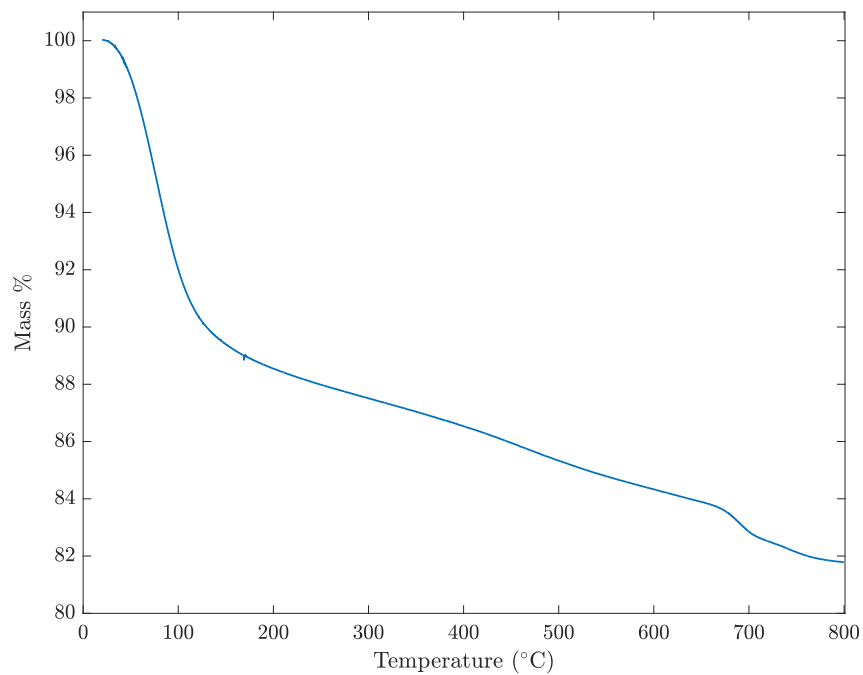


Figure 4.29: TGA curve of SWN.

stability up to 800°C, although they do show some loss of structure through hydroxyl groups degrading from around 600°C onwards.

## 4.4 Summary

The aim of this Chapter was to explore the physical properties of two types of commercially available nanoclay, namely Cloisite Na<sup>+</sup> and Lucentite SWN. These clays were chosen due to their known ability of gel formation within aqueous environments. The main results of this Chapter are:

- The two types of clay show significantly different average particle sizes, for the Cloisite Na<sup>+</sup> this is found to be  $26.01 \pm 1.46 \mu\text{m}$  and for SWN  $12.57 \pm 1.37 \mu\text{m}$ . However, we see that the average particle size shows a far more complex process, especially when in an aqueous environment. Here we note that several particle states can be present in unison: aggregates of particles, broken aggregates and single layers, meaning careful interpretation of size measurements is necessary. The aggregation tendency of the clay is also confirmed through measurement of the thermodynamic work of cohesion.
- Measurements of the clay surface charge have been made using a well documented method. The surface charge was found to be almost double in the Cloisite Na<sup>+</sup> when in comparison to the SWN. The effects of this surface charge on the colloidal nature of the clay will be explored in more detail in Chapter 5.
- From measurements of the surface free energy, we derive the surface polarity of the clay surfaces and show that the Cloisite Na<sup>+</sup> has a higher degree of polarity and is hence more hydrophilic than the SWN. The effects of this on the gel formation are investigated in Chapter 5 and the influence the hydrophilicity has on the clay when used as a surface coating are seen in Chapter 6.

The investigations of the surface and physical properties of the clay provide the background needed for a clear understanding of the colloidal nature explored in Chapter 5,

#### 4.4. Summary

---

and also allow prediction of the properties the clay will possess when exploited for the use as a surface coating.

## Chapter 5

# The stability and gelling behaviour of clay colloids

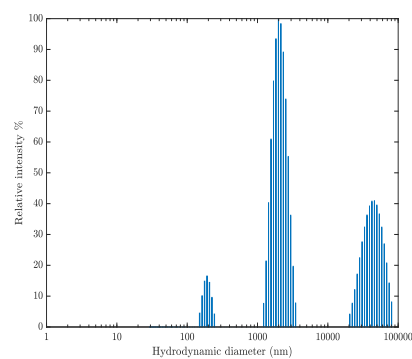
In order to prepare uniform gel coatings, firstly a uniform gel must be produced. This chapter explores the colloidal nature of clay, and the mechanisms by which they can undergo gelation. This work also investigates the effects of exfoliation of the clay layers on the colloidal nature and gelling behaviour, in order to produce more monodisperse colloids that can undergo gelation and produce more uniform structures.

### 5.1 Liquid phase exfoliation of clay particles

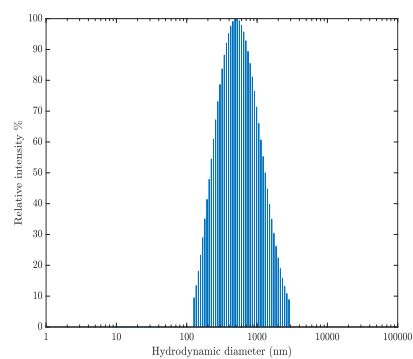
While many methods are exploited for the exfoliation of 2-D materials, such as: micromechanical cleavage [166], ion intercalation [167, 168], sonication-assisted [169], surfactant assisted [170, 171], etc., the efficiency and yield of single layers is often poor. An effective method that has recently seen popularity is liquid shear exfoliation (LSE). In this approach the material is dispersed into a suitable solvent, usually one with a similar surface tension value to the material surface energy, and mixed under high shear. This effect weakens the inter-layer Van der Waals attraction and causes the layers to separate out into solution. In this work the exfoliation of clay has been investigated using water as a solvent, due to both the high affinity of clay to water and the ability for it to swell in the presence of water. In order to exfoliate the clay layers, LSE was employed using a simple kitchen blender (Tefal Fruit Sensation BL142A42, Tefal UK) to provide the shear required. In order to investigate the effect of shearing time on the layer exfoliation process, size intensity distributions were obtained using DLS, to evaluate the particle dispersions as a function of blending time. Since it is likely the concentration of the colloid will need to be significant to produce the gel, the exfoliation treatment will be measured against colloids of 3.0 wt.%. In each case, colloids were produced by dispersing 3 g of clay within 97 g of ultrapure water. DLS samples were taken by pipetting from the central region of the exfoliated solution, in order to avoid any settled particles within the sample. The distributions obtained for Cloisite Na<sup>+</sup> at 3.0 wt.% are shown in Fig. 5.1. From the size distributions obtained it is clear that initially we see a range of particle sizes present, with peaks present around 300 nm, 2000 nm and 70  $\mu$ m. Drawing on the information presented within Chapter 4, we

## 5.1. Liquid phase exfoliation of clay particles

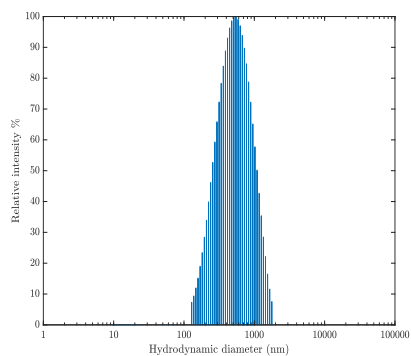
---



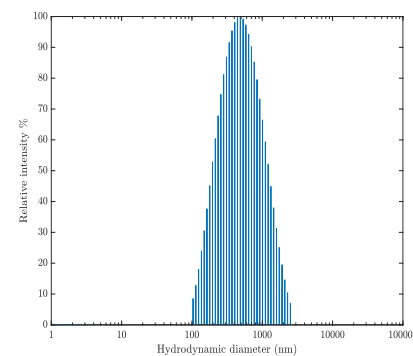
(a) 0 min treatment



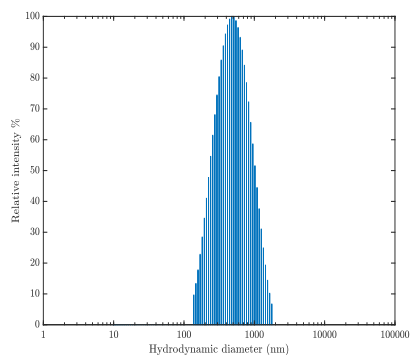
(b) 5 min exfoliation



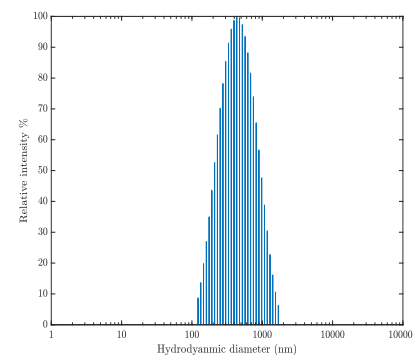
(c) 10 min treatment



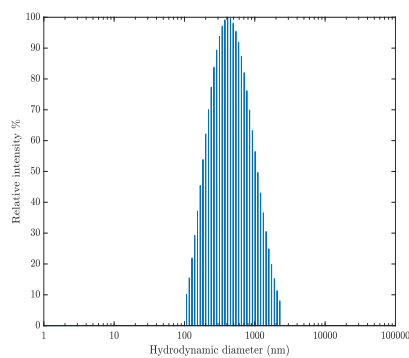
(d) 15 min treatment



(e) 20 min treatment



(f) 25 min treatment



(g) 30 min treatment

Figure 5.1: DLS particle size distributions obtained for Cloisite Na<sup>+</sup> at 3.0 wt.%, showing the effect of LSE treatment time on average particle size. Sub figures (a)-(g) show the increasing treatment time.

can conclude that this system is mostly attributed to a mix of single clay layers, aggregated clay particles and assemblies of the aggregates, for, the three peaks, respectively. After just 5 minutes of the exfoliation treatment the results suggest that the colloid has formed a reasonably monodisperse system, with only one peak now present centred around 700 nm, suggesting single clay particles. We can also see from the increasing exfoliation time, that the sample still shows a single peak situated between 500 and 800 nm suggesting this is indeed a monodisperse colloid, supported by polydisperse indexes of  $< 0.3$  for all samples measured from 5 minutes exfoliation time and upwards. Therefore, it is likely the size range observed is a true representation of the size of a single clay layer as apposed to a clay particle as previously thought. Due to the lack of significant change in particle size between longer exfoliation times, a time of 20 minutes was selected to be used for the exfoliation treatment process on Cloisite Na<sup>+</sup>. Samples referred to as exfoliated Cloisite Na<sup>+</sup> in the remainder of this thesis can be assumed to have been first treated using this method, before their measurements. It is also of note here that while these samples are referred to as exfoliated, what this actually means is that there is a high degree of layer exfoliation present within the system, not that it is perfectly exfoliated. Now the exfoliation of SWN will be investigated, with the resulting size distributions shown by the plots in Fig. 5.2.

The first thing of note with the SWN colloid is that the experiments were not possible to perform at a concentration of 3.0 wt.%. The simple reason for this is that the SWN gels too readily at the desired testing concentration, so it was not possible to perform the experiment under the same conditions. Therefore the sample was reduced to a concentration of 2.0 wt.% and the experiment performed (Sample preparation was done as above but with 2 g of clay and 98 g of water to achieve the desired concentration.) In contrast to the Cloisite Na<sup>+</sup>, the initial colloid shows a relative monodisperse system, with only a single peak observed, positioned around 300 nm. This would suggest the presence of single clay particles, however based on the results of the Cloisite Na<sup>+</sup>, it is possible this size range is representative of the single layer

## 5.1. Liquid phase exfoliation of clay particles

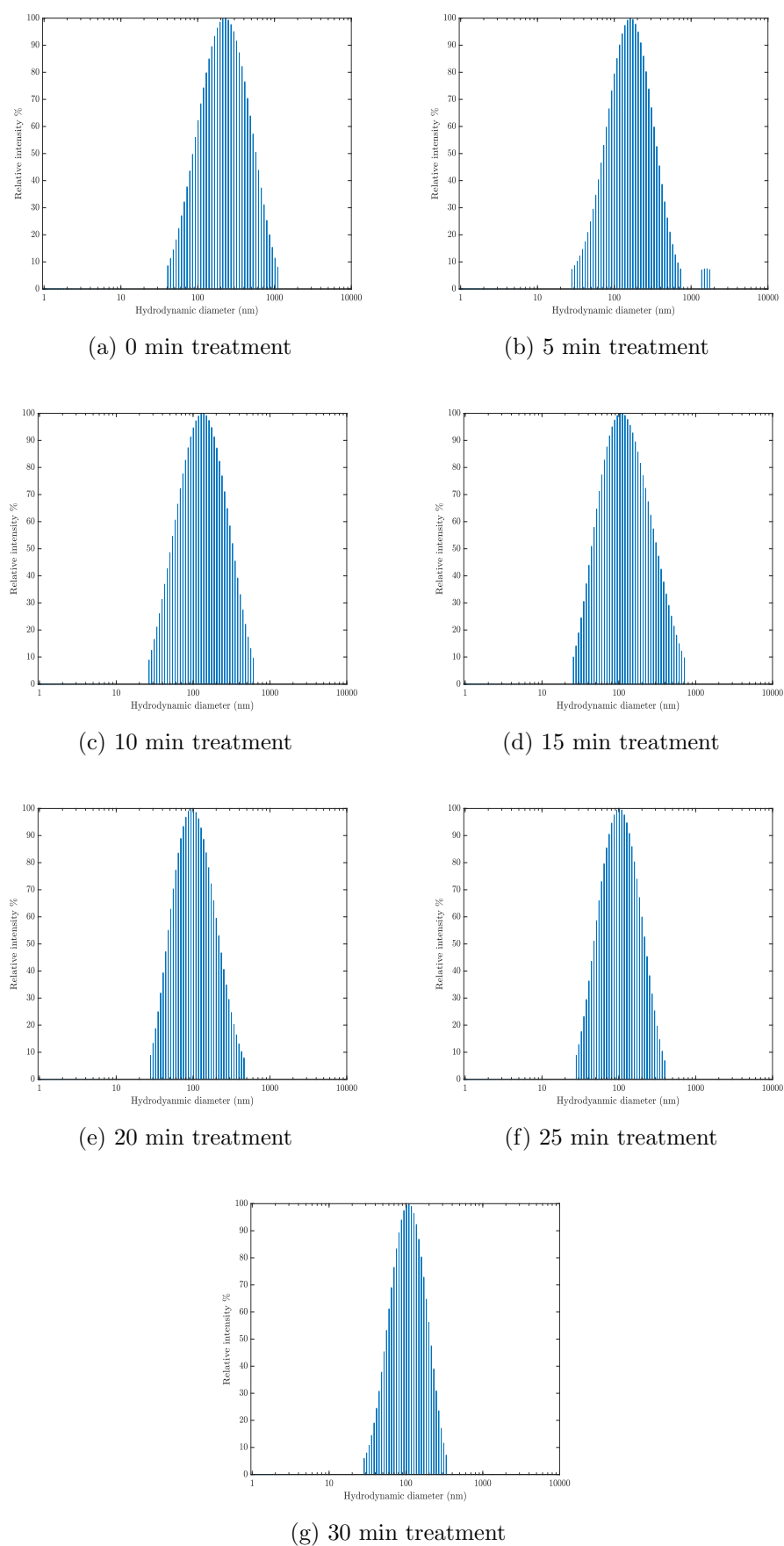


Figure 5.2: DLS particle size distributions obtained for SWN at 2.0 wt.%, showing the effect of LSE treatment time on average particle size. Sub figures (a)-(g) show the increasing treatment time.

size. After 5 minutes of the exfoliation treatment, there is a slight shift in the centre of the peak towards 200 nm, and we can also see the lower region is extending towards 20 nm. However, a secondary peak is seen just under 1100 nm which would suggest the presence of aggregates. Since this secondary peak is not observed in further samples, it can be assumed to be negligible. As the exfoliation treatment time is increased, a single peak is continued to be observed, supporting that the system is monodisperse, supported again by polydisperse indexes of  $< 0.3$  for all cases. As the exfoliation time is increased, the main change observed is that the position of the peak is shifting towards the left, and thus smaller average particle sizes. From 15 minutes of exfoliation time the centre of the peak is situated around 100 nm suggesting this to be the average size of the single clay layer. For consistency, with the Cloisite Na<sup>+</sup> the exfoliation time will be done at 20 minutes in total, and again exfoliated samples refer to a colloid with a high degree of layer separation.

## 5.2 Colloidal stability

The colloidal stability can be used to determine if the particles within the solvent remain well dispersed, with limited interactions between them. If the system is unstable and forms a gel state, then the first step of this process would involve particles aggregating together, which in turn would lead to a lower colloidal stability. Therefore, by observing the stability of colloids at different concentrations, an initial idea of the concentration that a gel starts to form can be determined. To determine the colloidal stability, the zeta potential ( $\zeta$ ) was evaluated at different colloid concentrations, where a value of  $\pm 30$  mV or greater is used as a baseline for a stable system. For each sample a fresh colloid was prepared, using the process described for the DLS measurements above. Around 1 ml of the sample was then loaded into the quartz measuring cell, and the zeta potential evaluated in triplicate. The results of these measurements are shown in Fig. 5.3. These results show that for the Cloisite Na<sup>+</sup> the stability of the colloid does not change significantly within the concentration range, with all the values either close to or above  $-30$  mV, suggesting a good stability of the sample and hence

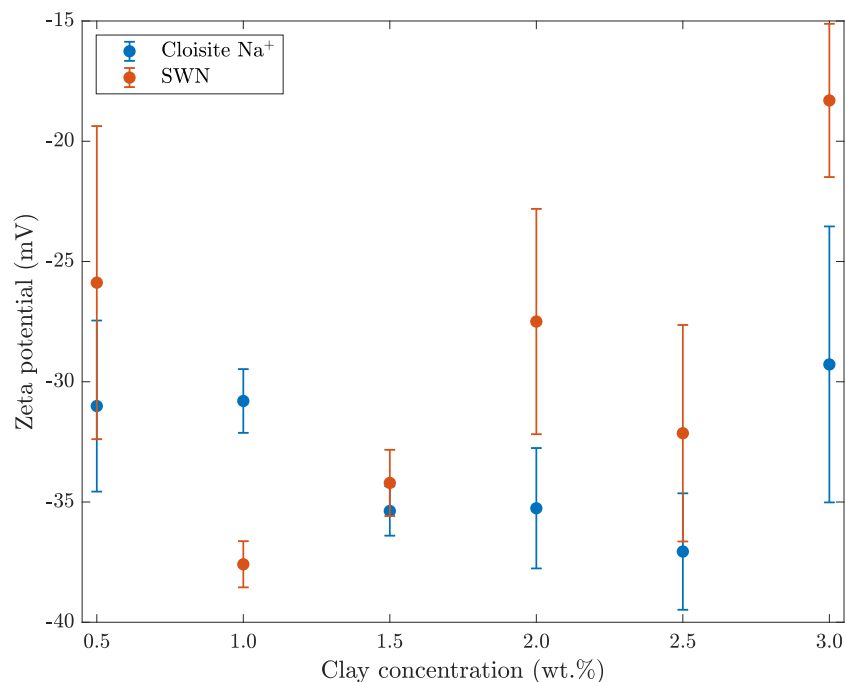


Figure 5.3: Stability of the two types of clay as colloidal solutions as a function of their concentration, evaluated through the zeta potential.

minimal particle interactions. Thus, it can be inferred that the necessary concentration for the gel network to begin forming is beyond 3.0 wt.%. Comparing this to the size distributions shown within Chapter 4 (Fig. 4.4), it is expected that the samples would maintain good stability as the size distributions typically show single peaks, suggesting monodisperse systems, and hence non-interacting particles. Whereas in the SWN colloids there is much more variation within the stability. Typically the stability shows a decrease as the concentration is increased, with 0.5 wt.% showing an exception to this, however the large error bar suggests it may be within the stable regime. Comparing to the size distributions obtained by the DLS (Fig. 4.5) it would be expected that the zeta potential would show a set of stable systems. This is because the size distributions show monodisperse situations, much like in the case of Cloisite Na<sup>+</sup>, which is observed in some cases. But a sudden transition from stable to unstable is seen between 2.5 wt.% and 3.0 wt.%, suggesting the onset of gelation within the system. This is similar to the effects observed within the exfoliation measurements as 3.0 wt.% of SWN showed a highly rapid gelling behaviour making it unsuitable to perform the sizing experiments.

This suggests that 3.0 wt.% may be the threshold concentration for the beginning of the gel formation in SWN, but Cloisite Na<sup>+</sup> is beyond this point.

### 5.2.1 The effect of layer exfoliation on colloidal stability

Although the stability of the colloidal clay has been investigated as a function of the concentration in the previous section, this considers the micro formed clay particles with little extent of layer exfoliation. Therefore, it is useful to also investigate the stability of colloidal clay as a function of the exfoliation time also. In order to understand this effect, the zeta potential was measured again for differing clay concentrations but as a function of the exfoliation treatment time. The results for Cloisite Na<sup>+</sup> are shown in Fig. 5.4. The results show that the exfoliation treatment does not appear to change

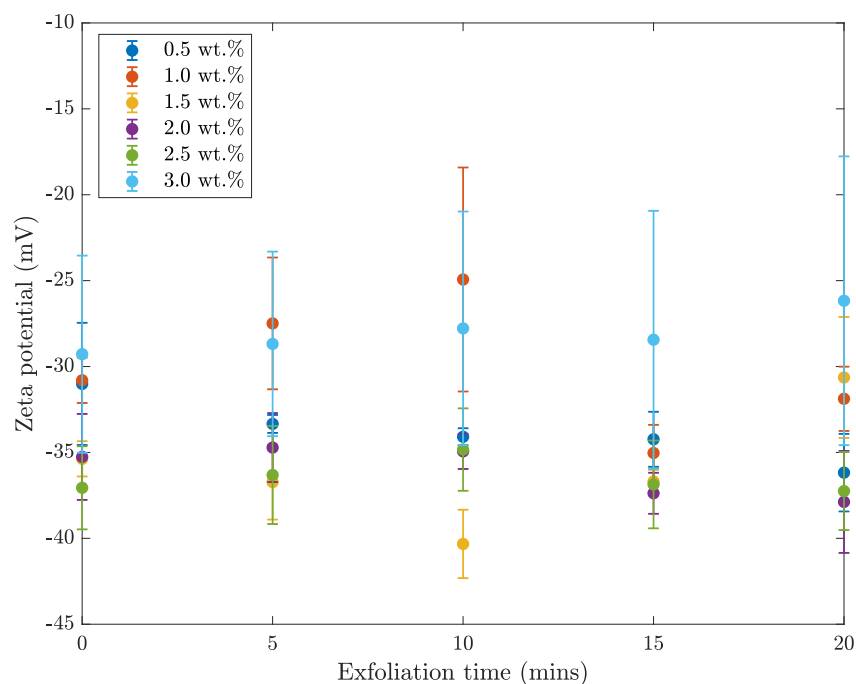


Figure 5.4: The stability of colloidal Cloisite Na<sup>+</sup> at varying concentration as a function of the exfoliation treatment time.

the stability of the colloid significantly as the values typically lie below  $-30$  mV, implying colloidal stability. The results of 3.0 wt.% show slight variation compared to the other concentrations, with an increased zeta potential, which could be suggesting that

the higher concentration and subsequent higher particle densities lead to more particle interactions, and subsequently reduce the stability of the system. This result perhaps is not surprising since it was seen that the critical concentration for gelation is clearly beyond that of 3.0 wt.%. Comparing the stability to the DLS exfoliation measurements, we can see that the size distributions become more consistent as the exfoliation time increases, which would perhaps suggest stability of the system. However, the size distributions are simply a snapshot of the average size of the particles in the colloid following the exfoliation process. It does not account for any subsequent particle interactions that may be occurring. Hence, the zeta potential gives us a clearer insight into the effect exfoliation has on the particles when separated from their bulk structure. For the case of the SWN the results are shown in Fig. 5.5. For concentrations below

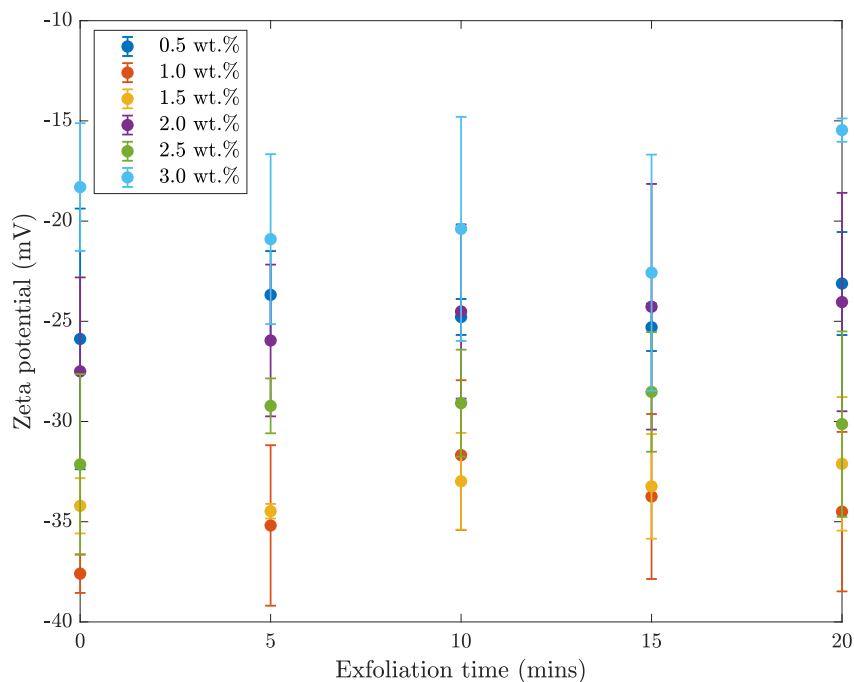


Figure 5.5: The stability of colloidal SWN at varying concentration as a function of the exfoliation treatment time.

2.0 wt.%, the samples show a reasonably consistent stability with values either around or below  $-30$  mV, as would be expected based on the previous stability measurements. As the concentration reaches 2.0 wt.% and increases further, the stability of the sample begins to show a tendency to reduce, with the zeta potential becoming smaller. This

is most noticeable in 3.0 wt.% where the zeta potential is either at or above  $-20$  mV, characteristic of a system that is moderately unstable. Comparing to that observed in the DLS size distributions, this again suggests that the colloid should be a stable system as the size distribution shows monodisperse peaks not suggesting the formation of aggregates in the system. However, for the reasons outlined above, the size distributions do not necessarily provide a clear picture of the stability of the system, as particle interactions that may subsequently take place may not be significant enough to appear within the weighted size distribution. It is clear from the zeta potential measurements, however, that the exfoliation treatment has an increased effect on the gelling nature of the SWN, with the interactions causing the stability to decrease further than that of the non-exfoliated case. We also continue to see here that the gelling behaviour of SWN is more pronounced than that of Cloisite Na<sup>+</sup>.

## 5.3 The early stages of particle interactions

An important aspect in the study of colloidal systems is understanding how the particles interact and either remain stable or unstable. It is possible to influence the stability of a colloid through effects such as: the addition of electrolytes or changing the sample pH. These effects can be used to either promote the stability or destabilise the colloid to promote particle-particle interactions. The stability of a colloid is usually assessed in one of two ways the tendency of the particles to aggregate or the tendency of the particles to sediment under the influence of gravitational forces. In this work the mechanism of particle interactions is considered. For particles within a colloid system the interaction potential for two individual particles is given as a sum of the attractive (van der Waals) and repulsive (electrostatic) components of the potential. When the attractive force dominates over the repulsive force, the particles are more likely to interact and begin the process of aggregation. A schematic diagram of the total interaction curve is shown by Fig. 5.6.

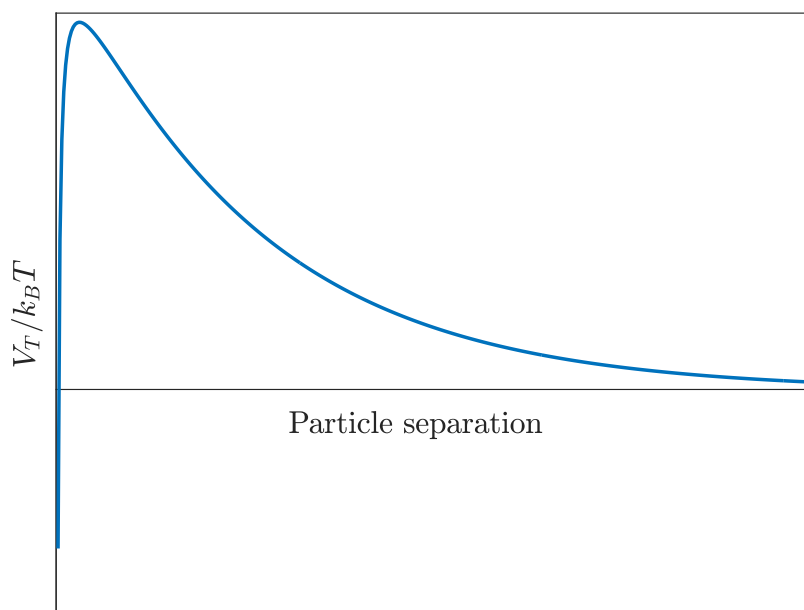


Figure 5.6: Schematic diagram of the total interaction potential curve for a charge stabilised colloid system [172].

### 5.3.1 The effect of salt concentration on colloidal stability and particle interactions

A typical way to influence the interaction potential within colloidal systems is to introduce counter ions. The introduction of the counter charged ions causes a reduction in the primary maximum of the interaction curve. At low electrolyte concentrations there is a long repulsive tail to the curve, which reduces as the electrolyte concentration increases. Along with this reduction, the height of the maxima decreases. At a certain concentration, a significant energy minimum develops where the van der Waals attraction is insensitive to the electrolyte concentration change. This is known as the secondary minimum. As the primary maximum falls to within a few  $k_B T$ , a large proportion of the particles will begin to interact and aggregate. When the primary minimum falls below zero, all particle collisions will lead to aggregation as there is no barrier to overcome for the interaction. This description is shown schematically by Fig. 5.7. The potential energy curve is difficult to obtain experimentally, therefore an

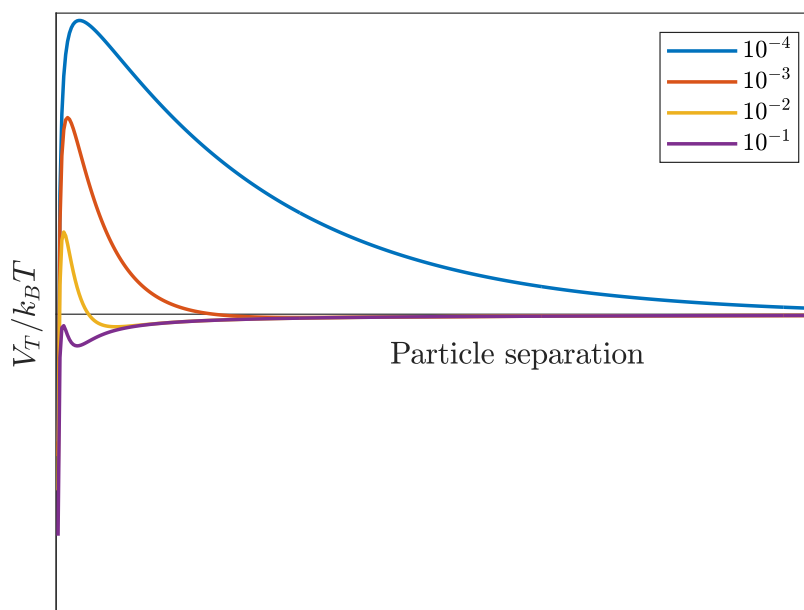


Figure 5.7: Schematic diagram showing how the addition of an electrolyte influences the total interaction potential curve for a charge stabilised colloid system.

alternative technique is often required to determine when the barrier for interactions is removed. A simple technique for the evaluation of this is to monitor the particle interaction rates. When the barrier for interactions is removed, the interaction rate for the particles saturates. DLS was employed to perform these tests by monitoring the hydrodynamic diameter of the colloidal particles as a function of time, under the influence of different concentrations of added NaCl. A plot of the hydrodynamic diameter against time will lead to a linear curve, with the gradient providing the aggregation rate constant,  $k$ . When the saturation point is reached and there is no longer an influence on the particle interaction rate, the rate constant for the removed barrier is referred to as  $k_d$ . The DLS measurements for Cloisite Na<sup>+</sup> at 0.5 wt.% are shown in Fig. 5.8. The determined aggregation rates and relative particle stability ratios are shown in Fig. 5.9. While the DLS data itself shows there is clearly a dependence of the particle interactions on the added salt concentration, it is difficult to infer from this figure alone. As the clay particles do not exist as a monodisperse colloid, it is easy to develop significant scatter within the results, leading to misinterpretation of the mea-

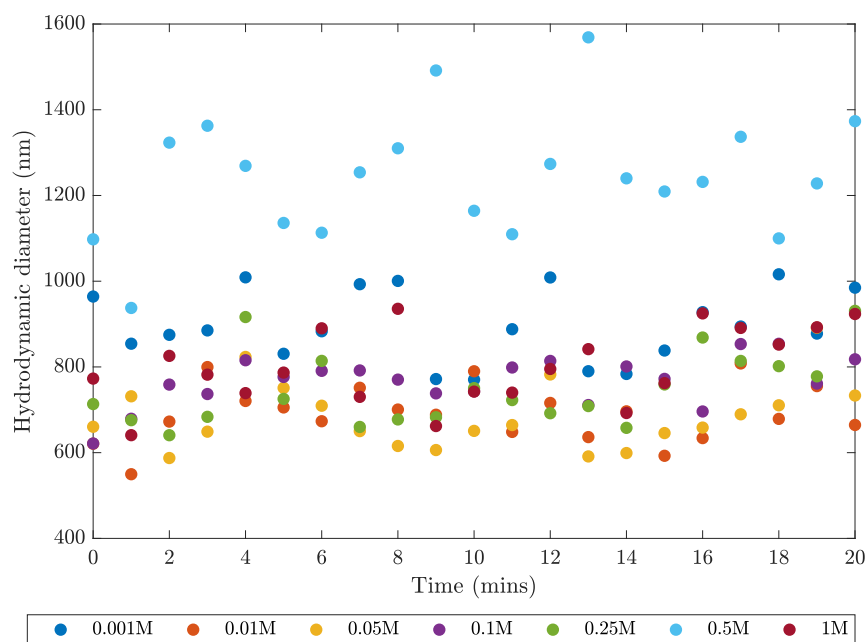


Figure 5.8: Time dependent DLS measurements of Cloisite  $\text{Na}^+$  0.5 wt.% showing the change in hydrodynamic diameter over time under the addition of small amounts of NaCl at different molarities.

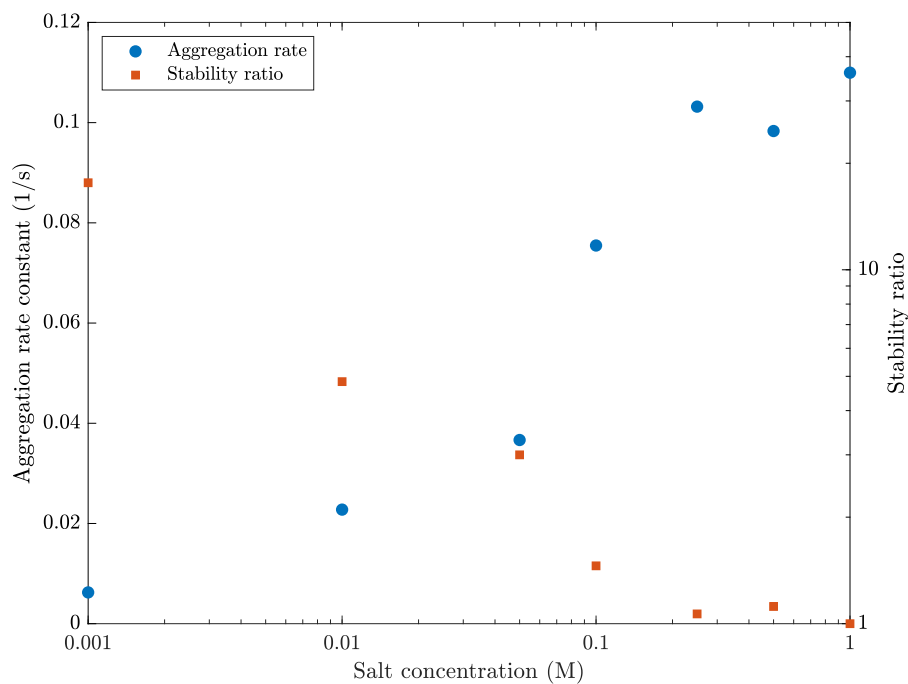


Figure 5.9: The determined aggregation rate ( $k$ ) and stability ratio ( $W$ ) of Cloisite  $\text{Na}^+$  0.5 wt.% colloid as a function of the added NaCl molarity.

surements. However, if we instead view the results using the aggregation rate constant and relative stability ratio, as seen in Fig. 5.9, it is clear there are two distinct regions. The first region is denoted as the slow regime where the addition of the electrolyte is reducing the interaction barrier. This effect continues up to the transition of the fast regime where the interaction barrier is overcome. The transition can be observed through either a saturation in  $k$  or  $W$  saturating to 1. The point at which this transition occurs is known as the critical coagulation concentration (ccc). To determine the value of this point the intersection of the two linear regions is determined. For the Cloisite Na<sup>+</sup> at 0.5 wt.% a ccc value of  $86.28 \pm 71.16$  mM of NaCl was determined. It is worth noting the large error arises due to the aforementioned scatter in the DLS data used for the determination of the rate constants. The meaning of this result is that adding a small amount of NaCl into the colloid can promote particle aggregation and hence gelation, provided the concentration of the NaCl is at least 86 mM. Now the SWN will be considered under the same procedure. The measured DLS results are shown in Fig. 5.10, with the subsequently determined aggregation rates and stability ratio in Fig. 5.11. The DLS data shows a similar pattern to that of the Cloisite Na<sup>+</sup>, the salt has the effect of increasing the rate of the particle interaction, but the effect is not directly clear from the DLS data, again due to the scatter encountered. The transition at the ccc point in the SWN is much more pronounced than in the case of the Cloisite Na<sup>+</sup> meaning a lower ccc point should be expected. Using the process outlined previously the ccc values were determined as  $47.13 \pm 30.69$  mM. The reason for this much smaller value to promote the aggregation in SWN could be attributed to the smaller average particle size, leading to a higher number density and subsequently a higher proportion of particle interactions, leading to faster aggregation and gelation. The lower surface charge of SWN could also play a role in the lower ccc value since the repulsive force between particles will be lower and hence a lower molarity of electrolyte would be required to reduce barrier for the particles to begin to interact.

The values determined for the ccc represent values that can destabilise the clay colloid,

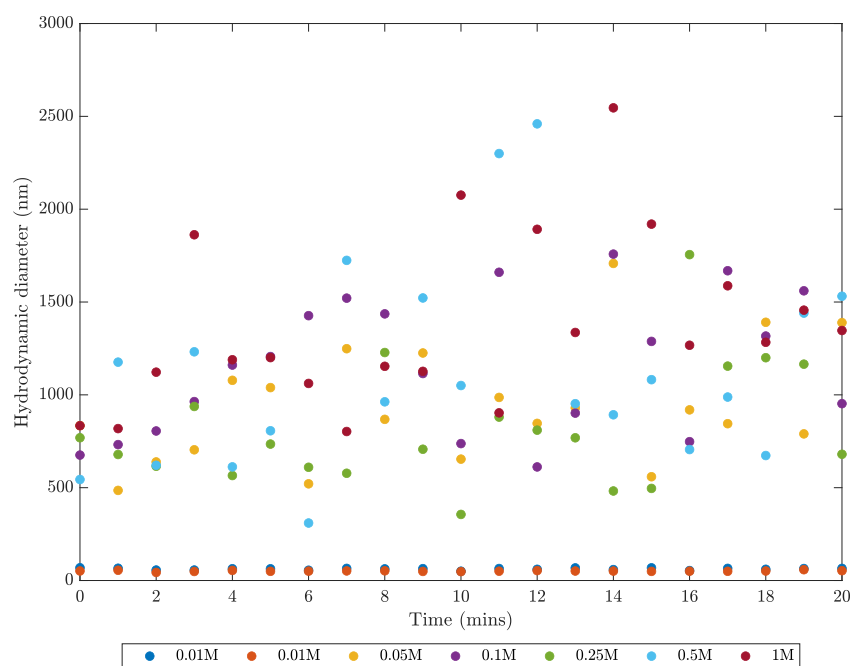


Figure 5.10: Time dependent DLS measurements of SWN 0.5 wt.% showing the change in hydrodynamic diameter over time under the addition of small amounts of NaCl at different molarities.

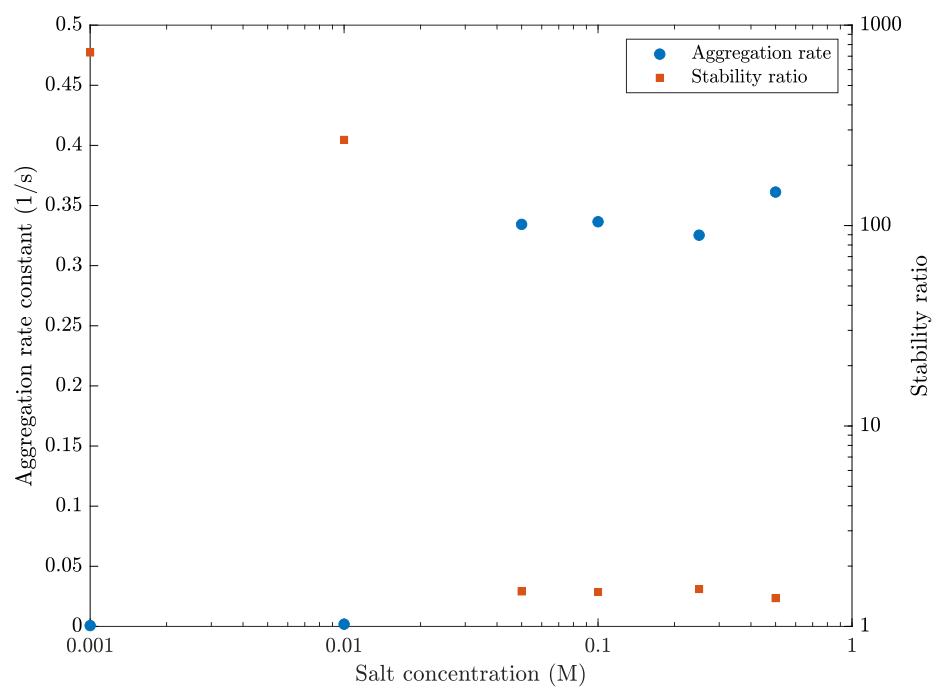


Figure 5.11: The determined aggregation rate ( $k$ ) and stability ratio ( $W$ ) of SWN 0.5 wt.% colloid as a function of the added NaCl molarity.

but there is no control over the state of the colloid, hence we likely have a state of particles, layers and aggregates. Therefore it is useful to understand how the ccc behaves for a more controlled system. In order to explore this, the same experiment was performed but using an exfoliated state colloid, so a system with more control can be explored. Again a colloid of concentration 0.5 wt.% was used for each experiment, and due to the exfoliation process being required, a fresh sample was prepared each time. The DLS measurements for Cloisite Na<sup>+</sup> are shown in Fig. 5.12, and the determined aggregation rates and stability ratios are shown by Fig. 5.13. In comparison to the

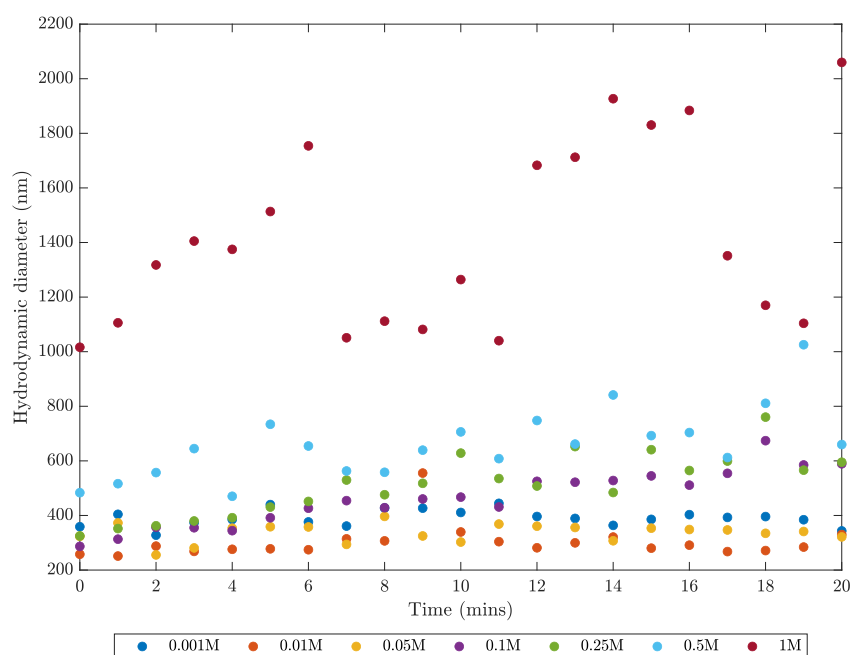


Figure 5.12: Time dependent DLS measurements of exfoliated treated Cloisite Na<sup>+</sup> 0.5 wt.% showing the change in hydrodynamic diameter over time under the addition of small amounts of NaCl at different molarities.

results obtained for the untreated Cloisite Na<sup>+</sup>, the DLS results now show a more clear dependence on the NaCl concentration. For relatively low concentrations (< 0.1 M), the results show that the average particle size remains relatively constant, as the concentration exceeds 0.1 M. The rate of particle interactions begins to increase, however some scatter still remains at higher concentrations suggesting that the particles are interacting more but a mixture of single and aggregated particles is being detected.

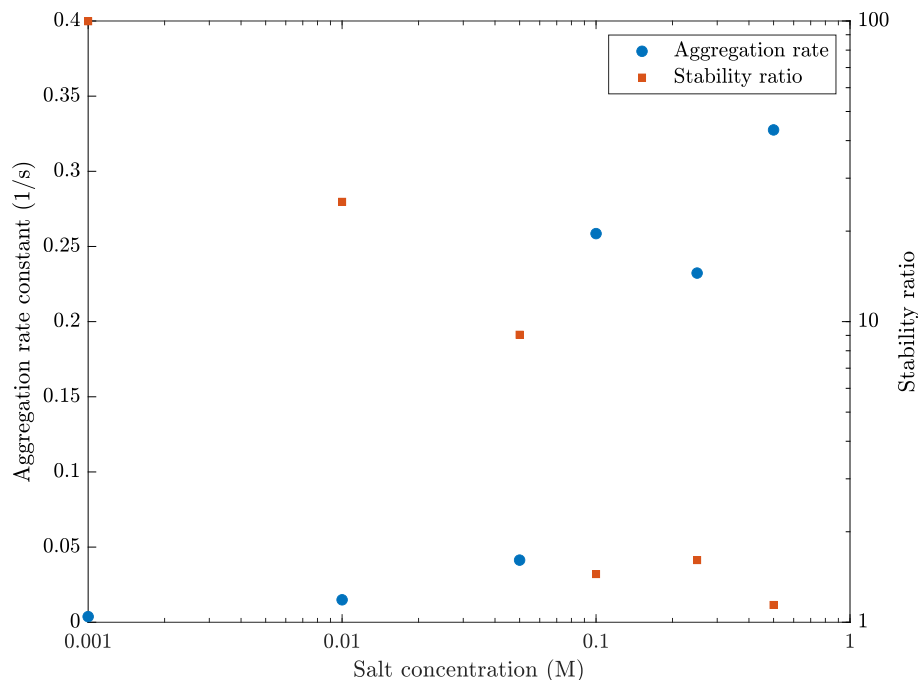


Figure 5.13: The determined aggregation rate ( $k$ ) and stability ratio ( $W$ ) of exfoliation treated Cloisite Na<sup>+</sup> 0.5 wt.% colloid as a function of the added NaCl molarity.

Looking at the aggregation rates there appears to be two regions of aggregation speed, the values do not seem to saturate as in the previous sample. However, when looking at the stability ratio, the distinction between the slow and fast regimes is clear. Therefore the ccc point can be determined by considering the intersection point again yielding a value of,  $84.19 \pm 65.82$  mM. It is interesting that the determined value is close to that determined for the untreated colloid. The possible reason for this similarity could be that the Na and Cl ions within solution are able to penetrate within the clay structure and reduce the repulsive potential, therefore the aggregation effects can be observed for any state of colloid. Although the exfoliated treated colloid has the advantage of providing a more monodisperse and reliable system for the measurement. As before the case of exfoliated SWN will be measured also, and this will also help to determine if the theory of the ions penetrating within the clay structure is reliable. The DLS measurements are shown in Fig. 5.14 and the aggregation rates and stability ratio in Fig. 5.15. Similar to the exfoliated treated Cloisite Na<sup>+</sup>, the exfoliated treated SWN shows similar behaviour in that the exfoliated treated colloid shows a lower degree of

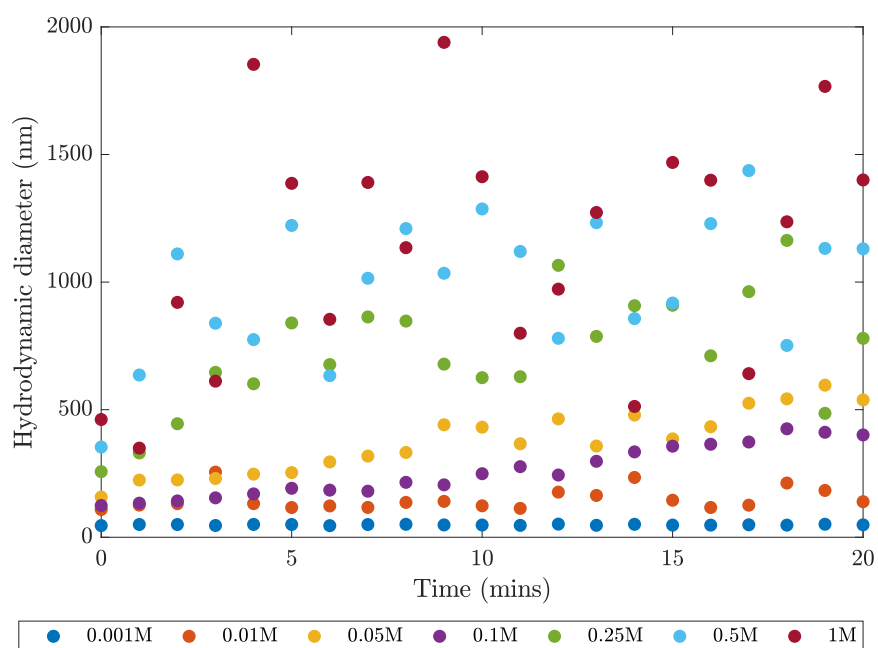


Figure 5.14: Time dependent DLS measurements of exfoliation treated SWN 0.5 wt.% showing the change in hydrodynamic diameter with the addition of small amounts of NaCl at different molarities.

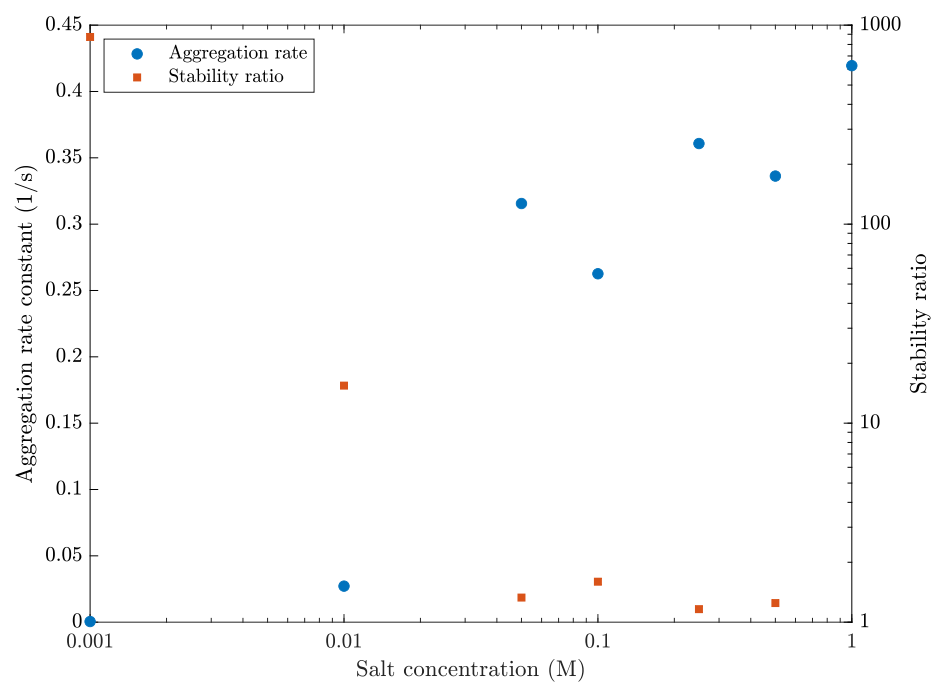


Figure 5.15: The determined aggregation rate ( $k$ ) and stability ratio ( $W$ ) of exfoliation treated SWN 0.5 wt.% colloid as a function of the added NaCl molarity.

scatter compared to the untreated colloid. The effect of the increasing gradient is also clear from this data, with the salt effect becoming significant from around 0.05 M. When looking at the aggregation rates, again the saturation doesn't appear to have been reached but the stability ratio shows the clear distinction between the slow and fast regimes, as before. Calculating the ccc point for the exfoliated SWN a value of  $43.96 \pm 61.42$  mM is obtained. The value obtained for the exfoliated SWN is similar to that of the untreated SWN therefore it is likely the ions are able to penetrate within the clay layers and promoting the aggregation of the particles.

#### 5.3.2 The effect of clay concentration on colloidal stability and particle interactions

Since the stability measurements suggest the stability of the colloids is dependent upon the concentration, it is logical to assume there will be a critical concentration for which the gel formation is a driving factor. Therefore, the particle interactions could be considered for varying clay concentrations, rather than changing additions of salt. The DLS measurements for Cloisite Na<sup>+</sup> are shown in Fig. 5.16. The aggregation rates can again be used to determine the stability ratio for the different clay concentrations and the intersection of the slow and fast regime will not provide a critical clay concentration for gelation. These results are shown in Fig. 5.17. As expected from the zeta potential results for < 3.0 wt.% of Cloisite Na<sup>+</sup>, the average particle size remains relatively stable showing little in terms of particle aggregation. As the concentration exceeds this, the increase in particle size becomes more apparent. From the plot, the aggregation rate appears to follow a more linear trend than that of the salt experiments with a saturation point, since the number density of particles increases at each iteration measured. However, if we use the higher aggregation rates as the  $k_d$  value, a stability ratio can be determined. From this, it is clear there is a transition from a slow non-gelling regime to a faster gelling regime, and this point occurs around 4.0 wt.% for the Cloisite Na<sup>+</sup>. This is further supported by an inability to make measurements for a 5.0 wt.% colloid. The case of the SWN clay can now also be considered with this technique. The DLS

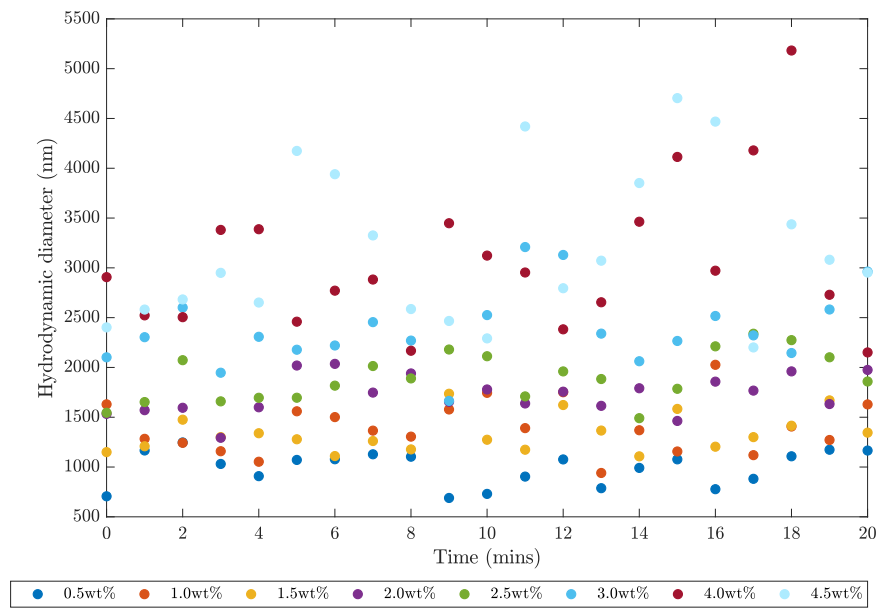


Figure 5.16: Time dependent DLS measurements of Cloisite Na<sup>+</sup> showing the change in hydrodynamic diameter as a function of the clay colloid concentration.

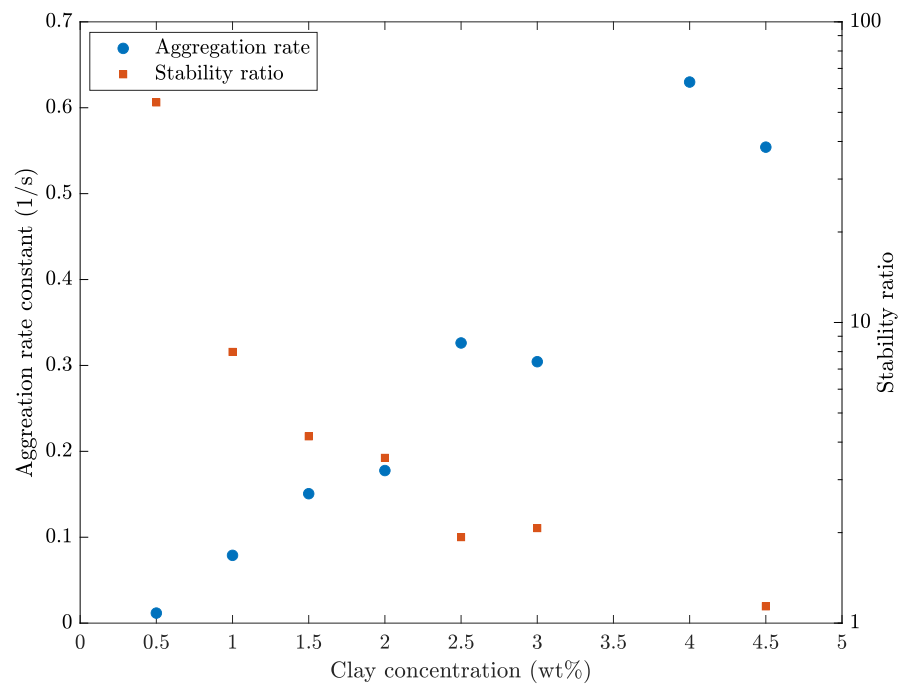


Figure 5.17: The determined aggregation rate ( $k$ ) and stability ratio ( $W$ ) of Cloisite Na<sup>+</sup> colloid as a function of the clay concentration.

measurements for this are shown in Fig. 5.18 and the corresponding aggregation rates and stability ratios in Fig. 5.19. Again, very similar results to that predicted by the

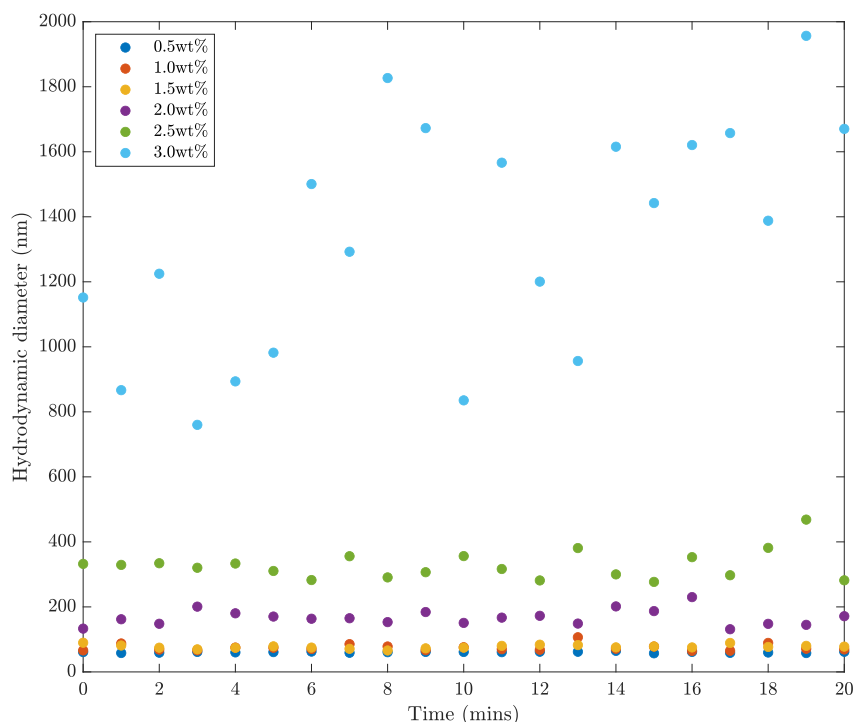


Figure 5.18: Time dependent DLS measurements of SWN showing the change in hydrodynamic diameter as a function of the clay colloid concentration.

zeta potential are observed for the interaction of the particles. The SWN remains stable up until 3.0 wt.% where the aggregation rate increases dramatically and the particle size becomes increasingly scattered, most likely attributed to a mixture of particles and aggregated particles in the system. When plotted as the aggregation rate, there is a very sudden and sharp change as the concentration changes from 2.5 to 3.0 wt.%, thus this shows the stability ratio as a gradual linear decrease to the critical gelation concentration for SWN, which is presented as 3.0 wt.%. Comparing the measurements for the two types of clay, it is clear there is a different mechanism occurring between the two types of clay which could be the cause for the differing level required for gelation to take effect.

As before, the case of the exfoliated colloid can also be considered to determine if

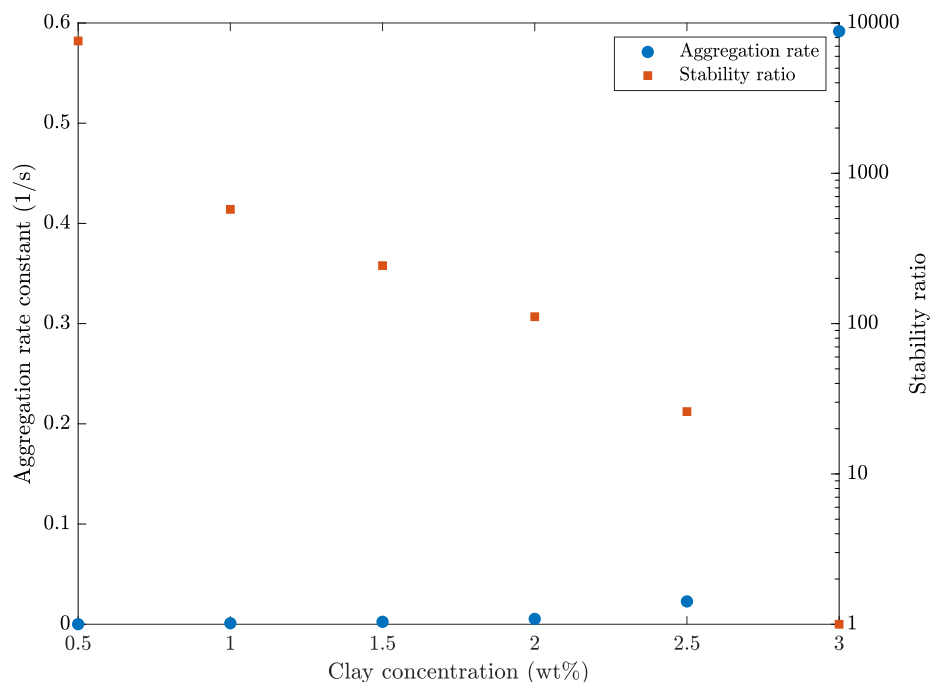


Figure 5.19: The determined aggregation rate ( $k$ ) and stability ratio ( $W$ ) of SWN colloid as a function of the clay concentration.

there is any change in the particle interaction rates. In each case a fresh sample was prepared and exfoliated for a time of twenty minutes before being measured using the DLS. The aggregation measurements are shown in Fig. 5.20 and the aggregation rates and stability ratios in Fig. 5.21 for Cloisite Na<sup>+</sup>. While there appears to be a similar effect to that of the untreated Cloisite Na<sup>+</sup>, with the aggregation rate starting to become apparent around 3.0 wt.%, the interactions are still measurable beyond 4.5 wt.% which was not possible in the untreated colloid. When looking at the aggregation rates, it is clear there are two regions of interactions, one of a slower mechanism, up to 3.0 wt.% and then a faster linearly increasing rate. From the stability ratio there is a slight shift in the critical gelation concentration towards 5.0 wt.%. While this isn't a huge increase between the two different colloids, it does provide some insight into the possible mechanism for gelation, as the exfoliated colloid has a higher number density of particles but a higher concentration for gelation, suggesting the particle interactions are reduced for the higher density of particles within solution. Now we will turn our attention to the exfoliated SWN colloid, the results of which are shown by Fig. 5.22

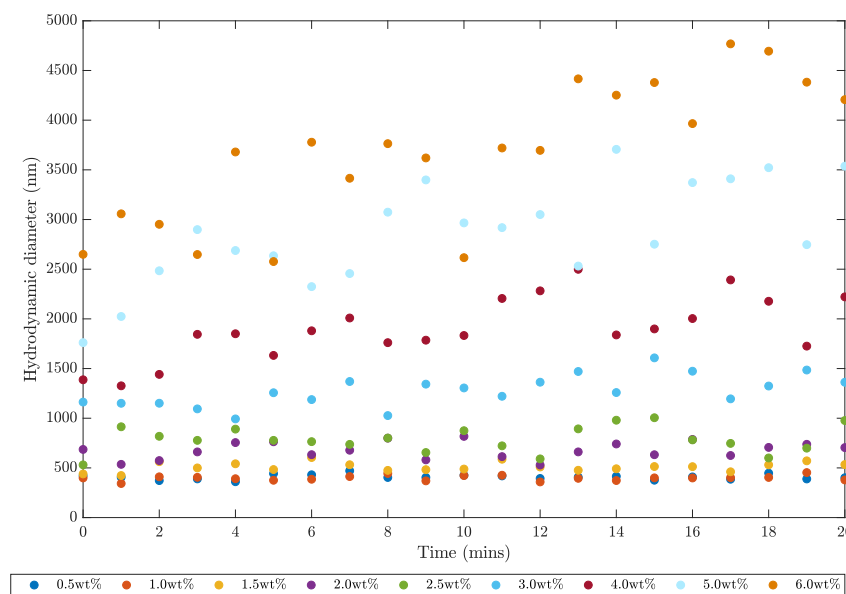


Figure 5.20: Time dependent DLS measurements of exfoliation treated Cloisite Na<sup>+</sup> showing the change in hydrodynamic diameter as a function of the clay colloid concentration.

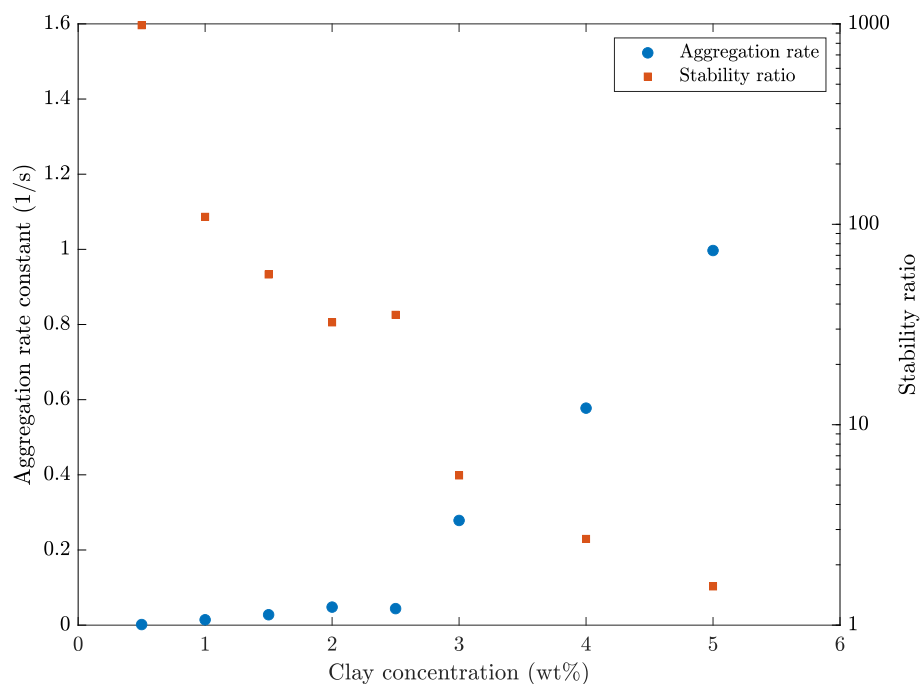


Figure 5.21: The determined aggregation rate ( $k$ ) and stability ratio ( $W$ ) of exfoliation treated Cloisite Na<sup>+</sup> colloid as a function of the clay concentration.

and Fig. 5.23, respectively. Here we can see that a consistent aggregation rate is

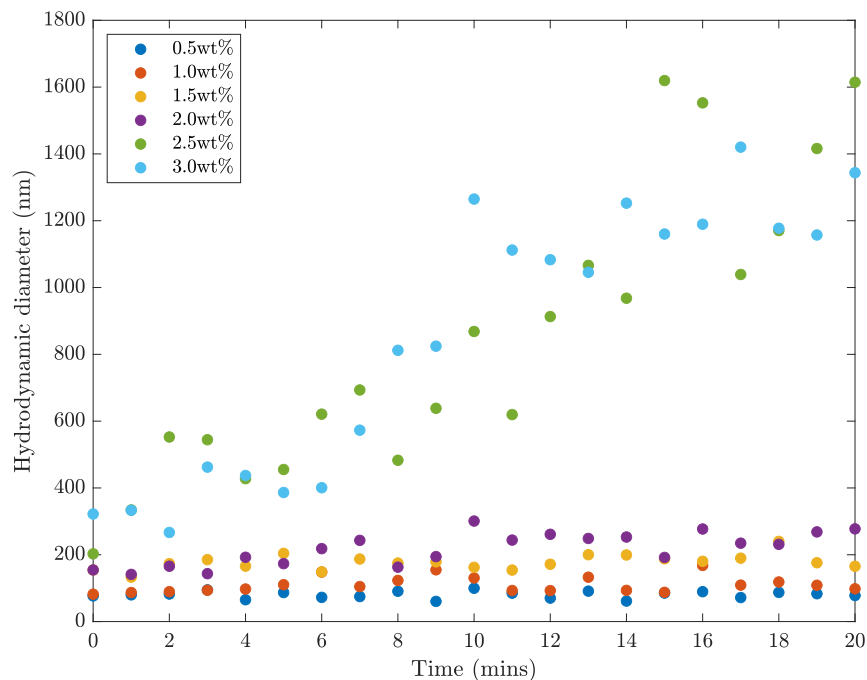


Figure 5.22: Time dependent DLS measurements of exfoliation treated SWN showing the change in hydrodynamic diameter as a function of the clay colloid concentration.

reached when the colloid concentration exceeds 2.0 wt.%, showing a clear onset in the gelation. When looked at in terms of the aggregation rate and stability ratio, this critical gel point is clearly identified from two distinct regions of slow and fast interactions. In comparison to the untreated colloid the concentration for forming a gel is reduced, thus this suggests that the higher number density of the particles within the colloid plays a role within the gelation process. While the DLS results imply a difference in gelation mechanism between the Cloisite Na<sup>+</sup> and SWN, the DLS itself cannot prove the difference between the different interaction mechanisms. Particle-particle interactions may not be the only effect within the colloid leading to the formation of the gel network, as previously thought.

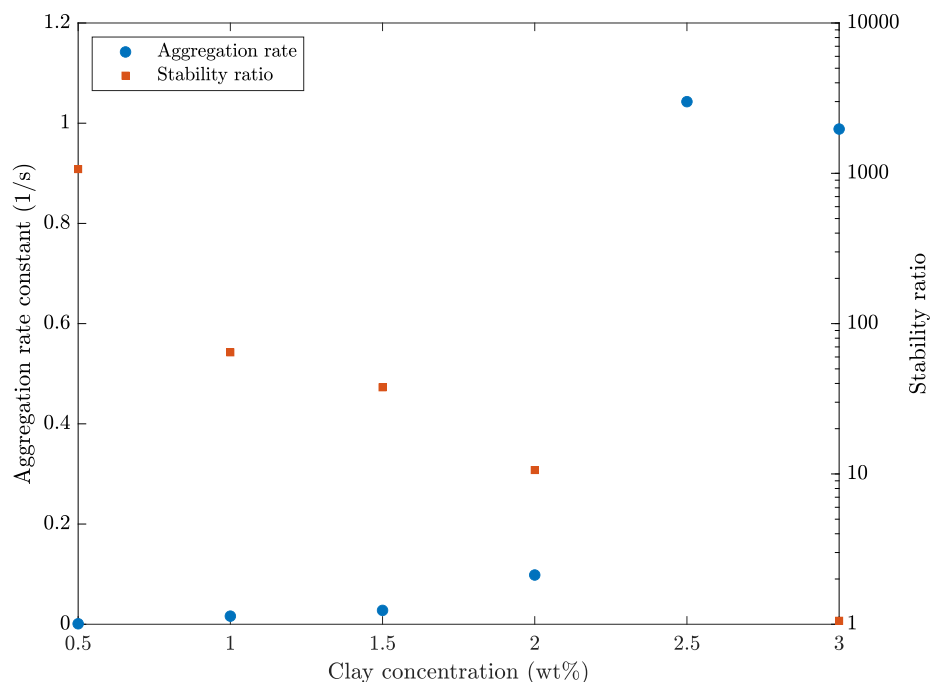


Figure 5.23: The determined aggregation rate ( $k$ ) and stability ratio ( $W$ ) of exfoliation treated SWN colloid as a function of the clay concentration.

## 5.4 Determination of the type of gel formed

The type of gel formed by the clay is important for the coating applications to be developed. If the gel structure is too strong, then it may not be possible to spread to form a continuous layer. Alternatively a continuous layer may be formed but retain its structure after the solvent evaporates, leaving pores. To determine the nature of the gel a simple viscometry test can be performed to observe the gel's behaviour under increased applied force. When sheared, the viscosity of the fluid can either increase or decrease, and these terms are known as rheopectic and thixotropic, respectively. Many gels possess thixotropic natures, which means the viscosity decreases under shearing but recovers once the shear is removed. Thixotropic behaviour is also an indication of a physically cross-linking gel network, as the particles will separate under high shear, but then return to their structural network once the shear is removed. Here, two concentrations of gel are investigated, as the nature of the gel should be independent of the concentration - provided a gel is formed. The nature of the gel has also been inves-

tingated for both the untreated and exfoliated colloids, to determine if this influences the gels' behaviour. The flow curves for Cloisite Na<sup>+</sup> 5 wt.% and SWN 3.0 wt.% are shown in Figures 5.24 and 5.25, and Figures 5.26 and 5.27, for the exfoliated particle gels. In each plot closed symbols represent shearing up and open symbols represent shearing down.

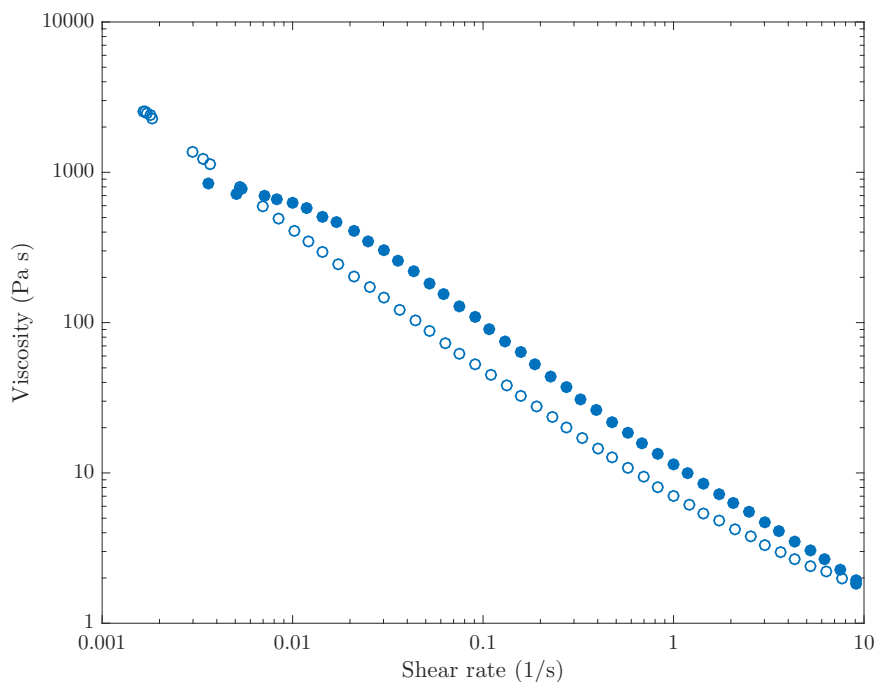


Figure 5.24: Rheological flow curve of gelled Cloisite Na<sup>+</sup> at 5.0 wt.%. Closed symbols represent increasing shear and open symbols represent decreasing shear.

In each case, the upward branch of the flow curves (closed symbols) show that the viscosity decreases with the shear rate, which is a characteristic behaviour of a shear thinning fluid. Returning back from the high shear, the shear thinning behaviour is still observed, however a hysteresis loop is developed. A hysteresis loop is an indication of a thixotropic material. As the increasing begins to breakdown the gel structure, it requires time to rebuild, hence, the viscosity follows a different path. The area of the hysteresis loop can be used to determine the energy consumed during the breakdown process. This provides a clear indication that the gels formed from the clay are thixotropic and most likely physically gelling systems since the structure can be easily broken down, unlike for a chemically cross linked gel.

#### 5.4. Determination of the type of gel formed

---

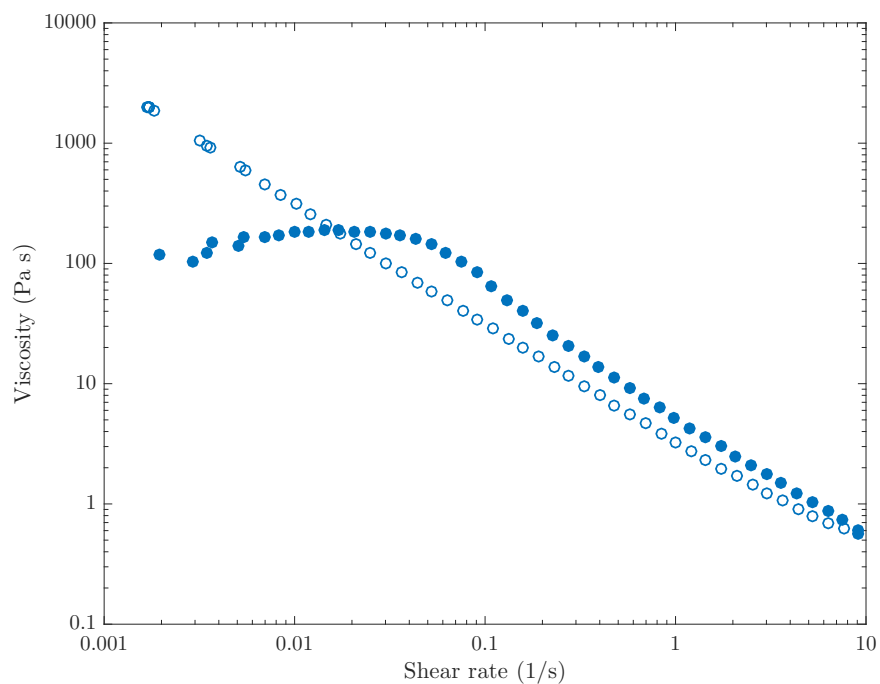


Figure 5.25: Rheological flow curve of gelled SWN at 3.0 wt.%. Closed symbols represent increasing shear and open symbols represent decreasing shear.

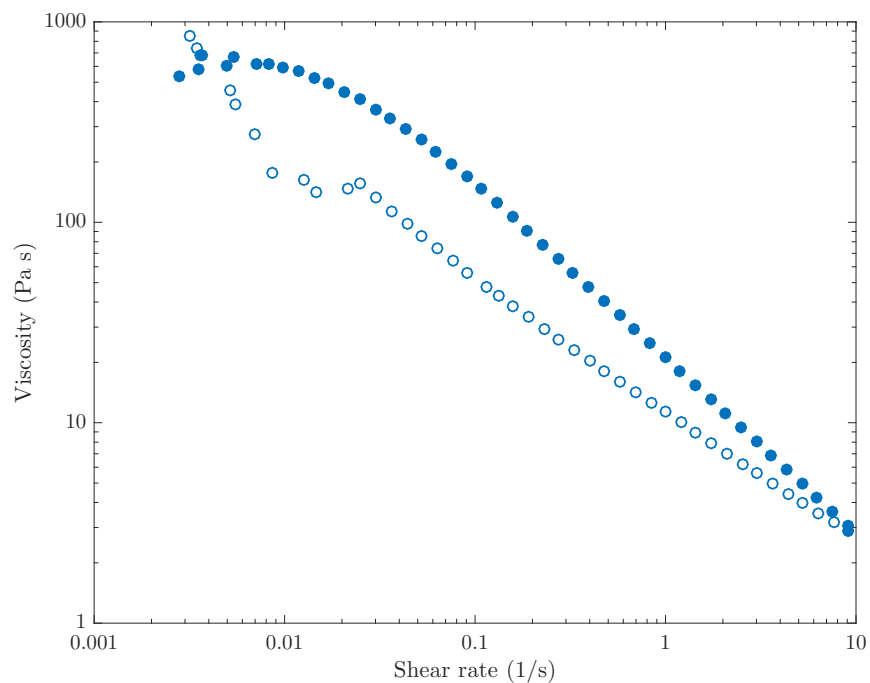


Figure 5.26: Rheological flow curve of exfoliation treated gelled Cloisite Na<sup>+</sup> at 5.0 wt.%. Closed symbols represent increasing shear and open symbols represent decreasing shear.

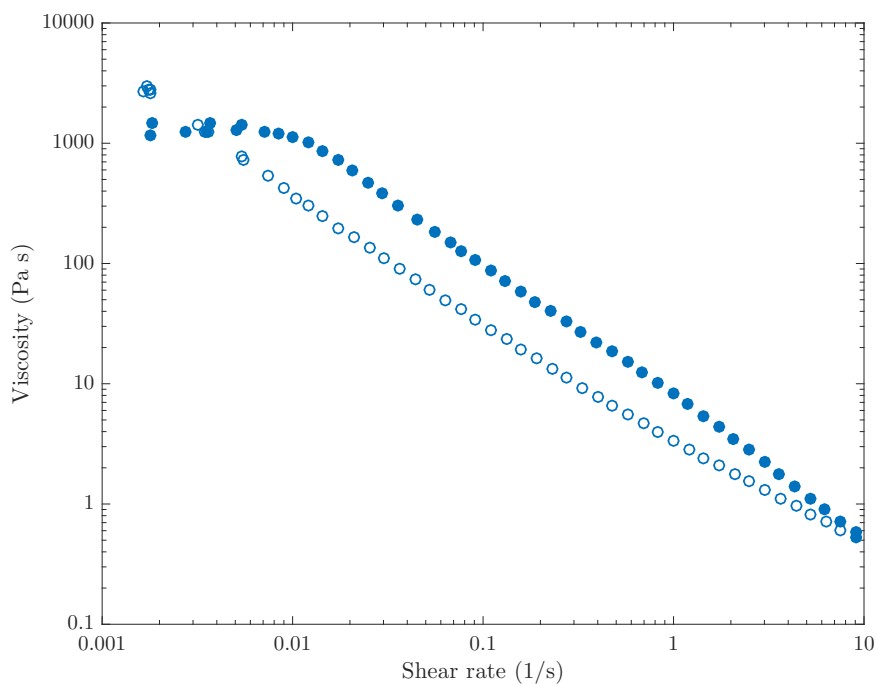


Figure 5.27: Rheological flow curve of exfoliation treated gelled SWN at 3.0 wt.%. Closed symbols represent increasing shear and open symbols represent decreasing shear.

As the gel will be applied as a coating, it is useful to know how it will respond under different shearing conditions. This can be modelled rheologically by using a 3 interval time test (3iTT). In this type of test a sample is sheared at a low rate to simulate the rest conditions, this is then increased to a high shear to simulate the breakdown on the structured network during the coating application. Then the shear is returned to the initial condition to simulate the drying period after application, when the structural regeneration begins. The sample viscosity is usually measured as a function of time during this test. Often the final section of this test is the most important as it reflects the amount of time needed for the sample to recover back to its initial rest conditions. The results of this test are shown in Figures 5.28 and 5.29 for the gels and Figures 5.30 and 5.31 for the exfoliated gels. In each case the gels show structural recovery after the shear is removed, showing they will be suitable for coating applications. For the SWN in both states, this recovery is very rapid, within 30 seconds the viscosity recovers back to the level of the initial state. In Cloisite Na<sup>+</sup> the recovery shows a

#### 5.4. Determination of the type of gel formed

---

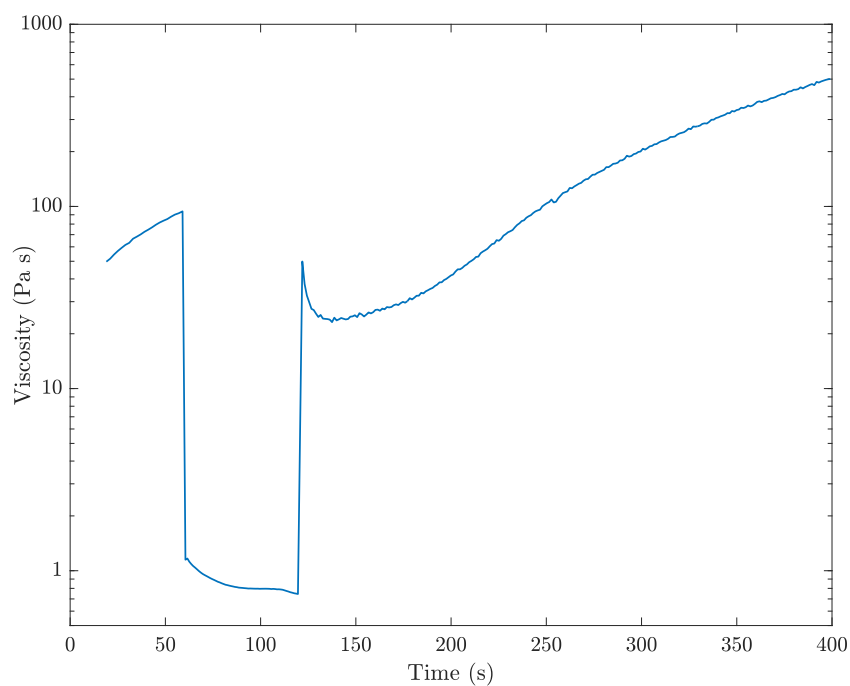


Figure 5.28: 3iTT of Cloisite Na<sup>+</sup> 5 wt.%. The test is performed in three steps: firstly a constant shear of 0.05 for 60 seconds, second a constant shear of 10 for 60 seconds and finally no shear and the recovery observed.

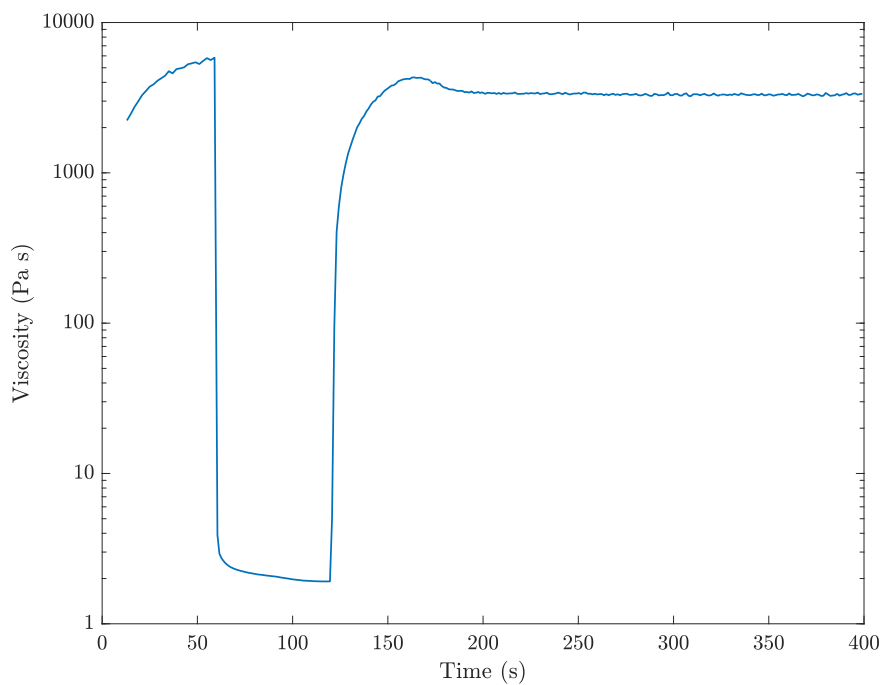


Figure 5.29: 3iTT of SWN 3.0 wt.%. The test is performed in three steps: firstly a constant shear of 0.05 for 60 seconds, second a constant shear of 10 for 60 seconds and finally no shear and the recovery observed.

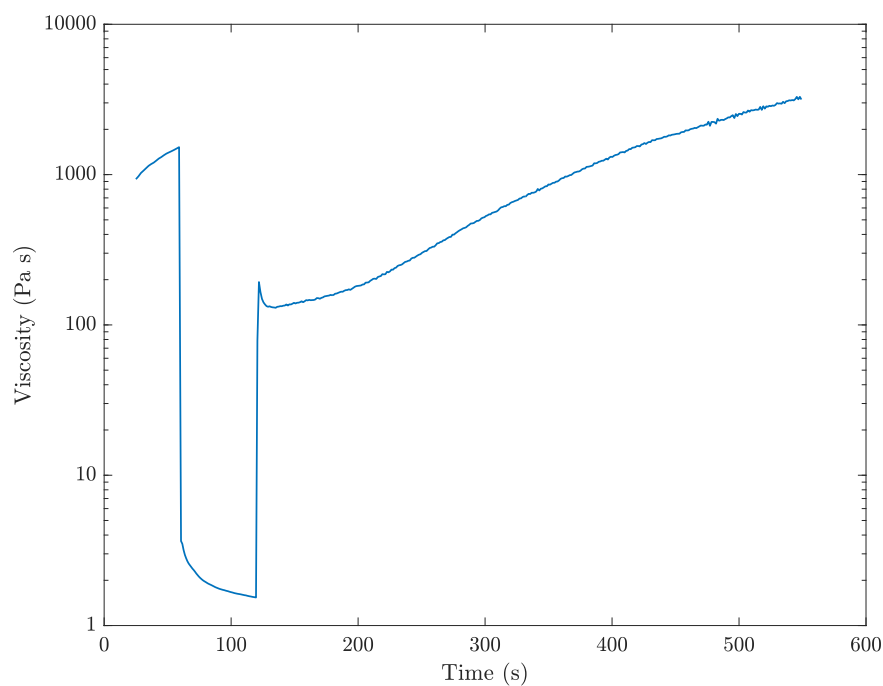


Figure 5.30: 3iTT of exfoliation treated Cloisite Na<sup>+</sup> 5.0 wt.%. The test is performed in three steps: firstly a constant shear of 0.05 for 60 seconds, second a constant shear of 10 for 60 seconds and finally no shear and the recovery observed.

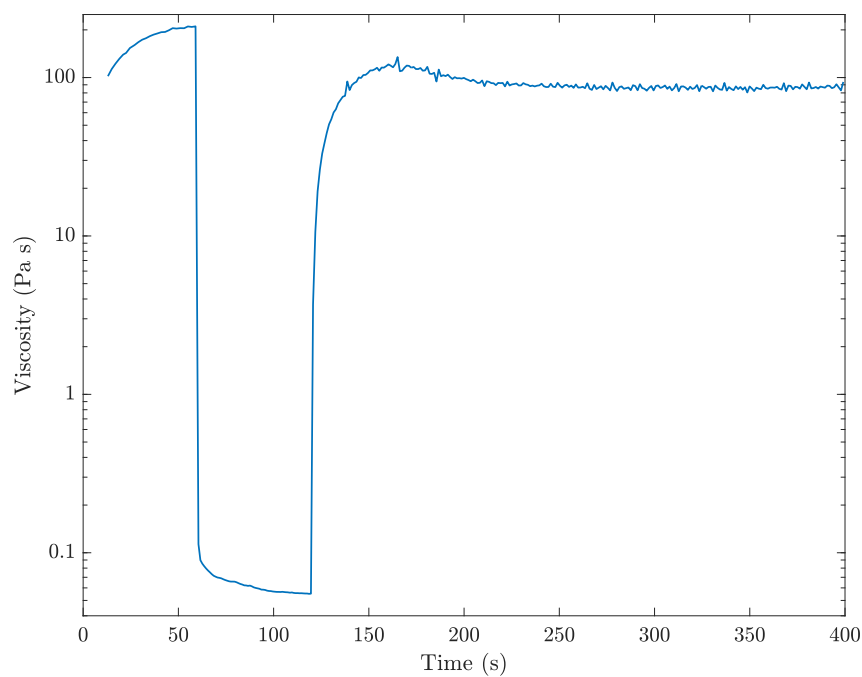


Figure 5.31: 3iTT of SWN 3.0 wt.%. The test is performed in three steps: firstly a constant shear of 0.05 for 60 seconds, second a constant shear of 10 for 60 seconds and finally no shear and the recovery observed.

slightly different behaviour. After the shear is removed, there is a spike in the viscosity, which then decays slightly before the structural recovery begins. This spike could be attributed to the nature of the gel and the mechanism by which the particles interact. In comparison to the SWN the recovery of the Cloisite Na<sup>+</sup> takes place on a much longer time scale (the order of minutes), and this recovery time is increased when the particles are exfoliated. This would suggest the SWN forms more reliable gels for coating applications as it can recover its gelled structure much easier than that of Cloisite Na<sup>+</sup>. The effects of this test can be further confirmed by simple “test tube experiments”. In which samples of the gel are produced, and subjected by an applied shear (by shaking) to disrupt the gel network and the samples monitored to determine if they return to their original structure. Fig. 5.32 shows this effect in the Cloisite Na<sup>+</sup> gel at 5 wt.% and Fig. 5.33 for the SWN 3.0 wt.% gel. What is observed here is similar to that seen in the 3iTT, the SWN much more readily recovers the gel network after being sheared in comparison to the Cloisite Na<sup>+</sup>. The 3iTT and observations also provide confirmation that the gel is a physical cross linking process.

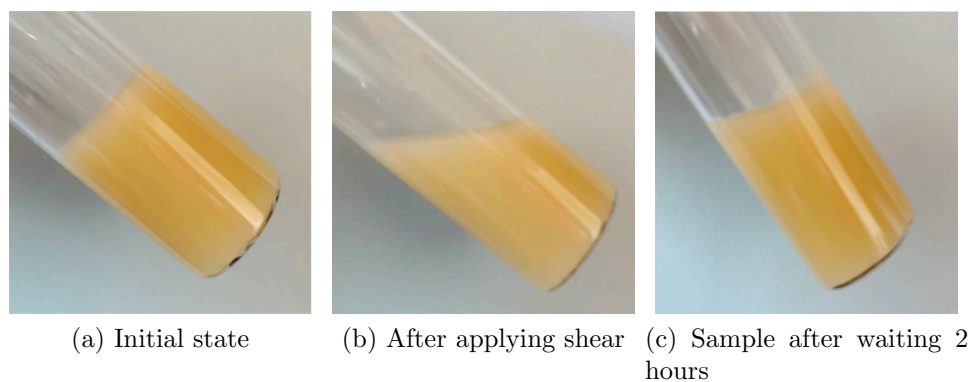


Figure 5.32: Physical observation of the physical cross linking gel network in Cloisite Na<sup>+</sup> at 5.0 wt.%. Sub-figures (a) - (c) show the change in the sample state with shear and subsequent recovery of structure.

## 5.5 Detecting the onset of gelation

Although the particle interactions have been studied already, these only consider a short time scale, which is arguably not long enough to observe any gelation effects

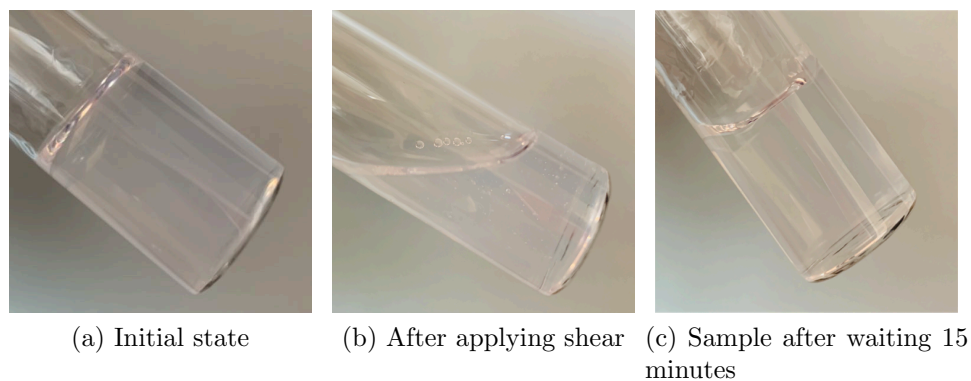


Figure 5.33: Physical observation of the physical cross linking gel network in SWN at 3.0 wt.%. Sub-figures (a) - (c) show the change in the sample state with shear and subsequent recovery of structure.

that may be present within lower concentration colloids. In order to study gelation at longer timescales, oscillation rheology tests can be performed. This allows monitoring of the storage and loss moduli, which represent the elastic and viscous properties of a viscoelastic material. For the monitoring of gelation it is typical to observe both these properties and identify the intersection of the two curves, which can be used to show the time taken for the gel to form. If a gel forms then it is typical that the storage modulus will continue to increase, showing the solid structure forming while the loss modulus saturates showing the loss of the liquid like properties. Due to the physical cross-linking nature of the clay colloids, it is necessary to perform these tests under a small oscillation force, so as not to disrupt the gelation mechanism. To determine an appropriate strain to apply, the linear viscoelastic regime (LVR) was first determined. In the LVR test the strain rate is varied, and for a given region there will be a linear regime, where the strain is independent of the liquid properties. A strain value within this linear region allows monitoring of a sample without disrupting it far from its equilibrium, allowing the gelation to be monitored. The LVRs for Cloisite Na<sup>+</sup> and SWN are shown by Figures 5.34 and 5.35. From this, a strain rate of 0.05 was chosen as this is appropriate for both types of clays linear regions, which is employed in all further oscillation measurements. The gelation effect has been studied across a range of sample concentrations and in the untreated and exfoliated treated samples.

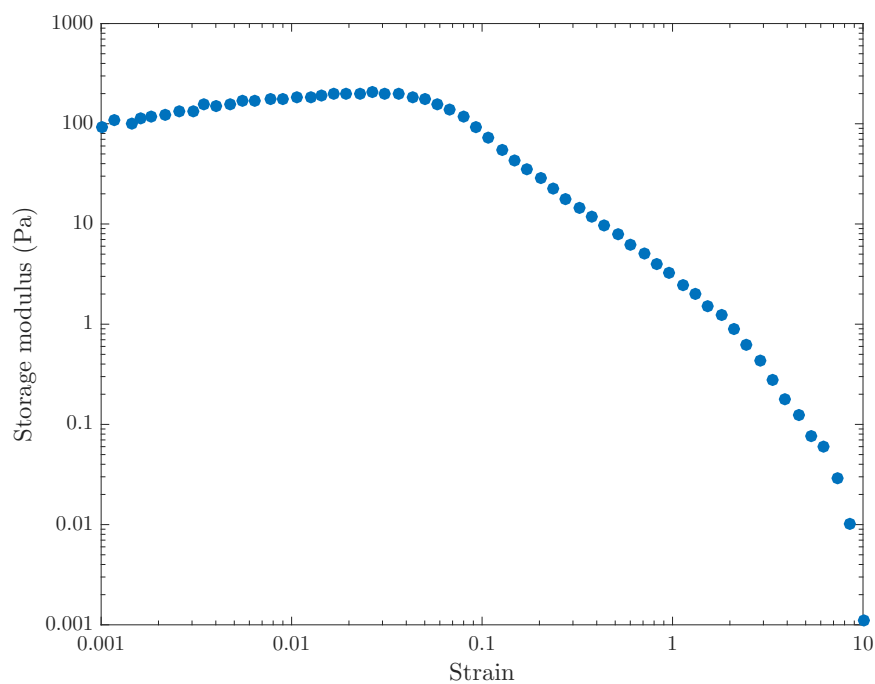


Figure 5.34: Rheological curve for determination of the linear viscoelastic region of Cloisite Na<sup>+</sup> colloid at 5.0 wt.%.

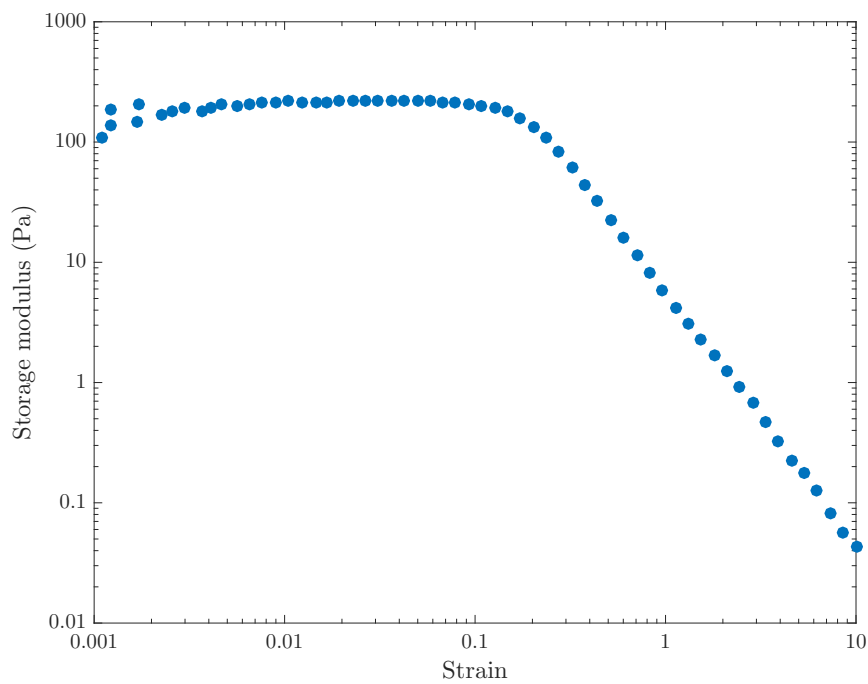


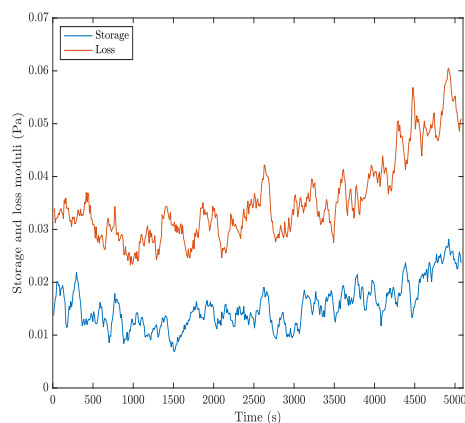
Figure 5.35: Rheological curve for determination of the linear viscoelastic region of SWN colloid at 3.0 wt.%.

### 5.5.1 Gelation in clay particle colloids

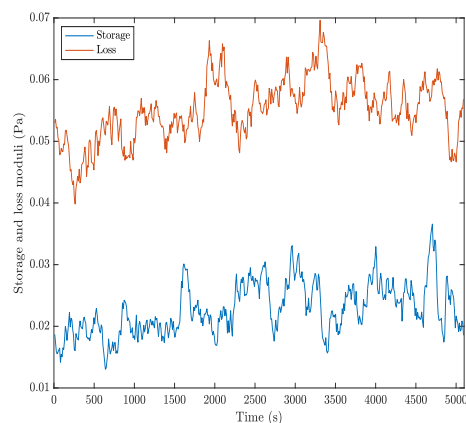
Firstly, the untreated colloids are considered. For each sample concentration the storage and loss moduli were observed to determine if the gelation occurs. The results for Cloisite Na<sup>+</sup> are shown by Fig. 5.36. From these results there is a clear agreement with the results obtained from the DLS. At 2.0 and 3.0 wt.% the loss modulus is the dominant factor showing mostly liquid like properties, and there is also a clear distinction between the storage and loss moduli. The lack of intersection of the two properties is a clear indication that a gel network has not been formed. When the concentration is raised to 4.0 wt.%, initially the loss modulus is the dominant factor which becomes over taken by the storage modulus after around 100 seconds. This cross over shows that the formation of a gel is taking place as the storage modulus continues to increase with time. However, as can be seen from the magnitude of the storage modulus, this is only a weak gel network. At 5.0 wt.% the onset of gelation is significantly reduced in comparison to 4.0 wt.% and the increased magnitude of the storage modulus shows a much stronger gel network is formed. When 6.0 wt.% is observed, there is a large gap between the two moduli even at the start which suggests the gel network is already forming before measurements can begin. In the DLS measurements the critical gel concentration was determined to be at 4.0 wt.% and we can see from the rheology measurements that the onset of the gel network forming is at 4.0 wt.%. The rheology measurements also give explanation as to why the DLS was unable to measure interactions for colloids above 4.5 wt.%. Since the gelation happens on such a rapid scale, the particle aggregates would become too large and outside the size range for which the DLS can accurately measure.

We can now consider the case of SWN. Again varying concentrations of clay have been investigated and these results are shown in Fig. 5.37. Similar to the Cloisite Na<sup>+</sup> for lower concentration colloids, 1.0 and 1.5 wt.%, the two curves exhibit separate moduli curves that do not intersect, showing that the colloid retains mostly liquid like properties and a gel network does not form. At 2.0 wt. % the formation of a weak

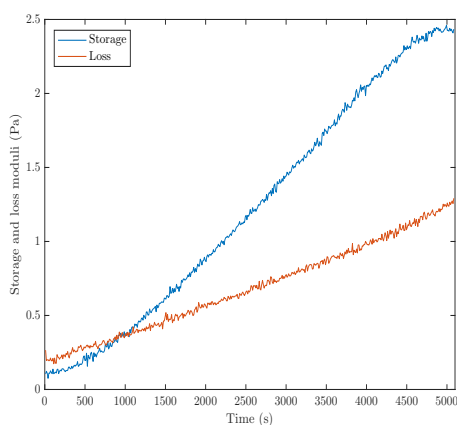
## 5.5. Detecting the onset of gelation



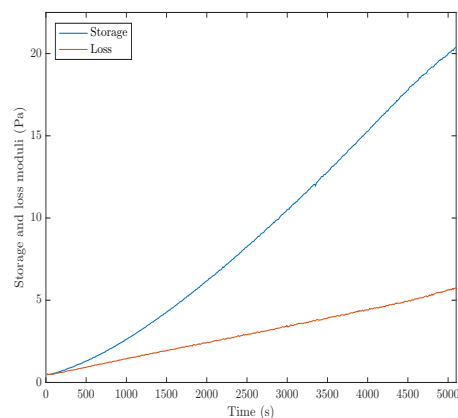
(a) 2.0 wt.%



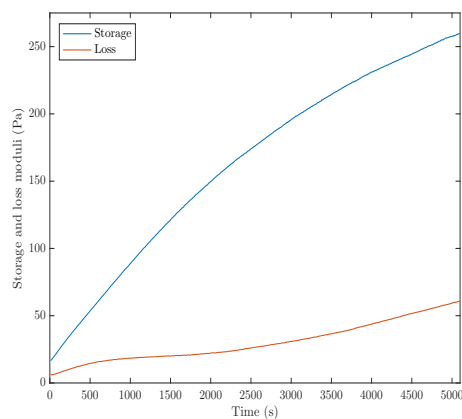
(b) 3.0 wt.%



(c) 4.0 wt.%



(d) 5.0 wt.%



(e) 6.0 wt.%

Figure 5.36: Monitoring of the gelation process in Cloisite Na<sup>+</sup>, through measurement of the rheological properties of storage and loss moduli. Sub-figures (a) - (e) show the results obtained at the given clay concentration. The vertical scale is chosen to best show the trend of the data.

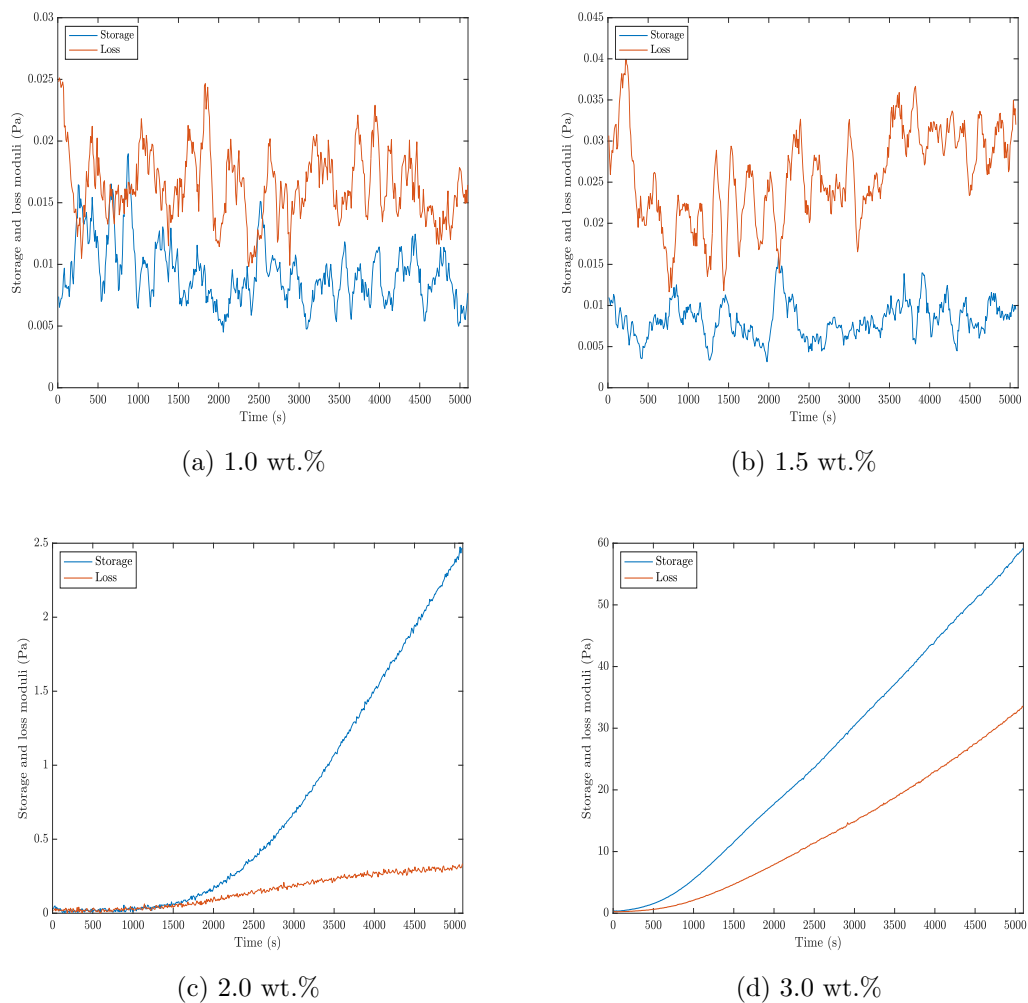


Figure 5.37: Monitoring of the gelation process in SWN, through measurement of the rheological properties of storage and loss moduli. Sub-figures (a) - (d) show the results obtained at the given clay concentration. The vertical scale is chosen to best show the trend of the data.

gel network is observed, with the onset beginning around 1500 seconds. In the DLS measurements the critical gelation concentration was determined to be at 3.0 wt.%. However, this may simply be because the onset of the gelation is beyond the time scale measured in the DLS. At 3.0 wt.% an early onset of gelation is observed, hence this appearing as the critical concentration.

Comparing the results for the two types of clay, it is clear there is a difference in the concentration at which both are able to form a gel, with Cloisite Na<sup>+</sup> being double that of SWN. The possible reasons behind this could be related to the particle aspect ratios, surface charge or interaction mechanism. SWN has both a smaller aspect ratio and lower surface charge in comparison to Cloisite Na<sup>+</sup>, and forms the gel at lower concentrations. However, it is necessary to determine how the particles interact to determine the dominant factor in the gel formation process.

### 5.5.2 Gelation in exfoliated clay particle colloids

We will now consider the gelation effects within exfoliated clay colloids. For a direct comparison of the effect of exfoliation on the gelling ability, the same concentrations of colloids were tested. Firstly, the results from the Cloisite Na<sup>+</sup> will be discussed and are shown by Fig. 5.38. For the exfoliated Cloisite Na<sup>+</sup> similar results are observed for that of the untreated colloid. For concentrations below 4.0 wt.% the two moduli show separate distinct curves with the loss modulus being dominant. The onset of gelation within 4.0 wt.% occurs on a similar time scale to that of the untreated colloid. However, for 5.0 and 6.0 wt.% the onset of gelation takes a longer period of time than that of the untreated colloid. This aligns with the results seen in the DLS where the critical gel concentration was reduced for the exfoliated colloid. The reduction in the ability to gel when the layers are exfoliated suggests that the particle interactions are not a dominant factor in the gel formation for this clay, as the higher number density of particles does not lead to shorter gelation times. It is necessary therefore to understand how the particles interact to confirm the reasons for the difference in gelation between

## 5.5. Detecting the onset of gelation

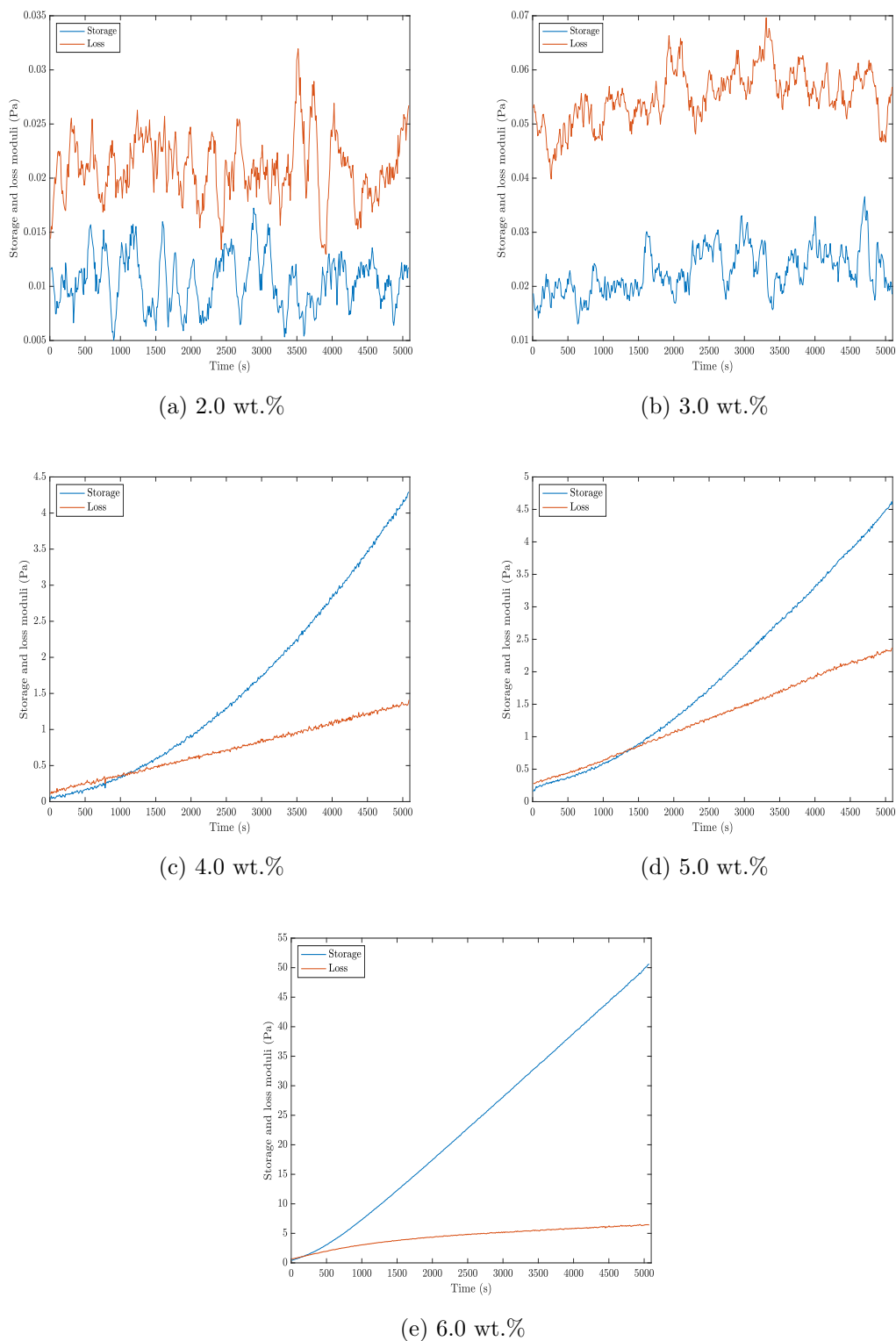


Figure 5.38: Monitoring of the gelation process in exfoliated treated Cloisite Na<sup>+</sup>, through measurement of the rheological properties of storage and loss moduli. Sub-figures (a) - (e) show the results obtained at the given clay concentration. The vertical scale is chosen to best show the trend of the data.

untreated and exfoliated colloids. We can now turn our attention to the case of SWN when in the exfoliated state. These results are shown in Fig. 5.39. Comparing the

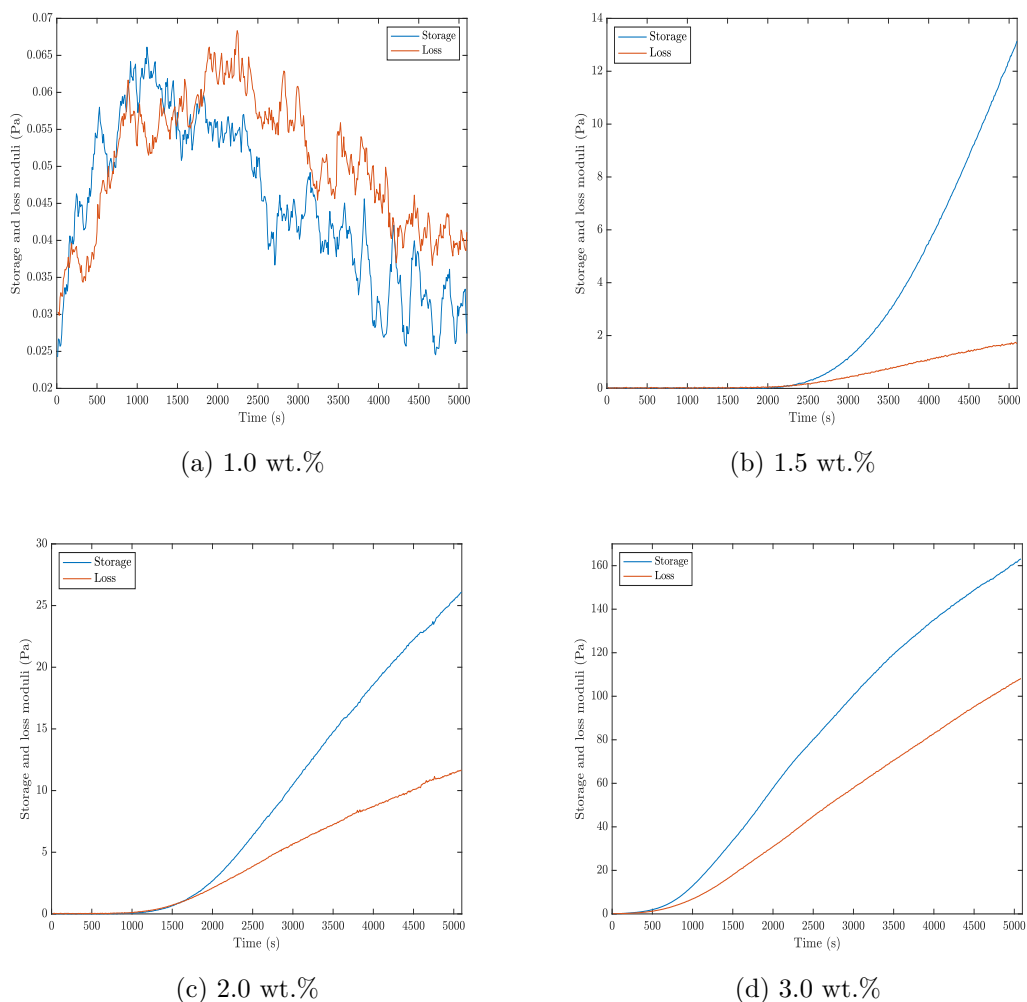


Figure 5.39: Monitoring of the gelation process in exfoliated treated SWN, through measurement of the rheological properties of storage and loss moduli. Sub-figures (a) - (d) show the results obtained at the given clay concentration. The vertical scale is chosen to best show the trend of the data.

exfoliated SWN to the untreated SWN again a significant difference is observed. Here the gelation begins at 1.5 wt.%, which is much lower than the 2.5 wt.% measured from the DLS. The reason for this difference can simply be attributed to the gel time which is beyond the scale during the DLS measurements, hence it not being detected. It is interesting to see the effect the exfoliation has on the gel formation, since even at the low concentration of 1.5 wt.% the magnitude of the storage modulus is greater than that observed for 2.0 wt.% of untreated colloid. Thus for this type of clay it is likely

the particles play a more significant role in the gel formation process, as shown by the significant decrease in gel forming concentration with the larger number density of particles within the colloid.

## 5.6 The role of particle interactions in the gelation process

Although the gelation has been explored by observing the colloidal nature and the concentration dependence for forming a gel, the actual mechanism behind the physical cross-linking process has not been determined. This interaction is theorised to be interactions between individual clay particles such as hydrogen bond formation. However, analytical techniques to probe this, such as proton NMR are unsuccessful in observing the interaction due to the thixotropic nature of the gel and the sample under going motion when tested. Therefore, in order to observe interactive forces within the colloid as it undergoes gelation, a technique is required that can both observe the phenomena and not disrupt it as it occurs. To achieve this, Neutron Compton Scattering (NCS) techniques were employed. NCS allows the properties of the atomic species present to be probed, and also does not disrupt the gelation process as it occurs. In this work NCS was performed using the VESUVIO spectrometer, at the ISIS facility in Rutherford Appleton Laboratories. VESUVIO is an inverted-geometry neutron spectrometer that is designed to measure nuclear momenta distributions with epi-thermal (eV energy) neutrons. Using VESUVIO, the momenta distributions of the protons within the systems have been explored, and the interactions characterised. In these experiments both types of clay were investigated in the solid state and in the exfoliated colloidal state at concentrations of 3.0 wt.%. The raw time-of-flight (ToF) data is first presented in Fig. 5.40, which is used to determine the momenta space distributions. The counts are normalised for ease of comparison. The raw ToF data can be used to determine the momenta distribution for the proton environments within each of the samples, and a measure of the binding energy can be evaluated from the fit of the data. The solid

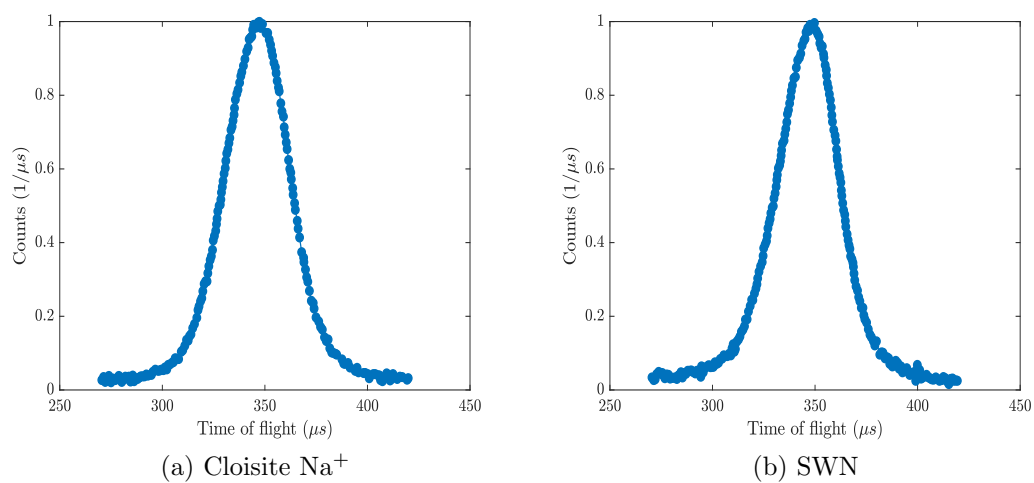


Figure 5.40: VESUVIO measured time-of-flight data for scattered neutrons from solid state clay samples. Sub-figure (a) and (b) show the results for Cloisite Na<sup>+</sup> and SWN, respectively.

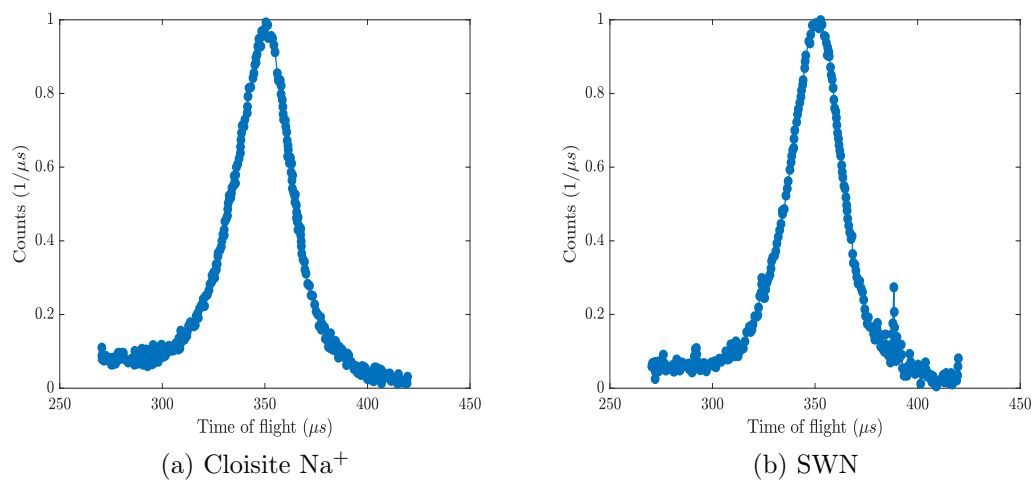


Figure 5.41: VESUVIO measured time-of-flight data for scattered neutrons from 3.0 wt.% colloidal clay samples. Sub-figure (a) and (b) show the results for Cloisite Na<sup>+</sup> and SWN, respectively.

sample evaluation is shown in Fig. 5.42 and the colloidal samples in Fig. 5.43. The

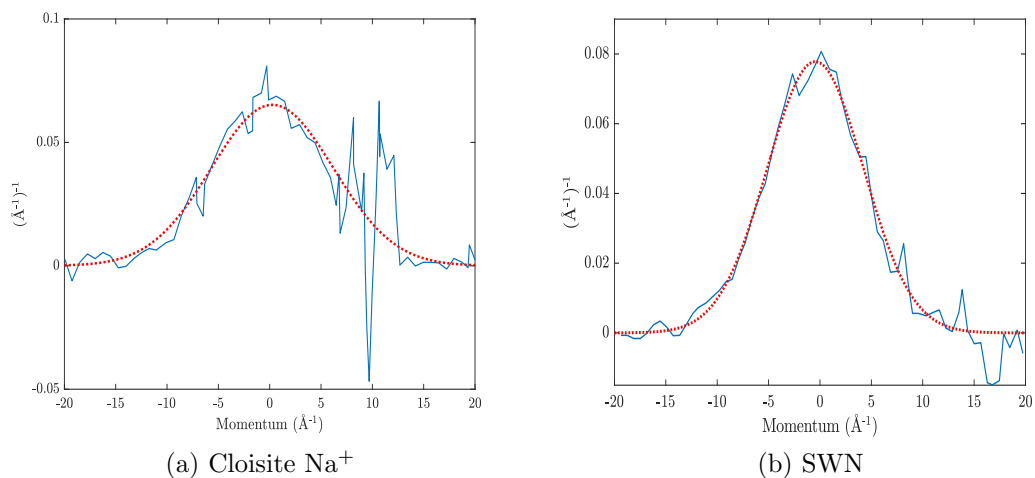


Figure 5.42: Analysed momenta distributions from the solid clay ToF data, the computed data is shown in blue with the best fit of the distribution given in red. Sub-figure (a) and (b) show the results for Cloisite  $\text{Na}^+$  and SWN, respectively.

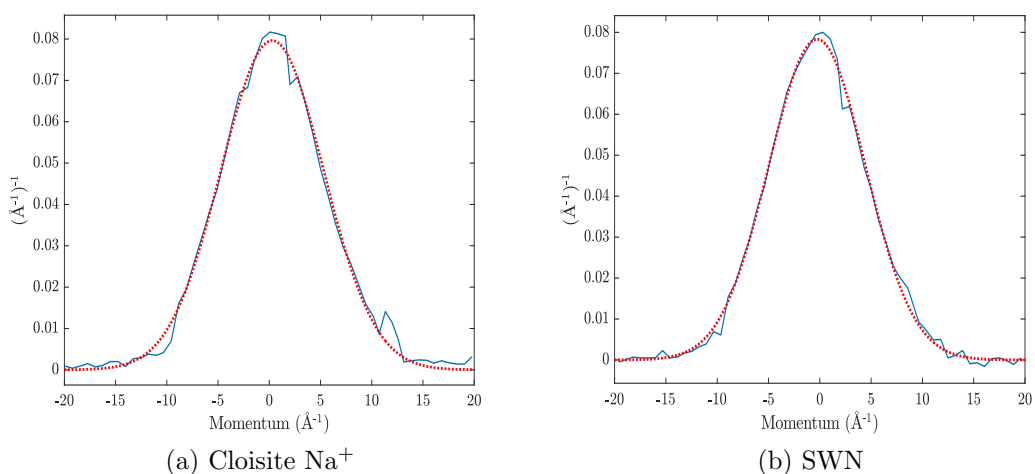


Figure 5.43: Analysed momenta distributions from the colloidal clay ToF data, the computed data is shown in blue with the best fit of the distribution given in red. Sub-figure (a) and (b) show the results for Cloisite  $\text{Na}^+$  and SWN, respectively.

hydrogen binding energy determined from the momenta distributions are presented within Table 5.1. In each case the binding of hydrogen is increased compared to that of pure water alone, this is more pronounced in Cloisite  $\text{Na}^+$  than SWN also. In the case of the Cloisite  $\text{Na}^+$  hydrating the sample causes the binding of the H to grow. We note there is a pronounced anisotropy within the hydrated Cloisite  $\text{Na}^+$ , in comparison to the dry case where the anisotropy vanishes. This may be due to the fact that in

Table 5.1: Evaluated hydrogen atom binding energy for the solid and colloidal clay samples. The binding of water is presented as a reference measurement.

Pure Water	Solid Cloisite Na <sup>+</sup>	3.0 wt.% Cloisite Na <sup>+</sup>	Solid SWN	3.0 wt.% SWN
$4.76 \pm 0.04$	$5.00 \pm 0.30$	$5.35 \pm 0.08$	$4.92 \pm 0.12$	$4.97 \pm 0.05$

the solid sample there are only protons within the structural OH group, where as in the liquid sample there are both the aforementioned OH groups and also H<sub>2</sub>O protons, where the latter is anisotropic. Whereas in the case of SWN going from the solid to the hydrated sample the binding only increases slightly, therefore we can conclude that the H is less bound in the SWN. From this we can determine that the SWN clay shows little interaction with the surrounding water molecules, which can be attributed to the self cross linking behaviour of the clay particles. Where as in the Cloisite Na<sup>+</sup>, the particles form strong hydrogen bonds with the surrounding water molecules, which causes them to structurally deform. This difference in behaviour could be attributed to the differing aspect ratio of the clays, as the smaller aspect ratio clay will have a higher particle number density for the same given concentration, and hence would have a reduced defusing path length for collisions. This would lead to a promotion of the H bond formation between clay particles, rather than between clay particles and water molecules. This result therefore provides strong evidence for the difference in the ability for these types of clay to form a physically cross-linked gel network.

## 5.7 Summary

This Chapter has attempted to explore both the colloidal nature and gelation mechanism of the two types of commercial nanoclay. The understandings from this Chapter lead directly into the work presented in Chapter 6, where the application of these developed gels are used as coatings. The key results of this Chapter are:

- The use of liquid shear exfoliation (LSE) has provided a simple and effective method by which single clay layers can be produced, with only water as a solvent preventing harmful environmental effects as can occur with other layer exfolia-

tion processes. Using LSE, controlled size range colloids can be produced, and also remove the effect of particle aggregates, leading to more uniform colloids to produce gel.

- Threshold concentrations are determined for the gelation to occur within the clay colloids. Agreement is observed between both early stage measurements using DLS and late stage measurements using rheology. We also note a significant difference in this threshold concentration between un-treated and exfoliation treated colloids.
- Neutron scattering experiments provide direct evidence of the physical interaction mechanism for the particles to form a gel network. Herein the measurements provide evidence that process is dominated by hydrogen bonding, but the SWN favours bonding with itself while the Cloisite Na<sup>+</sup> favours bonding to surrounding water molecules. Hence showing the reason for the different threshold point for gelation to occur.

The aim of this Chapter was to explore the colloidal nature and gelling properties of the two types of clay. Within the Chapter the stability and interactions of the colloid have been explored, and the mechanism behind the different gelling behaviour shown. The LSE allows a high degree of control of the state of the particles leading to the formation of the gel, and this will allow control over the continuous layer that is to be developed.

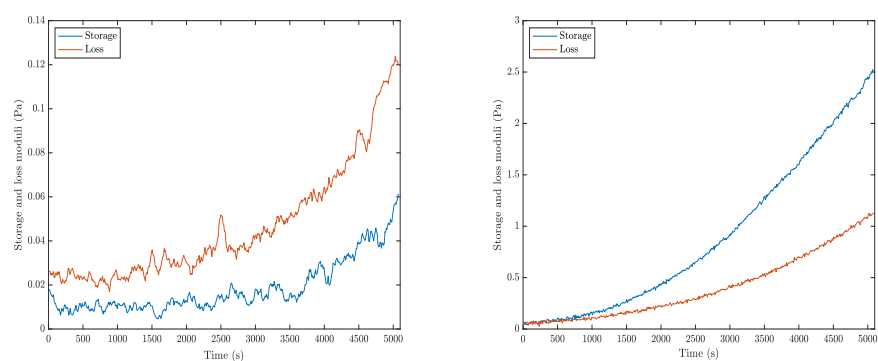
## **Chapter 6**

# **Development of novel nanodielectric materials**

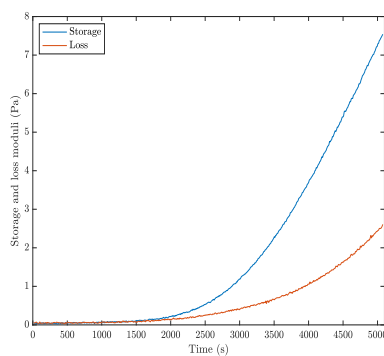
In this Chapter, the methods by which the developed clay gels can be applied to conventionally used polymer surfaces is investigated. This will explore the processes needed to develop the novel material and evaluate the key properties of the material.

### 6.1 Gel formation in mixed clay systems

In the previous Chapter, the gelation of clay colloids was studied. From this it was seen that the minimum concentration to produce a gel varied significantly between the two clays. While a simple solution would be to increase the concentration of the lower concentration gel forming SWN, this leads to a very strong gel forming within a few seconds, which makes it unsuitable for the exfoliation process. While the gels could be used at different clay wt.%, it is preferential to use the same concentration to allow more direct comparisons to be made. As seen Cloisite Na<sup>+</sup> at 3.0 wt.% is not suitable alone to form a gelled network. Therefore, mixed clay gels were investigated to see if a gel primarily consisting of Cloisite Na<sup>+</sup> could be formed at a maximum of 3.0 wt.%. Here combinations of 0.5 wt.%, 1.0 wt.% and 1.5 wt.% of SWN were incorporated with 2.5 wt.%, 2.0 wt.% and 1.5 wt.% of Cloisite Na<sup>+</sup>, respectively, to give a colloid of total clay concentration 3.0 wt.%. As before these colloids were monitored by oscillation rheology to monitor the gel forming process. Using the process outlined in the previous Chapter, approximately 1.25 ml of the prepared colloid was placed onto the bottom plate, and the geometry brought down to the experimental gap height, with the measurement performed at 25°C. The results of these tests are presented within Fig. 6.1. As can be seen from the Figure the inclusion of at least 1.0 wt.% of SWN into the Cloisite Na<sup>+</sup> can lead to formation of a gelled network. Unlike that of Cloisite Na<sup>+</sup> 3.0 wt.% alone as seen in Fig. 5.36, where a gel network was unable to form. It is also necessary to consider the exfoliation treated colloids, thus the same samples were produced, and then subjected to the exfoliation treatment for 20 minutes prior to measurements being performed. The exfoliation treated colloid was then measured using oscillation rheology as described above. These results are shown within Fig. 6.2. As in the non treated samples it is clear that the addition of at least 1.0 wt.% of



(a) Cloisite Na<sup>+</sup> with SWN 0.5 wt.%      (b) Cloisite Na<sup>+</sup> with SWN 1.0 wt.%



(c) Cloisite Na<sup>+</sup> with SWN 1.5 wt.%

Figure 6.1: Monitoring of the gel formation process in mixed Cloisite Na<sup>+</sup> and SWN colloids, through the use of oscillatory rheology. Sub-figures (a) - (c) show the differing amount of SWN added to the mix. The vertical scale is chosen to best show the trend of the data.

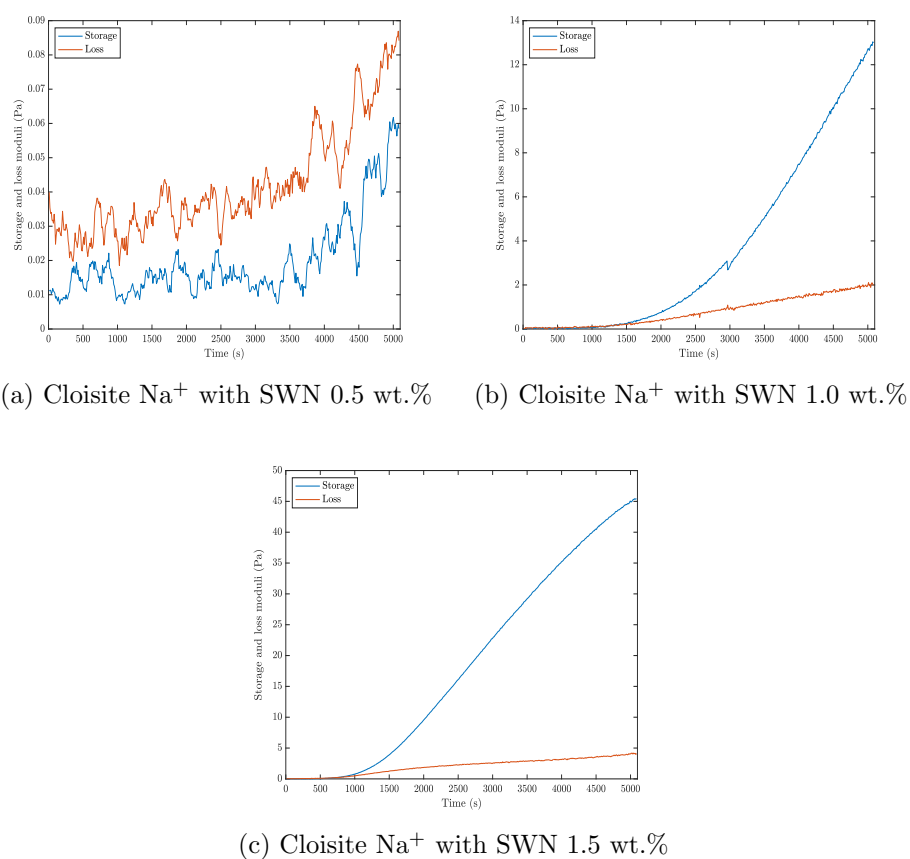


Figure 6.2: Monitoring of the gel formation process in exfoliated treated mixed Cloisite Na<sup>+</sup> and SWN colloids, through the use of oscillatory rheology. Sub-figures (a) - (c) show the differing amount of SWN added to the mix. The vertical scale is chosen to best show the trend of the data.

SWN can lead to a gel network forming in the colloid. Also as seen in the colloids of untreated clay, the exfoliated treated samples form much stronger networks as shown by the increased magnitude of the storage modulus. Therefore, the two gels selected for the coating process are formulations of Cloisite Na<sup>+</sup> 2.0 wt.% with SWN 1.0 wt.% and SWN 3.0 wt.%.

## 6.2 Preparing the polymeric film for coating

Polymeric materials are often used in insulation systems due to their typically high electrical resistance. However, many polymeric materials are not known for their mechanical strengths, hence the introduction of micro and nanocomposite technology. In this work polymeric films of low density polyethylene (LDPE) were selected for the composite material due to both the use of LDPE within current electrical insulation products but also to tackle the challenges associated with producing PE composites [173]. This polymer has a reported electrical breakdown strength of 79 kV/mm [174], which is slightly larger than that of the similar high density polyethylene (HDPE). It is thought that this occurs due to the lower crystallinity of LDPE, providing a greater resistance to electrical breakdown due to the effect of crystallinity on dielectric behaviour [175]. As shown in Chapter 5, the developed gels are produced from 3.0 wt.% solid content and 97.0 wt.% water content, due to the hydrophobic nature of many polymers, this may hinder the production of a water based gel coating. To determine how well the gel coats onto the LDPE surface, a sample of gel was spread onto an LDPE substrate and observed, as shown by Fig. 6.3. As can be seen from Fig. 6.3, the coated gel forms discrete drops or regions of gel on the polymer surface, showing that the LDPE in its current state is not possible to coat using the developed gel. This can be attributed to the polymer film having a lower surface energy than the surface tension of the gel being applied. To understand the wetting behaviour of the LDPE, firstly its surface energy needs to be determined. This was achieved using the OWRK approach. This was done by measuring the contact angle of diiodomethane and water upon the surface of the material, and applying the linear equation given by eqn. 3.5. The contact angle was



Figure 6.3: Physical observation of the effect of spreading the Cloisite Na<sup>+</sup> 2.0 wt.% with SWN 1.0 wt.% gel onto the LDPE surface for use as a coating. Note that the gel beads into discrete regions of drops rather than producing a uniform film of gel, due to the hydrophobic nature of the polymer.

determined as the average of the left and right angle for each droplet. The results of these measurements are shown in Fig. 6.4. From this measurement the surface energy was determined as  $39.43 \pm 0.44$  mJ/m<sup>2</sup>, with the polar and dispersive components of the surface energy as  $0.42 \pm 0.04$  mJ/m<sup>2</sup> and  $39.00 \pm 0.40$  mJ/m<sup>2</sup>, respectively. It is of note the surface energy is slightly higher than that reported in the literature [176], however the value is in line with other polymeric materials. The OWRK also offers the advantage of determining the wetting envelope for a solid surface. This can be used to predict the contact angle for a liquid with known components of surface tension, and determine its degree of wettability. The wetting envelope for LDPE is shown within Fig. 6.5 for a range of desired contact angles. As can be seen from the predicted wetting envelope, the contact angle for water is greater than 90°, supporting the observation that when the gel is coated onto the polymer surface, rather than spreading out to wet the surface, it beads into discrete drops of gel. Therefore, a method is needed to ensure the LDPE surface is compatible with the gel coating and allow a continuous film to be produced. This can be achieved by either increasing the polymer's surface energy or lowering the gel surface tension. Such an explanation can be determined by considering the spreading parameter,  $S$  [177],

$$S = \gamma_s - (\gamma_{sl} + \gamma_l) \quad (6.1)$$

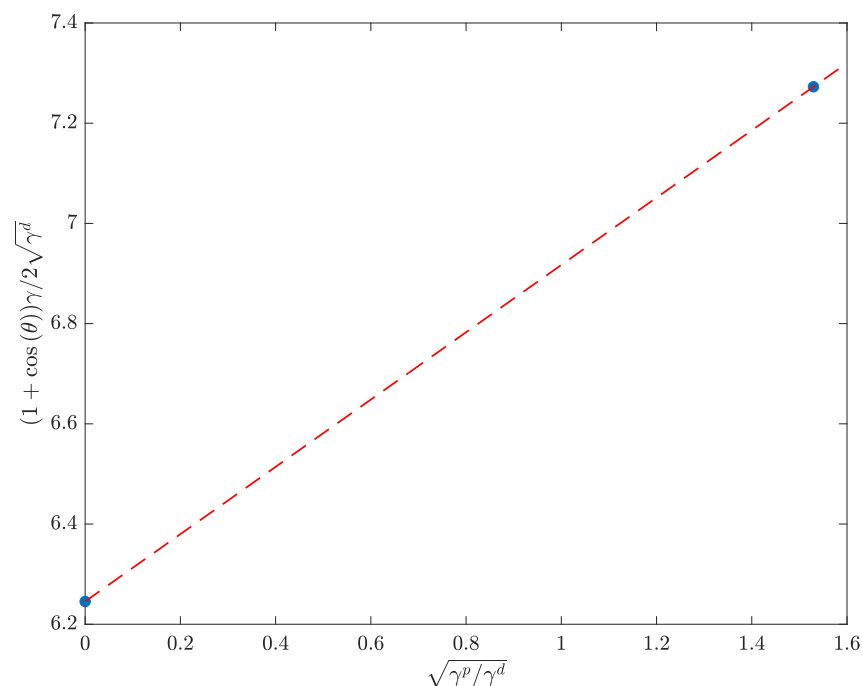


Figure 6.4: Determination of the surface free energy of LDPE through application of the OWRK method, with contact angle measurements of ultrapure water and diiodomethane on the sample surface.

for which  $\gamma_s$ ,  $\gamma_{sl}$  and  $\gamma_l$  are the surface tensions of the solid, solid-liquid interface and liquid, respectively. Where a value of  $S < 0$  leads to partial wetting, and  $S > 0$  leads to complete wetting.

### 6.2.1 Transforming the surface from hydrophobic to hydrophilic

From the contact angle measurement it is clear the polymer surface is hydrophobic in nature. Therefore, if the gel is to coat the polymer the surface needs to increase in its hydrophilicity. To achieve this the polymer was treated using UV/ozone irradiation using a UV ozone cleaner (Bioforce nanoscience, USA), with peak operating wavelengths of 184.9 nm and 253.7 nm. This promotes the formation of functional groups, such as hydroxyls and carbonyls, on the polymer acting to increase the surface hydrophilicity [178, 179]. To assess the effectiveness of the UV treatment the contact angle of water on the surface was measured as a function of the irradiation time to determine if there is a transition from hydrophobic to hydrophilic. These results are shown within Fig.

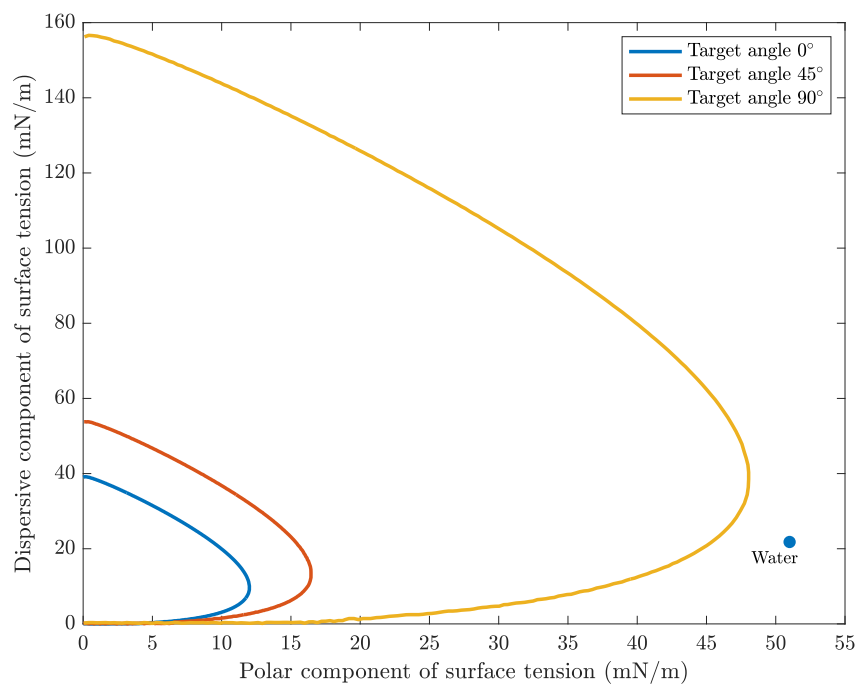


Figure 6.5: Predicted wetting envelopes for LDPE, showing the surface tension properties a liquid requires to from a contact of  $0^\circ$ ,  $45^\circ$  and  $90^\circ$ , as shown by the blue, orange and yellow curves, respectively. The blue marker shows the expected contact angle to be adopted by water on the surface.

6.6. As can be seen from the plot, there is a gradual decrease in the contact angle of

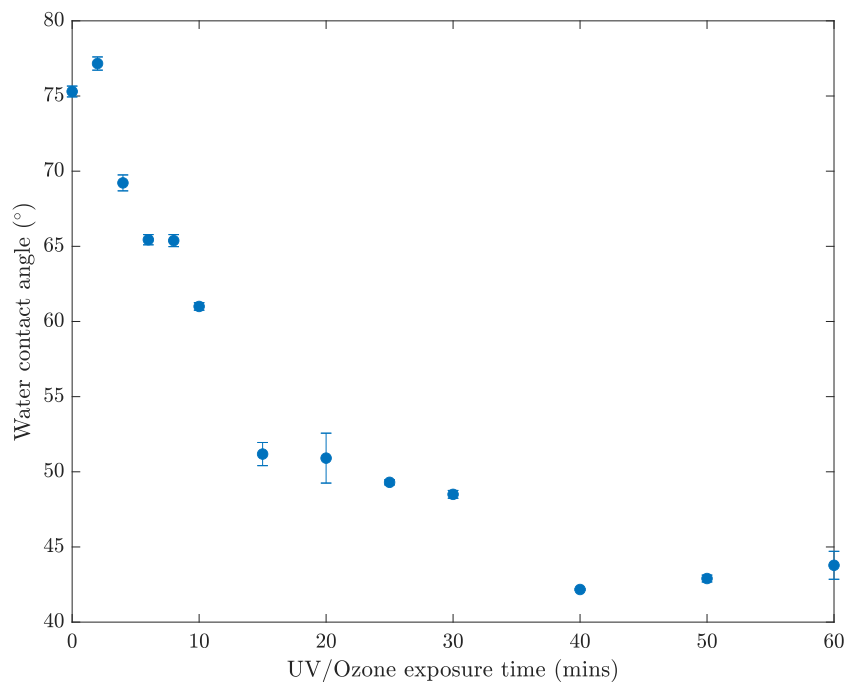


Figure 6.6: The variation of the water contact angle on the LDPE surface with increasing exposure to the UV/ozone irradiation.

water up to 15 minutes of irradiation time. This shows the surface becoming more hydrophilic due to the decreasing contact angle. Between 20 and 30 minutes of treatment, there is a slight plateau region, for a contact angle value of  $50^\circ$ . There is then a second decrease in the contact angle after a time of 40 minutes reaching a second plateau for a contact angle of around  $42^\circ$ . This value shows the surface has a much high degree of wettability after 40 minutes of treatment in comparison to the base polymer. Although longer times may see a reduction in the contact angle further, a time of 40 minutes was chosen for the irradiation time, as over exposure could lead to structural damage of the surface and subsequently effect the dielectric performance. In order to establish if there is any change to the surface after the irradiation treatment, optical images were taken before and after the process to assess the surface structure. These images are shown within Fig. 6.7. As can be seen in the Figure, there is minimal damage to the surface structure after the application of the UV/ozone treatment, meaning the chosen irradiation time is an acceptable amount, which will provide the hydrophilicity

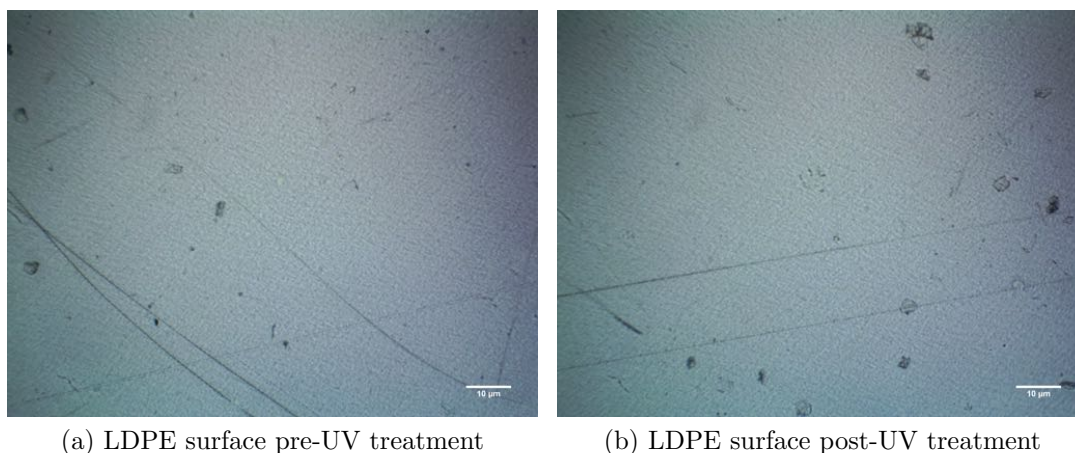


Figure 6.7: Optical images showing if there are any macroscopic changes to the LDPE surface after being exposed to UV/ozone irradiation. Sub-figure (a) shows the surface before and sub-figure (b) shows the surface after treatment, respectively. Scale bar represents 10  $\mu\text{m}$ .

increase and avoid external damage to the surface. The surface energy of the polymer following the irradiation process was again evaluated to determine the effect of the irradiation treatment on the surface energy, as it is desirable to gain an increase to cause the gel to become more wetting. The results of these measurement are shown in Fig. 6.8. From this plot the surface energy of the film is determined as  $64.75 \pm 1.34$   $\text{mJ}/\text{m}^2$ , with dispersive and polar components of  $46.76 \pm 0.36$   $\text{mJ}/\text{m}^2$  and  $17.99 \pm 0.98$   $\text{mJ}/\text{m}^2$ , respectively. This shows that not only has there been a significant increase in the polymer surface energy as desired, there has also been a large increase to the polar component of the surface energy suggesting the UV treatment has indeed produced a number of polar groups on the surface. Again the wetting envelope for the surface was evaluated as shown by Fig. 6.9. From these curves the contact angle of water should be around  $45^\circ$ , showing a transition to a more favourable wetting regime. While the treatment process does not provide a fully wetting surface (i.e. a contact angle of  $0^\circ$ ), after the treatment process gel coatings can be applied to the surface that provide a continuous coating rather than discrete drops as shown by the image in Fig. 6.10.

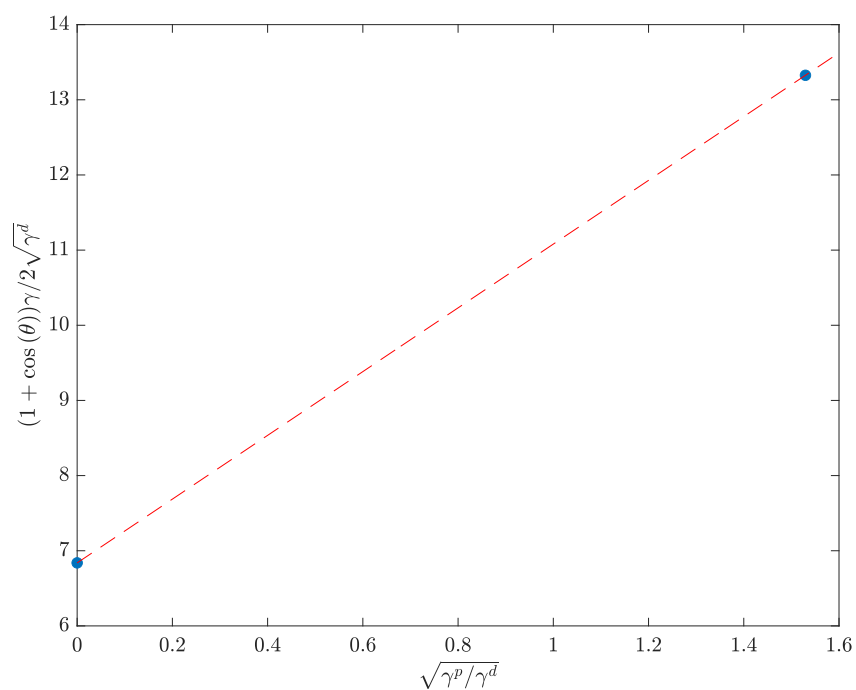


Figure 6.8: Determination of the surface free energy of the LDPE after treatment with 40 mins of UV/ozone irradiation, through application of the OWRK method, with contact angle measurements of ultrapure water and diiodomethane on the sample surface.

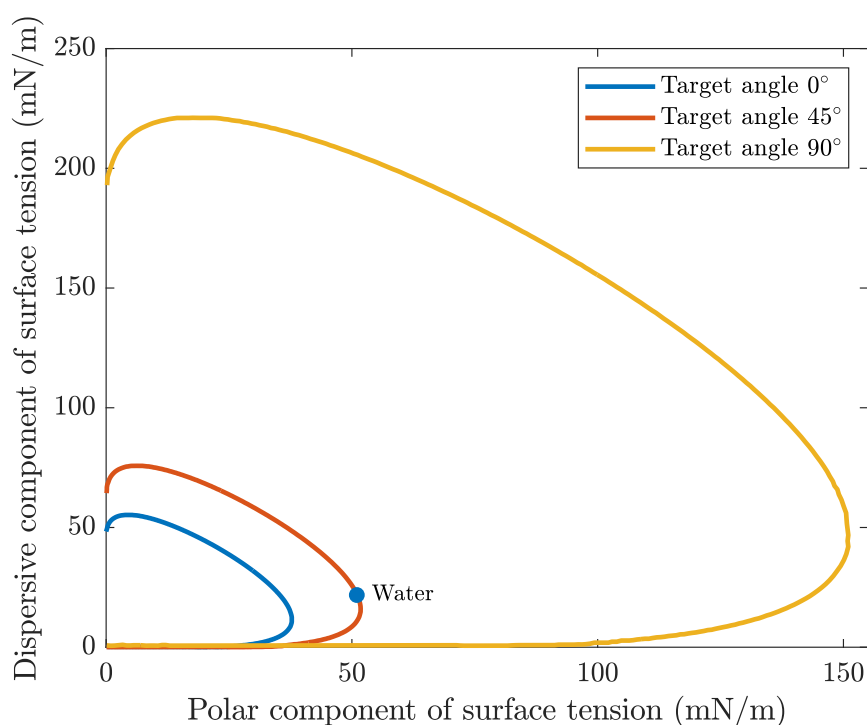


Figure 6.9: Predicted wetting envelopes for LDPE after treatment with 40 mins of UV/ozone irradiation, showing the surface tension properties a liquid requires to form a contact of  $0^\circ$ ,  $45^\circ$  and  $90^\circ$ , as shown by the blue, orange and yellow curves, respectively. The blue marker shows the expected contact angle to be adopted by water on the surface.



Figure 6.10: Physical observation of the effect of spreading the Cloisite  $\text{Na}^+$  2.0 wt.% with SWN 1.0 wt.% gel onto the LDPE surface after treatment with 40 mins of UV/ozone irradiation, for use as a coating. Note that the gel can now form a continuous film upon the surface due to the increased hydrophilicity of the surface

### 6.2.2 Improving surface compatibility

Although the surface was treated using the UV/ozone irradiation to increase the surface hydrophilicity, interaction between the coating and the surface occurs mostly through van der Waals and electrostatic interactions. Thus, this interaction strength is relatively weak. In order to improve the strength of this interaction, a treatment such as layer-by-layer (LbL) self assembly can be used, such that the coating will instead interact directly with clay particles rather than the polymer surface. LbL techniques are well documented [180] and can be used with a variety of materials; such as polymers, colloids, biomolecules, cells, etc. to produce thin films with highly controlled thickness. Along with the many materials that can be used for LbL coatings, there are also many methods that can be employed to achieve the build up of the individual layers. In this work the technique of immersive assembly using colloidal solutions has been employed. For this method the substrate is immersed into a positive colloid solution and then immersed into the negative colloid solution, with washing steps between. This process is repeated until the desired number of layers has been achieved. This approach is shown schematically in Fig. 6.11. To achieve a LbL coating on the LDPE film, colloidal solu-

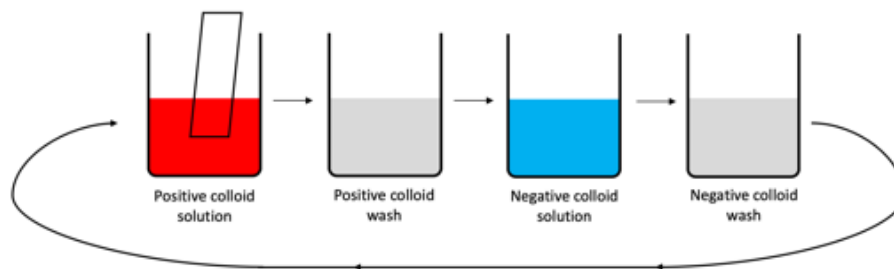


Figure 6.11: Schematic diagram showing the process by which immersive LbL assembly is performed.

tions of positively charged silica particles (LUDOX<sup>®</sup> CL colloidal silica, Sigma Aldrich, UK) at 0.5 wt.% in ultrapure water and negatively charged colloidal solutions of clay particles at 0.05 wt.% in ultrapure water. The clay solutions were first treated using the exfoliation process for 30 minutes in order to produce as highly a monodisperse colloidal as possible. To prepare the substrates for the LbL coating, they were first washed using ultrapure water to remove any dust or debris, and then placed into the

UV/ozone cleaner for the surface functionalisation. After the treatment process the LDPE was immediately removed and alternatively dipped between the positive and negative solutions with washing steps between. Each dipping session was done for 5 minutes duration before the next dipping step. This process was repeated until 6 layers were built up on the surface. The coated samples were then placed on easy release film and allowed to dry at room temperature ( $22 \pm 1^\circ\text{C}$ ).

The introduction of further surface treatments could subsequently change the desired surface properties. To determine if the LbL process has any effect on the surface properties the surface energy was again measured, as shown in Fig. 6.12. From this the

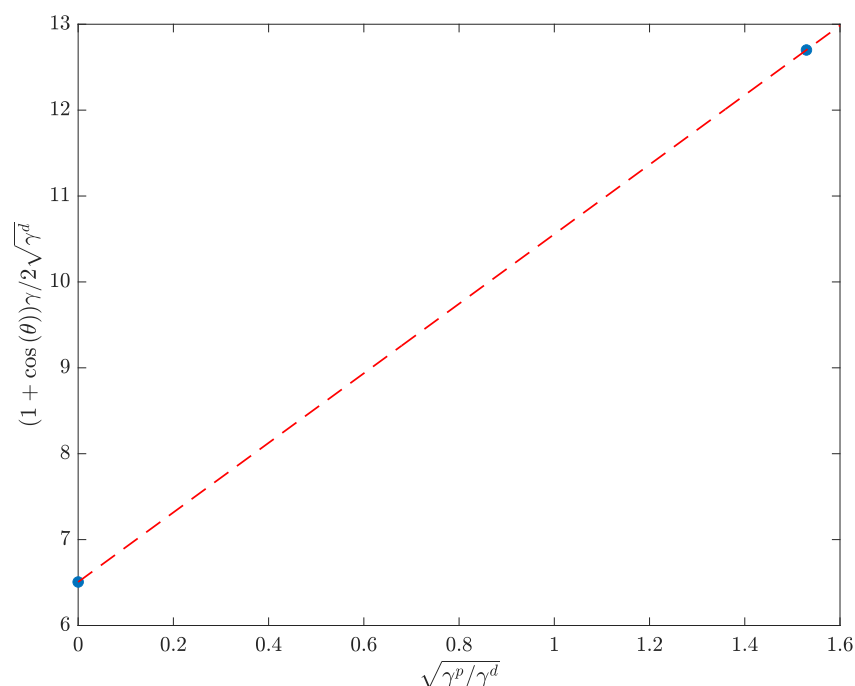


Figure 6.12: Determination of the surface free energy of the LDPE after treatment with 40 mins of UV/ozone irradiation and LbL treatment, through application of the OWRK method, with contact angle measurements of ultrapure water and diiodomethane on the sample surface.

surface energy can be determined as  $58.73 \pm 1.37 \text{ mJ/m}^2$ , with dispersive and polar components of  $42.34 \pm 0.21 \text{ mJ/m}^2$  and  $16.40 \pm 1.16 \text{ mJ/m}^2$ , respectively. While there is a slight decrease in the surface energy overall, the majority of this decrease is seen within the dispersive component thus the wetting ability of the surface should not be

hindered significantly. To confirm this the wetting envelope was produced as seen in Fig. 6.13. The expected contact angle of water on the LbL functionalised surface is

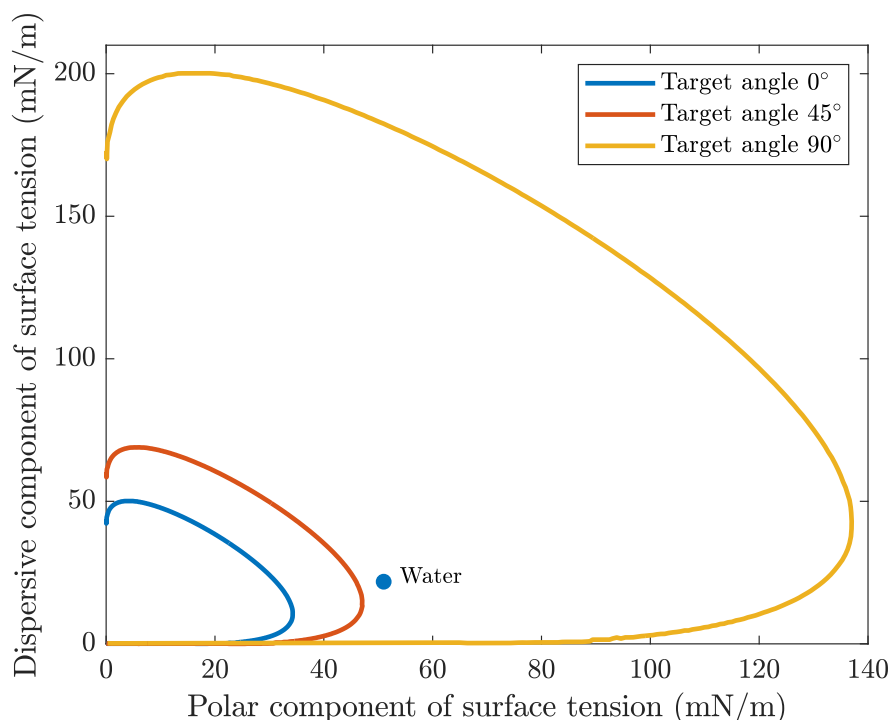


Figure 6.13: Predicted wetting envelopes for LDPE after treatment with 40 mins of UV/ozone irradiation and LbL treatment, showing the surface tension properties a liquid requires to form a contact of  $0^\circ$ ,  $45^\circ$  and  $90^\circ$ , as shown by the blue, orange and yellow curves, respectively. The blue marker shows the expected contact angle to be adopted by water on the surface.

predicted to be around  $50^\circ$ . As expected the change in the surface energy has led to a slight change in the expected contact angle, however it is not a significant enough change that it should cause problems for the wettability of the gel coating.

While the wetting envelopes provide a theoretical value of the water contact angle on the differently treated surfaces, it is useful to understand the true equilibrium contact on the surfaces to observe their real wettability. To assess this the contact angle of water on the surface was observed as a function of time to determine the equilibrium state. A  $5 \mu\text{L}$  droplet of ultrapure water was placed onto the surface and then monitored continuously for ten minutes, with contact angle measurements performed at 1 second intervals over the time period. The results obtained for the different sur-

faces are shown in Fig. 6.14. As can be seen in the Figure, the equilibrium contact

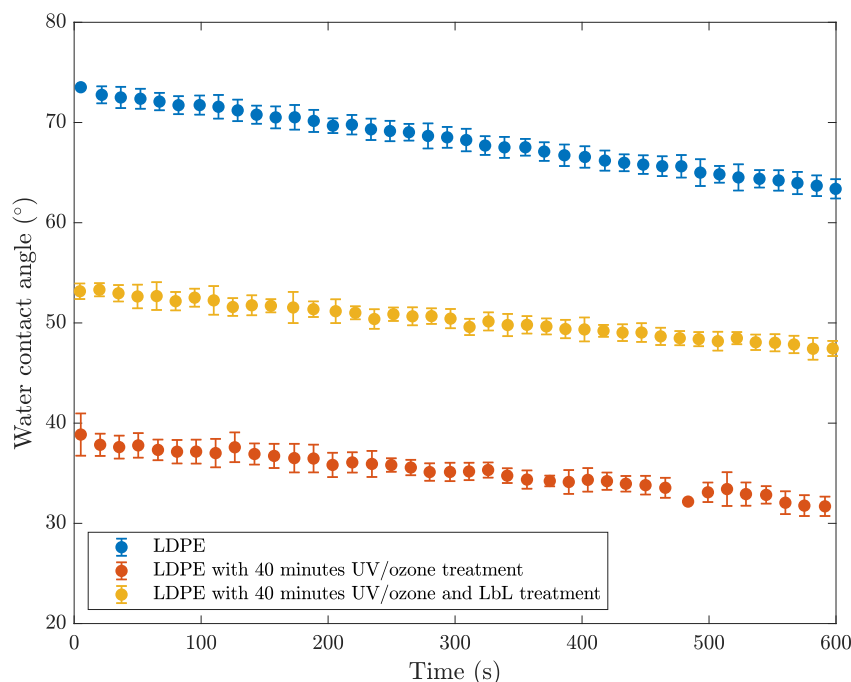


Figure 6.14: Dynamic contact angle measurements of ultrapure water on the treated LDPE surfaces, showing the variation in contact angle over 10 minutes.

angle are in agreement with that predicted by the wetting envelopes for the different surfaces. For both the UV treated and LbL treated surfaces the contact angle is within the hydrophobic wetting regime, and hence will be suitable to be coated. The gradual decrease in the contact angle with time is likely attributed to the evaporation of solvent as apposed to drainage into the surface. This was confirmed by visual observation of a droplet on the surface also.

### 6.3 The structure and morphology of the produced coating.

In order to produce the desired increase in electrical breakdown resistance, it may not be necessary to produce a significantly thick coating layer. However, the layer must be thick enough such that the polymer substrate is uniformly and fully coated. In

order to evaluate the effect of coating thickness, samples of polymer were prepared using the outlined process above and then coated using varying thicknesses of gel. The application of the gel was performed by placing the polymer onto a glass plate, with a small amount of gel placed onto the sample surface. This was then spread evenly over the substrate (around 30 seconds for full application) using a Universal Blade Applicator (Gardco Paul N. Gardner Company Inc., USA) set to the desired thickness. After application the samples were placed into a fridge and left to dry for 48 hours at a temperature of  $4 \pm 1^\circ\text{C}$ . Samples were dried at a low temperature to hinder the formation of cracks within the drying film.

Following the drying process a sample of the produced material was cut using a surgical blade and clamped laterally into an SEM sample observation clip and mounted onto a aluminium stub with carbon tape for SEM analysis. Prior to imaging the specimens were coated with 10 nm of gold to prevent sample charging effects. Several regions of the sample were observed under the SEM in order to give an idea of the uniformity of the coating applied. These results are shown by Figures 6.15 to 6.18.

As can be seen from the SEM analysis the observed thickness of the coating increases with the applied gel thickness, as expected. However, it is clear that large thicknesses of applied gel (i.e.  $400 \mu\text{m}$ ) leads to significant crack formation in the coated film, and this is also not localised to single regions of the coating. In the case of the much thinner gel coatings it appears as though regions of differing coating thickness are seen, due to the contrast of the image. Although this could be an imaging artefact and needs further investigation. It is clear that applying thicker coatings leads to more cracking and damage within the coated surface, which would lead to detrimental effects when subjected to electrical testing. It is of note that some of the images obtained for a  $400 \mu\text{m}$  coating show significant cracking in the surface. While these samples are prepared in the same way as other samples, it is likely the higher thickness of the coating either

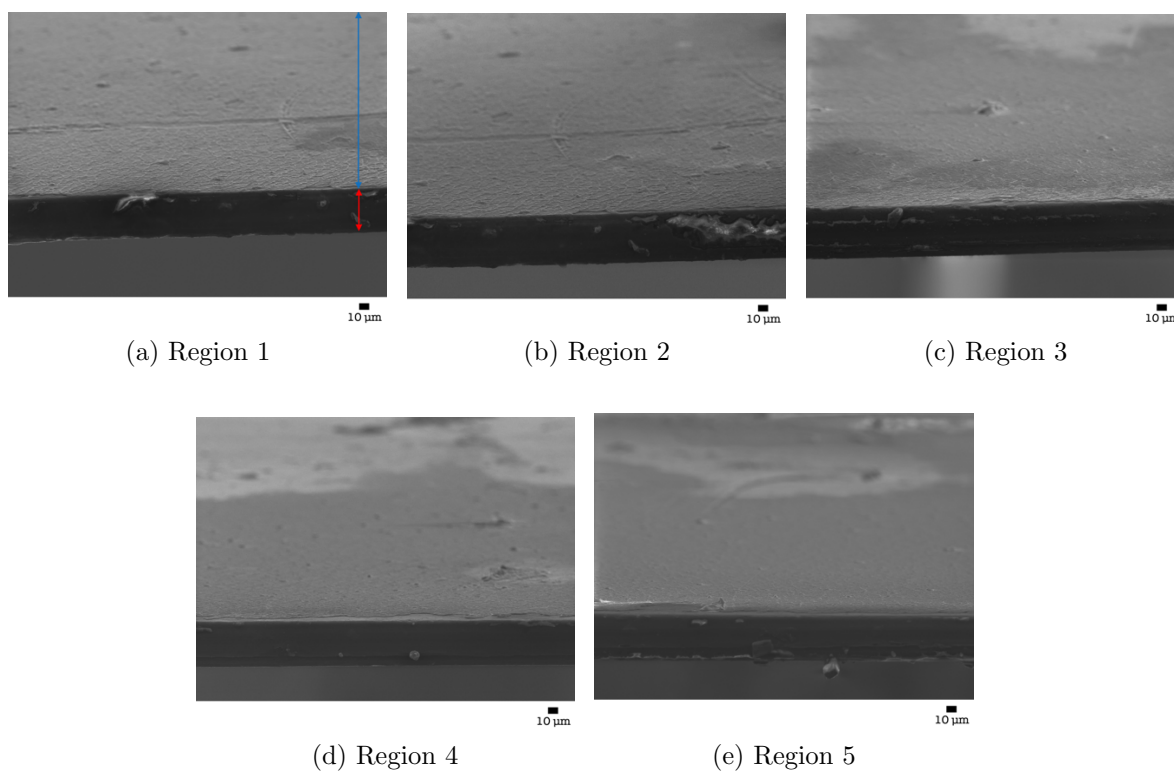


Figure 6.15: Low magnification SEM images showing the cross section of the clay coating on LDPE at 75  $\mu\text{m}$  clay coating applied thickness. Scale bar represents 10  $\mu\text{m}$ . The red arrow indicates the polymer layer, while the blue arrow indicates the coated surface. This designation applies across all the images.

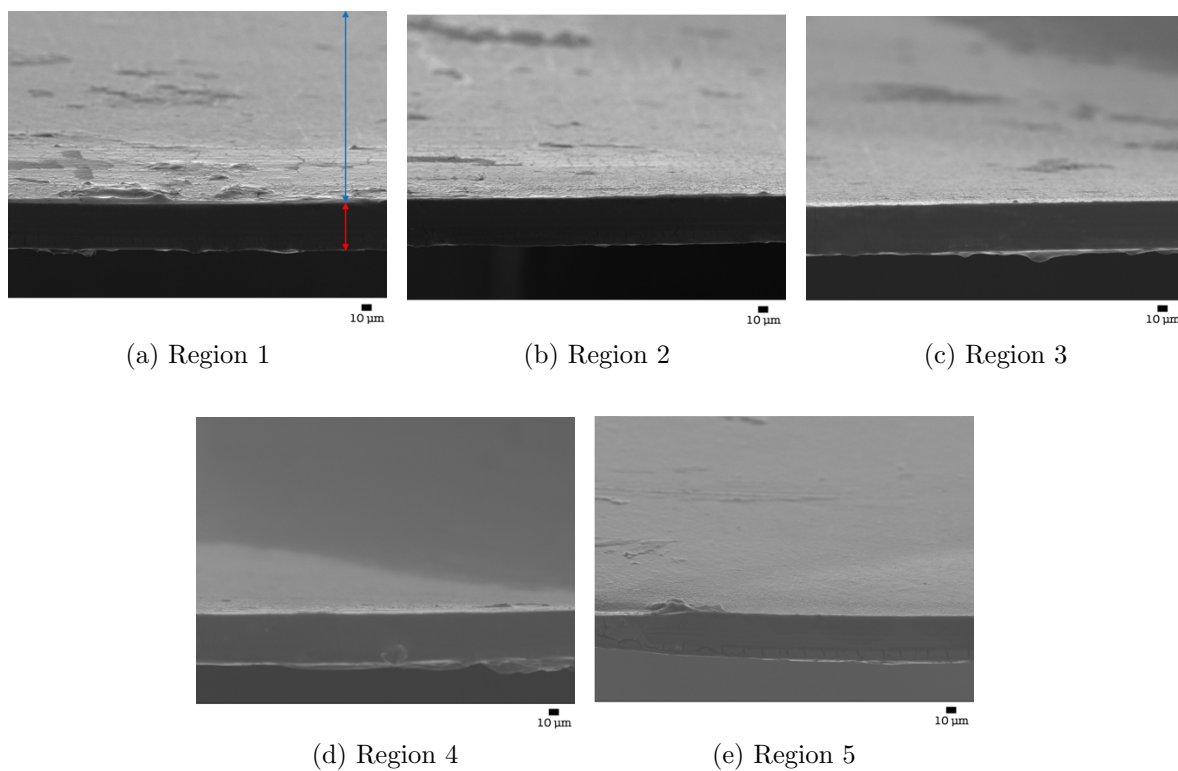


Figure 6.16: Low magnification SEM images showing the cross section of the clay coating on LDPE at 100  $\mu\text{m}$  clay coating applied thickness. Scale bar represents 10  $\mu\text{m}$ . The red arrow indicates the polymer layer, while the blue arrow indicates the coated surface. This designation applies across all the images.

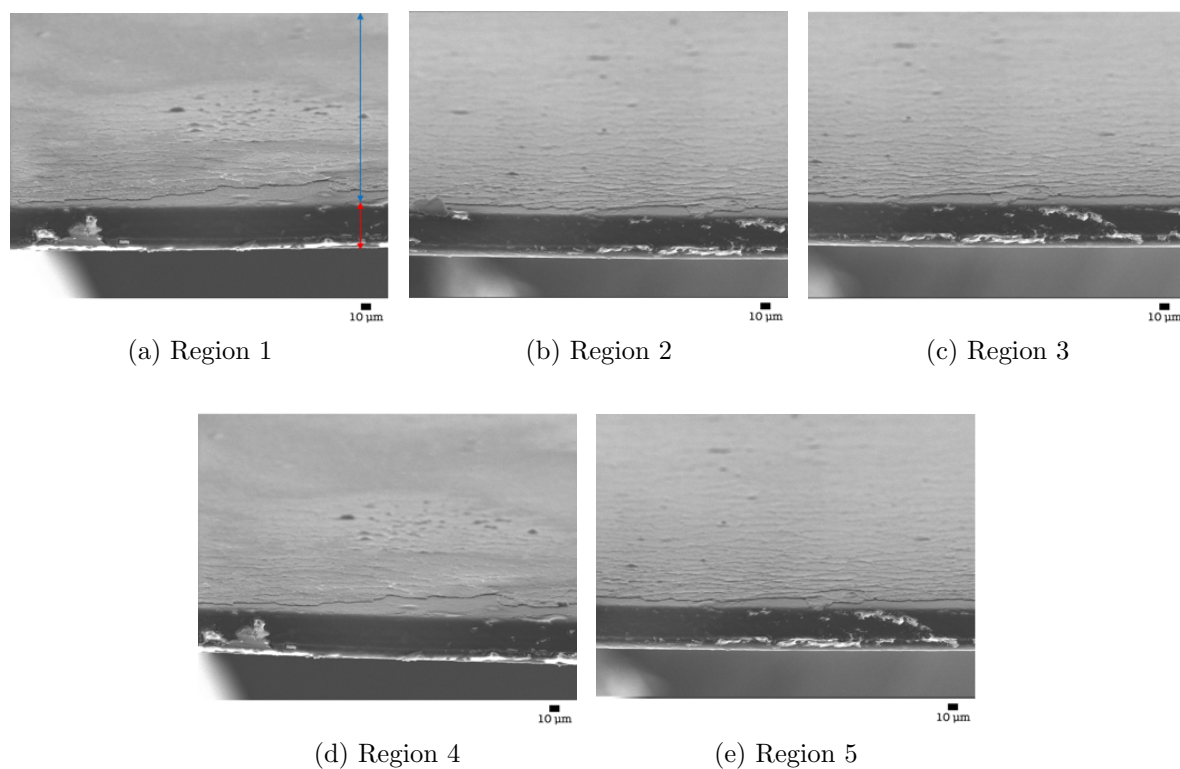


Figure 6.17: Low magnification SEM images showing the cross section of the clay coating on LDPE at 200  $\mu\text{m}$  clay coating applied thickness. Scale bar represents 10  $\mu\text{m}$ . The red arrow indicates the polymer layer, while the blue arrow indicates the coated surface. This designation applies across all the images.

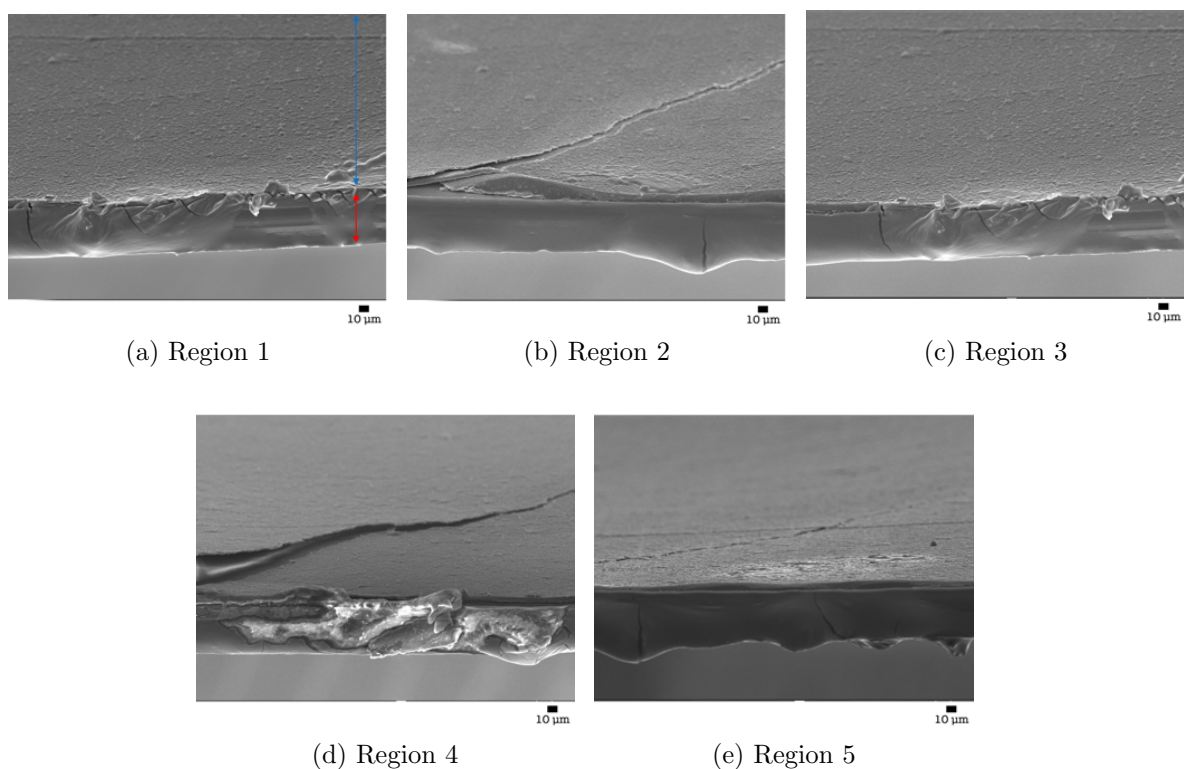


Figure 6.18: Low magnification SEM images showing the cross section of the clay coating on LDPE at 400  $\mu\text{m}$  clay coating applied thickness. Scale bar represents 10  $\mu\text{m}$ . The red arrow indicates the polymer layer, while the blue arrow indicates the coated surface. This designation applies across all the images.

cracked during the drying process or during the sample preparation for SEM analysis. Visual observation of 400  $\mu\text{m}$  coatings do not show visible cracks so it is likely these cracks are on the micro-scale and some may be artefacts of the cutting of the sample generating surface forces within the coating.

To determine the amount of clay present at each applied thickness, a sample of the prepared material was evaluated using TGA. Since the polymer film alone undergoes complete combustion within an air atmosphere, and the clay is thermally stable up to high temperatures ( $\sim 700^\circ\text{C}$ ), it can be inferred that complete combustion of the material will remove the polymer substrate and the clay within the applied coating will remain. Approximately 5 mg of each sample was cut into small sections using a surgical blade and placed into the TGA crucible. Samples were heated from  $30^\circ\text{C}$  to  $600^\circ$  under air. The measured thermograms for different coatings are presented within Fig. 6.19. From the thermograms it can be seen, that the LDPE combusts at

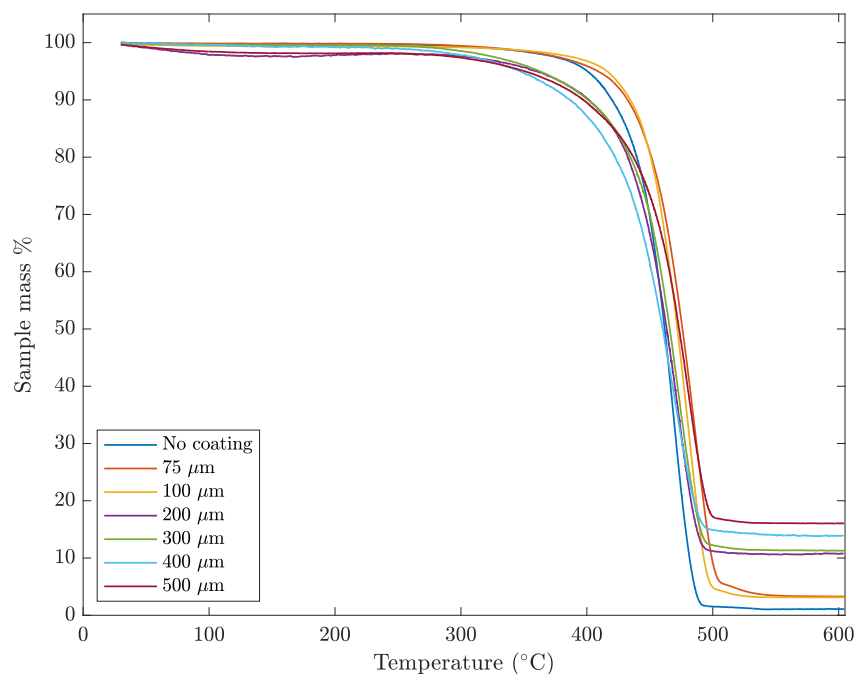


Figure 6.19: Typical obtained thermograms of coated samples heated to  $600^\circ\text{C}$  under an air atmosphere.

around  $500^\circ\text{C}$ . Therefore, in order to determine the mass of clay within the sample, the

mass percentage remaining at 600°C was selected, to ensure the complete removal of the polymer. The measured mass percentages were then plotted as a function of the applied coating thickness, as shown by Fig. 6.20. We can see that there is a reasonably

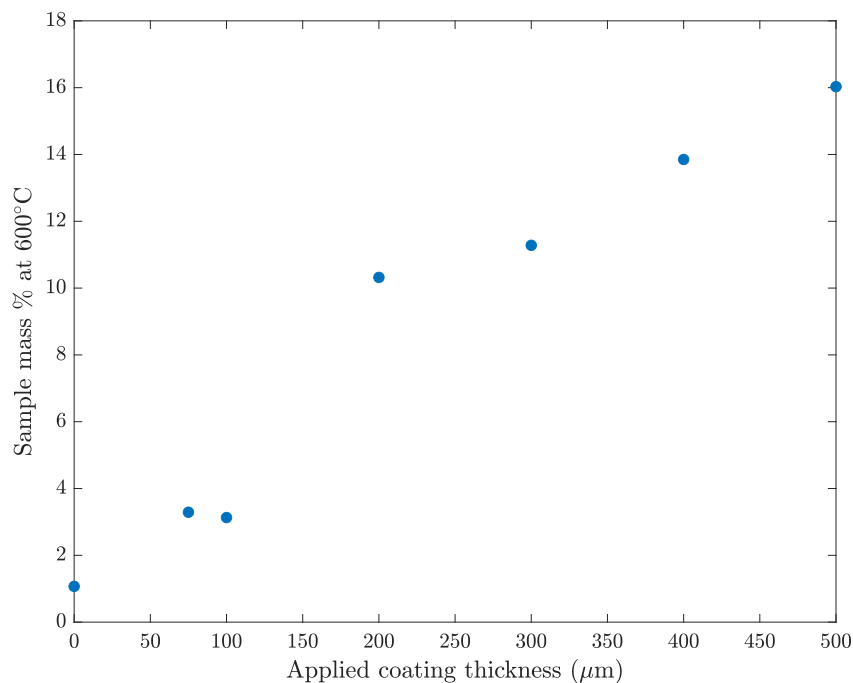


Figure 6.20: Variation of the clay mass percentage remaining at 600°C with the applied coating thickness.

linear relationship ( $R^2=0.923$ ) between the thickness of the coating and the clay mass percentage within the coating. This is to be expected based on the observation results from the SEM where the increased applied thickness leads to a greater thickness of coating. There is a slight discrepancy in the results for 200  $\mu\text{m}$  thickness, however repeat measurements show that this is a consistent result ( $11.69 \pm 1.37\%$ ). Measured samples typically showed  $< 5\%$  in variation between different regions. It is likely some variation will occur due to the sample coating and region selected for measurement and the nature of the measurement itself, potentially leading to the loss of some sample in the atmosphere. Conventional nanocomposites typically have filler loadings below 5 wt.% [181, 182], therefore for comparison to current materials, it is wise to have a coating with a similar clay loading percentage.



silane for the coating three trichlorosilanes with chain lengths of 8, 12 and 18 were tested on a glass microscope slide to determine which produced the greatest contact angle increase. Ultrapure water was sprayed onto the microscope slide, followed by a 1 mM solution of the silane in toluene being sprayed upon the slide. This was blown dry under a nitrogen air stream and baked in an oven at 150°C for 3 hours to complete the reaction. Once prepared a 5  $\mu$ L droplet of water was placed on the surface and allowed to equilibrate for two minutes before, the contact angle was taken. The results of this preliminary test are shown in Fig. 6.22. It is of note this test was more

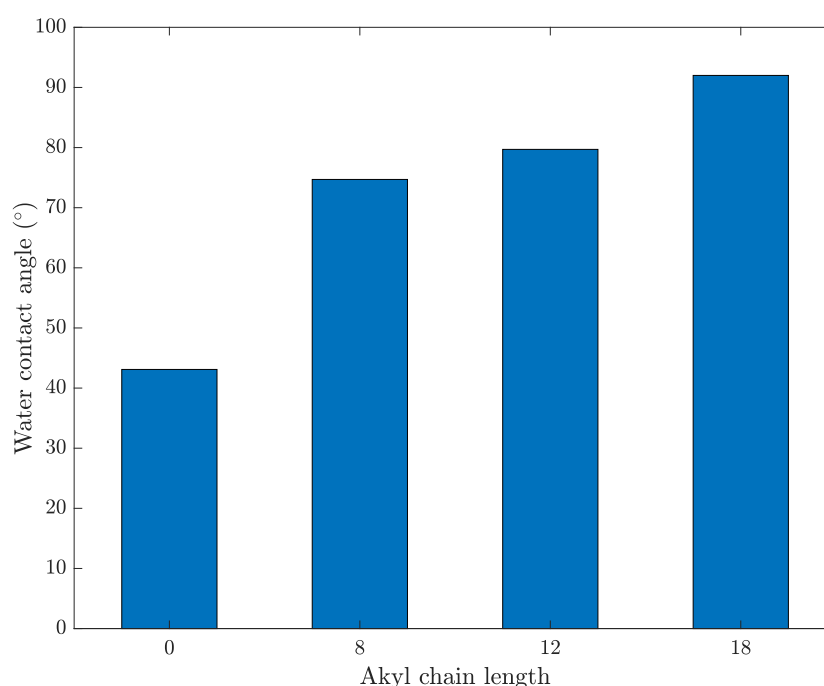


Figure 6.22: The contact angle of a water droplet on a glass slide coated using a trichlorosilane of varying alkyl chain length.

qualitative and the relative extent of increase of the alkyl chain was of most interest. Based on these measurements the silane chosen to produce the hydrophobic coating was trichloro(octadecyl)silane (Sigma Aldrich, UK), due to the long alkyl chain providing a high degree of surface hydrophobicity. To prepare the samples a layer of water was first lightly sprayed onto the coated substrate, followed by spraying a layer of 1 mM of silane in toluene. After coating the samples were dried under a nitrogen air flow and baked in an oven at 50°C for 12 hours, in order to complete the reaction. To

assess the hydrophobicity the contact angle of water was evaluated as a function of time to determine the increase in sample hydrophobicity and observe if there is any drainage of the into the coating. The differences between the hydrophobised and non-hydrophobised surfaces are shown in Figures 6.23 and 6.24 for Cloisite Na<sup>+</sup> and SWN, respectively. In both cases it is clear that the addition of the silane coating leads to an

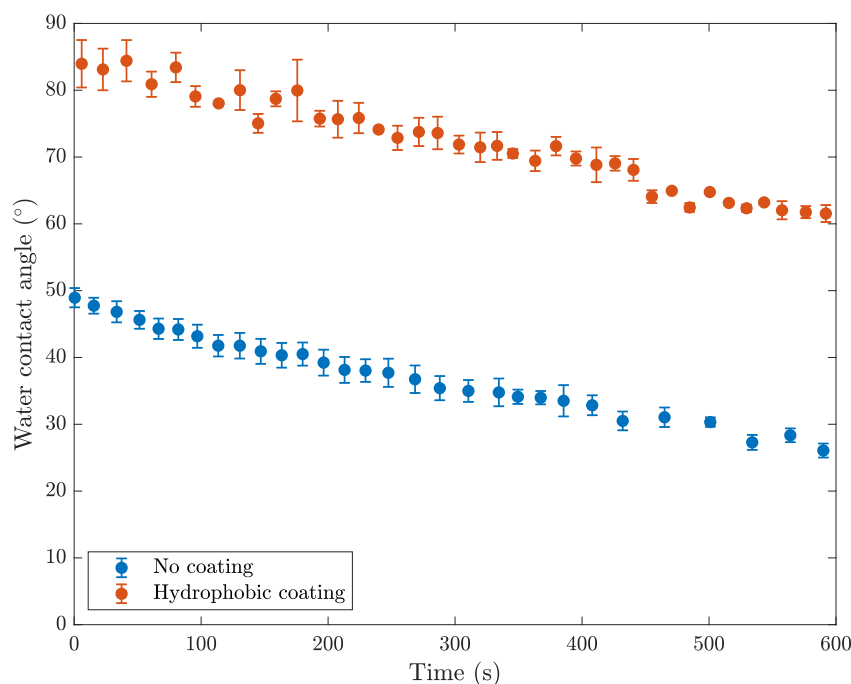


Figure 6.23: The change in water contact angle for the un-treated and hydrophobic treated Cloisite Na<sup>+</sup>/SWN gel coating.

increase of the water contact angle. In the case of the Cloisite Na<sup>+</sup> based coating the contact angle is increased by around 35°, showing a significant change to the wettability of the surface. For the SWN based coating the contact angle is increased by around 20°, which is slightly less than that observed for the Cloisite Na<sup>+</sup> coating. The gradual decrease in the contact angle is again most likely attributed to solvent evaporation as apposed to the solvent draining into the coating. The initial difference in the contact angle between the two types of clay coating can be attributed to the higher degree of hydrophobicity of SWN in comparison to Cloisite Na<sup>+</sup> as was determined in the iGC measurements.

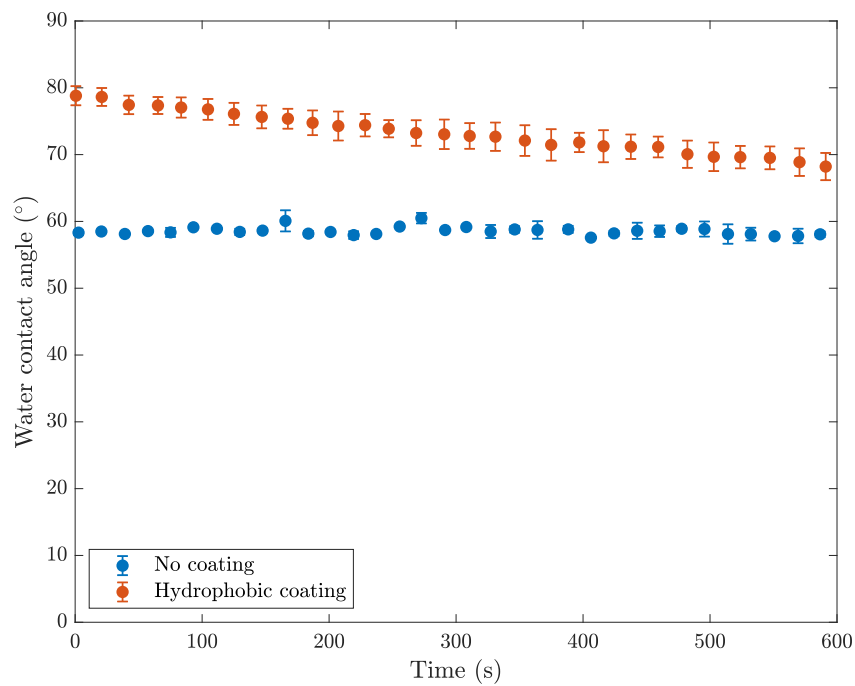


Figure 6.24: The change in water contact angle for the un-treated and hydrophobic treated SWN gel coating.

## 6.5 Final sample fabrication process

Based on the results presented within this Chapter the following procedure is followed for the production of samples for electrical testing.

- A polymer substrate is cut from a large sheet, typical sample size is 5 cm by 5 cm.
- The polymer surface is gently cleaned using water to remove dust and any debris.
- The polymer is treated for 40 minutes under UV/ozone - this applies to both sides of the film.
- Following UV treatment, the LbL process is employed giving six layers with a terminating clay layer.
- A small amount of gel is placed onto the polymer surface and then spread to the desired thickness using the doctor blade.

- The coated sample is placed into a fridge to dry for 48 hours.
- The hydrophobic coating process is applied to the surface
- The final sample is inspected for visible damage or impurities and then placed into a petri dish and sealed for transportation to the University of Southampton to be subjected to electrical testing.

## 6.6 Summary

The aim of this Chapter was to develop the continuous layer material to be used for dielectric application, the main aim of this thesis. In this Chapter the processes by which these materials can be made has been discussed, and further developments to the material are also shown. To summarise the key messages of this Chapter:

- The threshold concentration of Cloisite Na<sup>+</sup> leading to gel formation can be reduced by replacing some of the clay percentage mass with SWN clay. This subsequently leads to much stronger gel networks being formed (as seen from the storage modulus) and allows the two types of clay to be used to form coatings with the same solid percentage loading.
- Through the use of UV irradiation and layer-by-layer self assembly a process is developed that allows the nominally hydrophobic LDPE to become more wetting and allow a gel formed of predominantly solvent to fully wet the surface and provide a uniform layer for coating.
- Investigation of the coating shows a linear dependence between applied coating thickness and the relative mass percentage of clay within the coating. It is also clear that there is a limit to the applied thickness, in order to avoid the formation of surface cracking during the drying process. The treatment process allows a uniform layer to be spread upon the polymer surface and we note the drying film does not exhibit any retraction and shrinkage around the edges, most likely due to the careful and controlled drying process employed.

- A process of hydrophobising the coated surface through the use of trichlorosilane is presented, with success observed in the increase of water contact angle, and lack of solvent drainage into the coating. Helping to prevent the further adsorption of moisture and also allow different working environments to be explored.

In this Chapter the step by step process to develop the novel nanodielectric material has been presented, showing the needs for surface treatment to ensure compatibility and the uniformity of coatings produced. Using TGA methods the clay percentage loading within the coating has been evaluated and comparison to the percentage loading of filler nanocomposites can allow for comparison between the two methods for composite production.

## Chapter 7

# Electrical performance of the developed nanodielectric materials

In this chapter the electrical performance of the developed materials will be discussed, with particular interest in the high-voltage performance. Following the electrical results a discussion of the interpretation of the measurements is given along with any further improvements that can be made to increase the efficiency.

## 7.1 Samples produced for testing

Based on the results presented thus far, five distinct types of samples were produced for testing. These different sample types are shown in Table 7.1. For each type of sample,

Table 7.1: Types of samples prepared for electrical testing

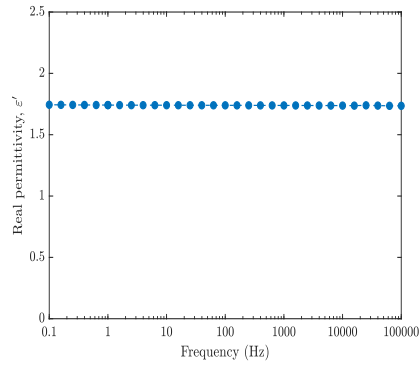
Sample type	Sample coating
1	LDPE with no coating
2	LDPE coated with Cloisite Na <sup>+</sup> 2.0 wt.% with SWN 1.0 wt.% gel
3	LDPE coated with SWN 3.0 wt% gel
4	LDPE coated with Cloisite Na <sup>+</sup> 2.0 wt.% with SWN 1.0 wt.% exfoliated gel
5	LDPE coated with SWN 3.0 wt.% exfoliated gel

five individuals were produced and transported to the University of Southampton. Each sample was produced using the method developed in Chapter 6, and any samples showing impurities or imperfections were removed and reproduced. An applied coating thickness of 75  $\mu\text{m}$  was used to produce this batch of samples.

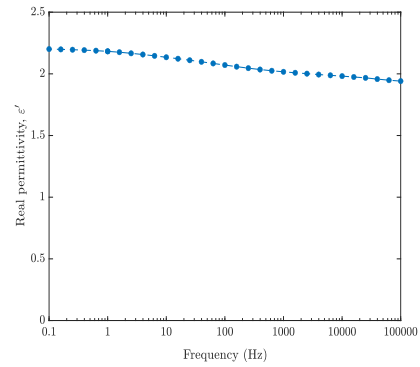
## 7.2 The dielectric response under alternating current

As discussed in Chapter 3, the permittivity of a material is typically expressed as a complex function of the frequency,  $\varepsilon^*(\omega)$ . For which the real and imaginary parts,  $\varepsilon'$ ,  $\varepsilon''$ , respectively, can be inferred to represent the energy storage (capacitance and inductance) and energy loss (resistance and conductance). A dielectric spectroscopy scan is most often employed in order to evaluate the permittivity response of a material.

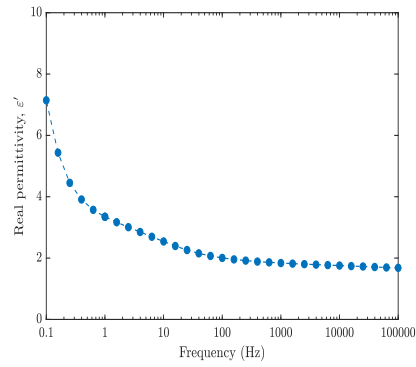
The measured permittivity of the prepared samples and original base polymer are shown in Fig. 7.1 for the real part of the permittivity and in Fig. 7.2 for the imaginary part of the permittivity. Looking at these results initially there appears to be a significant difference in sample type 3 - LDPE coated with 3.0 wt.% SWN. While it is possible this could be accurate it is more likely a sample issue, the increasing permittivity would suggest the presence of a large number of charge carriers, such as water. Therefore the focus of the results discussion will discount sample type 3. If we first consider the pure LDPE film (sample type 1) we notice that the real permittivity remains reasonably consistent over the frequency range tested, with an insignificant amount of loss present. This is similar to results observed for polyethylene (PE) [187], polypropylene (PP) [188] and polystyrene (PS) [189]. However, it is noted the measured value is slightly below the expected value (circa.  $\epsilon'_r = 2.3$  [190]), further measurements on LDPE at increasing thickness showed an increase from 1.5 to 2.2 from 50  $\mu\text{m}$  to 400  $\mu\text{m}$  in thickness [191]. Therefore, we can assume a systematic error related to the thickness of the sample may be present within the measurements. If we now consider the case of LDPE coated with a clay gel, in each case the real permittivity is increased slightly in comparison to the pure polymer, this is commonly seen in composite materials where a higher permittivity filler is added into a polymer matrix. It is also of interest to note that between sample type 2 and type 4, the increase in permittivity is slightly less in type 4 compared to type 2, which is again characteristic of nano fillers vs micro fillers. However, in general both types of gel coating appear to show similar responses of real permittivity. If we now consider the loss developed within the system, compared to the base polymer that shows virtually no loss, the produced samples do show noticeable loss peaks. The loss peak is most apparent with sample type 5 (exfoliated SWN) with a peak centred around 50 Hz, which would of course be detrimental to conventional electrical supplies. It is also clear the Cloisite Na<sup>+</sup> show much broader peaks in the frequency, and the degree of loss is increased with the exfoliation of the particles, possibly showing the loss is related to the number density of particles. However, it is likely the loss is related to the interface between the coating and polymer



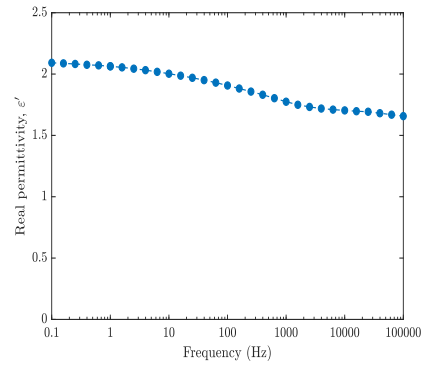
(a) Sample Type 1



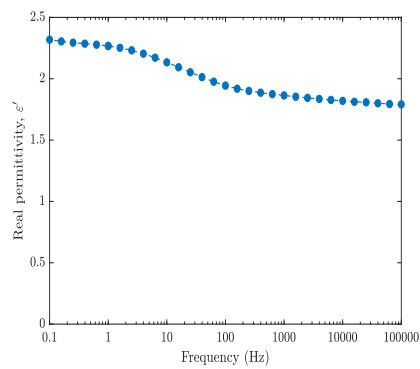
(b) Sample Type 2



(c) Sample Type 3

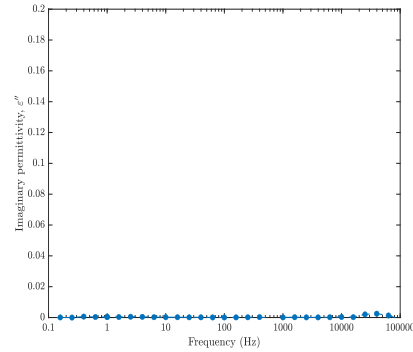


(d) Sample Type 4

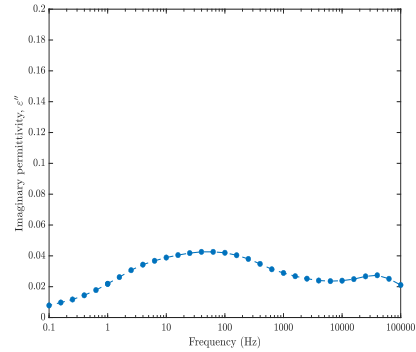


(e) Sample Type 5

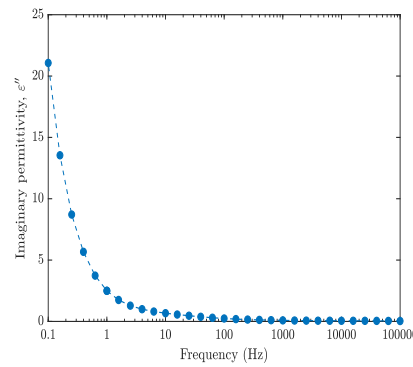
Figure 7.1: Measurement of the real permittivity for the samples produced. Sub-figures (a) - (e) show the results of different sample types. Refer to Table 7.1 for their designation.



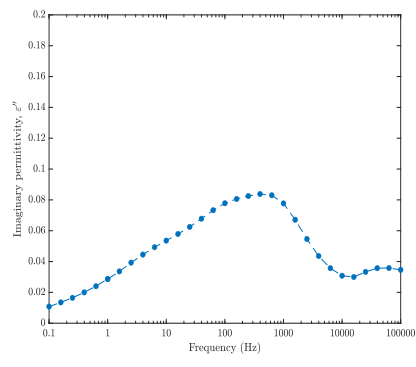
(a) Sample Type 1



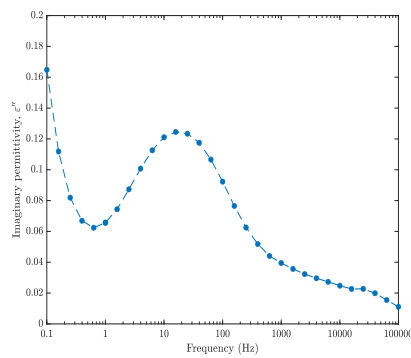
(b) Sample Type 2



(c) Sample Type 3



(d) Sample Type 4



(e) Sample Type 5

Figure 7.2: Measurement of the imaginary permittivity for the samples produced. Sub-figures (a) - (e) show the results of different sample types. Refer to Table 7.1 for their designation.

surface, leading to interfacial polarisation [192]. It is also possible that the presence of adsorbed water within the clay structure could lead to the increase in loss observed. While water typically resonates within the GHz region [193], the presence of hydrogen bonding can reduce this significantly [194]. Therefore, it is likely this loss peak could also be attributed to adsorbed water molecules forming hydrogen bonds to the clay structure, showing careful control of the moisture level may be necessary to avoid loss within the material. By evaluation of the  $\tan(\delta)$  we can also determine where the produced materials lie on the scale of perfect conductor to perfect dielectric using the scale shown in Table 3.2. The determined  $\tan(\delta)$  plots are shown in Fig. 7.3. From the

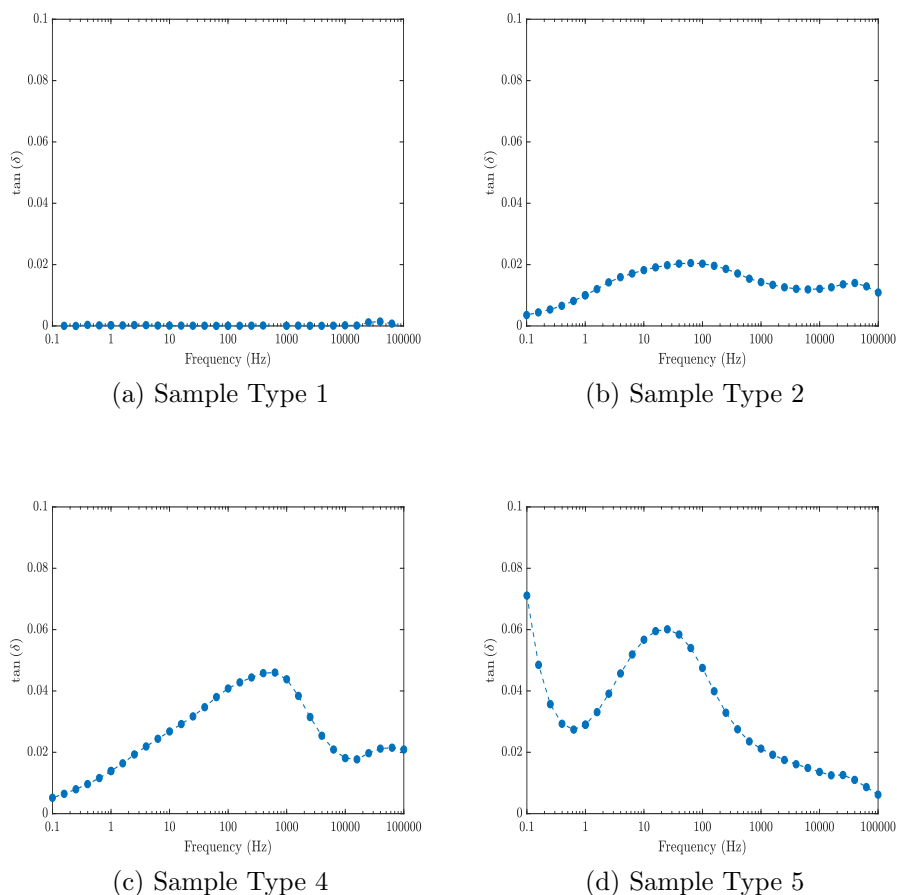


Figure 7.3: Determined measurements of  $\tan(\delta)$  for the samples produced, discounting sample type 3. Sub-figures (a) - (d) show the results of different sample types. Refer to Table 7.1 for their designation.

plots it is clear that all the samples are within the  $\ll 1$  category and therefore behave as good dielectric materials. However, as can be seen from the imaginary permittivity there are loss peaks present at significant frequencies for the desired applications that

need to be overcome.

Of interest is the unusual behaviour seen in sample type 3. Using the relation that,

$$\varepsilon'' = \frac{G}{\omega C_0} \quad (7.1)$$

in the limit of small frequencies, a linear response in  $\varepsilon''$ , would show the conductance is a constant. Thus the low frequency regime in sample type 3 has been investigated to see if it shows this property, as shown by Fig. 7.4. As can be seen from the

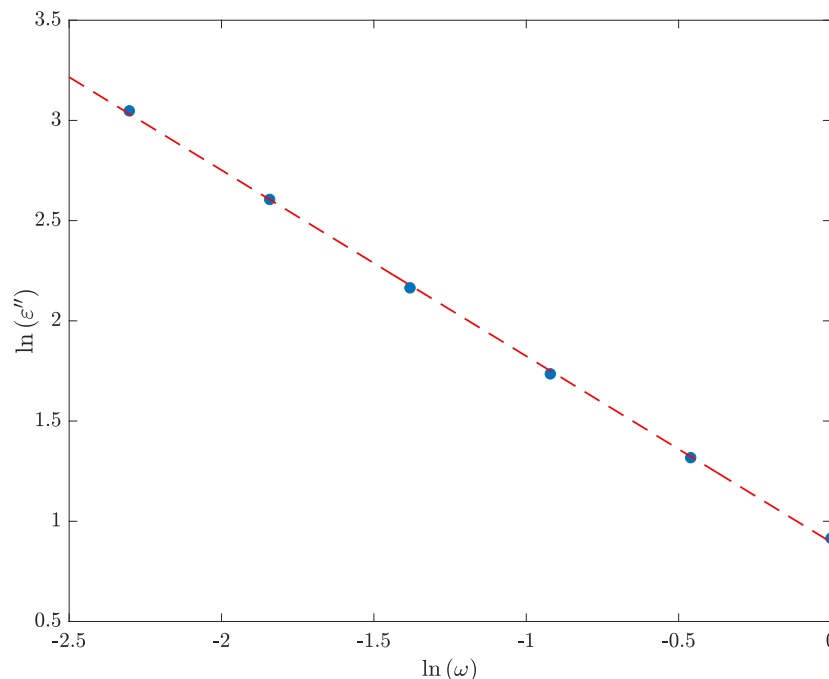


Figure 7.4: Evaluation of potential conduction behaviour in sample type 3 within the low frequency regime. Note the logarithmic axes scale.

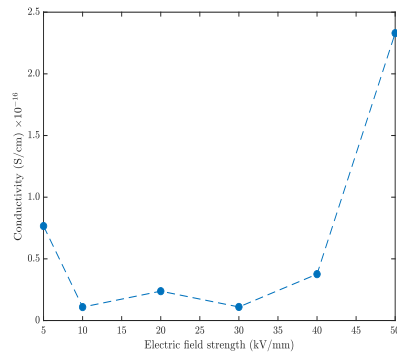
Figure, an inverse linear trend is seen ( $m = -0.928 \pm 0.008$ ), allowing us to infer the sample possesses a constant conductance, which is typically attributed to ionic migration [195]. Ionic migration only introduces loss into the system, so care needs to be taken that this loss does not enter the frequency range that the dielectrics would be applied to. Observing effects of ionic migration is not unexpected since the clay

contains adsorbed cations, to balance its structural charge and so under the influence of an electric field it is likely these cations will move about the structure. This result may also suggest the cations provide more of the loss than any adsorbed water, as this would resonant mostly within dipolar relaxation and persist to higher frequencies than what we observe. Overcoming the challenge of ionic migration due to the cations is a challenge, as removal of the cation species is usually done by a process of intercalation, as was the approach for the surface charge measurement shown in Chapter 4, and this would change the overall structure of the clay into an organoclay material which could have adverse effects of the gelling behaviour.

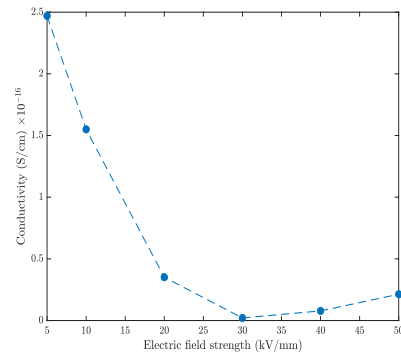
### 7.3 High field conductivity

In electrical insulators such as polymers, the electrons are bound tightly to the atoms within the material and thus do not flow freely. A perfect insulator doesn't exist as even the best of insulators have some free (mobile) charge carriers, which can carry current. In the process of electrical breakdown sufficiently high voltages generate electric fields that can pull electrons free of their atoms and allow current to flow. In the case of electrical components, insulators are typically used to prevent contact between conducting wires; preventing effects such as short circuiting, eddy currents and electrocution. Since it is typical that insulators require significant electric field strengths to become noticeably conductive, each sample in this work was subject to an electric field strength from 5 to 50 kV/mm for an hour duration and the most stable conductivity measurement in this time period was selected to produce a  $\sigma - E$  curve. It is of note that this process was performed in a continuous manner, which the voltage ramping to the next electric field strength at the end of the first testing hour. The resulting plots are shown in Fig. 7.5

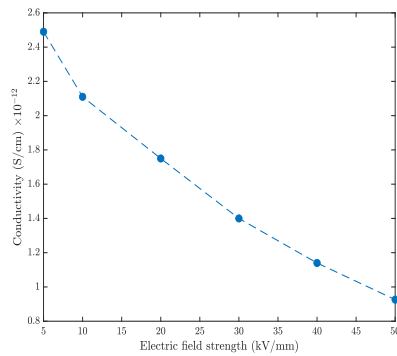
Here we note unusual behaviour within the conductivities measured. However, for sample types 1 and 4 the behaviour is as expected and can be explained as follows. What we observe for these two sample types is a steady increase in the electrical con-



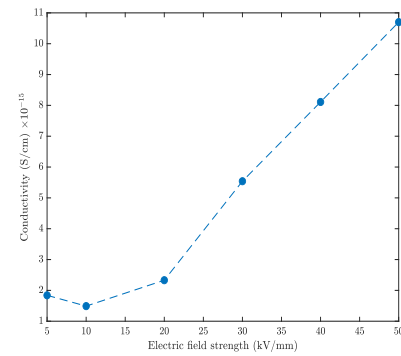
(a) Sample Type 1



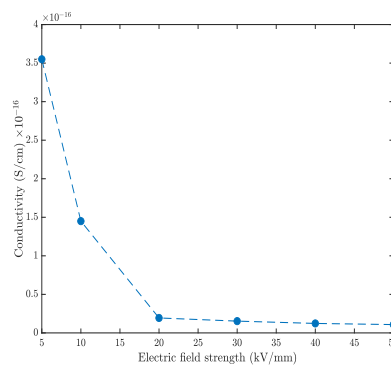
(b) Sample Type 2



(c) Sample Type 3



(d) Sample Type 4

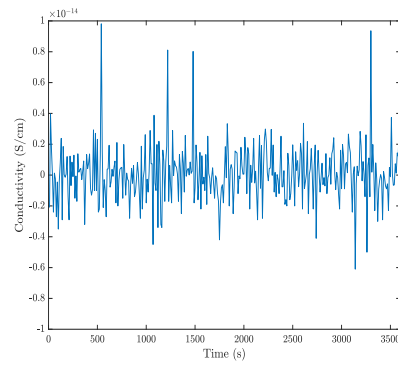


(e) Sample Type 5

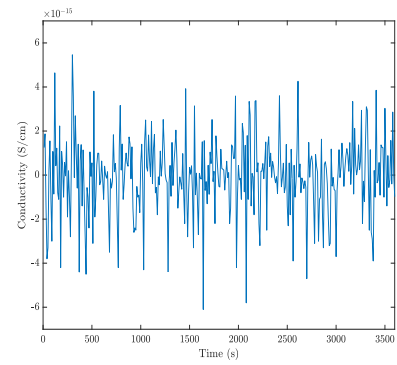
Figure 7.5: Measured  $E - \sigma$  curves for the samples produced. Note the scale on each plot which is chosen to show the trend most clearly. Sub-figures (a) - (e) show the results of different sample types. Refer to Table 7.1 for their designation.

ductivity with increasing electric field strength, as would be expected. This occurs due to the fact the increasing electric field provides enough force to pull the electrons away from their host atoms, and allow the charge to flow, hence under the increasing field where more force is supplied more electrons are freed and thus the electrical conduction increases. The question then becomes why do we observe the opposite trend within sample types 2, 3 and 5. Since electrical conduction is a property of free charge carriers, it stands to reason that these samples must contain a higher density of charge carriers. Since the materials are produced from a gel coating formed of clay which itself contains adsorbed cationic species and water molecules, it is highly likely it will contain more free charges than the LDPE polymer alone. Therefore it is possible the initial high values of conductivity are related to the movement of these free charges and as they migrate towards the anode or cathode, respectively the number of these free charges decreases, and thus the overall conductivity decreases with it. It is possible that under increased field strength the expected increase in conductivity may be observed. If this behaviour is attributed to free charge species within the coated layer, then a process for removing them needs to be employed. As discussed previously for cationic species, while this is possible through the use of organically modified clay materials, this is likely to hinder the gelation behaviour of the particles. A less difficult process is the removal of the water molecules. This can be achieved through simply heating the sample and forcing the water to evaporate from within the material. Further work on this would be required to confirm if water molecules present within the coating lead to the unusual conduction behaviour observed.

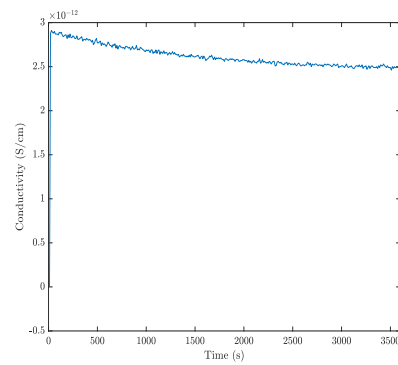
It is of note again that sample type 3 shows unusual behaviour, increasing in magnitude by a factor of 10 000. In order to understand this behaviour time time dependent conductivity was investigated. Fig. 7.6 shows the time dependent conductivity of each sample type, represented here for the start of the measurements at a field strength of 5 kV/mm. As can be seen from the plots, all samples except sample type 3 show a relatively constant conductance over their measurement time. The addition of the



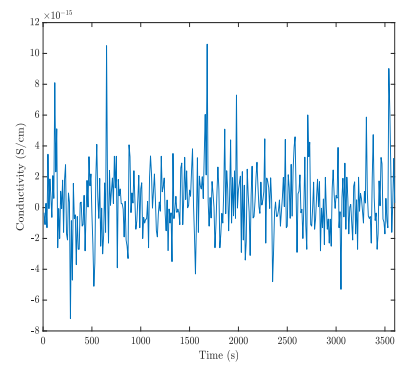
(a) Sample Type 1



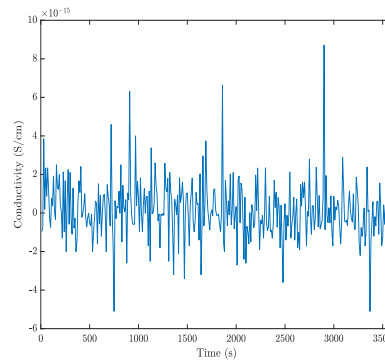
(b) Sample Type 2



(c) Sample Type 3



(d) Sample Type 4



(e) Sample Type 5

Figure 7.6: Time dependent conductivity measurements for the samples produced. Results shown in this Figure represent the start of the measurement process, where the electric field strength is 5 kV/mm. Sub-figures (a) - (e) show the results of different sample types. Refer to Table 7.1 for their designation.

coating does show a slight change to the conductivity of the sample, which has been observed for other filler particles [196–198], where filler particles aligned to the electric field direction, can act as trap sites reducing the flow of the electrical charges within the material. The unusual behaviour observed in sample type 3, could help to explain why it shows such high permittivity and conduction. As can be seen from the plot within 10 seconds of the measurement the conductivity increases rapidly from  $-1.80 \times 10^{-16}$  to  $2.88 \times 10^{-12}$  S/cm, which proceeds to slowly decrease throughout the measurement. This decreasing effect is observed throughout all the electric field strengths tested. This sudden jump in conductivity is likely related to free charge carriers within the material, which would suggest that either this material is not a suitable combination, or the sample itself is the cause of the unusual behaviour. Further testing on samples of this type would be necessary to determine if this is the true behaviour of the sample.

## 7.4 Electrical breakdown performance

Perhaps the most key property to evaluate a dielectric material is its electrical breakdown strength. In the simplest terms electrical breakdown is the point at which the dielectric material begins to conduct and subsequently becomes a conductor. This point is reached when the electrical field is equal to or greater than the materials dielectric strength. The electrical breakdown is measured by placing the test sample between two metal electrodes and ramping the voltage (to increase the electric field strength) until the sample becomes conductive, at which point the test ends and the voltage that lead to breakdown is recorded. This process is repeated across differing regions of the sample in order to determine the statistical mean of breakdown strength. The results are typically analysed using a Weibull probability distribution, where the shape parameter,  $\alpha$ , allows determination of the average breakdown strength and the scale parameter,  $\beta$ , represents the reproducibility of the results.

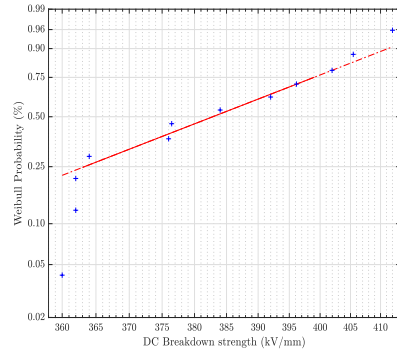
### 7.4.1 Under DC field

The Weibull plots of the base polymer and the coated polymer samples are shown in Fig. 7.7 for a DC voltage. The resulting output from the Weibull analysis is shown in Table 7.2, with a percentage comparison to the electrical breakdown strength of LDPE for each coated sample. When looking at the summary of the results as shown in Table

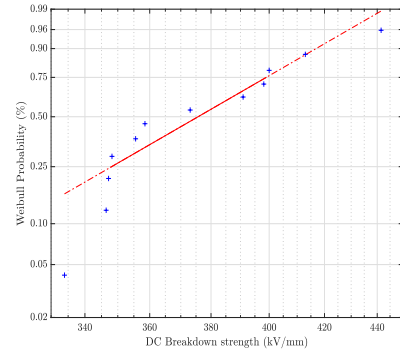
Table 7.2: Scale and shape parameter analysis for the Weibull plots of samples tested for DC electrical breakdown. Given uncertainties are the standard errors of the fits.

Sample Type	Scale ( $\alpha$ )	Shape ( $\beta$ )	% Change from LDPE
1	391.30±5.10	23.49±5.27	-
2	390.60±10.05	11.92±2.53	-0.18
3	417.57±13.27	9.64±2.12	6.71
4	335.32±13.02	7.86±1.79	-14.31
5	404.19±11.29	10.90±2.55	3.29

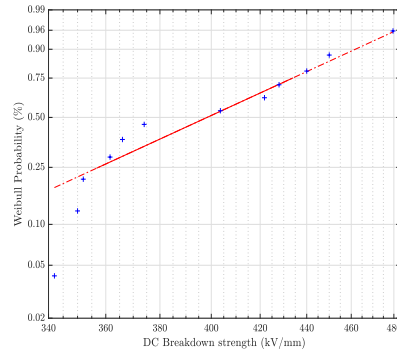
7.2, it is clear the desired significant increase to electrical breakdown strength has not been achieved. However, for sample types 3 and 5 there is an improvement to the breakdown strength, even if slight. Unusually the nanocomposite materials performed worse than their microcomposite alternatives, which is not very often observed for conventional filler particle composite materials. The reason for this poor performance under electrical breakdown testing is most likely attributed to the coating itself. For example even small regions where the coating is not completely uniform can present pathways for which the current can flow and lead to earlier breakdown of the material. This would also be the case should surface cracks have been formed on the material. The reasoning for the poorer performance of the Cloisite Na<sub>+</sub> based gel could be due to the combination of the two types of clay leading to a subsequently less ordered coating with a higher probability of crack formation. To understand the surface uniformity further investigations are required beyond that of the SEM. It is also useful to note that the shape parameters are greater than 1, which tells us the failure rate increases with time, this usually implies some form of ageing process. Which we can infer here to mean the material is weakening to the increasing voltage over time rather than weaker sections failing initially and the tougher parts failing after a longer time.



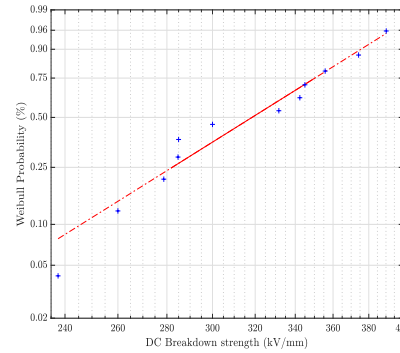
(a) Sample Type 1



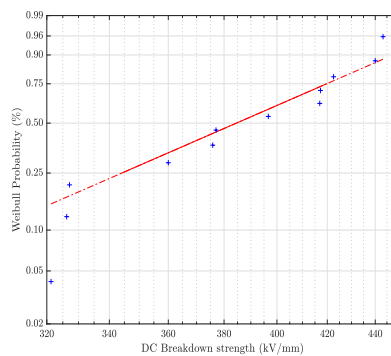
(b) Sample Type 2



(c) Sample Type 3



(d) Sample Type 4



(e) Sample Type 5

Figure 7.7: Weibull probability plots for the DC electrical breakdown measurements of the produced samples. Sub-figures (a) - (e) show the results of different sample types. Refer to Table 7.1 for their designation.

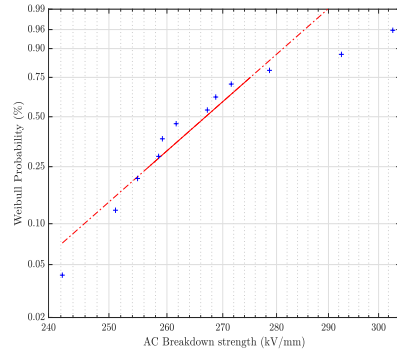
### 7.4.2 Under AC field

Now we will consider the samples breakdown performance under AC voltage conditions. The Weibull plots the samples tested under AC conditions are shown in Fig. 7.8. As before the analysis parameters from the fit and the percentage comparison to the base polymer, are shown in Table 7.3. Again here we can see that there is a

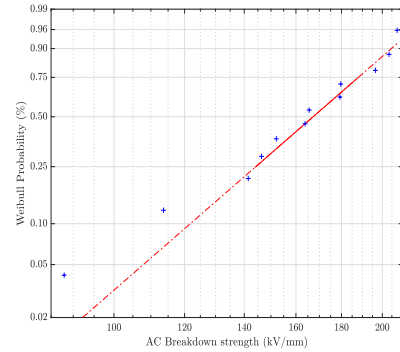
Table 7.3: Scale and shape parameter analysis for the Weibull plots of samples tested for AC electrical breakdown. Given uncertainties are the standard errors of the fits.

Sample Type	Scale ( $\alpha$ )	Shape ( $\beta$ )	% Change from LDPE
1	$275.60 \pm 5.46$	$15.50 \pm 3.22$	-
2	$174.91 \pm 9.15$	$5.78 \pm 1.37$	-36.53
3	$147.21 \pm 3.68$	$12.07 \pm 2.87$	-46.59
4	$157.45 \pm 5.82$	$8.22 \pm 1.87$	-42.87
5	$207.66 \pm 9.59$	$6.61 \pm 1.48$	-24.65

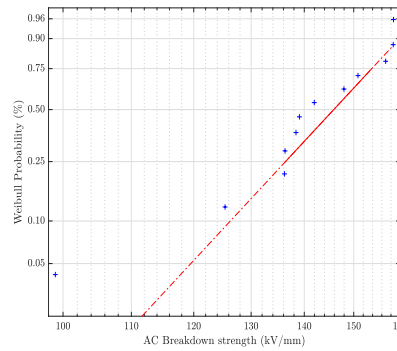
significant decrease in the breakdown strength, however for the SWN coated samples (type 3 and 5) there is a good improvement between the micro- and nanocomposite material. The difference between DC and AC breakdown strength which has been observed since the late 19<sup>th</sup> century [199] onwards [200, 201]. While there is still no singular theory for the mechanism of electrical breakdown, Li *et al.* [202] suggest a process of space charge accumulation which under AC voltages leads to higher charge accumulation and more significant field distortion, which in turn leads to lower breakdown strengths. They also observed a decrease in breakdown strength with increasing frequency through both simulation and experiment. The reasons for the much lower breakdown strength is likely attributed to the reasons discussed above for DC breakdown with regards to the sample coating. The presence of adsorbed water within the coating could also be playing a more significant role within the AC breakdown due to the accumulation of charge and causing further field distortions. While the breakdown results do not show any significant signs of improvement, the breakdown strength of the LDPE shows a much greater value than that reported in the literature [203, 204], between 130 to 210 kV/mm, dependent on sample thickness. Therefore the percentage difference observed in the samples may be much less than shown in Table 7.3.



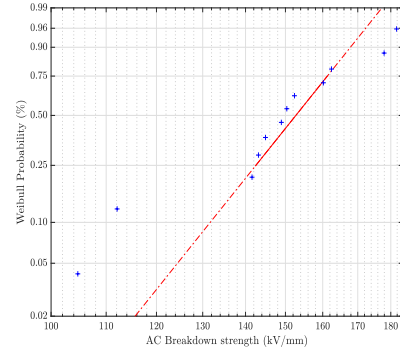
(a) Sample Type 1



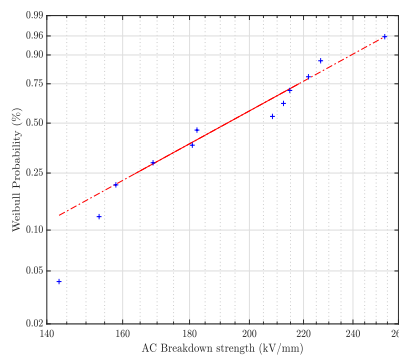
(b) Sample Type 2



(c) Sample Type 3



(d) Sample Type 4



(e) Sample Type 5

Figure 7.8: Weibull probability plots for the AC electrical breakdown measurements of the produced samples. Sub-figures (a) - (e) show the results of different sample types. Refer to Table 7.1 for their designation.

While it would be wise to also make measurements of the space charge accumulation within the samples to further interpret the breakdown results, knowledge of the sample itself is also of key importance as this is also likely to play a large role within the electrical breakdown performance, along with the conduction behaviour.

## 7.5 Considerations from electrical testing

Although the results obtained do not show the desired improvement to the electrical properties, they do help to identify issues with the design that can now be further investigated. The most obvious issue with the produced materials is that they may not possess enough clay in the coating to produce a uniform enough layer. While the results in Fig. 6.20 suggest the coating contains around 3% of clay by mass, akin to the filler loading for that of conventional nanocomposite materials, this may not be able to produce a sufficiently thick uniform coating. To fully assess the uniformity of the coating, conventional approaches, such as AFM for roughness measurements will not give true representations for the sample due to the size of the material. Therefore, an alternative method is needed that captures the entire surface structure. The technique used is known as contact angle mapping. In this approach droplets of a test liquid are placed at equidistant points onto the surface and the contact angle measured. The measured values are then extrapolated outwards radially using an inverse distance weighted approach, to approximate the contact angle across the surface. Through the use of enough droplets on the surface a good approximation for the surface uniformity can be determined from the value of the contact angle. For this measurement 5  $\mu\text{L}$  droplets of ultrapure water were used as the test liquid, with the drops positioned as shown by the image in Fig. 7.9. The surface morphology was evaluated using this method for the original LDPE substrate and a LDPE substrate coated with a 75  $\mu\text{m}$  film. A second test using a 200  $\mu\text{m}$  film was also investigated to evaluate the uniformity of thicker produced coatings. These results are shown in Figures 7.10 to 7.12, respectively. As can be seen from the figures, the contact angle variation between the

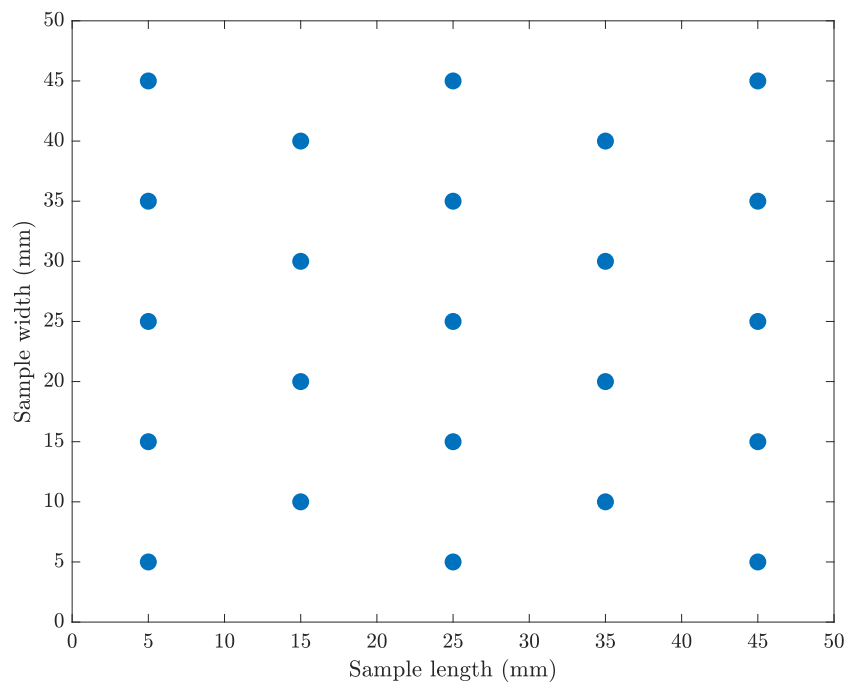


Figure 7.9: Positions for the placement of the droplets onto the sample surface.

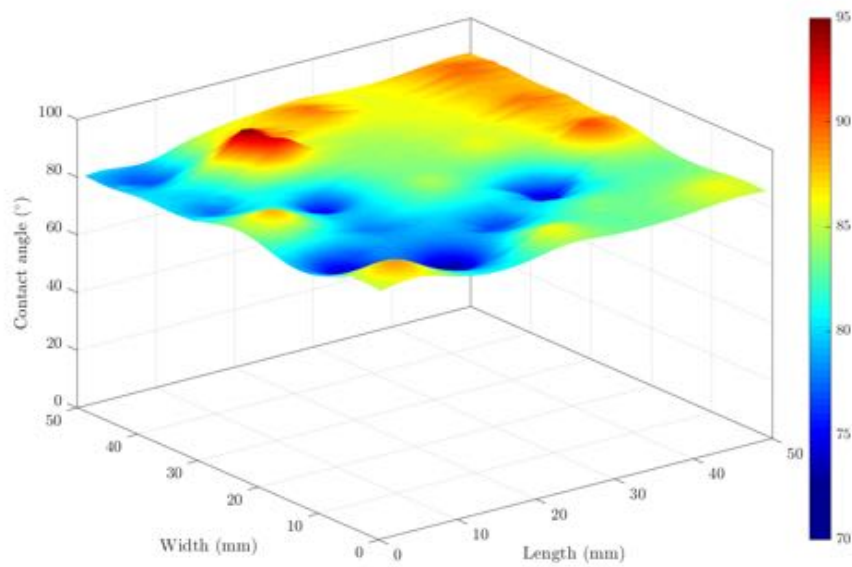


Figure 7.10: Surface uniformity evaluation through measurement of contact angles across the surface for the LDPE substrate. Colour bar is used as a guide to the vertical scale.

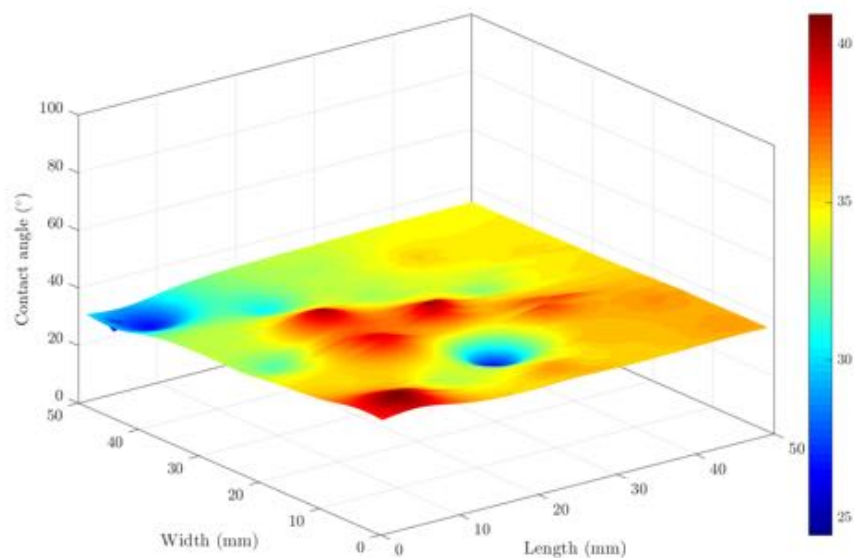


Figure 7.11: Surface uniformity evaluation through measurement of contact angles across the surface for the 75  $\mu\text{m}$  coated LDPE substrate. Colour bar is used as a guide to the vertical scale.

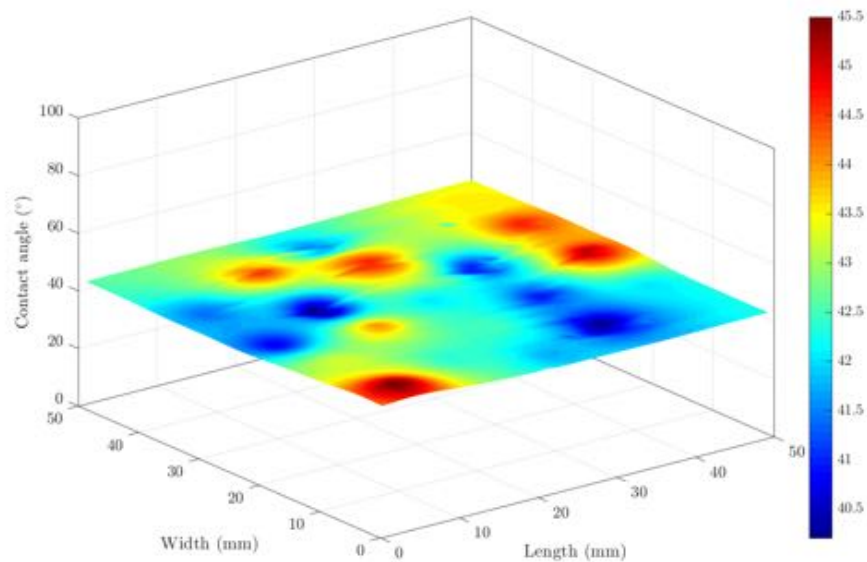


Figure 7.12: Surface uniformity evaluation through measurement of contact angles across the surface for the 200  $\mu\text{m}$  coated LDPE substrate. Colour bar is used as a guide to the vertical scale.

two coated samples is significant. In the 75  $\mu\text{m}$  coated sample, the contact angle ranges from 25 to 45 degrees, showing several regions of surface with high variation in contact angle. This suggests the surface to have differing levels of coating, which subsequently could be a leading cause of the lower breakdown strength. When compared to the 200  $\mu\text{m}$  coated sample, the contact angle shows a much smaller variation with the contact angle ranging from 40.5 to 45.5. This shows a much greater level of uniformity on the coating, even in comparison to the original polymer. Also of note is that the base LDPE layer shows a reasonable level of non-uniformity, with contact angles ranging from 70 - 95 degrees. This shows two factors; the first being a thicker coating leads to greater uniformity of the surface, care needs to be taken in the thickness to avoid the coating splitting and cracking, and the base polymer layer should be carefully placed to avoid unnecessary peaks and troughs which would subsequently effect the uniformity of the coating. Therefore, the next steps from this analysis would be to produce samples using a thicker coating, perhaps from 200  $\mu\text{m}$ , and determine if the uniformity of the surface plays a role in the electrical breakdown strength.

The second parameter identified to play a role in the dielectric performance is water content within the material. The clay itself is known to contain both adsorbed cations and water molecules, which could both play a role in the poorer than expected dielectric behaviour. The issue is that knowledge of the volume of the water and cations is difficult to measure. While one potential solution is to modify the natural clay using surfactant to form organically modified clay without the interlayer species, this then presents a problem in how to form the organoclay material into a gel suitable for coating. Therefore, the most viable method would be to remove the adsorbed water from within the clay layers. The simplest way to remove the adsorbed water is through heating for a sufficient time. As can be seen from the TGA curves of the clay in Chapter 4, the inter-layer water cannot begin to be removed until the temperature exceeds 300°C, and of course this is not viable for a polymer which melts at around 105°C. Therefore, an alternative approach is to heat the sample at a reduced temperature and

reduced pressure. This was achieved by drying the sample in a Gallenkamp Vacuum Oven OVA03100 (Gallenkamp and Company Ltd., UK), at 40°C and a pressure of 100 mBar. To determine the content of water within the sample, a thermogram was collected after heating for a set amount of time and the water content analysed using the relationship shown in eqn. 7.2.

$$\text{Water \%} = \frac{(\text{Composite mass \%})_{250^{\circ}\text{C}} - (\text{Polymer mass \%})_{250^{\circ}\text{C}}}{(\text{Composite mass \%})_{600^{\circ}\text{C}}} \quad (7.2)$$

Using this relation and the respective thermograms, the determined water content for increasing drying time, is shown in Fig. 7.13. As can be seen from the plot there is a

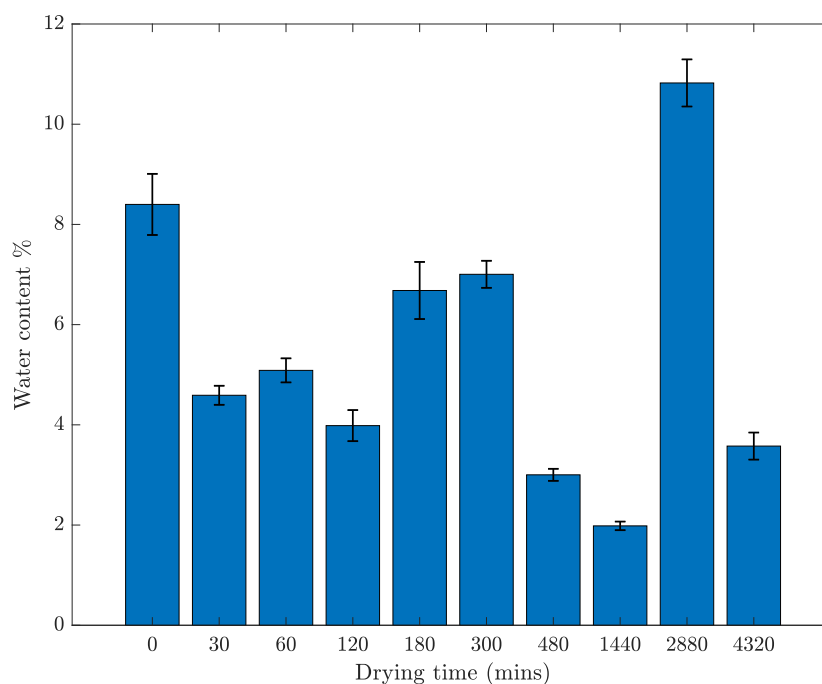


Figure 7.13: Determined water content for samples at varying vacuum oven drying times.

significant reduction in the determined water content even after a short period of time, as can be seen from the reduction of around 50% after 30 minutes of drying. With the increasing times there is a general trend towards decreasing water content, albeit with some outliers. The results show that the water content tends to saturate towards a

level of 2 - 3 %, and while this means that some water will remain in the sample, the level should be low enough that the effect of water should be minimal on the dielectric properties.

## 7.6 Summary

This Chapter explored the electrical properties of the materials developed from the previous Chapter. A comparison was made between the base polymer, un-treated colloid gels and exfoliated colloid gels for both types of gels produced. The key results from the electrical testing are:

- Dielectric spectroscopy measurements show that there is a minimal increase in the real permittivity in comparison to the base polymer, showing the capacitance of the dielectric material remains relatively unchanged also. A noticeable change however is seen in the imaginary permittivity with a peak centring around 50 Hz, which would lead to complications if the material is used for conventional electrical supplies. This effect is more prominent in SWN than Cloisite Na<sup>+</sup> where the peak is shifted towards slightly larger frequencies. The loss angle measurements show the material behaves as a good dielectric material.
- Unusual conducting behaviour is observed for several of the samples, and it is expected this behaviour is due to the adsorbed cationic species and water molecules within the clay coating, altering the conductivity of the material.
- A minor improvement to the electrical breakdown is seen within samples produced using SWN gel, with the Cloisite Na<sup>+</sup> gel samples showing much poorer performance in electrical breakdown strength. A much poorer performance is seen in AC electrical breakdown across the spectrum of samples, but this is an often seen effect that AC breakdown strengths are less than DC breakdown strengths.

While the produced materials did not provide the expected increased performance as was predicted, by further investigation suggestions to perform the electrical performance are presented. Key to this is the surface uniformity and while it was expected

this to be good, mapping data shows that this was not the case. However the mapping results suggest using a coating of 200  $\mu\text{m}$  will lead to a much greater surface uniformity, and hence improved electrical performance.

# Chapter 8

## Summary

In this final Chapter the aim of the thesis and its associated objectives will be discussed drawing the individual conclusions together to summarise the body of work. Avenues for further directions of this work will be discussed also.

### **8.1 Thesis summary**

The aim of this thesis was to develop a novel continuous layered insulation material for use in dielectric applications. The process to develop such a material involved the use of a nanoparticle layer applied through a gel coating technique. Therefore, this thesis is in essence focused on two tasks; development of a uniform nanoparticle gel network to be used for the coating and the subsequent development of the layered material and its electrical properties explored.

While there are many nanoparticles that are exploited for use within nanocomposite materials, the focus of this study was on nanoclay. The reasoning for this being that not only are they often employed but they exhibit a natural self-cross linking property that leads to gel formation [106, 205]. The development of the gel material formed the first objective of the thesis. The cross linking process was investigated through both dynamic light scattering and rheological experiments. Which provided knowledge on the gel formation ability, but did not account for the responsible mechanism. Therefore, a further method of neutron scattering was employed to fully understand the mechanism of the gelation. The understanding of the gelation process has allowed control over the formation of the gel network to be employed, and also allowed comparison between both micro- and nano- sized particle gels. It is noted that while the techniques employed to explore the gelation process would be appreciable to other particle systems, the self-cross linking behaviour means no further inclusion is needed to form the gel network, where as many other particles are likely to require a precursor or undergo a sol gel type reaction to form a gel system [206–208]. But as shown in Chapter 6 hybrid gel systems were formed using SWN as an initiator which would allow other clay hybrid gels to be formed, for example the addition of hexagonal boron nitride into a SWN

colloid can produce a hybrid gel that would provide a higher thermal conductivity than clay alone [209].

One of the biggest issues for conventional filler loaded nanocomposite materials is the compatibility between the filler particle and polymer matrix. For example, the LDPE polymer employed within this thesis, shows very poor compatibility to nanoclay due to their hydrophobic and hydrophilic natures, respectively [210, 211]. Typically, this problem is overcome through organic modification of the clay, leading to greater compatibility, but this removes the original self-cross linking behaviour. However, in this thesis, the employed process shows that only surface treatment is required to allow a compatibility between the gel coating and the polymer base layer. This technique therefore shows a new approach that would allow alternative polymer or nanoparticles to be used that were previously incompatible, to give greater improvement to the electrical properties of the composite material.

In Chapter 6, a detailed approach for the formation of the layered material is shown, with the key take away being that a continuous nanoparticle layer was formed upon a polymer surface, avoiding the formation of cracks or defects that would hinder the dielectric behaviour. Nominally the loading of nanocomposite materials is a maximum of 5 wt.%, thus the relative mass percentage of clay within the coating was aimed to be within the same range without compromising the properties of the material. The subsequent dielectric measurements however show a limitation of the developed material, with a poorer than expected performance observed. The possible reasoning behind this was explored. The primary explanation for the poorer than expected breakdown performance is likely attributed to the coating uniformity, as even small regions of non-uniformity would provide pathways for the current to deflect through and reduce the breakdown strength. Through mapping the surface uniformity it is clear the 75  $\mu\text{m}$  coating has regions of differing uniformity, which would subsequently explain the performance under electrical breakdown. Performing the same process for a 200  $\mu\text{m}$

coated sample, we can see an improvement to the surface uniformity, which would suggest it would show the expected increase under the electrical breakdown test. We also note unusual conductivity within the samples, and expect this to be attributed to an uncontrolled presence of charged species. This effect is a natural attribute of the clay particles as they adsorb water and cationic species to counter balance their charge. The presence of these species is likely to contribute to the unusual conduction behaviour observed. A process to dry the materials under vacuum to remove the adsorbed water has been shown to decrease the water content within the material, however removal of the cationic species, which while possible would most likely remove the gelling ability of the clay. An alternative approach is to use a nanoparticle species that doesn't adsorb water or poses free charge carrying species, but this would of course require a gel to be formed of the nanoparticle. While it was desirable to investigate the dielectric properties of materials coated with thicker applied coatings the finite time of the study did not allow this.

The work of this thesis presented a novel method for the formation of a novel nanostructured dielectric material through, the use of a continuous coating as opposed to the inclusion of filler particles. Therefore, this is advantageous in regard to the choice of the polymer matrix and filler particle, overcoming the compatibility issues often encountered. However, the developed materials are within the early stages of development and further work is required in order to evolve this novel technique.

## 8.2 Future work

As with any research the success of an element often leads to several new interesting avenues that warrant study. Therefore in this section, I will present some suggestions on the future direction of this topic building upon the results already obtained. The obvious starting point is to investigate the effects of different coating thickness on the electrical performance. As was shown in Chapter 7, increasing the applied coating thickness from 75 to 200  $\mu\text{m}$  leads to a significant improvement in the uniformity of the

gel coating produced, and it is likely the thin coating led to poorer than expected electrical breakdown. While a procedural background has been laid down for the process of producing coated polymer surfaces, there is no specific control on the nanoparticles that need to be employed. While nanoclay has been explored in this thesis due to the physical cross linking gelation process and the electrical resistance properties, the inclusion of other nanoparticle species such as graphene or hexagonal boron nitride can provide these same electrical resistivity properties but with the added benefits of non-linear conduction and thermal conductivity, respectively. Changing the nanoparticle to use as a coating may also lead to needing to study chemically cross linked gels, the methods employed in the thesis would allow the studying of this process, but this may change the coating process as the properties of chemically cross linked gels have not been explored here but are known to produce stronger and often more brittle materials when agitated. Like filler loaded nanocomposites the development of the technology will thrive along with the required needs at the time, and the use of nanoparticle species most attributed to the requirements of the task.

# References

- [1] Kutscher, C.F., Milford, J.B. and Kreith, F. *Principles of Sustainable Energy Systems, Third edition*. Mechanical and Aerospace Engineering Series. CRC Press, Florida, United States, (2018).
- [2] Commissariat à l'énergie atomique et aux énergies alternatives. ANASTASIA (Advanced NAno-Structured TApeS for electrotechnical high power Insulating Applications). Project ID: 228581, (2012).
- [3] Landel, R. F and Nielsen, L. E. *Mechanical properties of polymers and composites*. CRC press, (1993).
- [4] Jordan, J., Jacob, K.I., Tannenbaum, R., Sharaf, M.A. and Jasiuk, I. Experimental trends in polymer nanocomposites: a review. *Materials science and engineering: A*, **393**(1-2):1–11, (2005).
- [5] Kumar, S., Nehra, M., Dilbaghi, N., Tankeshwar, K. and Kim, K.H. Recent advances and remaining challenges for polymeric nanocomposites in healthcare applications. *Progress in Polymer Science*, **80**:1–38, (2018).
- [6] Müller, K., Bugnicourt, E., Latorre, M., Jorda, M., Echehoven Sanz, Y., Lagaron, J.M., Miesbauer, O., Bianchin, A., Hankin, S., Bölz, U. and Perez, G. Review on the processing and properties of polymer nanocomposites and nanocoatings and their applications in the packaging, automotive and solar energy fields. *Nanomaterials*, **7**(4):74, (2017).

- [7] Drude, P. Zur elektronentheorie der metalle [On the electron theory of metals]. *Annalen der physik*, **306**(3):566–613, (1900).
- [8] Mossotti, O.F. *Discussione analitica sull'influenza che l'azione di un mezzo dielettrico ha sulla distribuzione dell'elettricità alla superficie di più corpi elettrici disseminati in esso* [Analytical discussion on the influence that the action of a dielectric medium has on the distribution of electricity at the surface of several electric bodies scattered in it]. by types of r. D. room, (1846).
- [9] Clausius, R. *Die mechanische behandlung der electricität* [Mechanical treatment of electricity], volume 2. Vieweg+ Teubner Verlag, (1879).
- [10] Teachout, R.R. and Pack, R.T. The static dipole polarizabilities of all the neutral atoms in their ground states. *Atomic Data and Nuclear Data Tables*, **3**:195–214, (1971).
- [11] Mazur, J. Change of the Dielectric Constant of Nitrobenzene with Temperature. *Nature*, **126**(3191):993, (1930).
- [12] Smyth, C.P. and Hitchcock, C.S. The dielectric constants and transitions of solid ammonia, hydrogen sulfide and methyl alcohol. *Journal of the American Chemical Society*, **56**(5):1084–1087, (1934).
- [13] Debye, P. and Ramm, W. Hochfrequenzverluste und quasikristalline Struktur von Flüssigkeiten [High frequency losses and quasicrystalline liquid structure]. *Annalen der Physik*, **420**(1):28–34, (1936).
- [14] Stone, G.C., Boulter, E.A., Culbert, I. and Dhirani, H. *Electrical Insulation for Rotating Machines: Design, Evaluation, Aging, Testing, and Repair*. IEEE Pressy, Piscataway, NJ, USA, (2004).
- [15] Fowler, R.H. and Nordheim, L. Electron emission in intense electric fields. *Proceedings of the Royal Society of London. Series A, Containing Papers of a Mathematical and Physical Character*, **119**(781):173–181, (1928).

- [16] Zeller, H.R. and Schneider, W.R. Electrofracture mechanics of dielectric aging. *Journal of applied physics*, **56**(2):455–459, (1984).
- [17] Zeller, H.R. Breakdown and prebreakdown phenomena in solid dielectrics. *IEEE Transactions on Electrical insulation*, **22**(2):115–122, (1987).
- [18] Boggs, S.A. Theory of a defect-tolerant dielectric system. *IEEE transactions on electrical insulation*, **28**(3):365–371, (1993).
- [19] Dissado, L.A., Mazzanti, G.C.M.G. and Montanari, G.C. The incorporation of space charge degradation in the life model for electrical insulating materials. *IEEE Transactions on Dielectrics and Electrical Insulation*, **2**(6):1147–1158, (1995).
- [20] Mazzanti, G.C.M.G., Montanari, G.C. and Dissado, L.A. A space-charge life model for ac electrical aging of polymers. *IEEE Transactions on Dielectrics and Electrical Insulation*, **6**(6):864–875, (1999).
- [21] Mazzanti, G.C.M.G. and Montanari, G.C. Electrical aging and life models: the role of space charge. *IEEE Transactions on Dielectrics and Electrical Insulation*, **12**(5):876–890, (2005).
- [22] Kreuger, F.H. *Discharge Detection in High Voltage Equipment*. American Elsevier, New York, (1965).
- [23] Kao, K.C. New theory of electrical discharge and breakdown in low-mobility condensed insulators. *Journal of applied physics*, **55**(3):752–755, (1984).
- [24] O'Dwyer, J.J. *The theory of electrical conduction and breakdown in solid dielectrics*. Clarendon Press, (1973).
- [25] Hanscomb, J.R. High temperature electrical breakdown in sodium chloride. *Australian Journal of Physics*, **15**(4):504–512, (1962).
- [26] Hanscomb, J.R. Thermal breakdown caused by field-enhanced conduction in alkali halides. *Journal of Physics D: Applied Physics*, **2**(9):1327–1338, (1969).

- [27] Whitehead, S. *Dielectric Breakdown of Solids*. Clarendon, Oxford, (1961).
- [28] Zener, C. A theory of the electrical breakdown of solid dielectrics. *Proceedings of the Royal Society of London. Series A, Containing Papers of a Mathematical and Physical Character*, **145**(855):523–529, (1934).
- [29] Smith, R.A. *Wave Mechanics of Crystalline Solids*. Chapman and Hall, London, (1963).
- [30] Seitz, F. On the mobility of electrons in pure non-polar insulators. *Physical Review*, **73**(6):549–564, (1948).
- [31] O’Dwyer, J.J. Theory of high field conduction in a dielectric. *Journal of Applied Physics*, **40**(10):3887–3890, (1969).
- [32] Stark, K.H. and Garton, C.G. Electric strength of irradiated polythene. *Nature*, **176**(4495):1225–1226, (1955).
- [33] Fava, R.A. Intrinsic electric strength and electromechanical breakdown in polythene. In *Proceedings of the Institution of Electrical Engineers*, volume **112**, pages 819–823. IET, (1965).
- [34] McKeown, J.J. Intrinsic electric strengths of organic polymeric materials. In *Proceedings of the Institution of Electrical Engineers*, volume **112**, pages 824–828. IET, (1965).
- [35] Blok, J. and LeGrand, D.G. Dielectric breakdown of polymer films. *Journal of Applied Physics*, **40**(1):288–293, (1969).
- [36] Lawson, W.G. Effects of temperature and techniques of measurement on the intrinsic electric strength of polythene. In *Proceedings of the Institution of Electrical Engineers*, volume **113**, pages 197–202. IET, (1966).
- [37] Budenstein, P.P. On the mechanism of dielectric breakdown of solids. *IEEE Transactions on Electrical Insulation*, **EI-15**(3):225–240, (1980).

- [38] Knaur, J.A. and Budenstein, P.P. Impulse Breakdown in PMMA under Megavolt, Nanosecond Excitation. *IEEE Transactions on electrical insulation*, **EI-15**(4):313–321, (1980).
- [39] Lewis, T.J. Nanometric dielectrics. *IEEE Transactions on Dielectric and Electrical Insulation*, **1**(5):812–825, (1994).
- [40] Henk, P.O., Kortsen, T.W. and Kvarst, T. Increasing the electrical discharge endurance of acid anhydride cured DGEBA epoxy resin by dispersion of nanoparticle silica. *High Performance Polymers*, **11**(3):281–296, (1999).
- [41] Nelson, J.K. and Fothergill, J.C. Internal charge behaviour of nanocomposites. *Nanotechnology*, **15**(5):586–589, (2004).
- [42] Han, J. and Garrett, R. Overview of polymer nanocomposites as dielectrics and electrical insulation materials for large high voltage rotating machines. In *NSTI-Nanotech*, volume **2**, pages 727–732, (2008).
- [43] Tanaka, T., Montanari, G.C. and Mulhaupt, R. Polymer nanocomposites as dielectrics and electrical insulation-perspectives for processing technologies, material characterization and future applications. *IEEE transactions on Dielectrics and Electrical Insulation*, **11**(5):763–784, (2004).
- [44] Camargo, P.H.C., Satyanarayana, K.G. and Wypych, F. Nanocomposites: synthesis, structure, properties and new application opportunities. *Materials Research*, **12**(1):1–39, (2009).
- [45] Sheer, M.L. Advanced composites: The leading edge in high performance motor and transformer insulation. In *Proceedings of the 20th Electrical Electronics Insulation Conference*, pages 181–185. IEEE, (1991).
- [46] Nelson, J.K. Overview of nanodielectrics: Insulating materials of the future. In *2007 Electrical Insulation Conference and Electrical Manufacturing Expo*, pages 229–235. IEEE, (2007).

- [47] Nelson, J.K. *Dielectric polymer nanocomposites*. Springer, New York, (2010).
- [48] Stone, G.C., Boulter, E.A., Culbert, I. and Dhirani, H. Historical development of insulation materials and systems. In S. V. Kartalopoulos, editor, *Electrical Insulation for Rotating Machines: Design, Evaluation, Aging, Testing, and Repair*, chapter 3, pages 73–94. Wiley-IEEE Pressy, Piscataway, NJ, USA, (2004).
- [49] Pyrhonen, J., Jokinen, T. and Hrabovcova, V. Insulation of electrical machines. In *Design of rotating electrical machines*, pages 429–455, (2013).
- [50] Park, J.J. AC Electrical breakdown characteristics of an epoxy/mica composite. *Transactions on electrical and electronic materials*, **13**(4):200–203, (2012).
- [51] Kojima, Y., Usuki, A., Kawasumi, M., Okada, A., Kurauchi, T. and Kamigaito, O. One-pot synthesis of nylon 6-clay hybrid. *Journal of Polymer Science Part A: Polymer Chemistry*, **31**(7):1755–1758, (1993).
- [52] Fréchette, M.F., Trudeau, M., Alamdari, H.D. and Boily, S. Introductory remarks on nanodielectrics. In *Conference on Electrical Insulation and Dielectric Phenomena*, pages 92–99, (2001).
- [53] Cao, Y., Irwin, P.C. and Younsi, K. The future of nanodielectrics in the electrical power industry. *IEEE Transactions on Dielectrics and Electrical Insulation*, **11**(5):797–807, (2004).
- [54] Tanaka, T. and Imai, T. Advances in nanodielectric materials over the past 50 years. *IEEE Electrical Insulation Magazine*, **29**(1):10–23, (2013).
- [55] Tanaka, T., Bulinski, A., Castellon, J., Frechette, M., Gubanski, S., Kindersberger, J., Montanari, G.C., Nagao, M., Morshuis, P., Tanaka, Y. and Pelissou, S. Dielectric properties of XLPE/SiO<sub>2</sub> nanocomposites based on CIGRE WG D1. 24 cooperative test results. *IEEE Transactions on Dielectrics and Electrical Insulation*, **18**(5):1482–1517, (2011).

- [56] Krivda, A., Tanaka, T., Frechette, M., Castellon, J., Fabiani, D., Montanari, G.C., Gorur, R., Morshuis, P., Gubanski, S., Kindersberger, J. and Vaughn, A. Characterization of epoxy microcomposite and nanocomposite materials for power engineering applications. *IEEE Electrical Insulation Magazine*, **28**(2):38–51, (2012).
- [57] Castellon, J., Nguyen, H.N., Agnel, S., Toureille, A., Frechette, M., Savoie, S., Krivda, A. and Schmidt, L.E. Electrical properties analysis of micro and nano composite epoxy resin materials. *IEEE Transactions on Dielectrics and Electrical Insulation*, **18**(3):651–658, (2011).
- [58] Singha, S. and Thomas, M.J. Dielectric properties of epoxy nanocomposites. *IEEE Transactions on Dielectrics and Electrical Insulation*, **15**(1):12–23, (2008).
- [59] Tanaka, T., Kozako, M., Fuse, N. and Ohki, Y. Proposal of a multi-core model for polymer nanocomposite dielectrics. *IEEE Transactions on Dielectrics and Electrical Insulation*, **12**(4):669–681, (2005).
- [60] Kadhim, M.J., Abdullah, A.K., Al-Ajaj, I.A. and Khalil, A.S. Dielectric properties of epoxy/Al<sub>2</sub>O<sub>3</sub> nanocomposites. *International Journal of Application or Innovation in Engineering & Management*, **3**:468–477, (2014).
- [61] Castellon, J., Agnel, S., Toureille, A. and Frechette, M. Space charge characterization of multi-stressed microcomposites nano-filled epoxy for electrotechnical applications. In *Proceedings of the Conference on Electrical Insulation and Dielectric Phenomena (CEIDP)*, pages 532–535, (2008).
- [62] Magraner, F., García-Bernabé, A., Gil, M., Llovera, P., Dodd, S.J. and Dissado, L.A. Space charge measurements on different epoxy resin alumina nanocomposites. In *Proceedings of the International Conference on Solid Dielectrics (ICSD)*, pages 1–4, (2010).

- [63] Dissado, L.A., Mazzanti, G. and Montanari, G.C. The role of trapped space charges in the electrical aging of insulating materials. *IEEE Transactions on Dielectrics and Electrical Insulation*, **4**(5):496–506, (1997).
- [64] Gröpper, P., Hildinger, T., Pohlmann, F. and Weidner, J.R. Nanotechnology in high voltage insulation systems for large electrical machinery: first results. *Water Energy Int*, **70**:65–66, (2013).
- [65] Zweifel, P. and Fennessey, S.F. Thermal conductivity of reinforced composites for electrical application. In *Proceedings of the IEEE International Symposium on Electrical Insulation (ISEI)*, pages 1–4, (2010).
- [66] Zhang, C., Han, Z. and Stevens, C.G. Effects of micro and nano fillers on electrical and thermal properties of epoxy resin. In *Proceedings of the 10th International Electrical Insulation Conference (INSUCON)*, (2006).
- [67] Murata, Y., Sakamaki, M., Abe, K., Inoue, Y., Mashio, S., Kashiyama, S., Matsunaga, O., Igi, T., Watanabe, M., Asai, S. and Katakai, S. Development of high voltage DC-XLPE cable system. *SEI Technical Review*, **101**:55–62, (2013).
- [68] Xanthos, M. Polymers and polymer composites. In M. Xanthos, editor, *Functional Fillers for Plastics*, chapter 1, pages 1–18. Wiley-VCH Verlag GmbH & Co. KGaA, Weinheim, Germany, 2 edition, (2010).
- [69] Pleșa, I., Noțingher P.V., Schlögl, S., Sumereder, C. and Muhr, M. Properties of Polymer Composites Used in High-Voltage Applications. *Polymers*, **8**(5):173–236, (2016).
- [70] Huang, X., Jiang, P. and Tanaka, T. A review of dielectric polymer composites with high thermal conductivity. *IEEE Electrical Insulation Magazine*, **27**(4):8–16, (2011).
- [71] Okutan, E., Aydın, G.O., Hacıvelioğlu, F., Kılıç, A., Beyaz, S. K. and Yeşilot, S. Synthesis and characterization of soluble multi-walled carbon nanotube/poly (organophosphazene) composites. *Polymer*, **52**(5):1241–1248, (2011).

- [72] Hong, R.Y. and Chen, Q. Dispersion of inorganic nanoparticles in polymer matrices: challenges and solutions. In Kalia, S., Haldorai, Y., editor, *Organic-Inorganic Hybrid Nanomaterials*, pages 1–38. Springer International Publishing, Berlin Heidelberg, Germany, (2015).
- [73] Tayfun, U., Kanbur, Y., Abaci, U., Guney, H.Y. and Bayramli, E. Mechanical, flow and electrical properties of thermoplastic polyurethane/fullerene composites: Effect of surface modification of fullerene. *Composites Part B: Engineering*, **80**:101–107, (2015).
- [74] Peng, S., He, J. and Hu, J. Influence of surface modification on electrical properties of polyethylene SiO<sub>2</sub> nanocomposites. In *2015 IEEE 11th International Conference on the Properties and Applications of Dielectric Materials (ICPADM)*, pages 372–375, (2015).
- [75] Ma, D., Hugener, T.A., Siegel, R.W., Christerson, A., Mårtensson, E., Önnby, C. and Schadler, L.S. Influence of nanoparticle surface modification on the electrical behaviour of polyethylene nanocomposites. *Nanotechnology*, **16**(6):724–731, (2005).
- [76] Jölly, I., Schlögl, S., Wolfahrt, M., Pinter, G., Fleischmann, M. and Kern, W. Chemical functionalization of composite surfaces for improved structural bonded repairs. *Composites Part B: Engineering*, **69**:296–303, (2015).
- [77] Rong, M.Z., Zhang, M.Q., Zheng, Y.X., Zeng, H.M., Walter, R. and Friedrich, K. Irradiation graft polymerization on nano-inorganic particles: An effective means to design polymer-based nanocomposites. *Journal of Materials Science Letters*, **19**(13):1159–1161, (2000).
- [78] Lewis, T.J. Interfaces: Nanometric dielectrics. *Journal of Physics D: Applied Physics*, **38**(2):202–212, (2005).

- [79] Seiler, J. and Kindersberger, J. Insight into the interphase in polymer nanocomposites. *IEEE Transactions on Dielectrics and Electrical Insulation*, **21**(2):537–547, (2014).
- [80] Fothergill, J.C. Electrical properties. In Nelson, J.K., editor, *Dielectric Polymer Nanocomposites*, pages 197–228. Springer, New York, NY, USA, (2010).
- [81] Jonscher, A.K. *Dielectric Relaxation in Solids*. Chelsea Dielectric Press, London, UK, (1983).
- [82] Singha, S. and Thomas, M.J. Permittivity and tan delta characteristics of epoxy nanocomposites in the frequency range of 1 MHz-1 GHz. *IEEE Transactions on Dielectrics and Electrical Insulation*, **15**(1):2–11, (2008).
- [83] Kochetov, R., Andritsch, T., Morshuis, P.H. and Smit, J.J. Anomalous behaviour of the dielectric spectroscopy response of nanocomposites. *IEEE Transactions on Dielectrics and Electrical Insulation*, **19**(1):107–117, (2012).
- [84] Mackersie, J.W., Given, M.J., MacGregor, S.J. and Fouracre, R.A. The electrical properties of filled epoxy resin systems-A comparison. In *Proceedings of the 2001 IEEE 7th International Conference on Solid Dielectrics (ICSD)*, pages 125–128, (2001).
- [85] Fothergill, J.C., Nelson, J.K. and Fu, M. Dielectric properties of epoxy nanocomposites containing TiO<sub>2</sub>, Al<sub>2</sub>O<sub>3</sub> and ZnO fillers. In *Proceedings of the Conference on Electrical Insulation and Dielectric Phenomena (CEIDP)*, pages 406–409, (2004).
- [86] Smith, R.C., Liang, C., Landry, M., Nelson, J.K. and Schadler, L.S. The mechanisms leading to the useful electrical properties of polymer nanodielectrics. *IEEE Transactions on Dielectrics and Electrical Insulation*, **15**(1):187–196, (2008).
- [87] Pleșa, I., Ciuprina, F. and Notingher, P.V. Dielectric spectroscopy of epoxy resin with and without inorganic nanofillers. *Journal of Advanced Research in Physics*, **1**(1):2069–7201, (2010).

- [88] Mo, H., Huang, X., Liu, F., Yang, K., Li, S. and Jiang, P. Nanostructured electrical insulating epoxy thermosets with high thermal conductivity, high thermal stability, high glass transition temperatures and excellent dielectric properties. *IEEE Transactions on Dielectrics and Electrical Insulation*, **22**(2):906–915, (2015).
- [89] Tanaka, T. Interface properties and surface erosion resistance. In Nelson, J.K., editor, *Dielectric Polymer Nanocomposites*, pages 229–258. Springer, New York, NY, USA, (2010).
- [90] Iizuka, T., Uchida, K. and Tanaka, T. Voltage endurance characteristics of epoxy/silica nanocomposites. *Electronics and Communications in Japan*, **94**(12):65–73, (2011).
- [91] Tanaka, T., Matsuo, Y. and Uchida, K. Partial discharge endurance of epoxy/SiC nanocomposite. In *Proceedings of the Conference on Electrical Insulation and Dielectric Phenomena (CEIDP)*, pages 26–29, (2008).
- [92] Preetha, P. and Thomas, M.J. Partial discharge resistant characteristics of epoxy nanocomposites. *IEEE Transactions on Dielectrics and Electrical Insulation*, **18**(1):264–274, (2011).
- [93] Li, Z., Okamoto, K., Ohki, Y. and Tanaka, T. Effects of nano-filler addition on partial discharge resistance and dielectric breakdown strength of Micro- $\text{Al}_2\text{O}_3$  Epoxy composite. *IEEE Transactions on Dielectrics and Electrical Insulation*, **17**(3):653–661, (2010).
- [94] Li, Z., Okamoto, K., Ohki, Y. and Tanaka, T. The role of nano and micro particles on partial discharge and breakdown strength in epoxy composites. *IEEE Transactions on Dielectrics and Electrical Insulation*, **18**(3):675–681, (2011).
- [95] Li, S., Yin, G., Chen, G., Li, J., Bai, S., Zhong, L., Zhang, Y. and Lei, Q. Short-term breakdown and long-term failure in nanodielectrics: a review. *IEEE Transactions on Dielectrics and Electrical Insulation*, **17**(5):1523–1535, (2010).

- [96] Zhang, Y., Danikas, M., Zhao, X. and Cheng, Y. Preliminary experimental work on nanocomposite polymers: small partial discharges at inception voltage, the existence of possible charging mechanisms below inception voltage and the problem of definitions. *Journal of Electrical Engineering*, **63**(2):109–114, (2012).
- [97] Imai, T., Sawa, F., Nakano, T., Ozaki, T., Shimizu, T., Kuge, S.I., Kozako, M. and Tanaka, T. Insulation properties of nano- and micro-filler mixture composite. In *CEIDP'05. 2005 Annual Report Conference on Electrical Insulation and Dielectric Phenomena*, pages 171–174, (2005).
- [98] Ieda, M. Electrical Conduction and Carrier Traps in Polymeric Materials. *IEEE Transactions on Electrical Insulation*, **EI-19**(3):162–178, (1984).
- [99] Lau, K.Y., Vaughan, A.S., Chen, G., Hosier, I.L., Holt, A.F. and Ching, K.Y. On the space charge and DC breakdown behavior of polyethylene/silica nanocomposites. *IEEE Transactions on Dielectrics and Electrical Insulation*, **21**(1):340–351, (2014).
- [100] Yin, Y., Chen, J., Yang, J., Xiao, D., Tu, D., Yin, R. and Qian, H. Effect of space charge in nanocomposite of LDPE/TiO<sub>2</sub>. In *Proceedings of the 7th International Conference on Properties and Applications of Dielectric Materials*, pages 913–916, (2003).
- [101] Andritsch, T., Kochetov, R., Gebrekiros, Y.T., Lafont, U., Morshuis, P.H.F. and Smit, J.J. Synthesis and dielectric properties of epoxy based nanocomposites. In *Proceedings of the IEEE Conference on Electrical Insulation and Dielectric Phenomena (CEIDP)*, pages 523–526, (2009).
- [102] Roy, M., Nelson, J.K., MacCrone, R.K., Schadler, L.S., Reed, C.W. and Keefe, R. Polymer nanocomposite dielectrics—the role of the interface. *IEEE Transactions on Dielectrics and Electrical Insulation*, **12**(4):629–643, (2005).

- [103] Li, S., Yin, G., Chen, G., Li, J., Bai, S., Zhong, L., Zhang, Y. and Lei, Q. Short-term breakdown and long-term failure in nanodielectrics: a review. *IEEE Transactions on Dielectrics and Electrical Insulation*, **17**(5):1523–1535, (2010).
- [104] Nielsen, L.E. The thermal and electrical conductivity of two-phase systems. *Industrial & Engineering chemistry fundamentals*, **13**(1):17–20, (1974).
- [105] Han, Z., Wood, J.W., Herman, H., Zhang, C. and Stevens, G.C. Thermal properties of composites filled with different fillers. In *Proceedings of the IEEE International Symposium on Electrical Insulation (ISEI)*, pages 497–501, (2008).
- [106] Van Olphen, H. *An Introduction to Clay Colloid Chemistry: For Clay Technologists, Geologists and Soil Scientists*. Wiley, New York, 2 edition, (1977).
- [107] Mackenzie, R.C. A micromethod for determination of cation-exchange capacity of clay. *Journal of Colloid Science*, **6**:219–222, (1951).
- [108] Bardon, C. Recommandations pour la détermination expérimentale de la capacité d'échange de cations des milieux argileux [Recommendations for the experimental determination of the cation exchange capacity of clay media]. *Revue de l'Institut Français du Pétrole*, **38**(5):621–628, (1983).
- [109] American Petroleum Institute. Production Dept. *Recommended Practice Standard Procedure for Field Testing Water-based Drilling Fluids*, volume 13. American Petroleum Institute, (1990).
- [110] Hendershot, W.H. and Duquette, M. A Simple Barium Chloride Method for Determining Cation Exchange Capacity and Exchangeable Cations. *Soil Science Society of America Journal*, **50**(3):605–608, (1986).
- [111] Burrafato, G. and Miano, F. Determination of the cation exchange capacity of clays by surface tension measurements. *Clay Minerals*, **28**:475–475, (1993).

- [112] Greenland, D.J. and Quirk, J.P. Determination of the total specific surface areas of soils by absorption of cetylpyridinium bromide. *Journal of Soil Science*, **15**(2):178–191, (1964).
- [113] Young, T. III. An essay on the cohesion of fluids. *Philosophical transactions of the royal society of London*, **95**:65–87, (1805).
- [114] Shirtcliffe, N.J., McHale, G. and Newton, M.I. Learning from Superhydrophobic Plants: The Use of Hydrophilic Areas on Superhydrophobic Surfaces for Droplet Control. *Langmuir*, **25**(24):14121–14128, (2009).
- [115] Owens, D.K. and Wendt, R.C. Estimation of the surface free energy of polymers. *Journal of Applied Polymer Science*, **13**(8):1741–1747, (1969).
- [116] Ström, G., Fredriksson, M. and Stenius, P.E.R. Contact angles, work of adhesion, and interfacial tensions at a dissolving hydrocarbon surface. *Journal of Colloid and Interface Science*, **119**(2):352–361, (1987).
- [117] Jańczuk, B. and Białopiotrowicz, T. Surface free-energy components of liquids and low energy solids and contact angles. *Journal of Colloid and Interface Science*, **127**(1):189–204, (1989).
- [118] Wu, S. Calculation of interfacial tension in polymer systems. In *Journal of Polymer Science Part C: Polymer Symposia*, volume **34**, pages 19–30, (1971).
- [119] Wu, S. Polar and nonpolar interactions in adhesion. *The Journal of Adhesion*, **5**(1):39–55, (1973).
- [120] Van Oss, C.J., Chaudhury, M.K. and Good, R.J. Interfacial Lifshitz-van der Waals and polar interactions in macroscopic systems. *Chemical reviews*, **88**(6):927–941, (1988).
- [121] Zisman, W.A. Relation of the Equilibrium Contact Angle to Liquid and Solid Constitution. In F. M. Fowkes, editor, *Contact Angle, Wettability, and Adhesion*, chapter 1, pages 1–51. (1964).

- [122] Kiselev, A.V. and Yashin, Y.I. *Gas-adsorption chromatography*. Springer, 2013.
- [123] Card, T.W., Al-Saigh, Z.Y. and Munk, P. Inverse gas chromatography. 2. The role of “inert” support. *Macromolecules*, **18**(5):1030–1034, (1985).
- [124] Demertzis, P.G., Riganakos, K.A. and Kontominas, M.G. Water sorption isotherms of crystalline raffinose by inverse gas chromatography. *International Journal of Food Science & Technology*, **24**(6):629–636, (1989).
- [125] Lloyd, D.R., Ward, T.C. and Schreiber, H.P. *Inverse gas chromatography*. American Chemical Society, Washington, D.C., (1989).
- [126] Price, G.J. Calculation of solubility parameters by inverse gas chromatography. pages 48–58. In ACS symposium series, Oxford University Press, (1989).
- [127] Voelkel, A., Strzemiecka, B., Adamska, K. and Milczewska, K. Inverse gas chromatography as a source of physicochemical data. *Journal of Chromatography A*, **1216**(10):1551–1566, (2009).
- [128] Schultz, J.A., Lavielle, L. and Martin, C. The role of the interface in carbon fibre-epoxy composites. *The Journal of Adhesion*, **23**(1):45–60, (1987).
- [129] Schultz, J. Inverse gas chromatography-characterization of polymers and other materials. pages 185–202. In ACS symposium series, ACS Publications, (1989).
- [130] Voelkel, A. Physicochemical measurements (inverse gas chromatography). In Poole C., editor, *Gas Chromatography*, pages 477–494. Elsevier, Waltham, MA, USA, (2012).
- [131] Ho, R. and Heng, J.Y. A review of inverse gas chromatography and its development as a tool to characterize anisotropic surface properties of pharmaceutical solids. *KONA Powder and Particle Journal*, **30**:164–180, (2013).
- [132] Voelkel, A. Inverse gas chromatography in the examination of acid-base and some other properties of solid materials. In *Studies in Surface Science and Catalysis*, volume 99, pages 465–477. Elsevier, (1996).

- [133] Fowkes, F.M. Attractive forces at interfaces. *Industrial and Engineering Chemistry*, **56**(12):40–52, (1964).
- [134] Gamble, J.F., Leane, M., Olusanmi, D., Tobbyn, M., Šupuk, E., Khoo, J. and Naderi, M. Surface energy analysis as a tool to probe the surface energy characteristics of micronized materials - A comparison with inverse gas chromatography. *International journal of pharmaceuticals*, **422**(1-2):238–244, (2012).
- [135] Sing, K.S.W., Everett, D.H., Haul, R.A.W., Moscou, L., Pierotti, R.A., Rouquerol J. and Siemieniewska, T. Reporting Physisorption Data for Gas/Solid Systems with Special Reference to the Determination of Surface Area and Porosity. *Pure and Applied Chemistry*, **57**(4):603–619, (1985).
- [136] Langmuir, I. The adsorption of gases on plane surfaces of glass, mica and platinum. *Journal of the American chemical society*, **40**(9):1361–1403, (1918).
- [137] Brunauer, S., Emmett, P.H. and Teller, E. Adsorption of gases in multimolecular layers. *Journal of the American chemical society*, **60**(2):309–319, (1938).
- [138] de Boer, J.H., Lippens, B.C., Linsen, B.G., Broekhoff, J.C.P., Van den Heuvel, A. and Osinga, T.J. The  $t$ -curve of multimolecular  $N_2$ -adsorption. *Journal of Colloid and Interface Science*, **21**(4):405–414, (1966).
- [139] Barrett, E.P., Joyner, L.G. and Halenda, P.P. The determination of pore volume and area distributions in porous substances. I. Computations from nitrogen isotherms. *Journal of the American Chemical society*, **73**(1):373–380, (1951).
- [140] Provencher, S.W. CONTIN: a general purpose constrained regularization program for inverting noisy linear algebraic and integral equations. *Computer Physics Communications*, **27**(3):229–242, (1982).
- [141] Provencher, S.W. A constrained regularization method for inverting data represented by linear algebraic or integral equations. *Computer Physics Communications*, **27**(3):213–227, (1982).

- [142] Mayers, J. and Reiter, G. The VESUVIO electron volt neutron spectrometer. *Measurement Science and Technology*, **23**(4):045902, (2012).
- [143] Mayers, J. and Abdul-Redah, T. The measurement of anomalous neutron inelastic cross-sections at electronvolt energy transfers. *Journal of Physics: Condensed Matter*, **16**(28):4811–4832, (2004).
- [144] Andreani, C., Colognesi, D., Mayers, J., Reiter, G.F. and Senesi, R. Measurement of momentum distribution of lightatoms and molecules in condensed matter systems using inelastic neutron scattering. *Advances in Physics*, **54**(5):377–469, (2005).
- [145] Lovesey, S.W. *Theory of Neutron Scattering from Condensed Matter. Vol. 1: Nuclear Scattering*, volume 1: Nuclear Scattering. Oxford University Press, (1984).
- [146] Sears, V.F. Scaling and final-state interactions in deep-inelastic neutron scattering. *Physical Review B*, **30**(1):44–51, (1984).
- [147] Weibull, W. A statistical distribution function of wide applicability. *Journal of applied mechanics*, **18**(3):293–297, (1951).
- [148] Grim, R.E. *Clay mineralogy*. McGraw-Hill Book Company, Inc; New York; Toronto; London, (1953).
- [149] Murray, H.H. *Applied clay mineralogy: occurrences, processing and applications of kaolins, bentonites, palygorskitesepiolite, and common clays*, volume 2. Elsevier, (2006).
- [150] Brigatti, M.F., Galan, E. and Theng, B.K.G. Structure and mineralogy of clay minerals. In *Developments in clay science*, volume 5, pages 21–81. Elsevier, (2013).
- [151] Schneider, C.A., Rasband, W.S. and Eliceiri, K.W. NIH Image to ImageJ: 25 years of image analysis. *Nature methods*, **9**(7):671–675, (2012).

- [152] Gournis, D., Lappas, A., Karakassides, M.A., Töbrens, D. and Moukarika, A. A neutron diffraction study of alkali cation migration in montmorillonites. *Physics and Chemistry of Minerals*, **35**(1):49–58, (2008).
- [153] Breu, J., Seidl, W. and Stoll, A. Fehlordnung bei smectiten in abhängigkeit vom zwischenschichtkation [Disorder in smectites in dependence of the interlayer cation.]. *Zeitschrift für anorganische und allgemeine Chemie*, **629**(3):503–515, (2003).
- [154] Meunier, A. *Clays*. Springer Science & Business Media, (2005).
- [155] Lin-Vien, D., Colthup, N.B., Fateley, W.G. and Grasselli, J.G. *The handbook of infrared and Raman characteristic frequencies of organic molecules*. Academic Press Limited, London, United Kingdom, (1991).
- [156] Bergaya, F. and Vayer, M. CEC of clays: measurement by adsorption of a copper ethylenediamine complex. *Applied Clay Science*, **12**(3):275–280, (1997).
- [157] Andriani, Y., Jack, K.S., Gilbert, E.P., Edwards, G.A., Schiller, T.L., Strounina, E., Osman, A.F. and Martin, D.J. Organization of mixed dimethyldioctadecylammonium and choline modifiers on the surface of synthetic hectorite. *Journal of colloid and interface science*, **409**:72–79, (2013).
- [158] Van Oss, C.J., Good, R.J. and Chaudhury, M.K. The role of van der Waals forces and hydrogen bonds in hydrophobic interactions between biopolymers and low energy surfaces. *Journal of colloid and Interface Science*, **111**(2):378–390, (1986).
- [159] Della Volpe, C. and Siboni, S. Acid-base surface free energies of solids and the definition of scales in the Good-van Oss-Chaudhury theory. *Journal of Adhesion Science and Technology*, **14**(2):235–272, (2000).
- [160] Packham, D.E. Work of adhesion: contact angles and contact mechanics. *International journal of adhesion and adhesives*, **16**(2):121–128, (1996).

- [161] Kuila, U. and Prasad, M. Specific surface area and pore-size distribution in clays and shales. *Geophysical Prospecting*, **62**(2-Rock Physics for Reservoir Exploration, Characterisation and Monitoring):341–362, (2013).
- [162] Carrado, K.A., Thiyagarajan, P. and Elder, D.L. Polyvinyl alcohol-clay complexes formed by direct synthesis. *Clays and clay minerals*, **44**(4):506–514, (1996).
- [163] Auer, H. and Hofmann, H. Pillared clays: characterization of acidity and catalytic properties and comparison with some zeolites. *Applied Catalysis A: General*, **97**(1):23–38, (1993).
- [164] Dogan, M., Dogan, A.U., Yesilyurt, F.I., Alaygut, D., Buckner, I. and Wurster, D.E. Baseline studies of the Clay Minerals Society special clays: specific surface area by the Brunauer Emmett Teller (BET) method. *Clays and clay minerals*, **55**(5):534–541, (2007).
- [165] Mielenz, R.C., Schieltz, N.C. and King, M.E. Thermogravimetric analysis of clay and clay-like minerals. *Clays and Clay Minerals*, **2**(1):285–314, (1953).
- [166] Novoselov, K.S., Jiang, D., Schedin, F., Booth, T.J., Khotkevich, V.V., Morozov, S.V. and Geim, A.K. Two-dimensional atomic crystals. *Proceedings of the National Academy of Sciences*, **102**(30):10451–10453, (2005).
- [167] Zheng, J., Zhang, H., Dong, S., Liu, Y., Nai, C.T., Shin, H.S., Jeong, H.Y., Liu, B. and Loh, K.P. High yield exfoliation of two-dimensional chalcogenides using sodium naphthalenide. *Nature communications*, **5**:2995, (2014).
- [168] Zeng, Z., Yin, Z., Huang, X., Li, H., He, Q., Lu, G., Boey, F. and Zhang, H. Single-Layer Semiconducting Nanosheets: High-yield preparation and device fabrication. *Angewandte Chemie International Edition*, **50**(47):11093–11097, (2011).
- [169] Coleman, J.N., Lotya, M., O'Neill, A., Bergin, S.D., King, P.J., Khan, U., Young, K., Gaucher, A., and De, S., Smith, R.J., Shvets, I.V., Arora, S.K., Stanton, G.,

- Kim, H., Lee, K., Kim, G.T., Duesberg, G.S., Hallam, T., Boland, J.J., Wang, J., Donegan, J.F., Grunlan, J.C., Moriarty, G., Shmeliov, A. Nicholls, R.J., Perkins, J.M., Grieveson, E.M., Theuwissen, K., McComb, D.W., Nellist, P.D. and Nicolosi, V. Two-Dimensional Nanosheets Produced by Liquid Exfoliation of Layered Materials. *Science*, **331**(6017):568–751, (2011).
- [170] Lotya, M., Hernandez, Y., King, P.J., Smith, R.J., Nicolosi, V., Karlsson, L.S., Blighe, F.M., De, S., Wang, Z., McGovern, I.T. and Duesberg, G.S. Liquid phase production of graphene by exfoliation of graphite in surfactant/water solutions. *Journal of the American Chemical Society*, **131**(10):3611–3620, (2009).
- [171] Smith, R.J., King, P.J., Lotya, M., Wirtz, C., Khan, U., De, S., O’Neill, A., Duesberg, G.S., Grunlan, J.C., Moriarty, G., Wang, J., Minett, A.I., Nicolosi, V. and Chen, J. Large-scale exfoliation of inorganic layered compounds in aqueous surfactant solutions. *Advanced materials*, **23**(34):3944–3948, (2011).
- [172] Atkins, P. and De Paula, J. *Elements of physical chemistry*. Oxford University Press, USA, (2013).
- [173] Khanam, P.N. and AlMaadeed, M.A.A. Processing and characterization of polyethylene-based composites. *Advanced Manufacturing: Polymer & Composites Science*, **1**(2):63–79, (2015).
- [174] Ahmed Dabbak, S., Illias, H., Ang, B., Abdul Latiff, N. and Makmud, M. Electrical properties of polyethylene/polypropylene compounds for high-voltage insulation. *Energies*, **11**(6):1448, (2018).
- [175] Ieda, M. Dielectric breakdown process of polymers. *IEEE Transactions on Electrical Insulation*, **EI-15**(3):206–224, (1980).
- [176] Sanchis, M.R., Blanes, V., Blanes, M., Garcia, D. and Balart, R. Surface modification of low density polyethylene (LDPE) film by low pressure O<sub>2</sub> plasma treatment. *European Polymer Journal*, **42**(7):1558–1568, (2006).

- [177] De Gennes, P. and Brochard-Wyart, F. and Quéré, D. *Capillarity and wetting phenomena: drops, bubbles, pearls, waves*. Springer Science & Business Media, (2013).
- [178] Fisher, J., Reeves, E.A., Isaac, G.H., Saum, K.A. and Sanford, W.M. Comparison of the wear of aged and non-aged ultrahigh molecular weight polyethylene sterilized by gamma irradiation and by gas plasma. *Journal of Materials Science: Materials in Medicine*, **8**(6):375–378, (1997).
- [179] Gancarz I, Pozniak G, Bryjak M. Modification of polysulfone membranes: 3. Effect of nitrogen plasma. *European Polymer Journal*, **36**(8):1563–1569, (2000).
- [180] Richardson, J.J., Cui, J., Bjornmalm, M., Braunger, J.A., Ejima, H. and Caruso, F. Innovation in layer-by-layer assembly. *Chemical reviews*, **116**(23):14828–14867, (2016).
- [181] Gao, F. Clay/polymer composites: the story. *Materials Today*, **7**(11):50–55, (2004).
- [182] Hussain, F., Hojjati, M., Okamoto, M. and Gorga, R.E. Polymer-matrix nanocomposites, processing, manufacturing, and application: an overview. *Journal of Composite Materials*, **40**(17):1511–1575, (2006).
- [183] Hui, L., Schadler, L.S. and Nelson, J.K. The influence of moisture on the electrical properties of crosslinked polyethylene/silica nanocomposites. *IEEE Transactions on Dielectrics and Electrical Insulation*, **20**(2):641–653, (2013).
- [184] Radoń, A. and Włodarczyk, P. Influence of water on the dielectric properties, electrical conductivity and microwave absorption properties of amorphous yellow dextrin. *Cellulose*, **26**(5):2987–2998, (2019).
- [185] Silva, A.A., Dahmouche, K. and Soares, B.G. Nanostructure and dynamic mechanical properties of silane-functionalized montmorillonite/epoxy nanocomposites. *Applied Clay Science*, **54**(2):151–158, (2011).

- [186] Yu, J., Li, S., Hou, D., Jin, Z. and Liu, Q. Hydrophobic silane coating films for the inhibition of water ingress into the nanometer pore of calcium silicate hydrate gels. *Physical Chemistry Chemical Physics*, **21**(35):19026–19038, (2019).
- [187] Tomer, V., Polizos, G., Randall, C.A. and Manias, E. Polyethylene nanocomposite dielectrics: implications of nanofiller orientation on high field properties and energy storage. *Journal of Applied Physics*, **109**(7):074113, (2011).
- [188] Alkan, Ü., Karabul, Y., Bulgurcuoğlu, A.E., Kiliç, M., Özdemir, Z.G. and İçelli, O. Polypropylene/basalt thick film composites: structural, mechanical and dielectric properties. *e-Polymers*, **17**(5):417–425, (2017).
- [189] Praeger, M., Vaughan, A.S. and Swingler, S.G. A dielectric spectroscopy study of the polystyrene/nanosilica model system. In *2013 IEEE International Conference on Solid Dielectrics (ICSD)*, pages 859–862, (2013).
- [190] Hasegawa, Y., Ohki, Y., Fukunaga, K., Mizuno, M. and Sasaki, K. Complex Permittivity Spectra of Various Insulating Polymers at Ultrawide-Band Frequencies. *Electrical Engineering in Japan*, **198**(3):11–18, (2017).
- [191] Zhou, L. Private communication, (2019).
- [192] Montanari, G.C., Palmieri, F., Testa, L., Motori, A., Saccani, A. and Patuelli, F. Polarization processes of nanocomposite silicate-EVA and PP materials. *IEEE Transactions on Fundamentals and Materials*, **126**(11):1090–1096, (2006).
- [193] Kaatze, U. Complex permittivity of water as a function of frequency and temperature. *Journal of Chemical Engineering Data*, **34**(4):371–374, (1989).
- [194] Varghese, S., Kannam, S.K., Hansen, J.S. and P. Sathian, S. Effect of hydrogen bonds on the dielectric properties of interfacial water. *Langmuir*, **35**(24):8159–8166, (2019).

- [195] Das, S. and Ghosh, A. Ionic conductivity and dielectric permittivity of PEO-LiClO<sub>4</sub> solid polymer electrolyte plasticized with propylene carbonate. *AIP Advances*, **5**(2):027125, (2015).
- [196] Wang, S.J., Zha, J.W., Li, W.K. and Dang, Z.M. Distinctive electrical properties in sandwich-structured Al<sub>2</sub>O<sub>3</sub>/low density polyethylene nanocomposites. *Applied Physics Letters*, **108**(9):092902, (2016).
- [197] Pallon, L.K.H., Hoang, A.T., Pourrahimi, A.M., Hedenqvist, M.S., Nilsson, F., Gubanski, S., Gedde, U.W. and Olsson, R.T. The impact of MgO nanoparticle interface in ultra-insulating polyethylene nanocomposites for high voltage DC cables. *Journal of Materials Chemistry A*, **4**(22):8590–8601, (2016).
- [198] Pourrahimi, A.M., Hoang, T.A., Liu, D., Pallon, L.K., Gubanski, S., Olsson, R.T., Gedde, U.W. and Hedenqvist, M.S. Highly efficient interfaces in nanocomposites based on polyethylene and ZnO nano/hierarchical particles: A novel approach toward ultralow electrical conductivity insulations. *Advanced Materials*, **28**(39):8651–8657, (2016).
- [199] Hayden, J.L.R. and Eddy, W.N. Dielectric strength ratio between alternating and direct voltages. *Journal of the American Institute of Electrical Engineers*, **42**(7):706–712, (1923).
- [200] Li, W.G., Liu, Z.K., Wei, B., Qiu, M., Gao, X.J., Gao, C., Zhao, Y.Q., Li, S., Hou, J.Z. and Chen, P.P. Comparison between the DC and AC breakdown characteristics of dielectric sheets in liquid nitrogen. *IEEE Transactions on Applied Superconductivity*, **24**(6):1–6, (2014).
- [201] Koo, J.H., Hwang, J.S., Shin, W.J., Sakamoto, K., Oh, D.H. and Lee, B.W. Comparison of DC and AC surface breakdown characteristics of GFRP and epoxy nanocomposites in liquid nitrogen. *IEEE Transactions on Applied Superconductivity*, **26**(4):1–4, (2016).

- [202] Li, S., Zhu, Y., Min, D. and Chen, G. Space charge modulated electrical breakdown. *Scientific reports*, **6**:32588, (2016).
- [203] Eesaee, M., David, E., Demarquette, N.R. and Fabiani, D. Electrical breakdown properties of clay-based LDPE blends and nanocomposites. *Journal of Nanomaterials*, **2018**, (2018).
- [204] Awang, N.A., Ahmad, M.H., Malek, Z.A., Sidik, M.A.B., Nawawi, Z., Jambak, M.I. and Walidi, E.P. AC breakdown strength enhancement of LDPE nanocomposites using atmospheric pressure plasma. In *2017 International Conference on Electrical Engineering and Computer Science (ICECOS)*, pages 290–294. IEEE, (2017).
- [205] Van Olphen, H. Rheological phenomena of clay sols in connection with the charge distribution on the micelles. *Discussions of the Faraday Society*, **11**:82–84, (1951).
- [206] Qian, Z., Hu, G., Zhang, S. and Yang, M. Preparation and characterization of montmorillonite-silica nanocomposites: A sol-gel approach to modifying clay surfaces. *Physica B: Condensed Matter*, **403**(18):3231–3238, (2008).
- [207] Niederberger, M. Nonaqueous sol-gel routes to metal oxide nanoparticles. *Accounts of chemical research*, **40**(9):793–800, (2007).
- [208] Singh, L.P., Bhattacharyya, S.K., Kumar, R., Mishra, G., Sharma, U., Singh, G. and Ahalawat, S. Sol-Gel processing of silica nanoparticles and their applications. *Advances in colloid and interface science*, **214**:17–37, (2014).
- [209] Jelinek, J-T. Developing ultra-light foam with different properties using 2-D structured nanomaterials . Master’s thesis, Department of Chemistry & Forensic Science, Nottingham Trent University, (2019).
- [210] Yuan, Q. and Misra, R.D.K. Polymer nanocomposites: current understanding and issues. *Materials Science and Technology*, **22**(7):742–755, (2006).

- [211] Fu, S., Sun, Z., Huang, P., Li, Y. and Hu, N. Some basic aspects of polymer nanocomposites: A critical review. *Nano Materials Science*, **1**(1):2–30, (2019).